NOTE TO USERS

This reproduction is the best copy available.

UMI®

AN INVESTIGATION OF IRON LOSSES DUE TO ROTATING FLUX IN THREE PHASE INDUCTION MOTOR CORES

By

NICK STRANGES, B. Eng., M. Eng.

A Thesis Submitted to the School of Graduate Studies in Partial Fulfilment of the Requirements for the Degree Doctor of Philosophy

McMaster University

IRON LOSSES DUE TO ROTATING FLUX IN INDUCTION MOTOR CORES

DOCTOR OF PHILOSOPHY (2000)
(Electrical Engineering)

McMaster University
Hamilton, Ontario

TITLE: An Investigation of Iron Losses Due to Rotating Flux in Three Phase Induction Motor Cores

AUTHOR: Nick Stranges, B. Eng., M. Eng. (McMaster University)

SUPERVISOR: Professor Raymond D. Findlay

NUMBER OF PAGES: xxiii, 275

Abstract

In the past, the discrepancy between predicted and measured core loss values has led to the use of empirical scaling factors to improve correlation. Accurate prediction of core loss is important in the design of electrical machinery. Machine customers often demand guaranteed efficiency values at the quotation stage. If the guaranteed value is missed on delivery, they may impose penalties of as much as $5000 for every additional kW of loss. This thesis addresses one possible source of this discrepancy, that is, the failure to account for rotational iron losses.

A significant portion of an induction motor stator is exposed to flux that rotates in the plane of the machine laminations. Iron losses in rotating magnetic fields differ from those obtained under alternating flux conditions and are not accurately estimated from alternating loss measurements. In recent years, a great deal of research has occurred for the explicit purpose of developing a standardized test for measuring rotational iron losses. Work in this field has been motivated by the opinion that rotational iron loss data will be used by machine designers to refine the accuracy of core loss predictions in rotating machines. The hypothesis of this dissertation is that if iron losses due to rotational flux in the stator are calculated rigorously, some portion of the discrepancy between tested and calculated values of no-load iron loss will be accounted for. To test this hypothesis, the iron losses due to the fundamental frequency variation of the flux density have been calculated in several ways. The stator losses were calculated using alternating loss data available from standard tests and by rigorously accounting for the losses caused by rotational flux. While some differences have been noted, they are too small to account for any major portion of the discrepancy between tested and

calculated values of no-load core loss. The results of our investigation show the hypothesis to be false. If a standardized test apparatus for making rotational iron loss measurements were realized in the near future, it would benefit producers of electrical sheet and provide useful information to machine designers. However, as this investigation will show, the refinement to core loss calculation methodologies will not likely improve the correlation of tested to calculated values of core loss.

Acknowledgments

I would like to thank my supervisor, Dr. Raymond Findlay for his guidance, support, patience and encouragement during this research. Many thanks to the faculty and staff of the Power Research Laboratory. My stay at the Laboratory has provided wonderful memories.

The author would like to thank Mr. James H. Dymond of GE Canada for the many informative discussions on induction motors and machine design. He has been a superb mentor. Dr. Raymond Ong of GE Canada has also contributed greatly to the author's understanding of induction motors. Dr. Haran Karmaker, of the Engineering Laboratory in Peterborough, has contributed many informative discussions and explanations on the topic of loss mechanisms in synchronous machines. His breadth of knowledge concerning the topic has served as a great inspiration to the author. I also thank Dr. Konrad Weeber, a former employee of the Hydro Generator Engineering group. Konrad has served as an excellent mentor in the area of electromagnetic and electric machine theory. He is a rare individual who combines a superb understanding of theory with practical engineering ability. Many thanks to the management of the Engineering Department in Large Motors Technology, GE Peterborough for their constant support during my studies.

I thank Meredith Clark, my fiancee, for her constant support, patience, encouragement and understanding. Many thanks to my family for their encouragement. I especially thank my fellow graduate students in the Electrical and Computer Engineering Department for many helpful discussions and suggestions. Thank you Fran Hustak, Cheryl Gies, Barb MacDonald, Steve Spencer, Adam Mirianski, and Ray Gillan. You are the best support staff on campus.

I sincerely thank the Natural Science and Engineering Research Council of Canada for the financial support of this project.

Table of Contents

List of Figures

List of Tables

List of Symbols and Variable Names

a	Aspect ratio of an elliptical flux locus. Magnitude of the minor axis divided by the magnitude of the major axis.
a_n, b_n, c_n, ϕ_n	Fourier series coefficients.
A	Magnetic vector potential, magnitude (Wb/m).
$\overline{A}$	Magnetic vector potential (Wb/m).
A_{gap}	Air gap sectional area per pole (m^2).
A_H	Cross sectional area of a tangential field sensing coil (m^2).
$A_{tooth\ top}$	Average stator tooth sectional area per pole at the top half of the tooth (T).
$A_{tooth\ bottom}$	Average stator tooth sectional area per pole at the bottom half of the tooth (T).
A_{yoke}	cross sectional area of the stator yoke (m^2).
A_{tooth}	Average stator tooth sectional area per pole (m^2)
B	Flux density, magnitude (T).
$\overline{B}$	Flux density, vector (T).
$B_{tooth\ top}$	Average flux density for the top half of the tooth (T).
$B_{tooth\ bottom}$	Average flux density for the bottom half of the tooth (T).
B_1	Fundamental frequency component of a flux density waveform (T).
B_{maj}	Flux density along major axis of elliptically polarized flux density loci (T).
B_{rad}	Radial component of flux density (T).
B_{tan}	Tangential component of flux density (T).
Bore	Inside punching diameter or bore of the stator (m).
B_{yoke}	Stator yoke flux density (T).
B_{gap}	Air gap flux density (T).
B_{tooth}	Average flux density for entire tooth (T).
ΔB_T	Normalized sum of flux density reversals.
ΔB_i	Flux density reversal (T).
C_{s2}	Rotor iron loss coefficient.
D	Sample thickness (m).
d	Domain spacing (m).
D_{gap}	Air gap diameter (m),
DT	Depth of the stator slot (m).
D_2,E_4,F_6	Constants used to describe torque per unit volume of a sample.
E	Electric field strength, magnitude (V/m).
$\overline{E}$	Electric field strength, vector (V/m).
f	Frequency (Hz).
f_{slot}	Slot passing frequency (Hz).
$\overline{\mathcal{F}}$	Magnetomotive force (A-turn).

gap	Radial length of the air gap (m).
H	Magnetic field strength, magnitude (A/m).
$\overline{H}$	Magnetic field strength, vector (A/m).
I_{coil}	Coil current (A).
I_{NL}	No-load current (A).
j	Imaginary number, $j = \sqrt{-1}$
J	Current density, magnitude (A/m^2).
$\overline{J}$	Current density, vector (A/m^2).
$\overline{J}_m$	Magnetic polarization or intrinsic flux density (T). $\overline{J} = \overline{B} - \mu_0\overline{H}$
k_{ar}	Coefficient of rotational anomalous loss (W/kg).
k_{ha}	Empirical loss factor used in Steinmetz equation for determining alternating hysteresis loss.
$K_{anomalous}$	Anomalous loss factor.
k_a	Empirical constant used to estimate the anomalous loss.
K_{hyst}	Loss factor that corrects for minor loops.
k_{hc}	Correlation constant used to calculated K_{hyst}.
k_h	Hysteresis coefficient.
k_e	Eddy current coefficient.
K_{eddy}	Loss factor that corrects for the harmonics.
K_0, K_1, K_2	Anisotropy constants.
k_{stress}	A constant that accounts for punching stresses.
K_{iron}	Iron loss coefficient.
K_p	Winding pitch factor.
K_d	Winding distribution factor.
K_{pf}	Pole face loss coefficient.
L	Length and width of a square sample (m).
ℓ	Length of a coil (m).
L_{stack}	Stack length of the machine (m).
N	Number of turns.
n_w	Volume fraction of the sample where independent wall motions occur.
n_s	Volume fraction of the sample where domain rearrangements occur.
n_c	Volume fraction of the sample associated with reversible rotations of the domain magnetic moments (coherent rotations).
Nc	Number of conductor turns in series per phase.
N_{ducts}	Number of radial cooling ducts in the stack.
OD	Outside diameter of the stator (m)
$p(t)$	Instantaneous power (W).
P_{eddy}	Eddy current loss (W/kg).
P_{ha}	Hysteresis loss due to alternating flux density (W/kg).
P_r	Power loss due to rotating flux density (W/kg).

P_t	Total power loss due to rotating flux density with arbitrary locus (W/kg).
P_{th}	Total (sum of alternating and rotational) hysteresis loss (W/kg).
P_{tc}	Total (sum of alternating and rotational) classical eddy current loss (W/kg).
P_{ta}	Total (sum of alternating and rotational) anomalous loss (W/kg).
P_{cr}	Rotational classical eddy current loss (W/kg).
P_{ar}	Rotational anomalous loss.
P_{hr}	Hysteresis loss due to rotating flux density (W/kg).
P_{he}	Hysteresis loss due to elliptically polarized flux density (W/kg).
$P_{anomalous}$	Anomalous loss (W/kg).
P_{a0}	Empirical constant used to estimate the anomalous loss.
$P_{eddy,\ dist}(B_p)$	Eddy current loss for distorted waveform having a peak flux density B_p.
$P_{eddy,\ sine}(B_p)$	Eddy current loss for sinusoidal waveform having peak value B_p.
$P_{hyst,\ dist}(B_p)$	Hysteresis loss for distorted waveform having a peak flux density B_p.
$P_{hyst,\ sine}(B_p)$	Hysteresis loss for sinusoidal waveform having peak value B_p.
%P	Percent increase in the hysteresis loss averaged over the entire lamination width due to punching stresses.
P_{alt}	Power losses due to alternating magnetic flux (W/kg).
P_{yoke}	Iron losses in the stator yoke (W).
poles	Number of machine poles.
$P_{tooth\ top}$	Iron loss in the top portions of the stator teeth (W).
$P_{tooth\ bottom}$	Iron loss in the bottom portions of the stator teeth (W).
$P_{surface}$	Surface losses (W).
$R(\omega t)$	Instantaneous magnitude of an elliptical locus.
r_h	Ratio of rotational to alternating hysteresis loss determined by experiment.
r_e	Ratio of rotational to alternating excess loss determined by experiment.
$\overline{S}$	Poynting vector (W/m^2).
SFS	Stator stacking factor to account for lamination coating.
S_1	Number of stator slots.
t	Sheet thickness (m).
T	Period for one cycle of magnetization (s).
$\overline{T}$	Torque per unit volume of a sample (N/m^2).
T_H	Constant torque per unit volume of a sample due to rotational hysteresis (N/m^2).
T_a	Anisotropy torque per unit volume of a sample (N/m^2).
T_1	Torque per unit volume of a sample for one direction of rotation (N/m^2).
T_2	Torque per unit volume of a sample for opposite direction of rotation (N/m^2).
T_{avg}	Average stator tooth width (m).
v(t)	Voltage as a function of time (V).
V_{rms}	Root mean square voltage (V).
V_{ave}	Average value of a voltage (V).
W	Width of the lamination in inches between the cut edges.

W_{wr}	Energy loss (J/cycle) attributed to reversible domain wall motion.
W_{ha}	Alternating hysteresis energy loss (J/cycle).
W_{hr}	Rotational hysteresis energy loss (J/cycle).
W_{sr}	Energy loss (J/cycle) attributed to irreversible domain wall motion.
$W_{anisotropy}$	Anisotropy energy (J).
W_{tooth}	Width of the stator tooth at top of the slot (closest to air gap) (m).
W_{ducts}	Width of the radial cooling ducts (m)
W_{TY}	Width of the tooth at the yoke (m).
W_{TB}	Width of the stator tooth at the bore (m).
W_{TM}	Width of the stator tooth width at middle of the tooth length (m).
α,β,γ	Used to find $R(\omega t)$.
α_{lag}	Lag angle between magnetic polarization $\bar{J}_m$ and magnetic field strength in a rotating magnetic field.
$\alpha_1, \alpha_2, \alpha_3$	Direction cosines.
$\delta_2, \delta_4, \delta_6$	Constants used to describe torque per unit volume of a sample.
ζ	Empirical exponent used in Steinmetz equation.
θ	Inclination angle.
λ_1	Stator slot pitch (m).
μ	Permeability (H/m).
μ_0	Permeability of free space $4\pi x10^{-7}$ (H/m).
μ_r	Relative permeability.
ν	Reluctance (m/H).
$\frac{d\Pi}{dt}$	Instantaneous angular velocity a rotating flux density vector (rad/s).
ρ	Mass density (kg/m^3).
ρ_{res}	Resistivity (Ω-m).
σ	Conductivity (S).
Φ	Magnetic flux (Wb).
ω	Angular frequency = $2\pi f$ (rad/s)

List of Abbreviations

BC	Boundary condition
CRC	Cold rolled carbon
DF	Distortion Factor
FE	Finite Element
FEA	Finite Element Analysis
FEM	Finite Element Method
GO	Grain Oriented
FP	Fully Processed
MLQ	Motor Lamination Quality
NA	Not Applicable
NO	Non-oriented
nd	Normal direction
rd	Rolling direction
rms	Root mean square
SP	Semi-processed
td	Transverse direction
TH	Time-harmonic
TS	Time-stepped
TSM	Time-stepped magnetostatic

Chapter 1

Introduction

1.0 General Description of Induction Motors and the Importance of Accurate Core Loss Predictions

Induction motors are the "workhorses" of modern industry. They are used to convert electrical power into mechanical power in such applications as fans, compressors, ore crushing mills, conveyor belts, ship propellers, hoists, excavators, locomotives, and pumps to name only a few. A polyphase induction motor needs only a source of polyphase power to operate. Polyphase currents in the stator (the stationary portion of the machine core) produce a synchronously rotating flux wave. Relative motion between the stator flux wave and the machine rotor (the rotating portion of the machine) causes an induced voltage in the rotor winding. This induced voltage creates currents in the rotor winding. These induced rotor currents interact with the synchronously rotating stator field to produce torque. In this way, an induction machine may be started from a standstill; the mechanical load will accelerate until the speed of the rotor approaches that of the synchronously rotating flux wave. The rotor will always rotate slightly slower than the stator flux wave during operation, so that rotor currents will be produced by induction, and accordingly the machine will produce torque. The percentage difference in speed between the synchronous speed and the speed of the machine is called the machine "slip."

A rotating magnetic field is central to the operation of the induction machine. The field originates in the stator windings, travelling around the core, across the air gap, and back through the rotor. The magnetic core of the machine consists of the stator and rotor; both are built up from magnetic laminations. Slots are punched into the laminations to allow the

insertion of stator and rotor windings. Within the core of the machine, the rotating magnetic field causes the core to heat up because of magnetic hysteresis and induced eddy currents.

Even after a century of experience in building induction machines, the ability to predict no-load core losses consistently, eludes the modern design engineer. The standard deviation of the test to calculated ratios of core loss is large. Very often, the final product will exhibit core losses that are quite different from those predicted by design equations. Any uncertainty in the prediction of the motor performance at the design stage will inevitably pose a dilemma to the machine designer. An accurate estimate of the losses is essential when designing a large machine, (large referring to machines with outputs of several thousand kW or more). If guaranteed efficiencies are not met, some customers will assign substantial penalties on the manufacturer. Penalties as large as $5000/kW are common. Such penalties are imposed with the intent of offsetting the cost of energy associated with the additional losses in the machine. If the design equations overestimate the losses, it means that the designer is over designing the machine, raising the cost of the machine, and reducing the profit margin. If the losses are underestimated at the design stage, the manufacturer may be forced to pay penalties to the customer. Because of the great deal of uncertainty inherent in core loss predictions, many designers will choose a conservative design. The best grades of steel are used in the core, even though in some cases, a less expensive material may suffice. To have any chance of one day being able to predict core losses accurately, a better understanding of the underlying mechanisms producing core loss in machines is required.

Core losses affect not only the ability to predict efficiencies, but temperature distributions within the machine as well. Insulation life is reduced by excessive heat, and reduction of core losses helps reduce the overall temperature rise of the machine. Customers may also demand guaranteed temperature rises. Once the machine is manufactured, a heat run is done and the temperature rise of the machine is determined. If the rise is larger than guaranteed, the situation will be very difficult to improve. A considerable amount of time and

money may be spent trying to improve the ventilation of the machine to reduce the temperature rise. Machine shipment may be delayed, and in extreme cases, the purchaser may refuse the machine altogether. An accurate prediction of core loss helps the designer to predict the temperature rise and efficiency of the machine and avoid these costly situations.

1.1 Problem Definition

Machine designers have long known that the total core loss in a machine is not accurately predicted by the sum of the fundamental frequency losses in the yoke and teeth of the machine. The fundamental frequency losses are predicted by determining the flux density levels in the yoke and teeth of the machine. These flux densities are assumed to be alternating in nature, that is, unidirectional, but varying in magnitude with time. Once the flux densities are estimated, losses are attributed to the yoke and teeth based on iron loss measurements taken under alternating flux conditions. The assumption of alternating flux in the yoke and teeth of the machine is an oversimplification of the complex magnetic field distributions produced in the machine during operation. This may lead to estimates of losses that are incorrect.

One area of research, which has received a great deal of attention, is the study of rotational fluxes in the stator cores of electrical machines. Rotational losses are one component of the overall core losses. They occur at the roots of stator teeth and all along the inner portions of the stator yoke. If the locus of the x and y components of the fundamental frequency flux density is plotted, an ellipse is obtained as illustrated in figure 1.1. In this sense, the flux density is polarized. The flux density can be nearly circularly polarized at the roots of the stator teeth. Behind the stator slots the flux density polarization is more elliptical than circular, hence has less effect. Moving toward the back of the machine, the flux density becomes elliptically polarized all along the yoke of the machine. At the very back of the stator yoke, the flux can be considered purely alternating in nature. In the stator teeth

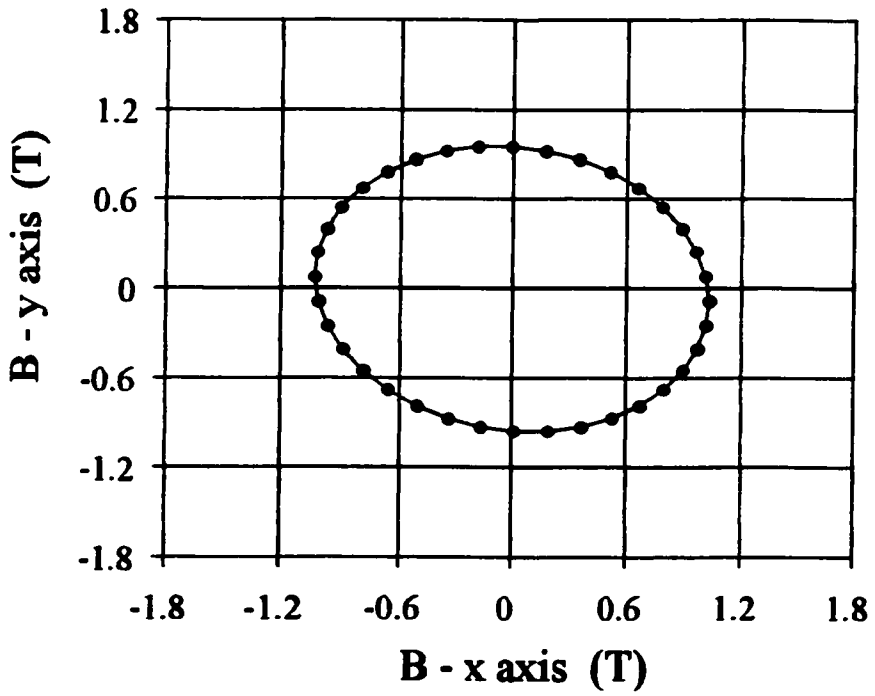

Figure 1.1 - Elliptical flux density polarization at the tooth root of an induction motor.

(outside the roots) the flux density is also alternating. For a given flux density, a rotating magnetic field will produce a higher loss than an alternating one. It is hypothesized that neglecting the effects of rotational losses in the stator of a machine may partially account for the additional losses not predicted by traditional estimation methods. This thesis is aimed at quantifying the impact on core loss predictions, resulting from a rigorous calculation of the fundamental frequency rotational losses.

To predict the fundamental frequency iron losses in a machine core accurately, the designer must have an accurate prediction of the flux density distribution in the machine from which loss data, taken under rotating flux conditions, can be used. Currently, only alternating flux loss data derived from Epstein tests or single sheet testers is available to the designer. The 25-cm Epstein test square with double lapped joints is described in detail in Chapter 4 -

Section 4.1. Measurements of alternating loss in the electrical sheet are determined using several 28 cm by 3 cm strips. The strips are arranged into a square and energized in a manner closely approximating a single phase transformer. Single sheet testers are discussed in Chapter 4 - Section 4.1.2. Measurements of alternating loss in the electrical sheet are performed on a large sheet of material rather than several strips. The international community has not yet agreed upon a standard test for measuring rotational losses, although a great deal of effort has been expended towards this goal as documented in the literature.

1.2 Significance and Motivation

This work is significant because it quantifies the contribution of rotational iron losses to the total no-load core loss in induction motors. A great deal of effort has been expended by the scientific community for the purpose of developing a standardized test for measuring rotational iron losses. Such a test has long been desired for the purpose of improving core loss predictions in rotating electrical machinery. This thesis shows that the inaccuracies caused by ignoring the effects of rotational flux in induction motors stators do not account for a significant portion of the discrepancy between tested and calculated no-load core loss. The underlying motivation towards the development of such a test is consequently drawn under question.

Until this work, the scientific community has believed that the development of a standardized test for making rotational core loss measurements would be of great value to machine designers. A few excerpts from the literature may help to illustrate this. On the proportion of rotational losses to total losses, Moses [1] claims that, "in motors it can amount to more than 50% of the total core loss". Sasaki et al [2] state that, "Rotational power losses are considered to be responsible for the major part of excess loss in the iron core of electrical machines". Fiorillo and Rietto [3] claim that, "The presence of rotational fluxes in the magnetic core of electrical machines is in general associated with extra losses". Enokizono

and Sievert [4] claim that the rotational magnetic flux in stator cores "produces a remarkable portion of the total magnetic loss. It is, therefore, important to measure the rotational loss of electrical steels with the highest possible accuracy". More recently, Zhu and Ramsden [5] state that, "Although it has long been realized that a considerable amount of the total core loss in the stator core of a rotating electrical machine is caused by the rotating magnetic field, alternating core loss models were generally employed [1]-[8] (the authors cite eight references) due to the lack of data and proper models for rotational core losses". Concerning yoke iron losses, Walker [6] states that "an analysis of core loss of some 70 hydroelectric generators showed that in order to allow for the effects of rotational hysteresis this specific loss has to be multiplied by 1.55."

The scientific community has stated the need to classify electrical sheets according to both alternating and rotational losses for quite some time. The belief has been that two electrical sheets with the same loss characteristics under alternating loss conditions do not necessarily have the same loss characteristics under rotational flux conditions. Measurements taken during the course of this work verify this statement. Based on current opinion, the material with the lower rotational losses is apparently preferable for use in a motor core since such a large portion of the stator is exposed to rotational flux. The results of this research show that the reduction of no-load core losses through use of materials with lower rotational losses may be much smaller than previously anticipated.

The time-harmonic (TH) formulation of the finite element method is commonly used to analyse three phase induction motors. In Chapter 6, we will see that the TH formulation yields all the information required to estimate the flux density polarization in every region of the machine stator. Losses due to rotational flux are easily estimated given one TH simulation at no-load condition and a family of measured loss curves. Use of the TH formulation was motivated by the realization that it offered a method by which rotational loss data could be incorporated into the design process with a minimum of computational

overhead. If lamination suppliers could provide rotational loss data via a standardized test, it could be put to practical use using the technique described in Chapter 6.

This research was initially motivated by Dofasco (a major Canadian steel producer). Dofasco wanted a test apparatus that would help in the development of Motor Lamination Quality (MLQ) steels. MLQ steels are inexpensive, low alloy materials specifically intended for use in small motor cores. A test that accurately predicted losses in steel samples under rotating flux conditions was deemed desirable for the purposes of developing materials better suited for use in motor cores. This research also addresses the need to define a way of incorporating rotational loss data into the design procedure. A great deal of work toward the development of a standardized test apparatus has occurred in the international community, but very little information concerning the use of this data during the design stage is available. Furthermore, the impact of rotational losses on overall no-load core loss has not been understood or quantified.

1.3 Contributions

The work compares the use of the time-harmonic finite element method with time-stepped magnetostatic solutions for the purpose of determining the degree of flux density polarization in the different regions of the stator core. The use of the time-harmonic formulation for this purpose is a novel approach to the problem. Comparison of the fundamental frequency flux density loci obtained by the two methods, suggests that the time-harmonic formulation is an acceptable method for determining the fundamental frequency flux density polarization.

This thesis explains a procedure for incorporating the data taken from rotational loss measurements into the design process. Detailed calculations of the fundamental frequency iron losses in five large induction machines are presented. These machines were subsequently built and tested enabling a comparison of test and calculated results. By coupling iron losses

measured under rotating flux conditions with the results of finite element studies, the author has quantified the effects of rotational losses on the overall core loss. Results of calculations for these five machines clearly demonstrate that rotational losses do not account for any large portion of the discrepancy between tested and calculated values of no-load core loss. This result constitutes the major original contribution of the research to the present state of knowledge concerning machine losses. The author believes that this result should encourage researchers to concentrate their efforts towards understanding iron losses to other areas that may lead to more fruitful results.

A further goal of the study was to determine what avenues of research might lead to the development of lower rotational losses in steels. A comprehensive review of the literature has shown that a substantial amount of work aimed at developing a standardized test procedure for making rotational loss measurements has occurred. Such a test has long been desired for the purpose of developing core materials with lower rotational losses. From careful consideration of the literature, the author has observed that the development of magnetic laminations with improved textures may lead to steels with lower rotational losses.

A test apparatus has been developed which allows for the measurement of iron losses under several flux conditions. Losses can be measured under alternating flux conditions at any angle in the plane of the sheet. The apparatus also allows rotational flux measurements to be made for any aspect ratio of polarization. The development of this apparatus does not constitute an original contribution to the state of the art. Many test apparatuses using similar approaches have been investigated by others and are described in the literature (see Chapter 3). Having stated this, the development of the apparatus did constitute a necessary step in the research. Since rotational iron loss data is not available from steel producers, the apparatus was required to measure the rotational iron loss characteristics of the materials used in the cores of the machines under study.

We have compared rotational and alternating loss curves for seven grades of electrical

sheet that are representative of the materials often used in motor cores. A comparative set of data using a single apparatus for all the materials was unavailable in the literature prior to this study. Four grades of non-oriented (NO) silicon steels and three grades of low carbon cold rolled motor lamination quality (MLQ) steels have been tested. The results show that the differences in losses can be substantial depending on whether the flux is alternating or rotational. Measurements also reveal that differences in rotational and alternating losses are dependent on the individual grade of steel. Rotational losses are not accurately predicted from measurements of alternating losses.

1.4 Overview

Chapter 2 reviews the basic concepts of ferromagnetism and how domain theory can be used to explain the differences between alternating losses and rotational losses. The effects of alloying agents and impurities on iron losses are reviewed. Texture is also described. Effects of composition and processing variables on alternating losses are well understood due to vast amounts of work done over many years. The same type of analysis on rotational losses is impeded by the lack of a standardized test. Consequently, little work is reported in the literature, and as a result, mechanisms by which rotational losses might be reduced by steel manufacturers are not well understood. For example, control of texture is identified as a possible means of reducing rotational losses.

Chapter 3 contains a literature review of rotational loss measurements and attempts to quantify the effect of rotational losses in machine cores. The theory of one dimensional (1D) or alternating loss measurements is presented. Rotational or arbitrary direction losses are often called two dimensional (2D) losses. These are also reviewed. Recent advances in rotational loss measurements are described. Advantages and disadvantages of the various techniques are reviewed. Past research concerning the quantification of rotational losses in electric machine cores is also reviewed.

Chapter 4 contains a description of the test apparatus used in this study. The apparatus uses a personal computer for the purposes of waveform generation and data acquisition. Two power supply amplifiers provide the magnetizing current to the test apparatus. The apparatus can produce flux densities of 1.5 T and greater in the samples. Measurements can be made under alternating flux conditions at any angle relative to the rolling direction (rd) of the sample. Various degrees of flux density polarization can be produced in the sample.

Chapter 5 contains the results of alternating and rotational losses made on seven grades of electrical laminations. Test results for three grades of motor lamination quality (MLQ) steels and four grades of non-oriented (NO) steels are presented. For the grade of steel used in the cores of the induction motors under investigation, loss measurements were made for various degrees of elliptically rotating flux. Anisotropy measurements were also made and are presented. All the cores of the machines under investigation are made from the same grade of steel. The measurements on the other six grades of materials were made to provide some insight about how the choice of materials might affect rotational losses in machine cores.

Chapter 6 describes the traditional method of estimating core loss from design equations. The finite element (FE) formulations used in this investigation are also described. A time-harmonic (TH) formulation was used as well as time-stepped magnetostatic (TSM) solutions. We will see that the TH formulation of the finite element method yields all the information necessary to determine the distribution of the fundamental frequency rotational flux in an induction motor core. The TH formulation is well established for the analysis of induction motors. If rotational loss data were made available to machine designers, the data could be incorporated into the design process by the method proposed in Chapter 6 of this thesis. Several methods of estimating the fundamental frequency iron losses in induction motors are compared and contrasted. As stated earlier, the hypothesis tested in this thesis is

that the rotational flux present in the yokes of the induction motors is responsible for some of the discrepancy between the tested and calculated losses. The analysis is limited to the fundamental frequency rotational losses. That is, we expected to establish what the difference in calculated values would be if the rotational losses were calculated rigorously and if the flux density in the stator cores was assumed alternating as is traditionally the case. If the difference obtained under the two assumptions were large, then we could conclude that the assumption of alternating flux was unjustified. As such, the analysis does not include the effects of rotor slotting harmonics nor slot passing frequency currents in the rotor bars. Such losses occur in addition to the fundamental frequency losses and as such were deemed beyond the scope of this particular study. This is not to say that they play a trivial role in the overall core loss of the machines. However, they will need to be addressed in a separate study with a finite element package that allows modelling of rotor motion and induced rotor currents (MagNet 2D Version 5.1a used in this study, has no such facility). Results of core loss calculations for five industrial induction motors are presented and compared with measured values.

Chapter 7 contains conclusions and additional considerations. We have found that for the machines studied and the material used in the cores, the rotational iron losses can be modelled using alternating loss data with little loss of accuracy.

Chapter 2

Electrical Steels

2.0 Introduction

This chapter describes magnetization and loss mechanisms as they relate to electrical lamination steels. To understand loss and magnetization processes in electrical steels, some understanding of ferromagnetic domain theory is necessary. A summary of ferromagnetic domain theory is presented in Appendix A. A clear understanding of the differences in the mechanisms of magnetization, as encountered with alternating and rotating magnetic fields, is also desired. The magnetization process and phenomenological differences between alternating and rotational hysteresis losses are described in Section 2.3.

The second half of the chapter also reviews the metallurgical factors that affect magnetic losses. The influence of alloying agents, impurities, processing variables, and texture on both alternating and rotational losses are reviewed and summarized. Particular attention has been paid to determining areas of basic research that may lead to further reductions of rotational and alternating losses.

2.1 Categories of Electrical Steels

Electrical steels are generally divided into three categories a) grain oriented (GO) silicon, b) non-oriented (NO) silicon, and c) motor lamination quality (MLQ) steels. GO silicon steels have a strong preferred texture in the rolling direction (rd). The preferred crystal orientation in the rd gives the steel superior magnetic properties in that direction when compared with the transverse direction (td). This stems from the superior magnetic properties of iron along the crystal lattice cube edge (see Appendix A and Section 2.5). GO

sheets are used in large high efficiency power and distribution transformers and large high speed generator segments.

NO silicon steels have essentially a random texture with nearly isotropic magnetic properties. These steels are used in rotating electric machines such as motors and generators. NO steels are available in semi-processed (SP) and fully processed (FP) form. End users must anneal SP steels in order to develop the desired magnetic properties. FP steels are shipped from the steel mill fully annealed with fully developed magnetic properties. NO steels generally contain silicon to increase the resistivity of the steel, thereby reducing eddy current losses. They are also usually provided with an insulating coating to reduce eddy currents between laminations.

MLQ steels are a subgroup of NO steels. In the 1950s, cold rolled carbon (CRC) steels were used in the cores of fractional horsepower and intermittent duty motors. Use of expensive silicon steels was not justified, since low core losses and high electrical efficiencies, were not deemed important in the small motor industry at that time. Carbon steels had a relatively low cost in comparison to silicon steels, but their magnetic properties were relatively poor. MLQ steels evolved from the need for an electrical steel that would cost less than silicon steels, but offered magnetic properties superior to those of CRC steels.

2.2 Magnetization Curve of Polycrystalline Ferromagnetic Material

Becker ([7] as cited by Kittel[8], [9-10] as cited by Bozorth [11]), suggested that two independent processes may increase the value of the resultant magnetic moment of a specimen influenced by an applied magnetic field. The two processes are:

1. An increase in the volume of domains that are favourably oriented with the applied field at the expense of unfavourably oriented domains. This is known as "boundary displacement".

2. Rotation of magnetization directions within domains towards the direction of the applied field.

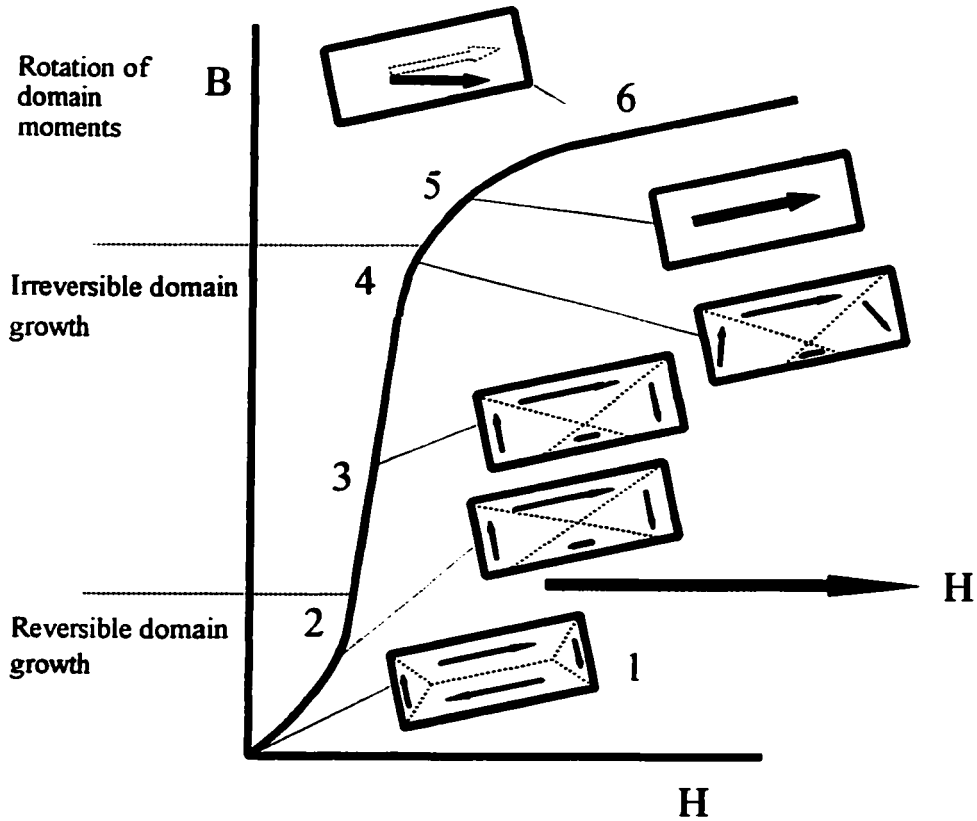

Figure 2.1 - Magnetization curve for a polycrystalline ferromagnetic material. Figure based on figure 6 in Kittel [8], figure 11-4 in Bozorth [11], figure 2 in Littman [12], and figure 9.44 in Plonus [13].

Domain or Bloch walls are described in Appendix A. Figure 2.1 illustrates a magnetization curve for a polycrystalline ferromagnetic material. The regions where each process dominates are marked. Note that the resultant vertical component of H will be cancelled by magnetic moments in adjacent grains.

The relationship of boundary displacement and domain rotation to the magnetization curve is discussed by Kittel [8], Bozorth [11], Littman [12], and Plonus [13]. The following

discussion is based on the arguments presented in [8, 11-13]. In weak fields the magnetization process proceeds by "reversible" domain wall motion as shown in figure2.1 at point 2 on the curve. The process is reversible because the domain walls have not moved over distances appreciable enough to encounter crystalline imperfections. If we remove H, the domain walls will move back (approximately) to their original positions as shown by the picture for position 1. This position corresponds to the unmagnetized state of the sample. As the H field is further increased (position 3), the domain walls begin to encounter various obstructions in the material. These obstructions may take the form of dislocations, precipitated impurities or grain boundaries. The domain walls tend to stick to these obstructions or become "pinned". A considerable amount of energy in the applied field is required to move these domain walls past these obstructions. Once the domain walls move past these initial obstructions, they shoot forward until they meet other obstructions. This results in small, rapid, discontinuous changes in the magnetization curve. These discontinuities are called "Barkhausen jumps" ([14] as cited by Bozorth [11]). The movement of domain walls in this region is "irreversible" since the domain walls are "pinned" as they begin to move back to their original positions upon reduction of the applied field.

As the increase in the magnetization proceeds, some magnetic moments within the domains will begin to rotate into more favourable directions as shown for position 4. Rotation of domain moments can only occur in fields that are large enough to overcome the anisotropy energy (anisotropy energy is defined in Appendix A, Section A2.1.3) of the material. The fields required for rotation are several orders of magnitude larger than those required to move a Bloch wall. According to Plonus [13], the anisotropy energy can be on the order of 50,000 times greater than the energy required to move a Bloch wall. Thus, until the "knee" of the magnetization curve is reached, increases in magnetization are largely due to the irreversible growth of domains having magnetic moments in favourable orientations. At the knee of the curve, domain wall movements will have continued to the point where only

one domain, will remain within a grain of the material (position 5). The magnetization of this grain will generally not lie parallel to that of the applied field. To increase the magnetization of the sample further, the magnetic moments of the domains must rotate to lie parallel to the direction of the applied field. This is shown at position 6. This rotational process is reversible but only occurs in very strong fields. The sample becomes saturated when the magnetization of the sample acquires the same value as the individual domains. Further increases in the flux density are due solely to the contributions of free space.

2.3 Alternating and Rotational Losses

2.3.1 Alternating Hysteresis

Now we consider the phenomenon of hysteresis. If the applied field is reduced, the magnetization curve will be retraced to a point somewhere above the knee of the curve. Once this point is reached, reverse domains will begin to form in each of the large single crystal domains found within the polycrystalline sample. The flux density in the sample does not reduce along the original magnetization curve. In fact, when the applied field is reduced to zero, a "remanence" flux density B_r remains in the sample as depicted in figure 2.2a). To reduce the flux density to zero, a field of value H_c must be applied in the reverse direction. This is known as the "coercive" force of the material. This phenomenon occurs because once the domains in the sample have been formed, additional energy must be expended to reorient them. The area of the hysteresis loop represents the energy per cycle lost in magnetizing the sample in a slowly reversing field. Hysteresis losses in electrical sheets are often estimated using the "Steinmetz Equation" [15]:

$$P_{ha} = K_{ha} f B_p^{\zeta} \qquad \text{W/kg} \tag{2.1}$$

where f is the frequency of excitation and the constants K_{ha} and ζ are chosen empirically to fit loss measurements taken on static hysteresis loops.

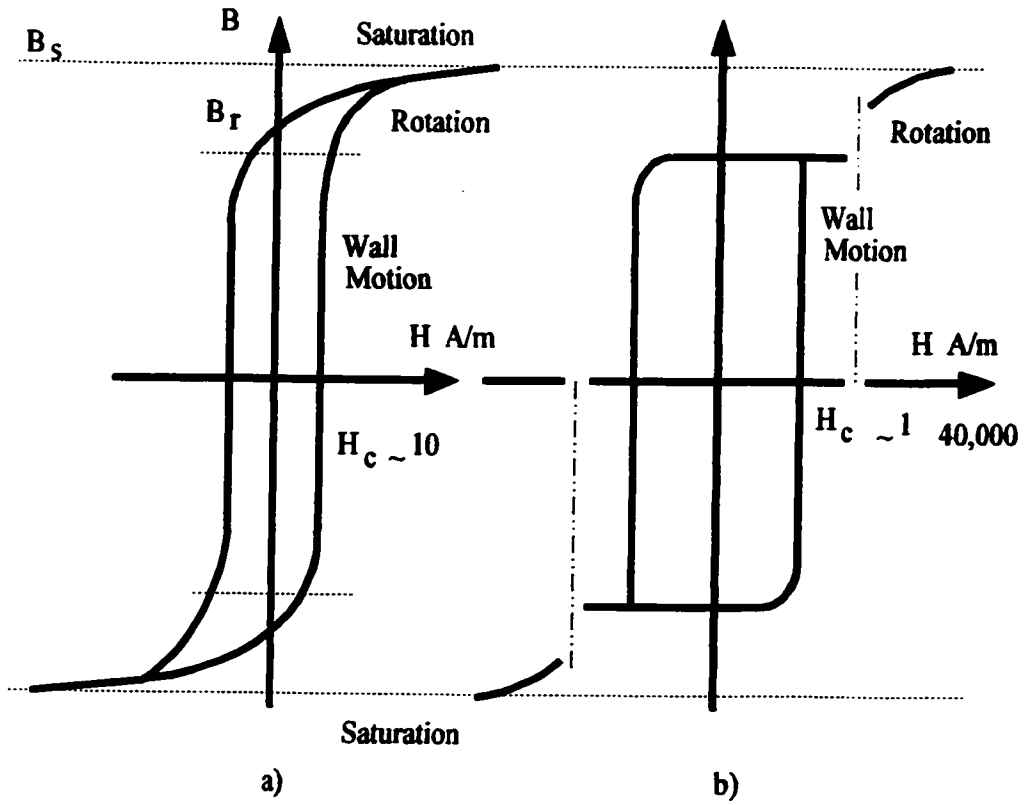

Figure 2.2 - Magnetization mechanisms in polycrystalline iron. a) Polycrystalline iron. b) Pure crystal of iron with its easy magnetisation axis not parallel to the applied field. Taken after figures 9.45a) and b) in Plonus [13].

As discussed by Plonus [13], the hysteresis loop for a soft ferromagnetic polycrystalline sample has two distinct regions. The approximately rectangular area in figure 2.2a) is primarily attributable to irreversible wall motion that brings the magnetization curve to about two-thirds of the saturation value. The approximately triangular areas near the tips of the loop are attributable to reversible domain moment rotations that bring the curve to saturation. The distinctness of these two regions becomes clearer when the hysteresis loop for a single crystal of iron is studied. Consider the case of an applied field that is not parallel to an "easy" axis of magnetization ("easy", "medium", and "hard" axes of magnetization are

described in Appendix A, Section A2.1.3). The finite area of the rectangular part of the hysteresis loop shown in figure 2.2b) represents loss due to the irreversibility of wall motion. Energy is taken from the applied field in creating the domain walls and moving them past obstructions in the crystal structure. Brailsford [16] has concluded that a substantial component of the observed static hysteresis loss in a ferromagnetic material is associated with the domain wall energy. He explains that the disappearance of a domain wall and subsequent reappearance is an irreversible process. When a domain wall disappears, the energy in the wall is released and manifests itself as heat. Approaching saturation, the curve has no area and therefore no loss. This represents the reversible process of domain rotation. The energy supplied by the field in rotating the domain moments is used in overcoming the anisotropy of the crystal and returned to the field as the field decreases. In a polycrystalline sample, some wall motion is still possible in large fields. This accounts for the broadening of the tips so that a smooth hysteresis loop results.

2.3.2 Rotational Hysteresis

The curve shown in figure 2.3 is taken after the work of Brailsford [16-19]. It shows the relationship between rotational and alternating hysteresis losses for a sample of 1.91% silicon iron. Note that for flux density values up to around the knee of the magnetization curve, the rotational hysteresis loss increases almost linearly. This is followed by a sudden flexure in the curve and a rapid rise in loss. A maximum point is reached, and then the loss begins to drop rapidly. At saturation, the loss approaches zero. The sample is composed of many grains. At high flux density levels approaching saturation, each grain will consist of one domain only. Very few domain walls will remain in the sample, and the rotating magnetic field causes the magnetic moments within each fully saturated grain to rotate at the same speed as the field. We have already seen that magnetization due to rotation of magnetic moments in domains is a reversible process. If the field is rotated quasi-statically (slowly, to

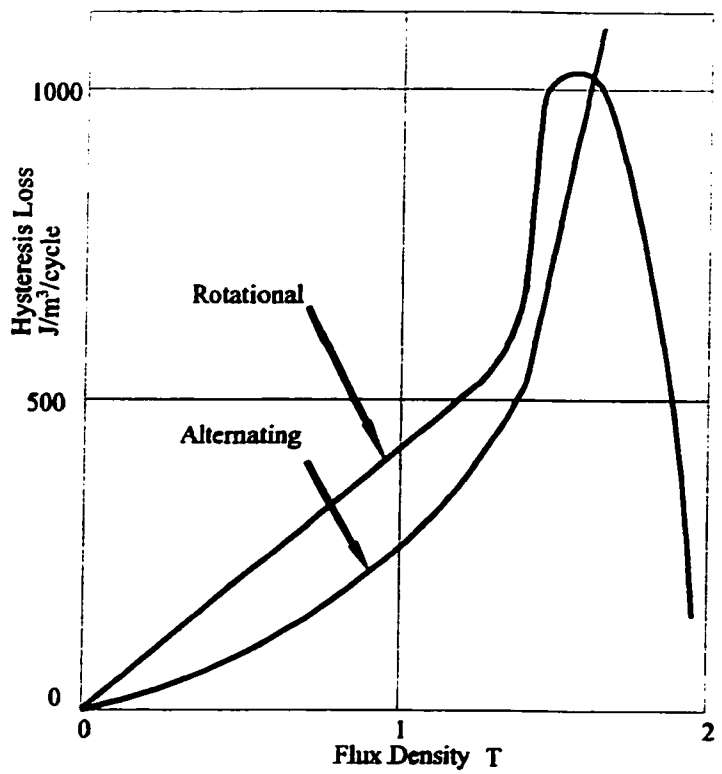

Figure 2.3 - Alternating and rotational hysteresis in a 1.91% silicon sheet steel as indicated by Brailsford [16-19].

avoid eddy currents), the loss will approach zero as saturation levels are reached.

Grimwood, Campbell and Evetts [20] have pointed out that a loss mechanism could exist in a rotating field that is not present in an alternating field. They believe that there exists an irreversible movement of the magnetic moment in an individual grain as it rotates past the hard direction of magnetization. In polycrystalline iron, all grains will become single domains magnetized in the easy direction closest to an applied static field. This occurs at a magnetization of approximately 83% of the saturation magnetization value. Grimwood, Campell, and Evetts argue that further magnetization increases take place by rotation of the moment out of their easy directions, but that in a static field, this is always a stable process and therefore lossless. This mechanism was discussed in the previous section, in relation to the tips of the hysteresis loop depicted in figure 2.2a). If the applied field rotates, all the

moments must rotate with it, and move past a hard direction of magnetization. The movement past the hard direction will be unstable, and therefore lossy, up to a certain threshold field. Beyond this threshold, the moment will remain in stable equilibrium at all angles. The authors obtained some validating evidence for this hypothesis. They compared the rms Barkhausen noise signals in rotating and alternating fields as functions of sample magnetization. In high fields, they found much greater levels of Barkhausen noise for rotating fields suggesting that an additional loss mechanism, not present in alternating fields, is at work.

In low magnetic fields corresponding to flux density levels below the knee of the magnetization curve, the rotational hysteresis loss tends to be larger than for the alternating case. This is illustrated by the curve shown in figure 2.3. In this region, magnetization proceeds by irreversible domain wall motion. Grimwood, Campell, and Evetts used a simple domain model to predict the ratio of rotational to alternating hysteresis losses in low magnetic fields mathematically. They predicted a value of $\pi/\sqrt{2}$ or approximately 2.22. They measured values of 2.5 for a 1.2% C steel, 2.3 for a pure iron sample, and 1.8 for a heavily cold rolled pure iron sample.

Fiorillo and Rietto [21] have attempted to predict the ratio of rotational to alternating hysteresis with some success. The prediction was made using the relation:

$$\frac{W_{hr}}{W_{ha}} = n_w \frac{W_{wr}}{W_{ha}} + n_s \frac{W_{sr}}{W_{ha}} \qquad \textbf{(2.2)}$$

where,

W_{hr} is the rotational hysteresis energy loss (J/cycle).
W_{wr} is the loss (J/cycle)caused by reversible domain wall motion (independent wall motions).
W_{ha} is the alternating hysteresis energy loss (J/cycle).
W_{sr} is the loss (J/cycle) caused by irreversible domain wall motion (domain rearrangements).
n_w is the volume fraction of the sample where independent wall motions occur.

n_s is the volume fraction of the sample where domain rearrangements occur.

The remaining volume fraction of the sample n_c is associated with reversible rotations of the domain magnetic moments (coherent rotations) with an assumed loss contribution of zero.

Boon and Thompson [22] studied rotational and alternating hysteresis losses in single crystals of silicon iron. They measured the rotational losses on discs, cut from single crystals with various planar orientations, using a torque magnetometer. Three discs, 0.4 mm thick and 10 mm in diameter, were mounted with simple crystallographic orientations 120° apart. Alternating losses in samples shaped like picture frames were measured. The legs of these picture frames were approximately 10 mm long and 2 mm x 2 mm in cross section. Boon and Thompson developed curves of rotational hysteresis loss, as a function of magnetic saturation, for the (100), (110), and (111) planes. Notation for the description of crystallographic planes is described in Section 2.5. All three curves were similar in shape, but quite different in magnitude. In each case, the loss value rose to a maximum at one half to two thirds of saturation, and fell to zero as magnetic saturation was approached. The maximum rotational hysteresis loss for the (111) plane was approximately ten times larger than the loss in the (100) plane. In the (110) plane, it was approximately six times larger than in the (100) plane. Boon and Thompson also evaluated the ratio of rotational hysteresis in each plane, to alternating hysteresis for each picture frame cut along the corresponding direction. The ratio was approximately 2:1 for flux densities up to 1.2 T in the (100) plane and the [100] direction. This ratio fell to zero as saturation was approached. For the (110) plane and [110] direction the ratio was around 10:1 at 0.4T. It then fell gradually to 8:1 at 1.2 T, and fell rapidly to zero as saturation was approached. For the (111) plane and [111] direction the ratio was approximately 7.5:1 up to 1.2 T and fell rapidly to zero at saturation.

Narita and Yamaguchi [23-24] conducted studies on single crystal disc specimens using a torque magnetometer. They also observed domain patterns. They found that the

rotational hysteresis in discs cut from the (110) and (111) planes increased as the thickness of the disc was reduced from 1.0 mm to 0.60 mm and finally to 0.35 mm. For the (110) crystal plane, the peak hysteresis loss was approximately 30% higher in the 0.60 mm disc and nearly 90% higher in the 0.35 mm disc. For the (111) plane, the peak hysteresis loss was approximately 60% higher in the 0.60 mm disc and approximately 240% higher in the 0.35 mm disc. In the (100) plane, the rotational hysteresis losses were nearly insensitive to the thickness of the disc. The highest rotational losses occurred in the (111) plane, followed by the (110) plane with the lowest loss occurring in the (100) plane. Using the results for the 0.35 mm discs and comparing the maximum loss values, the loss in the (111) plane was approximately six times larger than the losses in the (100) plane. The loss in the (110) plane was approximately three times larger than in the (100) plane. Narita and Yamaguchi concluded that in the high magnetization region, a considerable part of the loss could be attributed to the energy dissipation occurring during domain wall annihilation. They also related the rapid fall of the rotational hysteresis loss near saturation, to a decrease of the domain wall surface energy.

Zbroszczyck et al [25], studied the angular distribution of rotational hysteresis losses in 3.25% Fe-Si single crystals. They measured difference torques for disk shaped samples using a torque magnetometer (difference torques and torque magnetometers are described in Chapter 3, Section 3.2.3) and made domain wall observations for various field strengths. The following observations are notable. In the low field region, where the linear increase of rotational hysteresis losses with magnetization is evident, the angular distribution of losses is isotropic. In this region, only 180° domain walls take part in the magnetization process. In higher fields, the appearance of 90° domain walls (180° and 90° domain walls are described in Appendix A, Section A2.2) causes a more rapid increase in the rotational losses with an increase of magnetization. Also, the angular distribution of losses becomes anisotropic, with distinct maxima and minima at certain angles. The authors also point out that the domain

structures associated with rotational losses can take on very complicated three-dimensional patterns. Furthermore, they relate the mechanism of losses in high fields, to the reconstruction of these complicated domain patterns. Narita and Yamaguchi [23-24] suggest that this process of domain structure reconstruction may be identified with the creation and the annihilation of the domain walls.

2.3.3 Alternating and Rotational Eddy Current Losses

Presentations of "classical" eddy current theory are found in the works of J.J. Thomson [26], Latour [27], and Agarwal [28] to name a few. Classically, eddy current losses are given by:

$$P_{eddy} = \frac{\pi^2 t^2 B^2 f^2}{6\rho_{res}\rho} \qquad \text{(W/kg)} \qquad \textbf{(2.3)}$$

where t is the thickness of the sheet in metres, f is the frequency of the field in Hz, B is the peak flux density in T, ρ_{res} is the resistivity in Ω-m and ρ is the material mass density in kg/m^3. As discussed by Stewart [29], this formula is valid so long as the eddy currents are not large enough to produce a reaction field at the centre of the sheet and reduce the flux density there. Furthermore, the material is assumed isotropic with a constant permeability and resistivity. From this approximation we see, that classical eddy current loss estimates are inversely proportional to the resistivity of the material.

Del Vecchio [30] reports that, for elliptically polarized magnetic fields, the eddy current losses may be approximated by using the principle of superposition. The sum of the losses associated with the flux components along the major and minor axes will closely approximate the rotational eddy current losses. For the case of purely rotating flux densities, doubling the result of equation 2.3 gives the rotational eddy current loss. The results of Mayergoyz's [31] work also shows that classical eddy current losses for elliptically polarized

fields may be approximated using the principle of superposition, so long as the peak value of the magnetic flux density is uniform over the lamination cross section.

2.3.4 Anomalous Losses

2.3.4.1 Alternating Anomalous Losses

Total ac losses measured in electrical steels often exceed the sum of the measured hysteresis loss and the calculated classical eddy current losses [29,32]. The difference in losses is usually called the "anomalous" or "excess" loss. In the classical view of iron losses, the inherent assumption is that hysteresis losses vary with frequency (as in equation 2.1), and eddy current losses vary with the square of the frequency (as in equation 2.3). This would suggest, that if the loss per cycle in a sheet is plotted against frequency, the resulting plot would be linear. A result similar to that shown in figure 2.4 is more typical. At the lower frequencies, a distinct non-linearity is observed. In figure 2.4, the straight line with zero slope represents the hysteresis loss per cycle as determined from static tests. The classical eddy current loss per cycle is given by the difference between line b and line a. The difference between line c and line b gives the anomalous loss per cycle at a given frequency. In industry, the usual method of determining hysteresis losses involves the "separation of losses" method. Two measurements are made at a given flux density and two different frequencies. The loss per cycle associated with each measurement is plotted against frequency. A straight line is drawn between the two points. From this plot, the hysteresis loss per cycle is determined by the zero intercept and the slope of the line gives the eddy current loss per cycle squared. An examination of figure 2.4 shows that using this method may lead to overestimation of the hysteresis loss.

Robey [33] describes how the anomalous loss is attributable to micro eddy currents produced at the moving domain wall boundaries of ferromagnetic materials. Pry and Bean [34] (as cited in [35]), used a model based on a group of parallel and anti-parallel domains

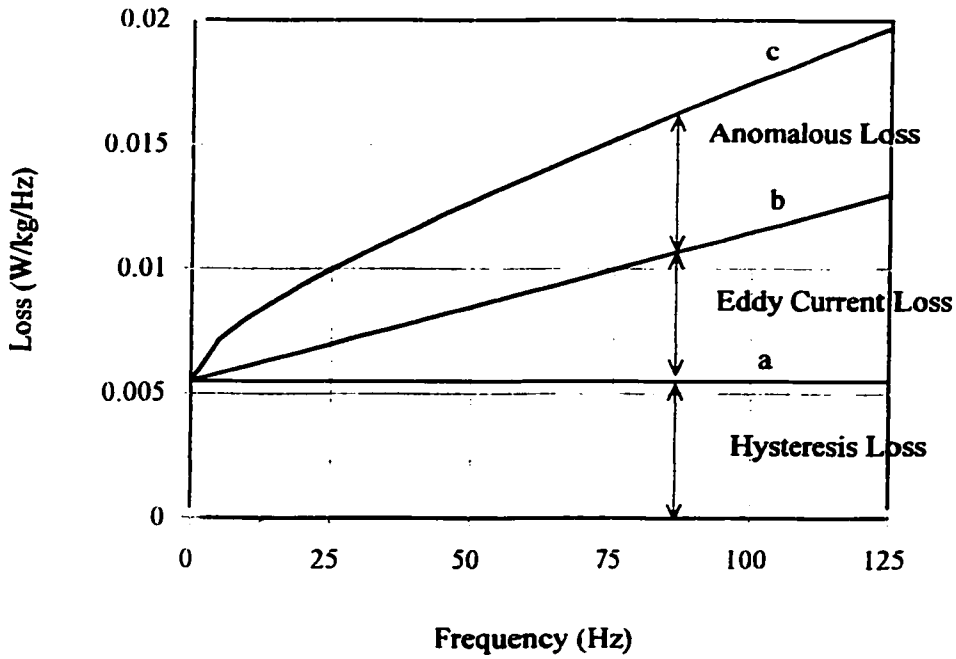

Figure 2.4 - Frequency dependence of alternating iron losses. Taken after figure 2 in Stewart [29].

to develop an equation that gave the anomalous loss factor as

$$K_{anomalous} = \frac{48}{\pi^3}\frac{d}{t}\sum_{n=1}^{\infty} n^{-3}\coth\frac{n\pi d}{2t} \tag{2.4}$$

where t is the sheet thickness (m), d is the domain spacing (m), and the summation is carried out for the odd values of n only. The result of this equation suggests that the anomalous loss factor can be affected through a choice of sheet thickness.

Stephenson's [36] study of low alloy (Si + Al < 1.1%wt) NO electrical steels suggests that the anomalous loss increases linearly with t^2/ρ_{res} according to the equation

$$P_{anomalous} = P_{ao} + k_a\frac{t^2}{\rho_{res}} \tag{2.5}$$

where P_{a0} and k_a are empirical constants. Measurements were made on six steel batches of varying composition. Each steel was produced in thicknesses of 0.35, 0.70, and 1.1 mm. Core loss measurements were made in a 25-cm Epstein frame at flux density levels of 0.5, 1.0, 1.5 and 1.7 T and at frequencies of 20, 30, 60, 120, and 200 Hz. The anomalous loss for each sample and operating condition was calculated by subtracting the measured dc hysteresis loss (Stephenson does not expand on which method he used) and the calculated classical eddy current loss from the measured total loss. Stephenson reports that in all cases the constant P_{a0} was positive, but for measurements at 0.5 and 1.0T, the constant k was negative. In approximately a fifth of the cases, the anomalous loss was also negative (an impossible situation). This result suggests that either the measured hysteresis loss or the calculated classical eddy current loss is too large. In about half the cases where the anomalous loss was negative, Stephenson also found that the calculation for the classical eddy current losses exceeded the total loss. The negative values of anomalous loss were found at the lower flux densities (and therefore higher permeabilities), higher frequencies and in the thicker specimens with lower resistivities. These results, led Stephenson to conclude that the negative values of anomalous loss were related to incomplete flux penetration into the sheet thickness. As discussed earlier, a uniform distribution of the peak flux density is an underlying assumption of the derivation of equation (2.3). Stephenson's work highlights some of the pitfalls associated with using the concept of the anomalous loss to compensate the shortcomings of our mathematical predictions of iron losses under all flux conditions and frequencies.

It should be noted that it is not really the loss that is anomalous. The anomaly is rooted in the classical model of eddy current losses that assumes both an isotropic and homogeneous material, whereas the material is neither. Furthermore, the assumption of a uniform distribution of peak flux density within the sheet is not entirely valid for all frequencies and flux density levels.

2.3.4.2 Rotational Anomalous Losses

The literature yields less information on anomalous losses in rotating magnetic fields. Early measurements by Cecchetti et al [37], suggested that the low frequency non-linearity did not occur with rotating magnetic fields. The authors used the rotating top method described in Section 3.2.2. They made their measurements over a frequency range of 1Hz to 22Hz. Measurements were made on samples of NO and GO 3% silicon sheet. Tan et al [38] reported a similar result for three grades of NO 3% silicon sheet. The authors used a rotating sample magnetometer described by Flanders, [39-40] for making measurements of rotational power loss over a frequency range of 20 to 80 Hz. They were unable to notice a significant dependence on frequency in their loss measurements. Based on these two investigations, it appeared that the anomalous loss did not exist in rotating magnetic fields.

Narita and Yamaguchi [41] reported measurements that did show the existence of rotational anomalous losses. They made measurements on a 0.345 mm thick NO material and showed that the anomalous loss was at least as large as the classical eddy current loss flux density values less than 1.1 T. Beyond that flux density value, the rotational anomalous loss approached zero as the sample became saturated. In 1990, Fiorillo and Rietto [42] reported measurements that showed a nonlinear relationship at low frequencies. They used an apparatus described in [3], making measurements in a frequency range between 1 and 50 Hz. The non-linearity occurred below 20 Hz. More recently, Spornic et al [43] have found a weak nonlinear behaviour at low frequencies. Further studies, using a standardized and internationally accepted method of measurement, are needed in this area of research. This would help clarify some of the ambiguities of the behaviour of the anomalous loss in rotating magnetic fields.

2.3.5 Effect of Harmonics on Losses

Harmonic effects on iron losses under alternating flux conditions were studied by

Nakata et al [44] and later by Lavers et al [45-47]. Lavers et al found that eddy current loss due to a distorted flux density waveform of peak value B_p is approximated by:

$$P_{eddy,dist}(B_p) = P_{eddy,sine}(B_p) \times K_{eddy} \tag{2.6}$$

where $P_{eddy,\,dist}$ = eddy current loss for distorted waveform having a peak flux density B_p,
$P_{eddy,\,sine}$ = eddy current loss for sinusoidal waveform having peak value B_p,
K_{eddy} = loss factor that corrects for the harmonics.

The loss correction factor is given by:

$$K_{eddy} = \left(\frac{B_1}{B_p}\right)^2 \sum_{n=1}^{N} \left(\frac{nB_n}{B_1}\right)^2 \tag{2.7}$$

Note that the phase angle of the harmonics is important and is taken into consideration indirectly by the term outside the summation in equation 2.7. When harmonics add so as to reduce the peak flux density (for instance figure 2.5), the sinusoidal eddy current loss in equation 2.6 is also lowered. If the harmonics add so as to increase the peak flux density (see for instance figure 2.6), the sinusoidal eddy current loss in equation 2.6 is also increased. The term outside the summation tends offset or normalize these effects.

Lavers et al [47] also presented an empirical method for correcting for additional hysteresis losses caused by minor loops. A flux reversal forms a minor loop, creating a small hysteresis loop within the fundamental frequency hysteresis loop. Individual flux reversals ΔB_i responsible for minor loops are defined as shown in figure 2.7. The minor loop correction was derived by analysing a series of loss measurements for a broad range of flux density waveforms. It is approximated by:

$$P_{hyst,dist}(B_p) = P_{hyst,sine}(B_p) \times K_{hyst} \tag{2.8}$$

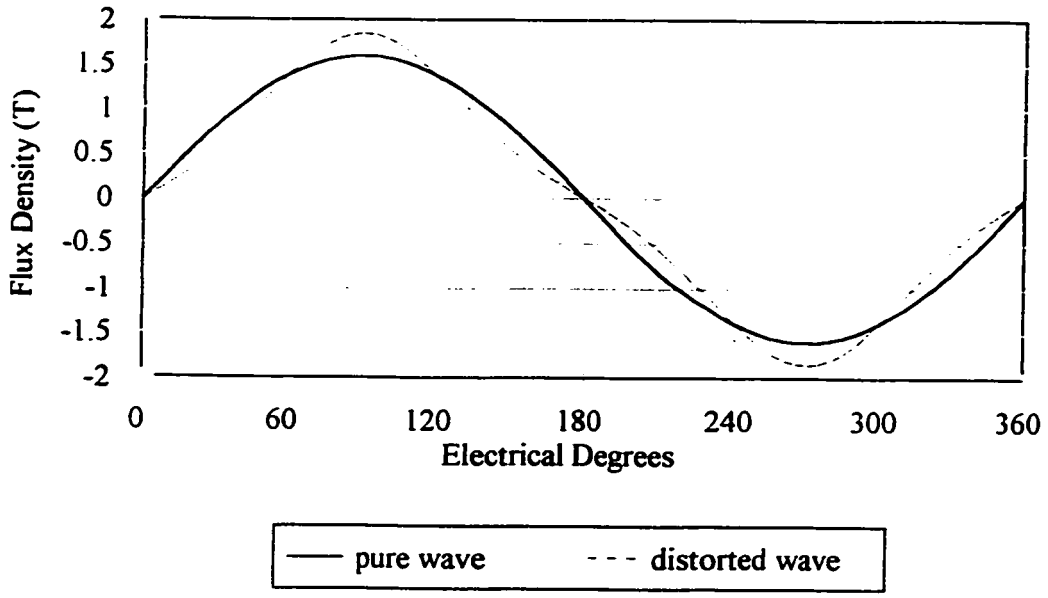

Figure 2.6 - Distorted waveform with increased peak flux density.

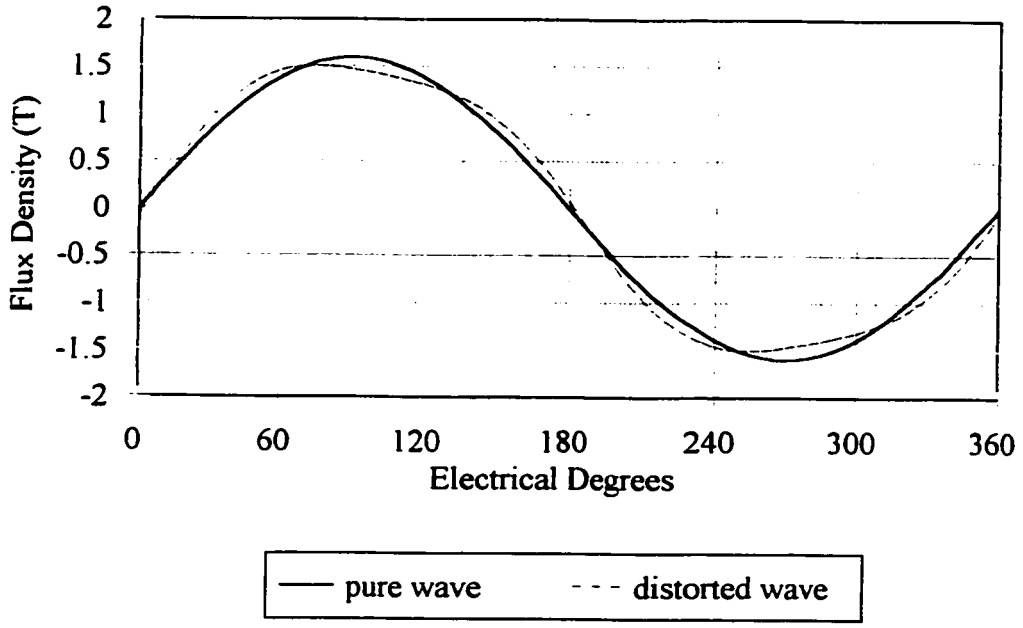

Figure 2.5 - Distorted flux density waveform. Saturation harmonics tend to lower peak flux density.

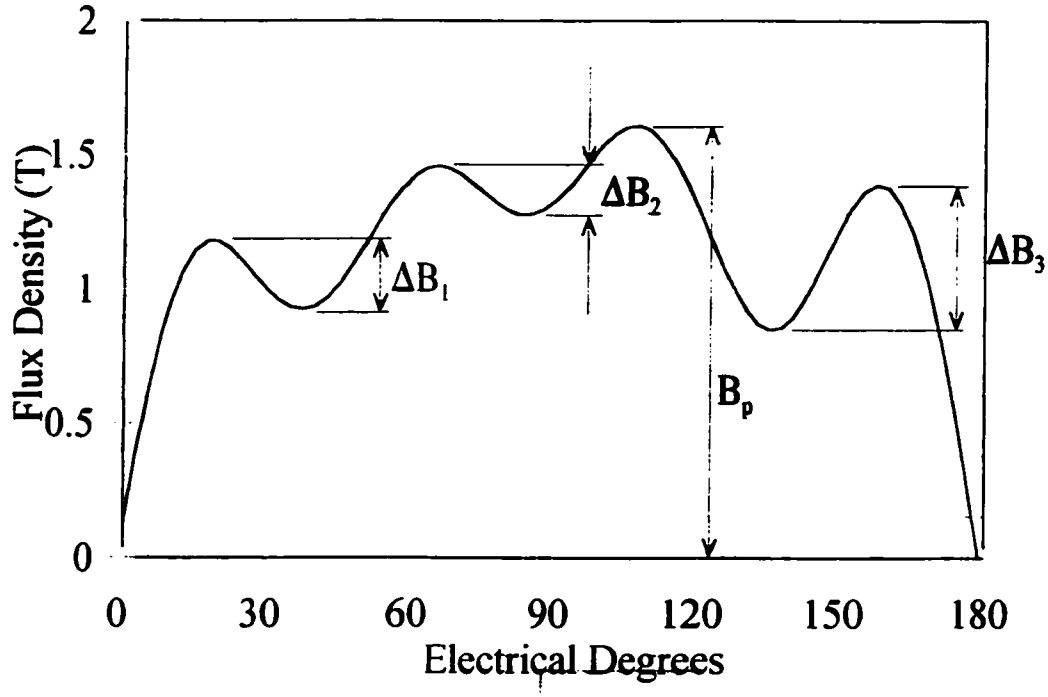

Figure 2.7 - Flux density reversals that result in minor hysteresis loops. Figure is taken after figure 2 in [41]

where $P_{hyst,\,dist}$ = hysteresis loss for distorted waveform having a peak flux density B_p,
$P_{hyst,\,sine}$ = hysteresis loss for sinusoidal waveform having peak value B_p,
K_{hyst} = loss factor that corrects for minor loops.

The loss factor is given as:

$$K_{hyst} = 1 + k_{hc}\Delta B_T \tag{2.9}$$

where a correlation study gives values of k_{hc} in the range of 0.6 to 0.7 depending on the material. In equation 2.9, ΔB_T is defined as:

$$\Delta B_T = \frac{1}{B_p}\sum_{i=1}^{N}\Delta B_i \tag{2.10}$$

Note that the Laver's method has only been investigated for losses in alternating flux

conditions and the work has not been extended to the case of rotational flux. In section 2.3.3, we saw that Del Vecchio [30] and Mayergosz [31] have both concluded that the classical eddy current losses may be estimated by using the method of superposition. From this we may conclude that equation (2.7) may be applicable to harmonic eddy current losses in rotating magnetic fields. No work concerning the applicability of equation (2.9) in rotating magnetic fields has been uncovered in the literature.

2.4 Effects of Metallurgical Processing and Chemistry on the Magnetic Properties of Electrical Steels

In the following section, we survey the methods used by producers of electrical steels to improve the magnetic properties of their product. The availability of standardized test methods (Epstein square and single sheet testers) has facilitated the study of loss reduction in alternating fields. The same cannot be said for rotational losses, for which a standardized test does not exist. As a result of this, there is much less information in the literature concerning the effects of metallurgical processing and chemistry as they relate to rotational iron losses. In this section, particular attention has been paid to identifying methods that may be used to reduce losses due to rotating magnetic fields. Lamination thickness, alloy content, grain size, impurity content, and material texture are all variables that affect losses in electrical steels.

2.4.1 Sheet Thickness

An examination of equation (2.3) shows that a reduction in lamination thickness reduces the eddy current loss quadratically. Reducing the material thickness from 0.64 mm to 0.48 mm results in reducing the classical eddy current losses in the material to approximately 58% of their original value. NO steels for use in motor cores are generally produced in thicknesses varying from approximately 0.36 to 0.79 mm. Over this range of

thicknesses, the effect of sheet thickness on hysteresis is negligible as suggested by the omission of a thickness term in equation (2.1). Applying the findings of Section 2.3.3, we may conclude that classical eddy current losses under rotating flux conditions are also reduced with sheet thickness. The effect of thickness on anomalous losses is less clear, but the result of equation (2.5) suggests that an increase of sheet thickness will increase the anomalous loss. The effect of sheet thickness on the rotational anomalous losses is not well understood. Work by Narita and Yamaguchi [23-24] suggests that rotational hysteresis in single crystal discs cut from the (110) and (111) planes increases as thickness is decreased (see Section 2.3.2). In polycrystalline sheet, the effect of sheet thickness on rotational hysteresis is not as well understood.

2.4.2 The Chemistry of Electrical Steels

2.4.2.1 Alloying Agents

Electrical steels are iron alloys with very low carbon levels. Alloying agents such as silicon, aluminum, manganese and phosphorus are added to increase the electrical resistivity of the material and improve its mechanical properties. Increasing the resistivity of the material reduces eddy current losses as suggested by the result of equation (2.3). This increase in resistivity will reduce both alternating and rotational eddy current losses. Additions of silicon and aluminum are also known to reduce hysteresis losses in alternating fields. No studies on the effects of alloying agents on rotational hysteresis losses have been found.

2.4.2.1.1 Silicon

Bozorth shows a curve (figure 4-6 in reference [11]) that indicates an approximately linear increase of resistivity in iron of ~11.6μΩ for every percent weight increase in silicon. This approximately linear relationship holds up to about 5% silicon. Bozorth attributes the

data for the curve to Yensen [48-49] (as cited in [11]). Arató et al [50] also found a value of 11.6μΩ/%wt through a regression analysis of twenty-six steels. Hou [51] reports a higher value of 12.8μΩ/%wt that he obtained through a regression analysis of five steels. This increase in resistivity reduces the eddy current component of core loss in electrical steels. The solid solubility of silicon in iron extends to about 15% below 800 °C [11].

Additions of silicon to iron generally reduce alternating hysteresis losses. Superior texture growth is promoted with the addition of silicon [51-52]. According to Matsumura and Fukuda [53], silicon additions also reduce the crystalline anisotropy constant K_1 (see Appendix A, equation A4 for a description of K_1). Alternating hysteresis loss is roughly proportional to the square root of K_1. Therefore, silicon is beneficial in the reduction of hysteresis loss. Silicon also reduces magnetic aging by inhibiting the precipitation of Fe_3C or Cementite [12], although this is rarely a problem in modern materials with low carbon levels.

Some disadvantages are encountered when iron is alloyed with silicon. The ductility of steel is greatly reduced with the addition of silicon [12]. In rapidly quenched, soft amorphous alloys, silicon contents of 6.5% are possible [38]. Takada et al [54] reported commercial production of 6.5% silicon sheet ranging in thickness from 0.1 to 0.5mm. According to the authors, coils can be produced by two processes; either a chemical vapour deposition process or a rolling process. In practical terms, 3.5%-4.0% is the maximum amount of silicon that may be alloyed with iron in sheets produced using a traditional steel rolling process. Beyond this point, steel sheets will become too brittle to process through cold reduction [55]. In general, as silicon content is increased, the elongation is decreased, and hardness, yield point, and tensile strength are increased [56]. Also according to reference [55], the punchability of the material decreases as silicon content is increased, but test results on this subject are not conclusive. Additions of silicon generally reduce the tendency of the material to burr during punching, but tool wear increases [57]. Silicon adversely affects the saturation induction of pure iron of approximately 2.16T [12]. This leads to a lower

maximum permeability at the normal working flux densities of electrical machines. The lower permeability occurs through a reduction in magnitude for the knee of the magnetization curve.

2.4.2.1.2 Aluminum

Iron resistivity also increases with the addition of aluminum, although not as effectively as with silicon [58]. Aluminum reduces alternating hysteresis losses by reducing the magnetocrystalline anisotropy constant K_1 of iron [53]. In one study by Bóc and Gróf [59], grain size increased as aluminum content was raised from 0.017% in one steel, and to 0.46% in a second steel. Both steels had similar chemical compositions (apart from aluminum content), and identical processing. According to Foley et al [58], core loss values and magnetic properties similar to those of 3% silicon steel can be achieved through addition of aluminum. The disadvantage of using aluminum as an alloying agent is that it easily reacts with impurities such as nitrogen to form inclusions. According to Brissonneau [60], many producers of electrical steel add small amounts of aluminum to induce grain growth since the inclusions serve as nucleation centres. Aluminum is less abundant than silicon, making it more expensive to use as an alloying agent. According to Littman [12], aluminum is less harmful to ductility than silicon.

2.4.2.1.3 Manganese and Phosphorus

Manganese increases the electrical resistivity of iron, but it is only about 50% as effective as silicon and aluminum (as in figures 2-29 and 2-30 in [11]). According to Lyudkovsky et al [61], phosphorus is even more potent than silicon in its effect on resistivity. However, they do not recommend phosphorus greater than 0.14% because of increased crack sensitivity during rolling.

According to Werner and Jaffee [62], MLQ steels once contained only manganese and phosphorus to help reduce eddy currents. Dunkle and Goodenow [63] report that small

amounts of both materials are added to steel to improve punchability and increase resistivity. If a steel is too soft, excessive edge burrs can result during punching. An improvement in punchability results from steel hardening, but care must be taken to avoid a steel that is too brittle.

Rastogi [64] found that increasing the manganese content, while maintaining a constant sulphur level, not only increased the resistivity of the steel but also increased grain size. He also found that manganese is beneficial to the development of a favourable texture. The increase in grain size is desirable since permeability increases with increasing grain size. When alloying iron with manganese, reducing sulphur levels is important (within economic reason) to avoid the formation of MnS inclusions.

Dunkle and Goodenow[63] found that increasing Mn levels up to 1.25% in motor lamination steels produced significant core loss reduction. In addition, they found a smaller decrease in permeability than experienced with the addition of Si and Al. Unfortunately, they found that this steel was very sensitive to decarburisation annealing conditions. Customers sometimes experienced higher core loss and lower permeability than those obtained under standard laboratory conditions. Liao's [65] findings substantiate the findings of Dunkle and Goodenow. Liao investigated the effects of 0.3 to 1.25% Mn on core loss. For Mn contents up to 1.25%, the core loss was improved nonlinearly as the Mn content was increased.

Hou and Wang [52] suggest that although phosphorus increases the electrical resistivity of steel, its overall effect on core loss is negative due to poorer texture development. They also found that the permeability of the steel is reduced because of grain refining in steels with higher percentages of phosphorus. Saturation induction is lowered with the addition of manganese and phosphorus as with most alloying agents except cobalt [12]. We may conclude that in small amounts, manganese is useful in improving the magnetic properties of steel. Phosphorus is useful if used in small quantities.

2.4.2.1.4 Antimony

The effects of antimony on the magnetic properties of electrical steels are described Lyudkovsky et al [66-68]. Small amounts of antimony may improve the permeability of NO steels. Antimony seems to reduce internal oxidation and promote favourable texture thereby improving permeability.

Although Si, Al and Mn are added to help reduce the eddy current component of total core loss, they adversely affect the magnetic permeability due to the formation of a subscale layer (region of internal oxidation). The subscale layer forms because of a great affinity for oxygen exhibited by Si, Al and Mn in comparison to iron. Lyudkovsky [66] reports that subscale forms below the surface of the lamination during the customer decarburisation anneal. According to [66-68], the thickness and morphology of the subscale layer depend on the following four factors:

1. solute concentrations
2. the oxygen potential of the annealing atmosphere
3. the duration of the anneal and
4. the annealing temperature

If a sufficient amount of Si, Al and/or Mn oxides are available near the surface of the lamination, subscale growth becomes diffusion limited. Antimony segregates to the grain boundaries and slows the diffusion of oxygen at grain boundary. Antimony lowers the diffusivity of the oxygen at grain boundary, and the rate of subscale formation is reduced. Addition of up to 0.08% Sb improves steel permeability, if S content is limited [66].

Small additions of Sb may also help improve texture in NO steels. Lyudkovsky and Rastogi [68] found that small additions of Sb promote the growth of (220) and (200) planes at the expense of (222) and (211) (unfavourable) planes during annealing at 790° C. It appears that Sb helps improve permeability after decarburisation annealing by reducing subscale formation and promoting the growth of a favourable texture.

2.4.3 Impurities

2.4.3.1 Sources of Impurities - Iron and Steelmaking

Carbon, sulphur, nitrogen and oxygen cause the most detrimental effects to the magnetic properties of iron-silicon alloys [12,56]. Carbon is introduced into molten iron ("pig iron" or "hot metal") in the blast furnace. Blast furnaces are described by Higgins [69]. Pig iron contains approximately 4% percent carbon and is not suitable for manufacturing electrical steels without further processing. In a blast furnace, iron bearing ores are charged into the top of the furnace along with coke and limestone. Air is blown through openings in the bottom of the furnace to enable the combustion of the coke in the charge, which produces carbon dioxide (CO_2). Coke in the furnace also reduces the CO_2 and forms carbon monoxide (CO). The CO gas reacts with the oxygen in the iron oxides of the ore and the reduced iron collects at the bottom of the furnace where it is periodically tapped. Most large integrated steel mills use pig iron from blast furnaces as the stating point for the production of electrical steels. Mills making smaller batches of specialty steels may use electric arc or induction furnaces to melt scrap metal as an alternative source of hot metal [70]. To reduce the carbon content of the hot metal a steelmaking furnace is required.

Primary steelmaking processes are used to refine a charge of hot metal and additional scrap. Oxygen processes are increasingly popular worldwide and are described by Deo and Boom [71]. High purity oxygen is blown under high pressure through or onto a bath of hot metal contained in a large vessel. Carbon, silicon, manganese, phosphorus, and to some extent sulphur, are oxidized during the process. The heat generated by these reactions is sufficient to melt added scrap and allow the formation of slag.

During the blowing procedure, carbon levels are reduced as the carbon combines with oxygen to form carbon monoxide and carbon dioxide. Deo and Boom [71] also describe secondary steelmaking procedures. Vacuum degassing in a ladle can further reduce carbon levels after primary steelmaking. As the molten steel is subjected to lower pressures, the

carbon in the steel will combine with oxygen to form carbon monoxide gas that bubbles out of the steel. According to Lyudkovsky, Rastogi, and Bala [61], carbon levels as low as 30 ppm are encountered after degassing. Phosphorus is removed during the primary steelmaking process through chemical interactions with the slag. Ilmenite ($FeTiO_3$) and fluorspar (CaF_3) may be added to decrease slag viscosity for better dephosphorisation [71]. Hot metal and steel desulphurisation may be used if necessary [61]. A variety of reagents may be used for desulfurisation [71]. Hou and Wang report sulphur levels as low as 40 to 60 ppm in low carbon electrical steels [52].

Deo and Boom [71] also describe mechanisms for the removal of nitrogen during the steelmaking processes. During the initial blow period in an oxygen steelmaking converter, nitrogen is removed as a result of carbon monoxide gas evolution. Nitrogen pickup can occur during the last stages of the blow. Vacuum degassing also aids in the reduction of nitrogen levels. One way to reduce the nitrogen content of electrical steels is to reduce the amount allowed to enter the molten metal. Lyudkovksy, Rastogi and Bala [61] recommend shrouding to reduce nitrogen pickup. Nitrogen levels of 10 to 40 ppm are typical at the end of the secondary steelmaking [71].

Oxygen enters the steel during the steelmaking stage. Silicon, manganese, and aluminum are added to deoxidize the molten metal [71]. Oxygen levels must be reduced to low as possible before adding alloying agents. Any remaining oxygen will combine with alloys such as Si, Al and Mn to form inclusions in the final product. Materials reported by various authors have oxygen levels of 30-490 ppm [36], 14-116 ppm [72], 185-210 ppm [68], and 83-93 ppm [52]. Günther et al [73] report laboratory prepared steels with oxygen levels of 4-9 ppm.

2.4.3.2 Effects of Impurities

Impurities such as carbon, sulphur, nitrogen, and oxygen detrimentally affect the

magnetic properties of steels. As discussed by Matsumura and Fukuda [53], impurities influence the magnetic properties of steel through the following three mechanisms:

1. Inhibited grain growth. Dispersed fine precipitates such as MnS and AlN inhibit the growth of grains.

2. Domain wall pinning.

3. Texture. Impurities can cause adverse effects on the recrystallized texture of the final product.

Cold reduction severely cold works the sheet. When a metal is cold worked, much of the strain energy expended in the plastic deformation is stored in the metal as dislocations and point defects [74]. The result is very poor magnetic and mechanical properties. The sheet is annealed to allow the microstructure of the steel to recover (annihilation of dislocations), recrystallize, and promote grain growth to an optimal size [75]. During the recovery stage, sufficient thermal energy is supplied to allow the dislocations to rearrange themselves into lower energy configurations. As the anneal proceeds, new strain free grains are nucleated in the recovered metal and begin to grow. Continued annealing allows the newly formed grains to grow until the structure is completely recrystallized. Solid solution alloy additions (such as silicon) increase the recrystallization temperature [74]. Grain growth is limited by dispersed fine precipitates, inclusions, impingement of other grains, and by the amount of energy input.

Two common precipitates that cause grain refinement are MnS and AlN. Shimoyama et al [76] have reported problems with fine grain structure due to zirconium nitrides. Grain growth is inhibited during annealing conditions when many fine precipitates are dispersed in steel and cause obstructions to the grain growth. Boc et al [72] have found that with additions of approximately 0.5% aluminum the number of large (5 to 10 μm) and fine (0.05 to 0.10 μm) inclusions is increased while the number of medium (0.7 to 1.5 μm) sized inclusions is decreased. The authors claim that the medium sized inclusions are harmful to

the magnetic properties because they are effective in obstructing grain growth. Observations of numerous scanning electron micrographs showed that the medium sized inclusions were often found at grain boundaries whereas the larger inclusions were found inside grains. In a later paper, Bóc et al [77] concluded that grain growth is also hindered as the number of fine precipitates increases. As grain size increases, hysteresis losses decrease and eddy current losses increase; therefore, an optimal grain size for core loss exists. For high silicon non-oriented sheets, researchers in Japan have found that 150 μm gives minimum core loss at 50 Hz [53,78]. The optimum value is around 100 μm for 1.85% NO silicon sheets [78]. It should be noted that this value will vary according to the frequency of magnetization and the alloy content of the steel. Grain size may also affect the anomalous loss. According to Rastogi and Lyudkovsky [79], large grained materials exhibit larger anomalous losses than fine-grained materials.

Besides causing grain coarsening, precipitates will also impede the motion of domain walls during the magnetization process thereby leading to increases in hysteresis losses and decreases in permeability. Matsumura et al [80] have taken photographs of pinned domain walls using a scanning electron microscope. The photos show how a 180° domain wall is prevented from moving when the grain is magnetized. The authors took photos under both dc and ac magnetizing conditions.

2.5 Texture

Electrical steels are polycrystalline in nature. Each individual grain has a crystallographic orientation that differs from that of its neighbour. The distribution of these orientations is generally non-random and the non-random distributions are called "preferred orientations" or "textures". Before describing textures, a quick review of the description of crystallographic directions and Miller indices is necessary. Smith [74] states that, "For cubic crystals the crystallographic direction indices are the vector components of the direction

resolved along each of the coordinate axes and reduced to the smallest integers... The letters u, v, w are used in a general sense for the direction indices in the x, y, and z directions respectively, and are written as [uvw]". Smith [74] also explains that, " Equivalent directions are called indices of a family or form". He gives the following example, for the cube edge directions that are equivalents:

$$[100],\ [010],\ [001],\ [\bar{1}00],\ [0\bar{1}0],\ [\bar{1}00] \equiv \langle 100 \rangle$$

The cubic face diagonals <110> and the cubic body diagonals <111> are also directions of a form.

Miller indices are used to describe crystallographic planes. For cubic crystal structures, Smith [74] states that the Miller indices, "are defined as the fractional intercepts (with fractions cleared) that the plane makes with the crystallographic x, y, and z axes of the three nonparallel edges of the cubic unit cell. The cube edges of the unit represent unit lengths, and the intercepts of the lattice planes are measured in terms of these unit lengths". He also states that, "The notation (hkl) is used to indicate Miller indices in a general sense where h, k, and l are the Miller indices of a cubic crystal plane for the x, y and z directions respectively". Planes of a family or form may also exist. Smith explains that, "the indices of one plane of the family are enclosed in braces as {hkl} to represent the indices of a family of symmetrical planes. For example, the Miller indices of the cubic surface planes (100), (010), and (001) are designated collectively as a family or form by the notation {100}".

2.5.1 Description of Textures

According to Hatherley and Hutchinson [75], "in rolled sheets, the nature of the texture is such that certain crystallographic planes are aligned parallel to the rolling direction and particular directions in these planes are parallel to the rolling directions. In sheets the texture can be specified by defining these crystallographic planes and directions". The

description is made using the notation {hkl)<uvw>. Hatherly and Hutchinson explain that, "This states that a plane of the form {hkl} is parallel to the rolling plane (i.e. its pole is parallel to the normal direction (nd)) and that a direction of the form <uvw> is parallel to the rd".

The "cube on edge" texture is shown in figure 2.8a). It is often referred to as the "Goss" texture after N.P. Goss who worked on the development of this texture in the 1930s ([81-83] as cited by Bozorth [11]). This texture is found in grain oriented materials and is described as {110}<001>. Grain oriented materials have grains with a predominance of cubic edge directions oriented along the rd, and face diagonal directions oriented along the td. This gives the material superior loss and permeability characteristics in the rd.

A random cubic texture is shown in figure 2.8b). The cube plane is parallel to the sheet surface, while the cube directions are randomly oriented in the plane of the sheet. In a material with true random cubic texture, the magnetic properties of the sheet would be completely isotropic. The loss and permeability characteristics of the material would be completely independent of the rolling direction. This texture is described as {100}<0vw>.

A doubly oriented or cube on face texture is shown in figure 2.8c). This material will have a predominance of cubic edge directions oriented along both the rd and the td of the sheet. The loss and permeability characteristics of the material would be best in the rolling and transverse directions of the sheet. At any other angle the characteristics would not be as good. This texture is described as {100}<001>.

A random texture material is depicted in figure 2.8 d). This material has an equal distribution of cubic edge directions in all directions. NO silicon steels usually fall into this group of materials. In practice, NO steels will exhibit a small amount of orientation in the rd. The losses will be lower, and the permeability higher, in the rd of the steel.

2.5.2 Formation of Texture

Favourable texture formation is dependent on careful control of processing variables

and anneal times. The formation of a cube on edge texture in grain oriented steels is the most familiar example of using favourable texture for an industrial application. This texture is depicted in figure 2.8 a). The ideal textures for use in motor cores are the random cubic texture or the double oriented cube on face texture as in figures 2.8b) and c).

2.5.2.1 Control of {111} Texture in Random Texture Materials

The amount of cold reduction and the quantity of inclusions in the steel affect texture. According to Matsumura and Fukuda [53], when a hot rolled sheet is cold rolled and recrystallized by annealing, grains develop with {111} planes from the vicinity of the grain boundary of the original hot rolled sheet. Furthermore, sheets with many inclusions will form many grains containing {111} planes in the plane of the sheet. This is considered to be attributable to the fact that inclusions in steel become nucleation sites for grains having {111} planes [78,80]. The texture with {111} planes is unfavourable for magnetic properties, but easily becomes the main component in industrial sheets after annealing. Therefore, impurities can compromise the magnetic properties of steel by helping to promote an unfavourable texture.

Lyudkovsky, Rastogi and Bala [61] attribute the predominance of {111} texture in batch annealed semiprocessed products containing Al and N to precipitation of AlN during recrystallization in the box anneal. Continuously annealed steels do not exhibit this problem because the heating rate is much faster and the material recrystallizes before AlN precipitation takes place.

2.5.2.2 Cubic Textures

Before 1970, a great deal of work was done on 3% silicon sheet with a {100}<100> or cube on face texture [52, 84-89]. Cube on face texture is desirable because it exhibits the magnetic properties of grain oriented steel in both the rd and td of the sheet. Furthermore,

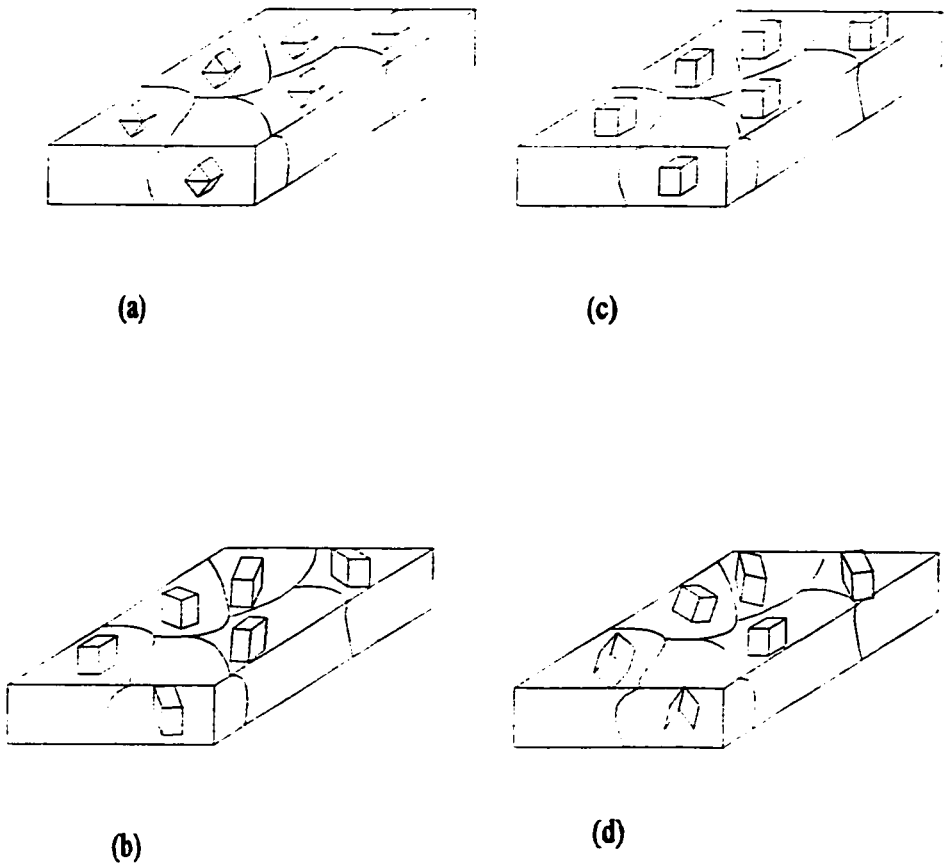

Figure 2.8 - Textures in electrical sheet steels. (a) "Goss" or "cube on edge" texture. (b) Random cubic texture. (c) Doubly oriented or "cube on face" texture. (d) Random texture.

the predominance of {100} planes suggest the lowest possible rotational loss of any texture (recall the results of work by Boon and Thompson [22] and Yamaguchi and Narita [23-24] as discussed in Section 2.3.2). Assmus et al [84-86] produced sheets with strong cubic texture through secondary recrystallization. The authors found that cubic oriented grains existed in the sheet after primary recrystallization (through an intermediate anneal). These grains grew to form large crystallites with diameters up to 5mm during a secondary recrystallization (through a final anneal). The grains with non-cubic orientation were almost completely consumed resulting in a sheet with nearly perfect cubic texture.

Kohler [87] describes a process where the sheet is hot rolled to a thickness of approximately 1.5 mm and then cold rolled to a thickness of 0.635 mm to produce a strong

Goss texture. The continuous strip is then cut into sheets and cross rolled to a thickness of 0.305mm. The sheets are then annealed at 1204 °C for eight hours in a hydrogen atmosphere containing 50 ppm hydrogen sulfide. The resulting sheet exhibits nearly 100% cubic texture. Stanley [89] describes a similar process, this time starting with a conventional grain oriented sheet and cross rolling to thickness a of 0.254 mm. The sheet is then annealed at 1066°C to 1232 °C in a hydrogen atmosphere with a dew point of -1.1 °C, for at least 5 hours.

More recently, Salz and Hempel [90] reported loss measurements for 0.50 and 0.65 mm thick sheets of a commercially produced cube on face material. They measured alternating losses in the rd, td, and at arbitrary angles to the rd. They also measured the rotational losses in the material. All measurements were made at 1.5 T and 50 Hz. The 0.65mm thick sheet exhibited losses of approximately 4.4 W/kg in the rd and 4.9 W/kg in the td. The alternating losses reached a maximum at approximately 63° to the rd where the losses were approximately 5.4 W/kg. Rotational losses at 1.5 T were approximately 7.3 W/kg and this was also the maximum loss under rotating flux conditions. In the 0.50mm thick sheet the alternating losses were 3.5 W/kg in the rd and 3.8 W/kg in the td. The alternating losses reached a very flat maximum at between 36° and 63° where the losses were approximately 4.3 W/kg over that range of angles. The rotational losses were approximately 5.4 W/kg at 1.5 T and rose to a maximum of about 5.7 W/kg at 1.55T. All the loss measurements were made on square samples using a horizontal yoke tester (see Chapter 3, Section 3.2.5.2). Unfortunately, the authors do not state the alloy content of the material or compare it with more conventional steel with similar alloy content.

A related texture is the {100}<0vw> or random cube texture. Steels with this texture should also exhibit low rotational losses due to the predominance of {100} planes. Random cube texture sheets were prepared as long ago as 1966 by Aspden, Berger and Trout [91]. Sheets were prepared by hot rolling at 1050 °C to a thickness of 3.8 mm, pickling, and cold rolling to a thickness of 0.45 mm. The experimental work was done on sheets of nearly pure

iron and an iron-manganese-sulfur alloy. The texture was obtained by annealing for 12 hours at 1050 °C or 1150 °C and cooling at 4 °C/h through the gamma to alpha transformation.

Werner [92] reports that his company used random cube sheet in the commercial production of aircraft generators in the late 1960's and early 1970's. The losses of this 3% Si material were less than 2.2 W/kg at a gage of 0.30 mm and a flux density level of 1.5 T. The use of the steel was discontinued due to the difficulties in producing it in economical quantities. Shimanaka et al [93] also reported a random cube texture steel. They produced the material by hot rolling to a thickness of 2 mm, annealing at 700 to 900 °C for 5 hours, cold rolling to a thickness of 0.47 mm and annealing in nitrogen for 1 hour at 840 °C. These authors produced the random cube texture in steels with a nominal silicon content of 1.85%. An addition of 0.08% Sb was used to aid in the formation of the favourable texture.

Researchers at the Laboratoire d'Electrotechnique de Grenoble [94] have also reported on laboratory trials of random cubic texture material. They do not elaborate on the method of production other than to say that it was produced using "a special hot rolling process in which a high heterogeneity of deformation is produced".

Shimanaka et al [78,95], reported a steel for commercial production with {hk0}<001> (i.e. intermediate between a grain oriented cube on edge and a doubly oriented cube on face texture). For a 0.35mm sheet with a nominal alloy content of 3.2% Si and 0.6% Al, they reported rd and td direction losses of 1.61 and 2.25 W/kg at 50 Hz and 1.5 T in reference [71] and rd and td direction losses of 1.59 and 2.23 W/kg at 50 Hz and 1.5 T in [95]. Alternating losses using the 50:50 arrangement were reported as 1.93 W/kg [78] and 1.91 W/kg [95]. This represented an improvement of approximately 13% over the best grade of fully processed NO steel produced by the company that employed Shimanaka et al. They also reported rotational losses of 3.3 W/kg at 50 Hz and 1.5 T although they do not state the method that they used for making the rotational loss measurements [78].

2.6 Effect of Mechanical Stresses on Magnetic Properties

Stresses (a stress is a force per unit area) can have an adverse effect on the magnetic properties of electrical steels. Stresses cause the metal crystals in electrical steels to distort, or strain (strains are measured as dimensionless fraction or percent elongation). The distortion of the crystal or atomic structure affects the relationship between magnetizing force and flux density, and in turn, affects all the magnetic properties of the steel [96]. If a stress is so low that it creates only an elastic strain in the metal, then removal of the load will permit the metal to return to a stress-free condition. If the material has been plastically deformed, the stresses will remain even after the load is removed.

Stamping, shearing, or slitting creates stress in the material. These stresses occur adjacently to the cut edge. The area adjacent to the cut edge will have extremely low permeability and high hysteresis loss. This area extends into the cut edge by a distance that is approximately equal to the lamination thickness [96]. Stresses have an increasingly important effect on core loss for laminations with small material gages and widths. Consequently, the effect of stresses will have a greater importance to manufacturers of small motors as compared with large motors manufacturers.

An early study by Cole [97] suggests that the magnitude of the effect of cutting stress on the core loss of NO silicon steel can be approximated by the simple relation:

$$\%P = \frac{k_{stress}}{w} \tag{2.12}$$

where,

%P is the percent increase in the hysteresis loss averaged over the entire lamination width,
w is the width of the lamination in mm between the cut edges, and
k_{stress} is a constant which is dependent on the thickness of the material, the physical properties of the material, and the flux density present in the material.

A value of k equal to 356 is given for a nominal 0.36 mm material similar to M-15 operating at 1T and 60 Hz. The value for 1.5T is 254. Bending of the electrical steel while uncoiling the material will also produce stresses that may adversely affect magnetic properties [96].

2.7 Stress-Relief / Decarburisation Annealing

Machine manufacturers may choose to anneal laminations made from fully processed NO steels to remove the stresses resulting from punching the steel into laminations, but this is not common practice [56]. The magnetic properties of semi-processed grades of NO and MLQ steels are only partially developed at the steel mill. Machine manufacturers must anneal the laminations after punching to develop their magnetic properties fully. The as-shipped materials often have high carbon levels (unless vacuum degassed) and this anneal is also necessary for decarburisation. Unlike NO steels, MLQ steels do not generally receive a coating of surface insulation. With MLQ steels, the final anneal allows a thin layer of blue oxide to form on the surface of each lamination. This oxide layer serves as an insulator between each lamination thereby helping to reduce eddy current losses. Decarburisation anneals improve the magnetic qualities of steels by promoting grain growth and reducing the carbon impurities in the steel. Grain growth during annealing is also promoted by straining the material with a 3-8% temper roll before the steel leaves the mill [56,70]. MLQ steels are usually provided with a matte finish [56]. The increased surface roughness promotes decarburisation by increasing the surface area through which the carbon may diffuse out of the steel. It also reduces the tendency for the laminations to stick together during annealing.

Summary

Magnetic losses in electrical sheets occur through a complex mechanism involving the movement of domain walls, the creation and annihilation of domain walls, and the rotation of the magnetization within a domain. At flux densities typical of those found in induction

motor cores, rotational hysteresis losses proceed by a process that is fundamentally different than is encountered under alternating fields. As the material saturates, the rotational hysteresis approaches zero. Since the magnetic losses encountered under rotating flux conditions are so different than those under alternating conditions, it would appear that a standardized test for rotational losses would be useful.

Investigators have conducted a great deal of research on alternating losses due to the availability of the standard Epstein test and single sheet testers. They have correlated the effects of composition and processing variables to losses and permeability measurements obtained on standardized alternating loss tests. Rotational losses are not as well understood due to the lack of a standardized test. The effects of chemistry and metallurgical processing as they affect alternating losses are well understood. Alloying agents decrease classical and anomalous eddy current losses by increasing the resistivity of the material. According to classical theory, eddy current losses in rotating fields will also be decreased in similar fashion through increases in resistivity. Additions of silicon and aluminum are also known to affect alternating hysteresis loss through the magnetocrystalline anisotropy constant K_1. The effects of alloying agents on rotational losses have not been studied in any detail. Anomalous losses under rotating flux conditions are not well understood and have not received sufficient attention in the literature. Researchers have determined that grain size affects eddy currents and alternating hysteresis losses and an optimal grain size will exist for each grade of steel. Again, the effect of grain size on rotational hysteresis losses has not been investigated.

Great advances have been made in clean steelmaking techniques. Hysteresis losses in alternating fields are reduced by decreasing impurities in electrical steels. When impurity levels are decreased, alternating hysteresis losses are reduced through a decrease in domain wall pinning, increased grain size, and improved texture development. The effect of reducing impurities on rotational hysteresis losses has not been investigated in any detail. Further reductions in core losses through reductions in impurity levels will be difficult to make since

modern electrical steels are already very clean.

The greatest prospect for improvements in both alternating and rotational losses comes from further developments in the control of texture. Rotational and alternating losses are greatly reduced through the development of cubic textures in the sheet. Cubic textured electrical steels could gain wide acceptance in the production of motor cores if economical methods of producing materials with these textures can be found. Systematic studies of composition and processing variables on rotational losses may lead to improvements in electrical steels for use in motor cores. A standardized test procedure for making loss measurements in rotating magnetic fields could benefit this area of research greatly.

Chapter 3

Magnetic Testing and Past Efforts to Quantify Rotational Losses in Electrical Apparatus

3.0 Introduction

Several methods are available for measuring losses in lamination steels under alternating flux conditions. The 25-cm Epstein test is used worldwide and standardized methods are available for making alternating loss measurements using single sheet testers. Over the last century, various methods for measuring rotational losses have been proposed but no method has been accepted for standardization. In this chapter, a state of the art is presented. A literature review of investigations concerning rotational losses in electrical machinery is also presented.

3.1 Alternating Loss Measurements

3.1.1 The Epstein Test

The 25-cm Epstein test square with double lapped joints is shown in figure 3.1. This test has been used worldwide in the steel and machines industry for may years to arbitrate the magnetic properties of electrical sheets. The Epstein test has remained popular because its results are repeatable and reproducible and the procedure is well documented in various standards. In North America the procedure is described in ASTM A343 [98]. This standard describes procedures for determining the specific core loss (W/kg), the specific exciting power (VA/kg), and the ac peak permeability.

The test equipment is simple. It consists of four solenoids (with two windings each), a mutual inductor, an ac power supply with a feedback loop, a flux voltmeter, an rms

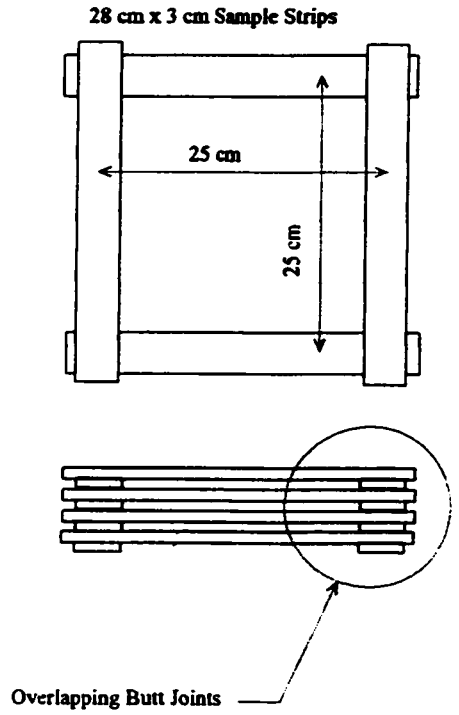

Figure 3.1 - Arrangement of sample strips to form an Epstein square.

voltmeter, an electrodynamometer wattmeter, and an ammeter. The flux voltmeter is a full-wave true average responding type voltmeter, with scale readings in average volts multiplied by the form factor 1.111 (so that its indications will be identical with that of a true rms meter for a purely sinusoidal voltage). It is used to evaluate the peak value of the flux density. The sample strips are sheared 3 cm wide and not less than 28 cm long (selection and preparation of test samples are described in ASTM A34 [99]). Samples are arranged into a square such that each limb of the square passes through one of the solenoids, thereby forming a simple transformer. A flux density value is set and then readings are taken from the wattmeter and ammeter. Alternating power losses in the steel are determined by subtracting the I^2R losses in the primary winding from the wattmeter reading. When NO materials are tested, half the samples are cut parallel to the rolling direction and half are cut in the transverse direction.

This arrangement is often called the 50:50 Epstein test. For GO materials, all the strips are cut parallel to the rolling direction.

A major concern with the Epstein test arises from the nonhomogeneous magnetic circuit presented by the double overlapping corners shown in figure 3.1. Wilkins and Drake [100] describe how this led to an anomaly in results between the Epstein test and the Lloyd-Fisher test that used butt joints rather than overlapping corners. At this point it was realized that the results obtained from the Epstein test were influenced by the geometry of the core and the properties of the steel. In the corner assembly of the square, flux travels in a direction normal to the plane of the laminations. This causes extra losses due to eddy currents in the plane of the sheet. Although the effective magnetic path length of the Epstein square is standardized at 94 cm, in reality it will vary with the material type, permeability, sample weight (stack height), and the flux density range. This problem has been considered often in the past, and the results of these investigations are summarized by Sievert [101-102] and Beckley et al [103]. Since all users of the standard test obtain measurements with the same systematic error, industry has largely ignored this error.

3.1.2 Single Sheet Testers

The Epstein test is used worldwide despite the problems involved with determining an effective magnetic path length. However, there is growing international interest towards replacing the Epstein test with single sheet tests. The main reason for this interest lies in the fact that the single sheet specimen is homogeneous in comparison to the double overlapping Epstein square. Most researchers in the area believe that the results from single sheet testers represent the properties of steel sheets better than the Epstein test. Since the measurements are made on a large sheet, the measuring error due to shearing stress is greatly reduced. The need for stress relief annealing of fully processed grades is thus reduced, offering another advantage to steel manufacturers.

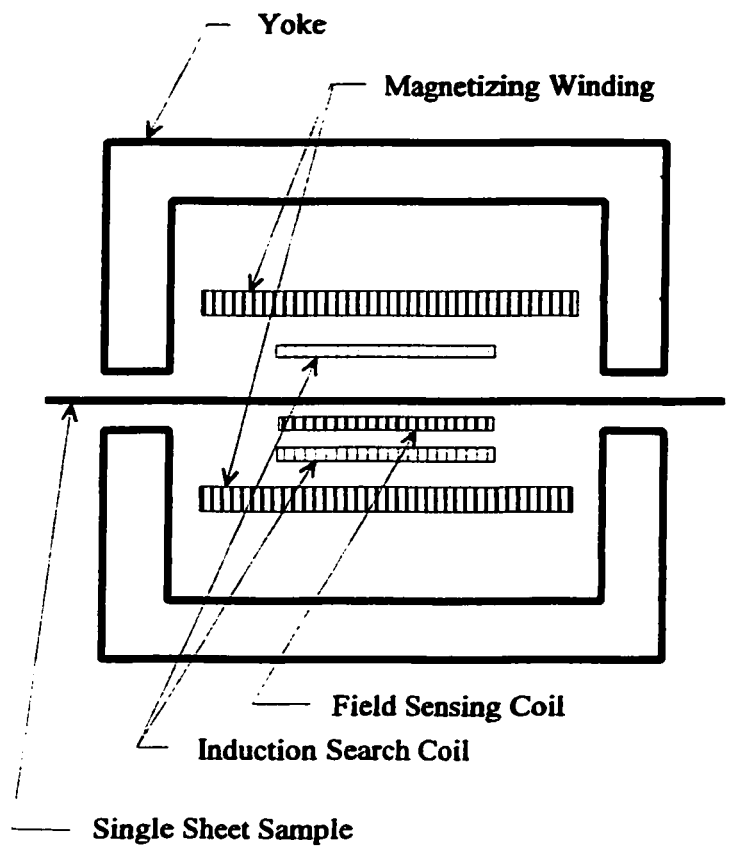

Figure 3.2 - Typical arrangement of s single sheet tester of the H coil type.

Single sheet testers were first proposed by Yamamoto and Ohya [104] and the advantages of the method were instantly recognized. The principle of operation is simple. A single sheet specimen is inserted into a nonconducting form on which a magnetizing winding is wound. The sheet and magnetizing winding are then placed on a yoke that completes the magnetic circuit. By varying the current through the magnetizing winding, the flux density (as determined with a second coil wound on the nonconducting form) may be set to the desired level. The field strength is determined using a tangential field sensing coil wound on a dielectric former placed near the surface of the specimen. Figure 3.2 shows the

basic features of a single sheet tester. This figure shows a double yoke construction (providing two parallel flux closure paths) although single yoke constructions are also possible. Core loss is then determined from the equation:

$$P_{alt} = \frac{1}{T\rho}\int_0^T \overline{B}\cdot\frac{d\overline{H}}{dt}dt \qquad \text{W/kg} \tag{3.1}$$

where T is the period of one cycle (s)
and ρ is the mass density of the material (kg/m^3)

For alternating loss measurements, only one component of the field quantities is of interest, so equation (3.1) simplifies to:

$$P_{alt} = \frac{1}{T\rho}\int_0^T B\frac{dH}{dt}dt \qquad \text{W/kg} \tag{3.2}$$

The integral portion of this equation yields the area of a dynamic hysteresis loop and gives the energy per unit volume expended in the magnetization process in one complete cycle.

Methods of using tangential field sensing coils to measure field strength are often referred to as "H coil methods." Nakata et al [105] later improved the H coil method proposed by Yamamoto and Ohya. By using two H coils placed at two different distances from the surface of the sheet, the authors improved the accuracy of the H field measurement. They accomplished this by linearly interpolating the field strength to the surface of the sheet.

Various authors [101,106] also proposed methods of determining H from the magnetizing current. This method is often referred to as the MC method. North America adopted this as a standard for single and double yoke fixtures [107]. The method is similar to the Epstein test method in that an effective path length is assumed and H is determined from $H\ell = NI$. This is a simplification of Ampere's Law that is strictly correct only if the reluctance of the yokes and contact regions is zero. This condition is only approximately

satisfied even if large masses of iron are used in the yokes, and the pole faces are properly machined. The method is very simple and a greater amount of reproducibility may be expected when compared with H coil methods [108]. The absolute accuracy of the MC method is questionable due to the lack of physical correspondence, between the field and current, resulting from the losses and magnetic reluctance of the yoke [109].

3.2 Rotational Loss Measurements

3.2.1 Baily's Method

Baily [110] first studied the phenomenon of hysteresis in iron and steel sheets subjected to rotating magnetic fields over a century ago. He used a simple apparatus that rotated an electromagnet around a stack of iron or steel discs mounted on a spindle. The discs were held in place to form a cylindrical armature. This armature was then mounted concentrically on pivot bearings, between the poles of an electromagnet. Although free to rotate at the bearings, the armature rotation was limited by a fixed spring. As the poles of the electromagnet were rotated, the armature would revolve until the torque exerted by the spring, equalled the torque due to the hysteresis and eddy currents in the specimens. Baily determined the power loss in the samples, from the torque exerted on the samples and the speed of rotation of the electromagnets. The theoretical eddy current losses were then subtracted to give an estimate of the rotational hysteresis losses. Baily's work established that the hysteresis in rotating magnetic fields is fundamentally different from hysteresis losses obtained under alternating flux conditions. Rotational hysteresis loss, when plotted against flux density, rises with increasing flux density, reaches a maximum, and then rapidly falls to zero as the sample reaches magnetic saturation. Weiss and Planer [111], extended the work of Baily in 1908. The authors measured rotational hysteresis losses in nickel, steel, soft iron and electrolytic iron.

More recently, Aouli [112] has built a device similar to Baily's but the circular disks

are replaced with slotted samples. These samples are used to simulate slotted machine laminations and are similar to induction motor rotor laminations. Global power loss in the laminations is derived from the torque produced on the samples. Measurement results have been reported in [113-115]. The device is used to study the global effects of rotational iron losses, but does not yield any information about the local iron losses under various degrees of flux density polarization.

3.2.2 Kelly's Rotating Top Method

In the 1950s, Kelly [116] used a rotating top method to study losses in 4-79 molybdenum Permalloy [117]. Cecchetti et al [37] later took up Kelly's technique to measure rotational power losses in GO and NO 3% SiFe electrical sheet steels. The authors observed that the rotational losses per cycle increase linearly with frequency for all values of magnetization. This is in contrast to observations made on alternating loss curves of GO material. Under alternating flux conditions the samples showed a nonlinear increase in losses per cycle, especially in the td of the sample. The nonlinear increase in loss per cycle was also observed in the rd of the sample but to a lesser extent.

3.2.3 Torque Magnetometers

In the late thirties, F. Brailsford published two papers [17,18] reporting the measurements of rotational and alternating hysteresis losses in four alloys of silicon steel. A torque magnetometer (see Section 3.2.3.1 for a description of this device) was used to make the measurements. Brailsford's work was motivated by two realizations:

1. Rotating electric machines exhibit iron losses that result from a combination of rotating and alternating magnetic fields within the core of the apparatus.

2. The existing literature of the time suggested that losses due to these two field conditions were fundamentally different.

Brailsford noted a sharp increase in the rotational hysteresis losses for all four materials at a flux density level corresponding to the knee of the saturation curve. Furthermore, his results showed that at low flux density levels (i.e., below 0.2 T), the rotational hysteresis could be as much as 2.6 times the alternating hysteresis loss. This ratio gradually reduced to a value approaching zero at the point of saturation.

Archenhold, Sandham and Thompson [118], measured rotational hysteresis losses in GO SiFe with the aid of an improved torque magnetometer [119]. The authors found that the ratio of rotational hysteresis to alternating hysteresis in the GO material was dependent on the thickness of the sample. The ratio increases with thin gauge samples. In samples less than 0.13 mm thick, the rotational hysteresis losses were up to ten times larger than the alternating hysteresis losses at flux densities less than 0.2 T. This ratio gradually reduced to three or four near the region corresponding to the knee of the saturation curve. At saturation the ratio was observed to be nearly zero.

Boon and Thompson [22] later used the torque magnetometer developed for the above study, to investigate rotational hysteresis losses in single crystals of iron. Measurements were made on 2.41% silicon-iron discs cut from single crystals with various planar orientations. Narita and Yamaguchi [23,24] later made rotational hysteresis loss measurements on single crystals of 4.3-4.5% silicon-iron. They also used a torque magnetometer in their investigations.

Yamaguchi and Narita [41] investigated rotational power losses in commercial grades of GO and NO silicon steels as an extension of earlier work [23,24] on single crystals. Rotational and alternating hysteresis losses of small discs were measured using a torque magnetometer. These same samples were then used to measure the rotational power losses at 60 Hz. An ac current through two intersecting coils produced the rotating magnetic field. The two intersecting coils consisted of a solenoidal coil whose axis was perpendicular to a set of Helmholtz coils. With this method, large excitation currents are required due to a lack

of flux closure paths through a system of yokes. The loss in the sample was measured using a thermocouple and the flux density in the x and y directions were measured by search coils wrapped around the sample. The authors separated the eddy current losses from the total rotational power losses since they had measurements for the rotational hysteresis losses.

Yamaguchi and Narita also estimated the eddy current losses by adding the losses in the x and y directions estimated by the classical eddy current formula. The difference in the value of observed eddy current losses to the calculated classical losses is often called the "anomalous loss." Yamaguchi and Narita showed that the anomalous loss was greatest at a value of approximately 1.1T and reduced to zero at saturation for a NO steel. The authors also investigated the possibility of estimating the rotational power losses as the sum of the losses found under alternating flux conditions in the x and y directions of the sheet. They found that the estimate was reasonable for elliptically polarized flux densities with small aspect ratios and for low flux density levels. As flux density was increased and the polarization became more circular the estimate became less accurate.

Tan et al [38] have used a rotating sample magnetometer described by Flanders [39,40], for making measurements of rotational power loss in various magnetic materials. The authors measured losses over a frequency range of 20 to 80 Hz. Measurements of rotational losses were taken on six amorphous alloys, one sample of 6.5% random textured silicon iron and three grades of NO silicon steel. The amorphous alloys were a factor of five to ten lower in rotational losses than the 6.5% silicon steel that in turn was a factor of two lower than the best grade of NO silicon steel.

3.2.3.1 Torque Magnetometers - Theory of Measurement

The torque magnetometer was developed by Brailsford [17,18]. Consider a disc of isotropic magnetic material suspended from its centre in a horizontal plane containing an applied field. In the absence of eddy currents, a uniform torque will be required to rotate the

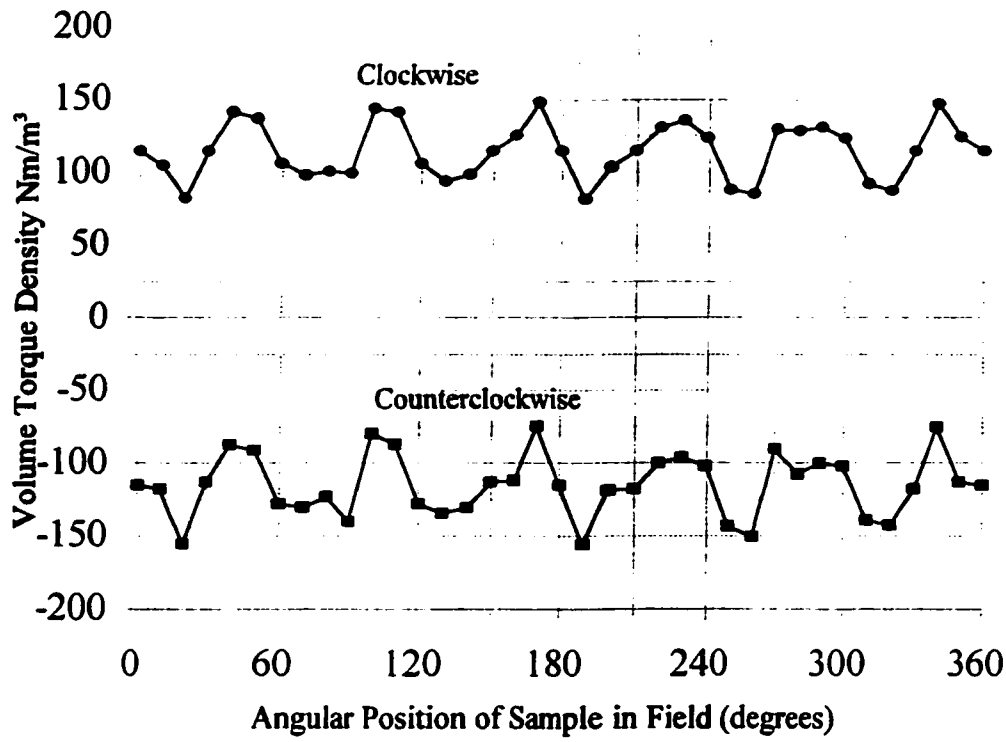

Figure 3.3- Torque curve for a hypothetical composite disc sample, based on figure 10 from Brailsford [17].

disc. The work done in one revolution represents the rotational hysteresis per cycle.

If $\overline{H}$ is the applied field strength and $\overline{J}_m$ is the magnetic polarization or intrinsic flux density, then $\overline{J}_m$ will lag $\overline{H}$ by an angle α_{lag} such that the torque per unit volume of the sample is given by [17]:

$$\overline{T} = \overline{H} \times \overline{J}_m = HJ_m \sin\alpha_{lag} \tag{3.3}$$

When a disc of anisotropic ferromagnetic material is slowly rotated in a magnetic field, a torque due to the anisotropy of the sample will be exerted on the disc. In addition, a torque due to rotational hysteresis will also exist. The anisotropy torque will depend on the orientation of the disc and the strength of the magnetic field. A torque curve is obtained

when the torque per unit volume on the sample is plotted against the angular position of the sample with respect to the orientation of the field. The torque curve obtained when the sample is rotated in a clockwise direction, will not coincide with the torque curve obtained when the sample is rotated in a counterclockwise direction. Figure 3.3 illustrates this point. Rotational hysteresis loss per cycle of rotation (J/m^3/cycle) is represented by half the area between the two resulting torque curves. Note that the loss is given as an energy density.

If a crystal is magnetized by an applied field, the stored energy is dependent on the direction of the magnetization. As discussed in Appendix B this is given by:

$$W_{anisotropy} = K_1(\alpha_1^2\alpha_2^2 + \alpha_2^2\alpha_3^2 + \alpha_3^2\alpha_1^2) + K_2(\alpha_1^2\alpha_2^2\alpha_3^2) \qquad \textbf{(3.4)}$$

The crystal will experience a torque acting to restore it to a position of minimum stored energy. The anisotropy torque of the sample can be several orders of magnitude larger than the torque caused by rotational hysteresis thereby making it difficult to discern the rotational hysteresis loss. Brailsford [17] has shown by theory and experimental observation that for a polycrystalline material, the anisotropy torque per m^3 exerted on a thin disc in an applied field is given quite generally by an equation of the form:

$$T_a = D_2 \sin 2(\alpha_{lag} + \delta_2) + E_4 \sin 4(\alpha_{lag} + \delta_4) + F_6 \sin 6(\alpha_{lag} + \delta_6) \qquad \textbf{(3.5)}$$

where D_2, E_4, F_6, δ_2, δ_4, and δ_6 are constants depending on the material and the particular crystal arrangement. (For a full development of this equation, refer to Brailsford's original work [17].) If three identical discs are superimposed so that the corresponding diameters of the discs are displaced with 120° between them, then the torque per m^3 for the composite disc is given by an equation of the form:

$$T_a = F_6 \sin 6(\alpha_{lag} + \delta_6) \qquad \textbf{(3.6)}$$

The torque due to the anisotropy of the sample has therefore been reduced to the last term

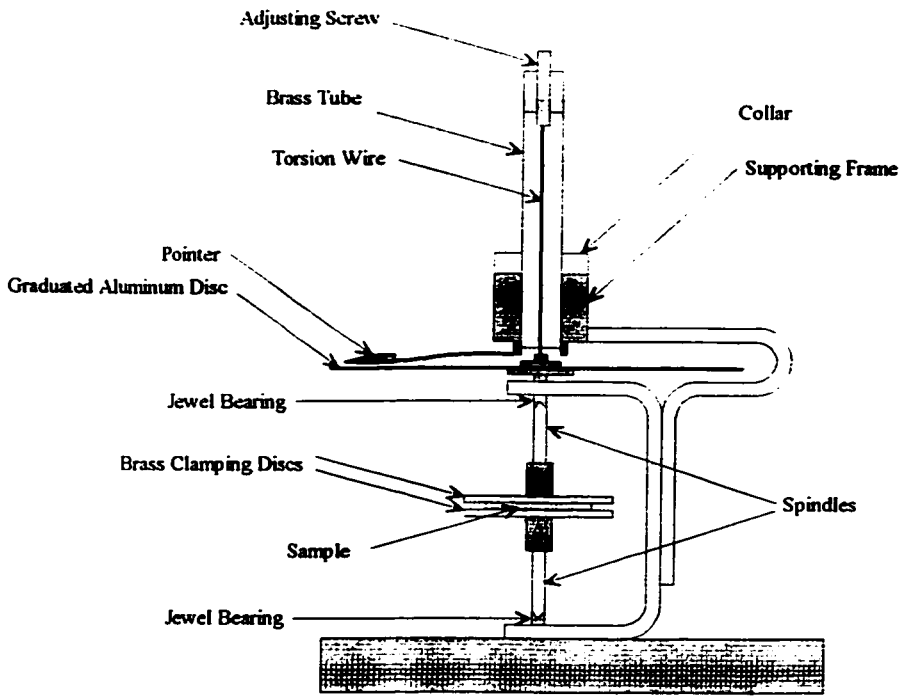

Figure 3.4 - Basic parts of a torque magnetometer, based on figure 5 in Brailsford [17].

of the equation. Increasing the number of discs can eliminate this term but the term is usually small enough that doing so is not necessary.

If the torque T_H due to the hysteresis loss is added, then for one direction of rotation of the composite disc we have:

$$T_1 = F_6 \sin 6(\alpha_{lag} + \delta_6) + T_H \tag{3.7}$$

and for the reverse direction of rotation:

$$T_2 = F_6 \sin 6(\alpha_{lag} + \delta_6) - T_H \tag{3.8}$$

The average torque due to hysteresis is given by taking the mean value of $\frac{1}{2}(T_1 - T_2)$. Figure 3.4 illustrates the basic features of a torque magnetometer.

3.2.4 Thermal Methods

Young and Schenk [120,121] used measurements of heating transients to determine iron losses in elliptically polarized magnetic fields. The fields were produced in a 2.54 cm cube of stacked laminations. Two orthogonal fields were produced using a pair of "C" cores with magnetizing coils. One core was excited by a magnetizing coil connected to the main supply through a variable auto transformer. The other core was excited by a magnetizing coil connected to an auto transformer fed by a three phase induction motor that was connected to the main supply and used as a phase shifter. Two mutually perpendicular one turn pick up coils were wound around the specimen to measure the two components of flux density. By exciting one core at a time, the authors could compare the losses to those obtained by the standard Epstein test. The two methods were found to yield results to within 15% when distortion was not present in the flux density waveform. Young and Schenk compared loss measurements due to elliptically polarized magnetic fields with estimates made from alternating loss measurements. These estimates were made by summing the alternating loss at the flux density level of the major axis of the ellipse locus, with the alternating loss at the minor axis of the flux locus. Young and Schenk concluded that the losses due to elliptically polarized flux were less than or equal to the estimates from alternating loss data. They also concluded that the losses are overestimated by the sum of the alternating losses with increasing flux densities and aspect ratios approaching one (i.e., a purely rotating field).

Boon and Thompson [122] measured alternating and rotational power loss at 50 Hz in 3% silicon iron sheets. They used a thermometric method described by Ball and Lorch [123] to make their measurements. The test specimen consisted of a 25.4 mm square of silicon iron to which thermocouples were attached. The specimen was in the centre of a stack of similar samples. Alternating or rotational flux was obtained by using C cores mounted in mutually orthogonal positions, the method being essentially the same as that described for Young and Schenk [120,121].

Measurements were made for hot rolled silicon steel with random orientation, commercial Goss or "cube on edge" oriented silicon steel, and "four square" or cubic oriented silicon steel. Four square silicon steel is a doubly oriented material. It has grains with [100] crystal orientations in both the rd and td of the sheet. The authors found that the alternating power loss in the rolling direction was very similar for the four-square and the Goss oriented material. However, rotational losses were remarkably different. The four-square material exhibited much lower losses than the Goss oriented material.

3.2.5 Field Sensing Methods

3.2.5.1 The Magnetic Core Loss Comparator of Kaplan

Kaplan [124] used a magnetic core loss comparator [125] to study core losses resulting from rotating flux. Losses were determined under rotating and alternating flux conditions for both GO and NO steels. Losses were also measured for three elliptically polarized flux conditions. Kaplan noted higher levels of loss with the rotating flux condition than with the alternating flux for any given flux density. When comparing the two grades of steel, he concluded that the relative increase in loss due to the rotating field was much greater in the GO material than in the NO material. Cross shaped samples were used with each leg of the sample inserted in a magnetizing coil. Using this arrangement, Kaplan was only able to produce rotating fields to flux densities of 1.1T in the GO material and 0.9T in the NO material.

3.2.5.2 Horizontal Yoke Methods

Brix [126] used a torque magnetometer to measure rotational power loss for frequencies ranging from 30 to 100 Hz. The results obtained from this apparatus agreed closely with the results obtained by a second method used by Brix et al [127]. In the second method, cross shaped samples were used with the field sensing method to obtain the

rotational power loss. The cross shaped samples were magnetized using a pair of yokes on which magnetizing coils had been wound. Flux density levels were obtained by search coils wound through holes drilled in the sample. Magnetic field strength was measured using a pair of tangential field sensing coils. Brix et al obtained rotating flux densities in the cross shaped samples up to 1.2 T, compared with 1.6T using the torque magnetometer. Arabi and Moses [128] used a similar method of cross shaped samples and the field sensing technique to measure the rotational losses in five grades of NO silicon steel. The authors were unable to achieve flux density levels above 1.1T. They reported that the loss under rotational flux conditions was up to three times larger than the losses under alternating flux conditions.

Brix, Hempel and Schulte [129] used an improved arrangement of samples and yokes to measure the rotational power losses in a sample of NO silicon steel. Crossed shaped samples were replaced by square samples. Each sample was placed in a magnetic yoke such that a small air gap surrounded the sample on all four sides. The cross section through the yoke was much larger than the thickness of the sample such that the reluctance offered by the yoke was small in comparison. Using this arrangement, the authors measured rotational power losses in a sample of NO silicon steel to a flux density level of 1.7 T. A pair of tangential field sensing coils was used to measure the field strength, and the "tip" or "needle" method (see Section 3.3.3) was used to measure the flux density in the sample.

Sasaki et al [2] developed a measurement system that used a standard Epstein strip as a sample. They used tangential field sensing coils to measure the magnetic field strength. Search coils were wound along diagonal lines of a square insulator into which the specimen was inserted. Addition and subtraction of the two search coil voltages gave signals proportional to the rate of change of flux density in the rd and td of the specimen. The sample was magnetized using excitation windings wrapped on a pair of yokes. One yoke consisted of a C core. The Epstein strip was placed across the legs of the core, shorting the magnetic circuit. A second yoke was constructed in a way that created a small air gap around

the sides of the Epstein strip. Using this system of yokes, a rotating magnetic field could be created in a 35 mm by 35 mm area of the Epstein strip. The authors measured rotational power losses to a flux density level of 1.6T in a NO grade of steel and to 1.2T in a GO grade.

The results of rotational power loss measurements obtained by the "field sensing" method have been compared with those obtained by using the initial rate of rise method. Fiorillo and Rietto [3] measured the losses in a stack of discs by using the stator of a three phase motor to create a rotating field. Rotational losses were measured in soft iron, 3% GO silicon steel and 3% NO silicon steel. The two methods of measurement gave very similar results. In a further extension of their work, Fiorillo and Reitto investigated the relationship between energy loss and frequency for both rotating and alternating magnetic fields [42]. The results of this study suggested that the increase of loss per cycle with increasing frequency was nonlinear in both rotating and alternating magnetic fields. This result contradicts the observations made by Cecchetti et al [37]. They found that the increase in loss per cycle with frequency was linear in rotating fields and nonlinear in alternating fields.

Enokizono et al [130] used an apparatus similar to the one described by Brix et al [129] to measure the rotational power losses in GO and NO silicon steels. The apparatus used in this study was further described by Enokizono et al in several other publications [4,131-132]. In the initial apparatus described in reference [4], the needle method was used to measure the time rate of change of the flux density in the sample. This was later changed to search coils through drilled holes [130]. Enokizono, Suzuki and Sievert [133] also measured magnetostriction in GO and NO samples under rotating flux conditions. Their results show that rotational magnetostriction in silicon steel is larger than the conventional alternating magnetostriction. This helps explain why rotating machines and transformers often exhibit higher levels of noise than predicted by rolling direction measurements of magnetostriction under alternating flux.

3.2.5.2.1 European Intercomparison

Recently, a paper was published which describes a European intercomparison of rotational power loss methods [134]. The following six teams of researchers participated in the project:

PTB Phys. - Technishe Bundesanstalt, Braunschweig, Germany
J. Sievert, H. Ahlers

IWE Inst. fur Werkst. der Elektrotech, Aachen, Germany
M. Birkfeld, K.A. Hempel

LEG Lab. d'Electr. de Grenoble, Saint Martin-d-Here, France
B. Cornut, A. Kedous-Lebouc

IEN Instituto Electrotecnico Nazionale G. Ferraris, Torino, Italy
F. Fiorello, A.M. Rietto

EBG Gesellschaft fur Elektromagn. Werkstoffe, Bochum, Germany
T. Kochmann

WCM Wolfsan Centre for Magnetics Technology, Cardiff, UK
A. Moses, T. Meydan

The various researchers used a wide range of methods. Most participants used field sensing methods applied to square samples. IEN applied the thermal method on circular samples and WCM used the thermal method on one of their samples as a supplement to their field sensing method. Tangential field sensing coils were used to measure H fields except for the EBG and IWE groups who chose to use Rogowski-Chattock Potentiometers (RCPs are described in Section 3.3.6.2). Two grain oriented and six non-oriented grades of material were tested and the selection of materials was made in a way that included a wide range of grain sizes, silicon contents, thickness and loss characteristics. Before cutting the samples from 500mm x 500mm parent sheets, the sheets were characterized on a single sheet tester at the PTB facilities. Table 3.1 summarizes the methods used by each group. The bottom entry shows how our (Power Research Laboratory - PRL) experimental set up compares.

Table 3.1 - European Intercomparison

Research Team	Loss Measurement Method	Sample Shape/Size (mm)	Geometry of measurement area (mm^2)/Sensor	
			B	H or thermal
EBG	Field Sensing	Square/60	60x60/CF	35.1x35.1/RCP
IEN	Thermal	Circle/90	42x42/HO	20x20/Thermal
IWE	Field Sensing	Square/60	60x60/CF	35.1x35.1/RCP
LEG	Field Sensing	Square/80	20x20/HO	20x20/TFS
PTB	Field Sensing	Square/80	28x28/TP	20x20/TFS
WCM	Field Sensing, Thermal	Square/100	20x20/HO	20x20/TFS
PRL	Field Sensing	Square/80	20x20/HO	20x20/TFS

CF - Coils wrapped around sample
HO - Windings fed through holes
TP - Tip method
RCP - Rogowski-Chattock Potentiometer
TFS - Tangential Field Sensing coil

The main quantity of the intercomparison was the iron loss measured under purely rotating flux and alternating flux directed at 0°, 45°, and 90°to the rolling direction. The measurements were made at 0.8, 1.0 and 1.2T for the grain oriented materials and 1.0, 1.2, 1.4 and 1.5 T for the NO materials. All measurements were made over the clockwise and counterclockwise directions and then averaged to remove any errors due to misalignment of samples.

For the GO materials the overall agreement between setups was poor. The measurements made by the WCM group gave results that were up to twice as high as the average of the other measurements, leading the remaining teams to question the result. Subsequently a software bug was discovered. The results obtained by EBG, IWE, LEG, and the thermal measurement made by WCM all agreed very closely with each other.

For the case of the NO steels, the agreement between measurements was best for the grades of steel with the lowest silicon contents. This was true for the rd measurements as well as those at 45°, and 90°. These results were also in good agreement with single sheet tester measurements made at the PTB facilities. Results obtained by LEG, PTB, and IEN were in close agreement for both the 270-35A (highest quality grade) and the 470P50 (medium quality grade) material. This result is promising since PTB and LEG both used field sensing techniques in which the B measurement was made in the region of interest (LEG using search coils through drilled holes and PTB using the tip method). The H field was measured using tangential field sensing coils. IEN used a thermal method suggesting that the results obtained by LEG and PTB are acceptable. The setups used by EBG and IWE are quite similar but the differences obtained in their results are sometimes remarkably high. RCPs and search coils wrapped around samples were used in the EBG and IWE setups. Difficulties associated with the RCP method are discussed in Section 3.3.6.2.

Overall agreement among the various researchers was relatively poor. The fact that there were cases where the agreement was fairly good, and that these cases are for materials most often used in motor and generator applications, is encouraging. Interest in rotational loss measurement techniques is primarily focussed on NO alloys, because these are the materials that will experience two-dimensional flux conditions in motors and generators. The researchers concluded that developing a standard test would be much easier if they concentrated their efforts on NO materials.

3.2.5.2.2 Other Efforts

Apart from the methods used in the inter-comparison described above, several other descriptions of methods have been recently published in the literature. Zhu and Ramsden [135], used the field sensing method with the tangential H sensing coils sandwiched between the sample and an identical sample that formed a guard sheet.

Kedous- Lebouc et al [136] published some results on rotational loss measurements that they made on GO silicon steel, NO silicon steel, and some nickel-iron (Ni-Fe) sheet. The (Ni-Fe) sheet is an interesting material because it has "easy" magnetization directions in both the (100) and the (010) directions that are the rolling and transverse directions of the sheet. For the NO silicon steel, the authors show that up to flux density levels of 0.8T, the sum of the alternating losses in the rolling and transverse direction approximates the value of the rotational loss. Beyond that level of induction the rotational losses are markedly smaller than the sum of the alternating losses. The rotational losses of the Ni-Fe sheet are systematically lower than the sum of the alternating losses in the rolling and transverse direction. The details of the apparatus used in their investigations are given in [137] and appear to be the same as those summarized for the LEG group in table 3.1.

A paper by Alinejad-Beromi, Moses and Meydan [138] describes a tester utilizing the field sensing technique for measuring the rotational losses in a 100 mm x100 mm sample. The apparatus is similar to one described for the WCM group in table 3.1. The authors had not yet implemented the thermal method to supplement the field sensing measurements. They were also using the tip method instead of drilled holes with search coils. The authors used the torque method of measurement (see Section 3.3.5) and characterized the losses in NO 2.7% Si-Fe, GO 3.2% Si-Fe, and some amorphous strip material. Losses in the amorphous strip were remarkably lower than in the silicon steel.

Morino, Ishihara, and Todaka [139] describe a tester utilizing the field sensing method. They used rectangular samples (300 mm x 60 mm), search coils wound through drilled holes to measure flux density, and tangential field sensing coils to measure the H field. The paper does not present any rotational losses. Instead, they used the apparatus to make iron loss measurements at various angles to the rolling direction, for a sample of GO silicon steel. The same tester was used in a later investigation [140]. The rectangular sample was replaced with a cross shaped sample (a 60 mm x 60 mm square with 20 mm tabs extending

from each of the four sides).

Hasenzagl et al [141] and Iványi et al [142] have described a horizontal yoke test that uses a hexagonal shaped sample. This hexagonal sample is 8 cm along each edge and has a total sample area of 166 cm^2. A yoke assembly consisting of a six pole system with six magnetizing coils is used to magnetize the sample. The apparatus can be fed from a three phase power source. The authors used the apparatus to study magnetization processes in GO steels. They point out that the larger sample area of the hexagonal sample (when compared with an 8 cm x 8 cm square sample) is advantageous for finding the average losses in GO materials that generally have large grain sizes.

3.2.5.3 Vertical Yoke Testers

Some researchers have investigated the possibility of using vertical yoke testers to make 2D magnetic measurements. Figures 3.5 and 3.6 illustrates some key features of a vertical yoke system. A double yoke system is illustrated with separate H coils on the top and bottom of the sample to measure the x and y components of the field strength. Enokizono et al [143] have analysed a vertical yoke system using the 2D finite element method and have drawn some interesting conclusions. They have found that a square sample with little overhang (sample extension protruding beyond the vertical sides of the magnetizing yokes) provides the most uniform field distribution in the sample. Furthermore, the length of the air gap between the yokes and the sample has an influence on the measurement of the field strength and the measured loss. The optimum gap length for their device was 0.01 mm. The work mentioned above was used in designing a vertical yoke system that was later built [144]. Yokes were constructed using a C core construction and a stacked lamination construction. With the C core construction, it was found that a considerable amount of flux in the x direction would spread along the sample and into the y direction yokes. The reverse was also true in the y direction. The stacked lamination yokes help alleviate this problem since the

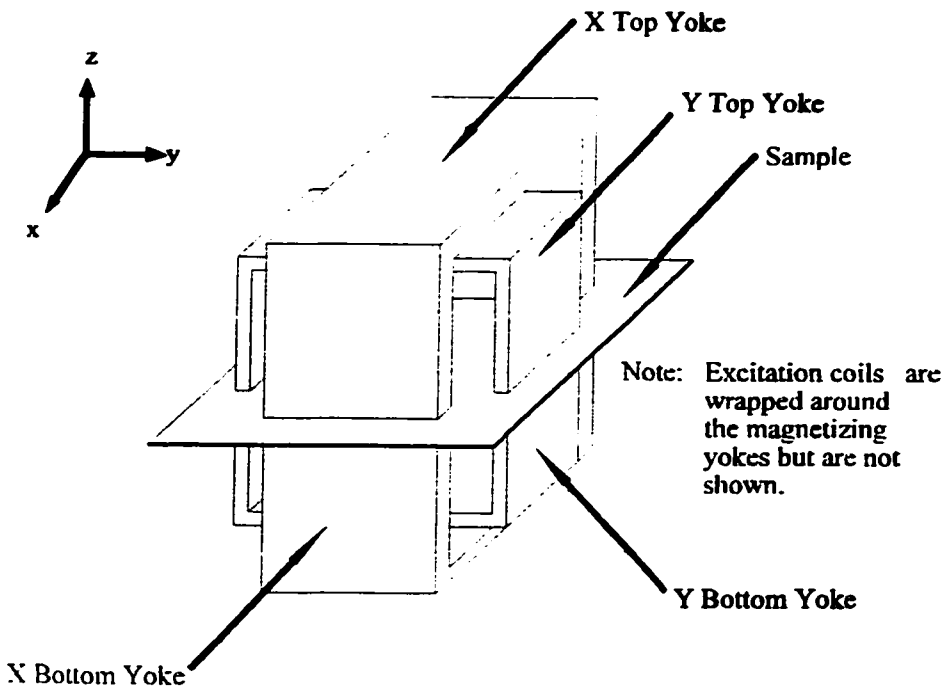

Figure 3.5 - Magnetic circuit of typical vertical yoke tester.

normal direction in a sheet of electrical steel has a relatively higher reluctance. Also, each sheet is separated by a minute distance due to the coating on the laminations thereby increasing the reluctance even further. Figure 3.7 helps illustrate this point.

Nencib et al [145] performed a 3D finite element analysis that agrees with the results of Enokizono et al [143]. Nakata et al [146] built a double yoke tester for measuring the magnetic properties of GO silicon steels along arbitrary directions rather than for rotational loss measurements. The authors of the previously mentioned studies do not state what motivated the use of a vertical yoke construction instead of the more popular horizontal yoke construction.

At least one advantage of the vertical yoke system is apparent. When making measurements on fully processed steels, the effect of edge strains in the sample is avoided

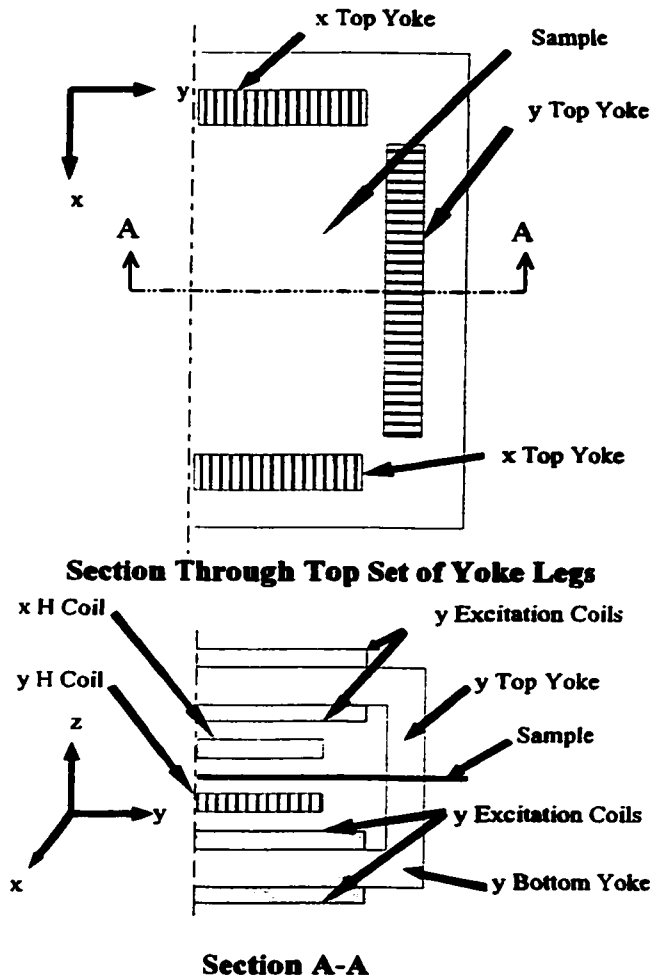

Figure 3.6 - Arrangement of vertical yoke tester.

with the vertical yoke arrangement. In this author's experience, useful results for fully processed materials, are difficult to obtain, without subjecting the material to a stress relief anneal. After shearing, the edges of the sample will be highly strained. When using a horizontal yoke system, a small air gap surrounds the sample and the induced flux must enter the sample through the sample edges. It is difficult to magnetize the sample if edge strains are present. With a vertical yoke system this problem is avoided because the flux will enter the sample in a normal direction with respect to the plane of the lamination. This is an

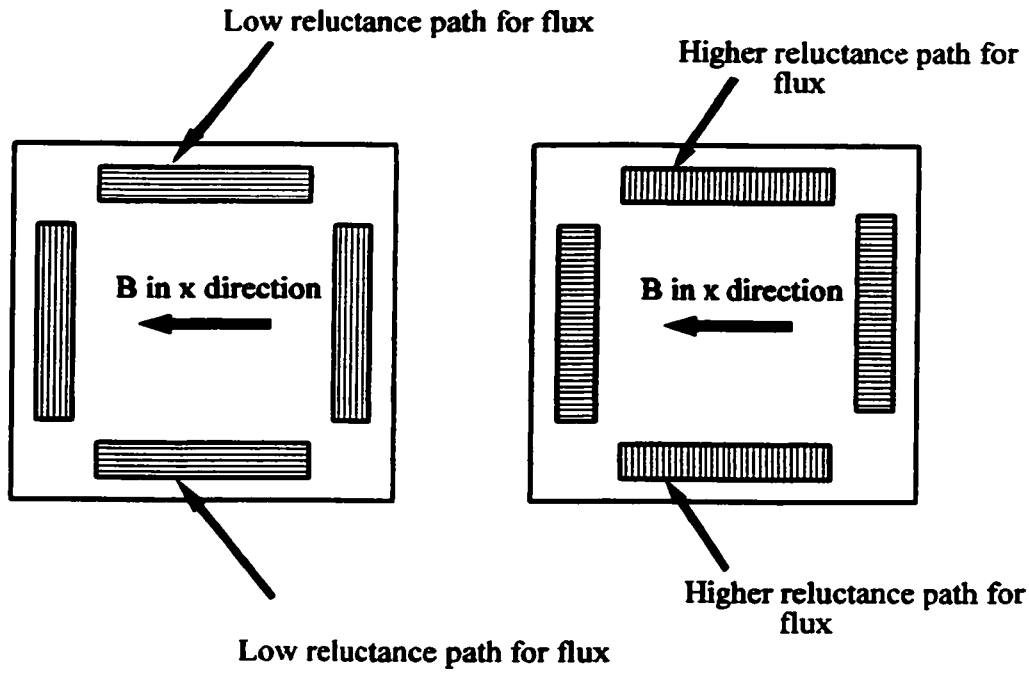

C core type construction Stacked lamination type constuction

Figure 3.7 - Comparison of yoke construction for vertical yoke tester.

important point because fully processed materials are rarely stress relief annealed after punching into laminations to reduce the cost of the machine. Therefore, testing the material for core loss without having to anneal it is desirable. In this manner, it is possible to obtain results which better correlate with the behaviour of the material after core assembly.

3.3 Field Sensing Method - Theory of Measurement

3.3.1 Poynting's Theorem

To understand the theoretical considerations behind making core loss measurements in electrical laminations, we consider the Poynting vector:

$$\overline{S} = \overline{E} \times \overline{H} \tag{3.9}$$

The cross product of the electric field strength vector and the magnetic field strength vector,

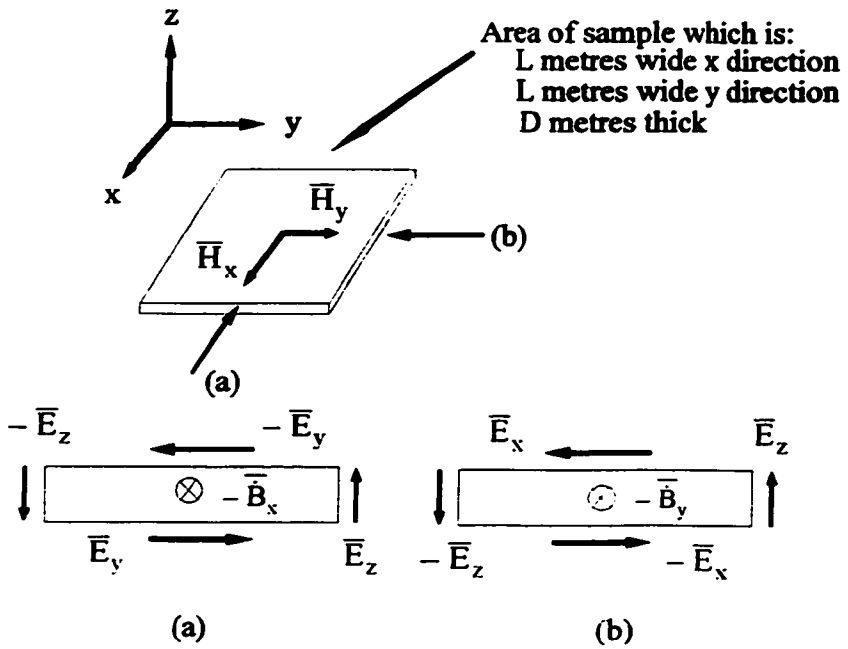

Figure 3.8 - Fields in the volume of the sample under investigation.

at the surface of a material, gives the Poynting vector. The resulting vector is perpendicular to the plane in which the electric and magnetic fields lie, and represents a surface power density with SI units of W/m^2. Plonus [13] explains that Poynting's Theorem may be stated as:

$$\iint_S \left(-\overline{E}\times\overline{H}\right)\cdot d\overline{S} = \iiint_V \overline{H}\cdot\frac{\partial\overline{B}}{\partial t}dV + \iiint_V \overline{E}\cdot\overline{J}dV \qquad (3.10)$$

The negative value of the Poynting vector integral represents the flow of energy through the surface of the sample (i.e., the volume V enclosed by the surface S is receiving energy). Field vectors on the left side of the equation occur on the surface of the material.

Field vectors on the right are the quantities enclosed by the surface (i.e., inside the material). The first term on the right-hand side of the expression gives the rate of increase of the magnetic energy in the volume or the hysteresis loss. The second term on the right gives the energy dissipated as ohmic or eddy current losses.

3.3.2 Search Coil Methods

Consider the sample illustrated in figure 3.8. The dimensions of the sample are L metres wide by L metres long and D metres thick. Front and side views of the sample are labelled (a) and (b) and show the orientation of the field quantities on the surfaces and interior of the sample. If we consider the power streaming into the six surfaces of the sample we can write the instantaneous power as:

$$p(t) = -2(\overline{E}\times\overline{H})\cdot\overline{A} \tag{3.11}$$

Looking at the right edge of the sample, the front edge of the sample, and the top surface of the sample, $\overline{A}$ is defined as:

$$\overline{A} = DL\hat{i} + DL\hat{j} + L^2\hat{k} \tag{3.12}$$

Multiplying by 2 takes care of the other three surfaces. Note that the z component of the H field is zero and that on the front face of the sample the z component of the E field is in the negative direction. The instantaneous power streaming into the front and back surfaces may now be written as:

$$p(t)_{Front + Back} = -2\begin{vmatrix} \hat{i} & \hat{j} & \hat{k} \\ E_x & E_y & -E_z \\ H_x & H_y & 0 \end{vmatrix}\cdot DL\hat{i} \tag{3.13}$$

On the right face of the sample the z component of the E field is in the positive direction. The instantaneous power streaming into the right and left surfaces may be written as:

$$p(t)_{Right\ -\ Left} = -2\begin{vmatrix} \hat{i} & \hat{j} & \hat{k} \\ E_x & E_y & E_z \\ H_x & H_y & 0 \end{vmatrix} \cdot DL\hat{j} \tag{3.14}$$

Now note that on the top surface of the sample, the y component of the E field is in the negative direction. The instantaneous power streaming into the top and bottom of the sample is written as:

$$p(t)_{Top\ -\ Bottom} = -2\begin{vmatrix} \hat{i} & \hat{j} & \hat{k} \\ E_x & -E_y & E_z \\ H_x & H_y & 0 \end{vmatrix} \cdot L^2\hat{k} \tag{3.15}$$

Summing equations (3.13) through (3.15) the expression for the instantaneous power simplifies to:

$$p(t) = -2DLH_yE_z - 2DLH_xE_z - 2L^2(H_yE_x + H_xE_y) \tag{3.16}$$

Faraday's Law of Induction can be written in the integral form:

$$\int_l \bar{E}\cdot d\bar{l} = \frac{\partial}{\partial t}\int_S\int \bar{B}\cdot d\bar{S} \tag{3.17}$$

Refer again to the sample illustrated in figure 3.8. The flux density is an average value over the sample surface S. If search coils are wrapped around the outside of the sample such that their axes lie in two orthogonal directions, it is possible to measure the time rate of change of the average magnetic flux densities in the x and y directions. It is possible to write the following expressions by evaluating Faraday's Law along the path followed by each search

coil :

$$DL\frac{\partial B_x}{\partial t} = -2LE_y - 2DE_z \tag{3.18}$$

$$DL\frac{\partial B_y}{\partial t} = -2LE_x - 2DE_z \tag{3.19}$$

These can then be written as:

$$-\frac{\partial B_x}{\partial t} = 2\frac{E_y}{D} + 2\frac{E_z}{L} \tag{3.20}$$

$$-\frac{\partial B_y}{\partial t} = 2\frac{E_x}{D} + 2\frac{E_z}{L} \tag{3.21}$$

The average power loss in the sample (W/kg) is calculated using:

$$P_r = \frac{1}{T\rho}\int_0^T \left(H_x\frac{\partial B_x}{\partial t} + H_y\frac{\partial B_y}{\partial t} \right) dt \tag{3.22}$$

The equivalent instantaneous power loss in the volume of the sample is given by the expression:

$$p(t) = DL^2\left(H_x\frac{\partial B_x}{\partial t} + H_y\frac{\partial B_y}{\partial t} \right) \tag{3.23}$$

If we substitute equations (3.20) and (3.21) into (3.23) we arrive at the same expression as (3.16). This shows that the formulation given by equation (3.22) is consistent with Poynting's Theorem if the search coils are wrapped around the sample. If the search coils are wrapped around the interior portion of the sample through drilled holes, the same formulation holds. The difference is that the z directed components of the E field occur at the edges of the drilled holes rather than at the edges of the sample.

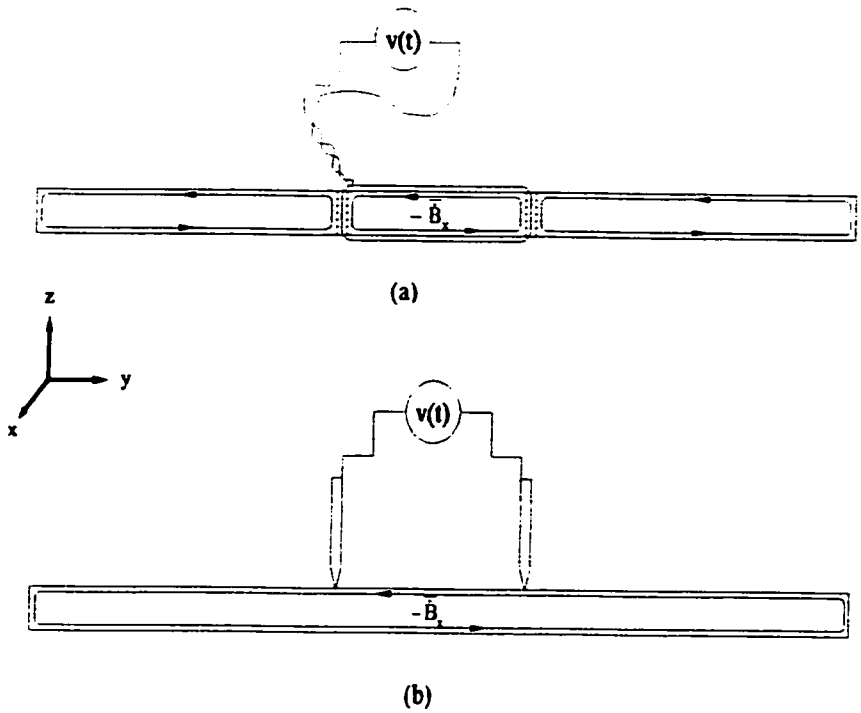

Figure 3.9 - Comparison of search coil and needle method of measuring flux density.

3.3.3 Needle or Tip Method of Measuring Flux Density

The needle or tip method has been used for several years [129,147] and has also been described by Pfützner [148]. When using this method, the z directed components of the E field are not taken into account. The loss equation is formulated based on the assumption that all the energy streams into the top and bottom of the sample. In the interior of a thin lamination, no z component of the E field exists since any eddy currents in the volume of the sample will flow along the upper and lower surfaces of the sample. For instance, consider the top surface of the sample in figure 3.9b) with the E and H fields in the same orientation as in figure 3.8:

$$\overline{A} = L^2\hat{k} \tag{3.24}$$

The expression for instantaneous power loss is then given as:

$$p(t) = -2\begin{vmatrix} \hat{i} & \hat{j} & \hat{k} \\ E_x & -E_y & 0 \\ H_x & H_y & 0 \end{vmatrix} \cdot L^2\hat{k} \tag{3.25}$$

This can be rewritten as:

$$p(t) = -2L^2(H_xE_y + H_yE_x) \tag{3.26}$$

A direct application of the above equation gives the average rotational power loss in the sample by the needle method:

$$P_r = -\frac{2}{T\rho DL}\int_0^T (H_xV_y + H_yV_x)dt \tag{3.27}$$

where V_x and V_y are the voltages between two pairs of needle electrodes oriented in perpendicular axes and L is the distance between the needles. The needles form a half turn winding along the surface of the sample. The flux density in the sample is determined using the expressions:

$$-\frac{\partial B_x}{\partial t} = 2\frac{E_y}{D} \tag{3.28}$$

$$-\frac{\partial B_y}{\partial t} = 2\frac{E_x}{D} \tag{3.29}$$

Avoiding a contribution to the induced voltage waveform by the flux in the air between the two needles, is not easy when using the needle method.

Table 3.2 - Comparison of Search Coil and Needle Method

	Coils Surrounding Sample	Coils Through Drilled Holes	Needles in Contact With Sample
Advantages	Produces a high voltage.	High voltage. High local resolution	High local resolution.
Disadvantages	Poor local resolution in large grained materials. Demagnetization due to inclusion of edge effects.	Influence on magnetization process (cold work due to drilling). Eddy current path in z direction	Low voltage (noise). Air flux contribution. Requires removal of surface insulation.

3.3.4 Comparison of Search Coil and Needle Method

The advantages and disadvantages of the search coil and needle methods are summarized in table 3.2. When using search coils around the sample, a comparatively high voltage is induced in the coils. This is due to the large cross sectional area of the sample in which the average flux density is contained. Wrapping multiple turns around the sample may further increase the voltage. The disadvantage associated with this method is that on creation of a rotating magnetic field in a sample, the field will be purely rotating solely in the central area of the sample. At the edges of the sample, the uniformity of the field will be greatly reduced.

Drilling holes in the centre region of the sample and winding search coils through the holes avoids this problem. This method gives a high local resolution and can obtain a high voltage if using multiple turns. The drawback to this method is that by drilling holes in the sample, the material in the region of the hole is cold worked and this reduces the magnetic quality of the material. This problem can be alleviated in semiprocessed materials by applying

a stress relief anneal before measurement. The arguments in the proceeding section highlight the second problem.

By drilling holes in the sample, eddy current paths in the sample will allow a contribution to the losses due to a z component of the E field along the vertical length of each hole. Increasing the size of the sample and the area of measurement, could reduce this problem by reducing any contribution to the losses by the z directed field as a percentage of the total measured value. The needle method offers a second solution to the problem of the z directed E fields but introduces problems of its own. High local resolution of the measurement is offered by the needle method, but the voltage produced between the needles is small and susceptible to noise. The area formed by the needles and connecting leads forms an area that will link flux in the air surrounding the sample. Avoiding the contribution of the air flux to the induced voltage is difficult. The air flux contribution will lead to errors in both the flux density measurement and the loss measurement.

The difference in the theoretical formulation of loss, using the search coil method and the needle method, is pointed out as a possible source of variation in results obtained when using the two methods. Measurements of both flux density and loss will differ between the needle method to search coil method; in the needle method, the z component of the E field does not appear in the expressions for either quantity. The difference in the loss calculation is compounded by the difference in the setting of the flux density level when using equations (3.28) and (3.29) as opposed to search coil voltages given by equations (3.20) and (3.21).

3.3.5 Torque Method

Some authors [139,131,149-150] had proposed using the equation

$$P_r = \frac{2\pi}{\rho T^2}\int_0^T |\overline{H}\times\overline{B}|\,dt \qquad \textbf{(3.30)}$$

to measure the rotational power loss. This equation is equivalent to equation (3.22) for the case of circular polarization only. If a magnetic material is subject to a constant magnitude rotating magnetic field, then, due to a spatial lag of the flux density, a torque is exerted on the material. If the material is not allowed to move the loss per unit mass in overcoming this torque can be calculated using equation (3.30). I rejected this formulation from the start because I realized it could not be used to evaluate the losses in an elliptically polarized field. Sievert [151] also points out that equation (3.30) gives losses that can be higher than those found from equation (3.22) for elliptically polarized fields. This would infer that the losses due to the alternating portion of the field were negative, which is clearly incorrect. Atallah and Howe [152], finally, explained this anomaly by pointing out that equation (3.30) should be written as

$$P_r = \frac{1}{\rho T}\int_0^T \frac{d\Pi}{dt}|\overline{H}\times\overline{B}|\,dt \qquad \textbf{(3.31)}$$

where the instantaneous angular velocity (the time derivative of Π) of the flux density vector can vary substantially over a cycle. This represents the main difference from equation (3.30) in which this velocity is taken as the constant $2\pi/T$. Equation (3.31) will give the portion of the loss from the rotating component of the magnetic field for elliptically polarized fields. Researchers have abandoned the torque method and the field sensing methods given by equations (3.22) and (3.27) have been largely accepted due to their generality.

3.3.6 Methods of Measuring the H Field

3.3.6.1 Tangential H Coil Method

Careful consideration of Poynting's Theorem has shown that it is not the tangential component of the H field inside the sample but instead the surface quantity that we must

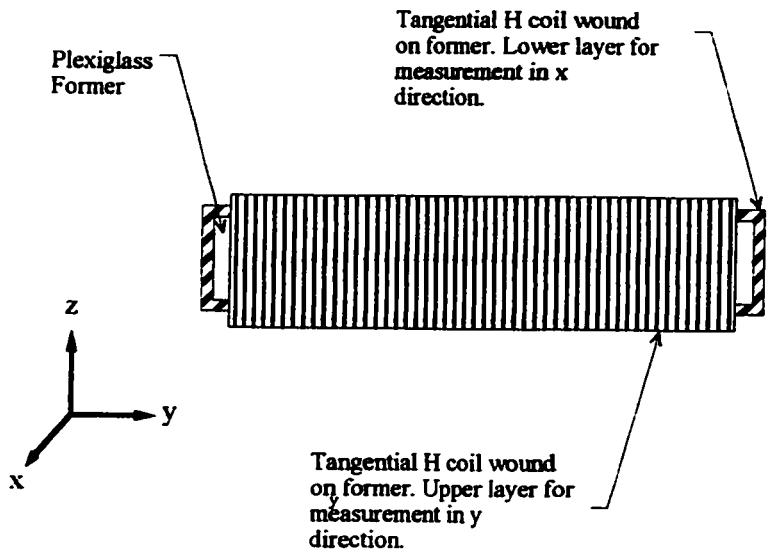

Figure 3.10 - Tangential H sensing coils wrapped in orthogonal directions on a plexiglass former.

measure. A tangential H coil cannot measure the H field inside the surface of the sample because of eddy currents within the sample. Recall, that at the boundary of two different mediums, the tangential component of the H field is discontinuous by a surface current density flowing at the interface between the conducting and non-conducting media. The induced eddy currents in the sample give this surface current density. Using a multi-turn coil wound on a thin nonmagnetic former, we can measure the magnetic field strength at the surface of the sample. The time derivative of the field strength is measured according to Faraday's Law of Induction:

$$V_H = -N\frac{d\phi}{dt} = -NA_H\mu_o\frac{dH}{dt} \tag{3.31}$$

where N is the number of turns on the former, ϕ is the flux linked through the coil and A_H is the cross sectional area of the coil. By using a rectangular former, two orthogonal coils can

be wound one on top of the other as depicted in figure 3.10. This gives the field strength in the x and y directions of the sample. Tangential H coils were used in this investigation to obtain measurements of the time derivative of the magnetic field strength. The magnetic field strength H, is obtained by numerical integration of the voltage waveform given by the coil.

3.3.6.2 Rogowski-Chattock Potentiometer

According to Zijlstra [153], the Rogowski-Chattock potentiometer (RCP) is used to measure differences in magnetic potential or a magnetic field strength inside a piece of matter. It consists of a U - shaped coil wound on a non-magnetic former as illustrated in figure 3.11. The two ends of the coil lie in one plane and are butted against the sample under investigation. The flux enclosed by the coil is proportional to the potential difference (mmf) between its two ends. The principle of operation is of the RCP is given by Zijlstra [153] and also by Mikulec [154]. The coil is placed in a magnetic field and the path going along the coil axis is path I while the path outside the coil (in the material) is path II. If no current is present, we obtain the mmf between one end of the coil located at P_1 and the other end located at P_2 as:

$$\mathcal{F}(P_1) - \mathcal{F}(P_2) = \int_{II} \bar{H}_{II} \cdot d\bar{l}_{II} = \int_{I} \bar{H}_{I} \cdot d\bar{l}_{I} \qquad \textbf{(3.32)}$$

Consider the cross sectional area of turns of a U-shaped coil to enclose an area S. The flux enclosed by the RCP is given by the expression [154]:

$$\Phi = \mu_o n S \int_{I} \bar{H} \cdot d\bar{\ell} \qquad \textbf{(3.33)}$$

where n is the number of turns per unit length which is a constant along the axis of the coil.

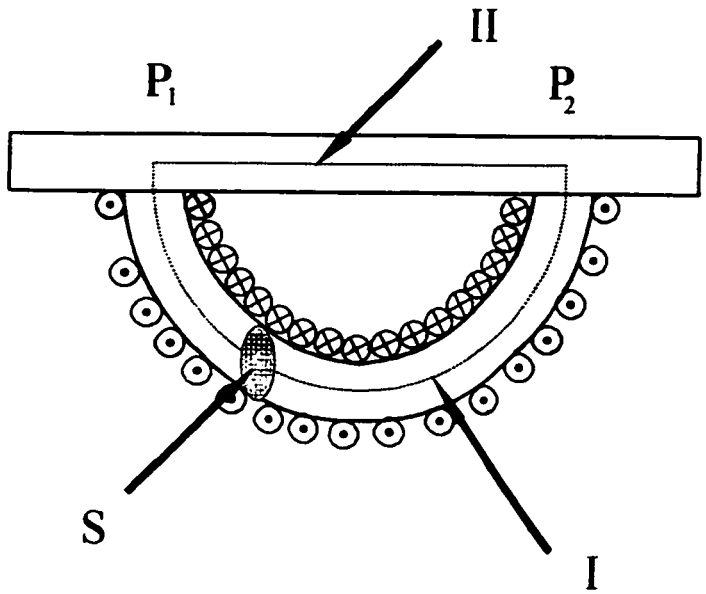

Figure 3.11 - The Rogowski-Chattock Potentiometer (RCP). Based on figure 1.35 from Zijlstra [153].

According to Zijlstra [153] this can be written as:

$$\Phi = \mu_o n S \ell H_l \tag{3.34}$$

where ℓ is the distance between P_1 and P_2 and H_l is the field component along line I joining these two points. The factor $nS\ell$ must be determined by calibration in a known field. In a time varying field, the RCP will produce a voltage given as:

$$v(t) = \frac{d\Phi}{dt} = \mu_o n S \ell \frac{dH_l}{dt} \tag{3.35}$$

Therefore, given the factor $nS\ell$ and the voltage produced by the coil, the time derivative of the field strength can be determined.

Salz and his fellow researchers [147,155,90] have used the Rogowski-Chattock potentiometer in several investigations. Salz states that the RCPs are standing on the surface

of the sample. According to Zijlstra [153], "if the coil is placed with its end faces against a flat piece of matter in which a homogeneous field is present the tangential component of the field inside the matter is measured." However, we must consider that this statement is only true in the absence of eddy currents. The derivation above is dependent on the assumption that no currents are enclosed within the area contained in paths I and II. We have already seen that with time varying magnetic fields, the tangential field inside the sheet and at the surface of the sheet is not the same due to eddy currents! We have also seen by careful consideration of Poynting's Theorem that it is the surface field that needs to be measured. To rectify the situation, we must understand that in case of time varying fields and conductive samples, path II in figure 3.11 should be taken along the surface of the sample rather than inside the sample.

The operation of the Rogowski-Chattock potentiometer is less straightforward than that of the tangential H coil method. Obtaining a uniform winding on a U shaped former is also difficult. To use an RCP, it must be calibrated in a known field. The RCP offers no apparent advantages to tangential H coils. Therefore, the RCP method was rejected in favour of the tangential H coil method in the present study.

3.4 Rotational Losses in Transformer T-Joints

Moses et al [156] studied the heating effects of the spatial distribution of flux density in transformer core T-joints. In further investigations by Moses and Thomas [157,158], measurements in two T-joint arrangements showed a complex flux density loci. When this flux density variation was separated into its harmonic components, the authors found that rotational flux occurred. In the first T-joint arrangement, the first and third harmonic flux density vectors described elliptical paths in the material but rotated in opposite directions in the region of interest. The first harmonic described an ellipse with its major axis inclined at a small angle to the transverse direction in the lamination. Conversely, the third harmonic

described an ellipse with its major axis aligned close to the rolling direction. Rotational fluxes were noted in the second T-joint also but to a reduced level, owing to an improved arrangement of the lamination butt joints. The authors concluded that the rotating fundamental and harmonic fluxes, and flux travelling in a direction perpendicular to the plane of the laminations, could cause the high localized loss in the T-joints of transformer cores.

The distribution of rotating flux and iron loss in T-joints of transformer cores was also studied in Japan by Narita et al [159]. To measure the distribution of rotating flux in the T-joint, the authors punched 1mm diameter holes into the laminations at a spacing of 12.5 mm, forming a grid. Twenty-three orthogonal search coils of five turns each were wound through these holes. Coil outputs were digitized and analysed by computer. The localized iron loss in the T-joints was measured by the initial rate of rise method similar to the method of Ball and Lorch [123]. Three types of transformer cores were investigated. One core consisted of 90° overlapping laminations in both the T-joints and corner joints. The laminations were made of 0.35 mm thick NO silicon steel. A second core represented the type of core most often used in the transformer industry. Both the T-joints and corner joints were made of 45° overlap joints. Laminations for the second core were made of 0.35mm thick GO silicon steel. A third core was made of the same material as the second core. The corner joints were made from 45° overlap joints and the T-joints were made from 90° overlap joints.

In the first core, a circular rotating flux was produced at a point a short distance from the central point of the T-joint. The rotating flux became flat and elliptic away from this point. For the oriented silicon steel cores, the direction of the magnetic flux vector was strongly influenced by the magnetic anisotropy. The locus of the flux density took on the shape of a very flat ellipse with the major axis parallel to the rolling direction. In all three cores, the rotating flux was produced over a large area of the T-joint. Moses et al [158] had only measured the rotating flux over a small portion of the 45° and 45°/90° joints around the overlapped part of the core sheets. Narita et al [159] were able to show that the

additional losses due to rotating flux, normally directed flux and additional harmonics would make the average iron losses in the T-joint larger than in the central leg of the transformer core. For the first core the average loss was 20% higher in the T-joint, for the second core the loss was 80% higher and for the third core the loss was 32% higher. This shows the importance of accurately modelling the loss mechanisms in the T-joint of a transformer core. If the losses are not modelled in great detail the losses in the core will be incorrectly estimated and the occurrence of local hot spots in the transformer core cannot be accurately predicted.

3.5 Past Research Into Quantifying Rotational Flux and Rotational Losses in Electric Machine Cores

The literature contains little on efforts to quantify the effect of rotational losses in the cores of rotating electric machines. Most of the effort to date has been focussed on creating a standardized test apparatus for measuring rotational losses in silicon.

Radley and Moses [160-161] studied the magnetic flux and power loss distribution in a model of a turbogenerator stator core. The model core was built up using grain oriented silicon segmental punchings with the rolling direction of the sheet parallel to the direction of the yoke and the transverse direction parallel to the teeth. The authors mapped the regions of rotational flux in the model core by using pairs of orthogonal search coils wound through drilled holes in the steel. Strong rotational components of flux were noticed in the roots of stator teeth and to a smaller degree behind the stator slots. Local power loss distribution was studied using thermocouples and the "initial rate of rise temperature technique" described by Ball and Lorch [123]. The average loss at the positions closest to the tooth roots and stator slots was 2.69 W/kg compared with 1.97 W/kg near the outer edge of the core. This suggests that the areas where the rotational flux is the strongest also have the largest losses.

Lorenzen and Nuschler [162] analysed the flux distribution in the stator of a synchronous machine using a finite difference approach. Calculations were made for a 115

MVA machine with 10 poles. One pole pitch of the machine was modelled using approximately 11,000 mesh nodes. To get the time-dependence of the magnetic flux density for each element, 36 field calculations per half a period were carried out. The radial and tangential components of the flux density for each location of the machine were then stored and served as the basis of the power loss calculation. Rotational power loss data was obtained using an apparatus developed by Brix et al [127]. Loss values were determined for various degrees of elliptical polarization using purely sinusoidal excitation. The fundamental component of the radial and tangential flux density in each area of the machine was determined and an aspect ratio for the elliptical polarization was established. The power losses due to the fundamental component of the flux density in every area of the stator core were determined using the measured data for various elliptical polarizations. Harmonics in the flux density were handled empirically using eddy current correction factors described by Lavers et al [45-47] (see section 2.3.5). Unfortunately, the authors only present a figure illustrating the specific fundamental frequency (apparently without harmonic effects) power loss distribution along a tooth axis, from the bore of the machine, to the outer diameter of the core. Lorenzen and Nuschler do not elaborate on whether or not they found their method of calculation to be superior to more traditional methods.

Enokizono [163] studied the flux distribution in a model core of a three phase induction motor driven by an inverter. The model was set up to simulate locked rotor conditions. Rotational flux patterns were measured using a series of orthogonal search coils at various locations in the core. The measurements revealed a large component of rotational flux at the tooth roots of the machine. Enokizono also did a time-stepping finite element analysis of the problem and showed the presence of rotational flux in the same areas as determined by experimental measurement on the model core. No attempt was made at quantifying the losses in the model core.

Jamil, Baldassari and Demerdesh [164] used a set of 192 sequential finite element field

solutions, over a span covering 360°electrical of rotor motion, to derive the flux density variation in the core of an induction machine. Time variations of the radial and tangential components of flux density variation within each element were derived from the field solutions. These were then decomposed into individual harmonic components. The authors quantified the rotational flux in each element of their model by decomposing the flux density variation into radial and tangential components. Losses in each element were by taking the sum of the losses under alternating flux conditions (from Epstein tests) for the radial and tangential components individually. An attempt to quantify the effect of harmonics on core losses was made by using the method outlined by Lavers et al [45-47] (see section 2.3.5). The flux density waveform reported for the tooth of the machine was very nearly sinusoidal. The highest harmonic in the radial direction was the fifth at 1.16% and in the tangential direction the third harmonic was 3.63% of the fundamental. This suggests that the effects of rotor permeance variations are small in the stator. The authors mention that, "Upon computation of the flux density waveforms (radial and tangential) in the laminated stator core and solid rotor core of the motor, the instantaneous profiles of these flux densities were used to calculate the total core losses". They found that the inclusion of the harmonics increased the predicted losses by approximately 45% over the sinusoidal losses. Unfortunately, the authors do not elaborate on whether the bulk of these additional losses were found in the solid rotor core. Given the small harmonic content of the flux density in the stator teeth, and the fact that the stator was laminated but the rotor was not, this is likely the case.

A similar approach was taken by Atallah and Howe [165] in their investigation of permanent magnet dc machines. Rotational losses in the machine were estimated by adding the losses associated with the corresponding orthogonal alternating flux density components. This was done although figure 3 in [165] (showing rotational and alternating losses for the core material) shows that this estimate is not valid at flux densities above 1.0T.

Shirkoohi and Yahya [166] studied the localised flux distribution and iron losses in

the core of a three phase induction motor using small search coils and thermistors. Rotational flux patterns were mapped by using orthogonal pairs of search coils at various locations in the core. The orthogonal coils were then connected to a spectrum analyser by which the magnitude and phase angle of fundamental and harmonic components of flux density were measured. The authors observed elliptically polarized flux in the core and alternating inside the teeth. The highest degree of polarization was observed at the tooth root, and the polarization gradually decreased moving toward the outer diameter of the machine. A small degree of polarization was also noticed at the tooth tips.

Bertotti et al [167-168] studied iron losses in an induction motor core by combining a finite element analysis with physical models of iron loss. The authors attempted to compute iron losses based on independent formulations for the hysteresis, anomalous and classical eddy current losses under general elliptical flux patterns. Their model requires prior knowledge of static hysteresis losses and 50 Hz power losses under alternating sinusoidal flux and pure rotational flux. The authors assumed that the hysteresis losses associated with an elliptical flux could be estimated by assuming a linear relationship with the aspect ratio of the flux density ellipse. The hysteresis losses due to elliptical flux were given by Bertotti et al as:

$$P_{he}(B_{maj}) = P_{ha}(B_{maj}) + P_{ha}(B_{maj}) \times a(r_h(B_{maj}) - 1) \tag{3.36}$$

where,

P_{he} is the hysteresis loss due to elliptical flux,
P_{ha} is the hysteresis loss due to alternating flux,
B_{maj} is the flux density along the major axis of the ellipse,
a is the aspect ratio of the ellipse, and
r_h is the ratio of the rotational to alternating hysteresis loss as determined by experiment.

In [167] a similar approach was applied for the excess or anomalous loss but r_h is replaced by r_e, the ratio of the rotational excess loss and the alternating excess loss. The curves for r_h and r_e given in [167] are very similar in behaviour and magnitude. In the earlier

study, Bertotti et al [168] assumed that the anomalous losses were approximately the same as the classical eddy current losses and modelled both using the same formula. The classical eddy current losses were calculated by superposition of the eddy current losses due to the harmonics in the major and minor axes of the flux density locus.

The loss formulation was applied to a model induction motor core for which the flux distribution was calculated by means of the finite element method. For each element of the mesh, the components of the elliptical flux locus along the major and minor axes were established. In reference [168] Bertotti et al modelled the stator and rotor slots and found that the position of the rotor did not significantly influence the loss prediction. Using the three term model described above, they predicted 60.9 W of loss and measured 101.7 W at rated machine voltage.

In reference [167], the machine was modelled with a slotless rotor assumed to rotate at synchronous speed. Values predicted by the proposed methodology were compared with values predicted by assuming that the flux density in each element was purely alternating. A substantial difference in the results was found in regions of the core where the rotational flux was predominant. In the region behind a stator tooth, the losses calculated by the conventional method were 2.51 W/kg and 3.04 W/kg by the proposed method. The losses computed over the whole stator core show a difference of less than 10%. No comparison was made with measured losses.

Leonardi, Matsuo and Lipo [169] investigated iron losses in synchronous reluctance machines using a series of magnetostatic finite element solutions. The flux density in each element was decomposed into tangential and radial components using a method similar to that already mentioned for Jamil et al [164]. The power loss per kg for the nth harmonic was obtained for the kth element from the classical expression:

$$P_{i,k,n} = k_h f_n B^{\zeta}_{i,k,n} + k_e t^2 f^2_n B^2_{i,k,n} \qquad \textbf{(3.37)}$$

where,

k_h is the hysteresis coefficient,
i (=x or y) is one of the orthogonal components of B,
f_n is the harmonic frequency,
ζ is the hysteresis loss exponent,
k_e is the eddy current loss coefficient,
and t is the lamination thickness.

The rotational losses were thus estimated by summing the alternating losses in the two orthogonal components of the rotational flux.

Recently, Enokizono and Sadanaga [170-171], investigated field and loss distributions in a two pole, three phase induction motor. They did not state the rating of the machine but they did give the outside diameter of the machine as 720mm, suggesting a medium size industrial motor. The rotor of the machine had open slots that were trapezoidal with the narrow part of the slot closest to the machine air gap. The authors used a finite element method formulated so that a reluctivity tensor was used in the analysis. The more conventional method of defining the reluctivity of a material involves using the relationship

$$B = \frac{1}{\nu} H \tag{3.38}$$

where ν is the inverse of the permeability of the material and is obtained from a BH curve. In this sense, the reluctivity is described as a scalar quantity. Enokizono and Sadanga used a tensor relationship to define the reluctivity in each element under rotating flux conditions. They defined the tensor relationship as

$$\begin{bmatrix} H_x \\ H_y \end{bmatrix} = \begin{bmatrix} \nu_{xx} & \nu_{xy} \\ \nu_{yx} & \nu_{yy} \end{bmatrix} \begin{bmatrix} B_x \\ B_y \end{bmatrix} \tag{3.39}$$

The tensor values were determined using a horizontal yoke tester described in [4,130-131]. The measured tensor was defined for each locus of the flux density through three parameters; the maximum flux density, the axis ratio of the locus of the flux density, and the inclination

angle of the locus from the rolling direction of the material. The three parameters are defined through the following relations:

$$\begin{bmatrix} B'_x \\ B'_y \end{bmatrix} = \begin{bmatrix} \cos\theta & \sin\theta \\ -\sin\theta & \cos\theta \end{bmatrix} \begin{bmatrix} B_x \\ B_y \end{bmatrix} \tag{3.40}$$

$$B^2_{max} = B^2_x + \frac{B^2_y}{a} \tag{3.41}$$

$$a = \frac{B_{x\,max}B_{y\,min} - B_{y\,max}B_{x\,min}}{B^2_{max}} \tag{3.42}$$

where B_{max} is the maximum value of the flux density, a is the aspect ratio, and θ is the inclination angle. The primed values of flux density in equation (3.40) represent flux densities rotated through the inclination angle, onto a new coordinate system. Under alternating flux conditions, the permeability tensor reduces to

$$\begin{bmatrix} H_x \\ H_y \end{bmatrix} = \begin{bmatrix} \nu_{xx} & 0 \\ 0 & \nu_{yy} \end{bmatrix} \begin{bmatrix} B_x \\ B_y \end{bmatrix} \tag{3.43}$$

After a time-stepped analysis of the flux density in the machine, the locus of the flux density in each element is obtained, then the elements of the tensor are obtained through the parameters defined above and data obtained from the rotational loss tester.

Enokizono and Sadanaga calculated the rotational losses in each element according to equation (3.22). Note that they did not use measured losses in a sample of the core material to assign losses according to the flux density. Instead, they attempted to use the calculated field quantities to calculate the losses. They also compared this result with the conventional method of the FEM using the scalar permeability. In this second method, they used measured losses for various inclination angles. In this way, the losses were calculated assuming alternating flux conditions throughout the machine but the anisotropy of the losses

in the sheet was accounted for. Alternating losses for numerous flux densities and inclination angles were also measured with the rotational core loss tester. It is interesting to note that the NO material under investigation exhibits a significant amount of loss anisotropy. At 1.4T, the material exhibits approximately 1.6 W/kg of loss in the rd and approximately 2.4 W/kg in the td.

The results of the conventional method (scalar reluctivity) show that the loci of the flux density and the field strength in the stator core were insensitive to which radial position is under investigation. For instance, the loci of the flux density at a certain radial position behind a tooth are very nearly identical to the loci at the same radial position behind every other tooth. The same observation can be made for the loci of the field strength. The results of the tensor analysis suggest that the loci of the flux densities are somewhat dependent on the anisotropy of the sheet. At the tooth roots of some teeth, the flux density polarization is stronger or weaker depending on which tooth is under observation. Although the anisotropy only slightly affects the flux density loci, the same cannot be said for the field strength loci. Here, the authors were able to show large differences in the loci obtained in the stator behind the various slots and teeth. Enokizono and Sadanaga also show a comparison of measured flux density and field strength loci with calculated results from the tensor formulation. They give no indication of how these quantities were measured. The authors concluded that the "calculated results are almost in agreement with the measured ones", although the results shown in their figures 9-12 [171] bring this conclusion into question.

Enokizono and Sadanaga also show loss distribution figures for the results obtained with the scalar reluctivity , the tensor reluctivity, and for measured losses (once again no details were given on the method of measurement). They compare the calculated losses of the scalar and tensor methods for a flux density level they describe as average of $B_{max} = 0.286$. No units are given for the flux density, but apparently this is a case where the machine is operating at a very low flux density. They show no losses in the machine using the scalar

formulation but with the tensor formulation the losses are small loss in the stator and rotor (less than 0.7W/kg everywhere in the machine). A comparison of the loss distribution for the tensor formulation and the measured losses is also presented. Unfortunately, they give the calculated losses for average $B_{max} = 0.4$ at an unspecified slip, and the measured losses for average $B_{max} = 0.311$ and a slip of 0.0357. The authors concluded "that the calculated results are in good agreement with the measured one". Curiously, the authors also claim "the loss in the rotor core was larger than in the stator core". In their figures, they show the highest loss distributions in the rotor yoke. This seems questionable, since the main field in the rotor yoke varies at the main field frequency multiplied by the slip (i.e. for the measured case the frequency in the rotor yoke would be (50Hz)(0.0357) or 1.79Hz).

Zhu and Ramsden [5] analysed the iron losses in a three phase, six pole, permanent magnet motor. They formulated the rotational losses with circularly polarized flux density using a three term model such that

$$P_r = P_{hr} + P_{er} + P_{ar} \tag{3.44}$$

where P_{hr} is the rotational hysteresis loss, P_{er} is the rotational classical eddy current loss (given as twice the loss under alternating flux conditions as discussed in section 2.3.3), and P_{ar} is the rotational anomalous loss. The rotational anomalous loss is modelled by the equation

$$P_{ar} = C_{ar}(fB)^{1.5} \tag{3.45}$$

where C_{ar} is the coefficient of rotational anomalous loss, which varies with B and eventually reduces to zero once the material is saturated.

Zhu and Ramsden separated the loss components by measuring the total rotational losses per cycle P_r/f over a range of frequencies between 0 and 200 Hz, extrapolating the curve to 0 Hz to obtain the rotational hysteresis loss per cycle, and then subtracting the

calculated rotational eddy current loss per cycle and rotational hysteresis loss per cycle from the total rotational loss per cycle to give the rotational anomalous loss per cycle. The coefficient k_{ar} was then obtained by fitting the data over a range of flux densities and frequencies, and found to be constant up to 1.4T. The authors note that k_{ar} will decrease and approach zero as the material becomes saturated. Zhu and Ramsden used a curve fitting function (derived from the equations of torque vs. slip for a single phase induction motor) to extend their data for rotational hysteresis losses from 1.4T (last measured point) to 1.8 T.

They extend the formulation presented above to the case of elliptically polarized flux densities. The authors attempt to predict the losses due to an elliptically polarized flux density based on measurements of losses under alternating flux conditions and circularly polarized flux conditions. They suggest the equation

$$P_t = aP_r + (1 - a^2)P_{alt} \tag{3.46}$$

where a is the aspect ratio of the elliptical flux density locus (i.e. B_{min}/B_{maj}), P_r is the core loss with circular flux density evaluated at B equal to B_{maj}, and P_{alt} is the alternating core loss also evaluated at B equal to B_{maj}. Figure 7b) in [5] shows good correlation for measurements for a 0.35mm NO silicon steel (for aspect ratios of 0.1 to 1.0 in steps of 0.1) at 1.25T and 50 Hz.

The radial and tangential component waveforms of the flux density in each element of the motor stator model were obtained from a sequence of FE solutions. In each element, the total core loss due to arbitrary flux density is calculated from

$$P_t = P_{th} + P_{te} + P_{ta} \tag{3.47}$$

where P_{th} is the total (sum of rotational and alternating) hysteresis loss, P_{te} is the total classical eddy current loss, and P_{ta} is the total anomalous loss. The authors obtained a series of elliptical harmonic flux density vectors by expanding the arbitrary waveform in each element by a Fourier series analysis. They also explain that the major axis B_{nmaj} and the minor axis

B_{nmin} of the nth harmonic flux density vector can be determined by a coordinate rotation for the standard equation. The total hysteresis in each element was obtained by summing up the hysteresis contributions from these harmonics (i.e. they assume the losses from the harmonics add according to linear superposition). For each harmonic the hysteresis loss was predicted from the corresponding alternating and rotational hysteresis losses according to equation (3.46). Zhu and Ramsden formulated the losses in each element as follows. The total hysteresis loss in each element was calculated from

$$P_{th} = \sum_{n=0}^{\infty}\left[P_{rhn}a_k + (1-a_n^2)P_{ahn}\right] \tag{3.48}$$

where a_n is the aspect ratio of the nth harmonic flux density, P_{rhn} is the rotational hysteresis loss with flux density B_{nmaj} obtained from curve fitting, and P_{ahn} is the alternating hysteresis from

$$P_{ahn} = k_{ha}nfB^{\zeta}_{nmaj} \tag{3.49}$$

where $k_{ha} = 0.0192$, and $\zeta = 1.79$ obtained from the Steinmetz law of alternating hysteresis described in section 2.3.1.

The classical eddy current loss in each element is modelled as

$$P_{te} = \frac{\pi^2 t^2}{6\rho_{res}\rho}\sum_{n=0}^{\infty}(nf)^2\left(B^2_{nmaj} + B^2_{nmin}\right) \tag{3.50}$$

The total anomalous loss in each element is calculated as

$$P_{ta} = \frac{k_{ar}}{(2\pi)^{1.5}}\frac{1}{T}\int_0^T\left[\left(\frac{dB_{rad}(t)}{dt}\right)^2 + \left(\frac{dB_{tan}(t)}{dt}\right)^2\right]^{\frac{3}{4}}dt \tag{3.51}$$

The authors explain that the constant $(2\pi)^{1.5}$ is a factor applied to k_{ar} so that equation (3.51) is consistent with equation (3.45) for a circular flux density polarization. B_{tan} and B_{rad} are the radial and tangential components of the flux density respectively. The authors were able to

predict the losses in the permanent magnet motor within 13% of the measured losses at a speed of 1200 rpm.

Concerning yoke iron losses, Walker [6] states that "an analysis of core loss of some 70 hydroelectric generators showed that in order to allow for the effects of rotational hysteresis this specific loss has to be multiplied by 1.55." No details of the analysis are given.

Summary

The theory of 2D loss measurements has been presented along with a survey of the various techniques that are currently under investigation by various researchers. A very diverse group of researchers are currently trying to establish the most effective test method for determining losses in electrical sheet steel in 2D fields. European and Japanese researchers are conducting the bulk of the work. With NO materials, the results of a European intercomparison have shown promising results. For grain oriented materials, the results differ considerably. We can attribute some differences obtained by researchers to the plethora of measuring techniques currently under investigation. The differences in the needle and search coil methods have been discussed and each method will invariably lead to differences in results. Furthermore, it is suspected that the use of the RCP for determining the magnetic field strength can be troublesome if they are not carefully calibrated. Matters are complicated further by the various sample sizes and measuring areas under consideration. One encouraging result of the European intercomparison is that researchers obtained similar results from setups using field sensing methods and thermal methods.

All the apparatuses used in the European intercomparison were of the horizontal yoke type. Other researchers are investigating the possibility of using vertical yoke testers. Vertical yoke testers are advantageous as they alleviate the effects of edge strains in a sample. Flux can enter the sheet in the normal direction at the outer portions of the sample. When using horizontal sheet testers, flux must enter the sample edges strained during shearing. This

situation is particularly troublesome in fully processed materials. In semiprocessed materials this is less problematic since the material will receive a decarburisation anneal before testing and this anneal also helps remove stresses.

Measurements of rotational hysteresis losses using torque magnetometers are less frequently found in the literature than they once were. For the case of a purely rotating magnetic field, the torque magnetometer allows direct measurement of the rotational hysteresis loss. This avoids the use of the two frequency method of loss separation, which does not properly characterize anomalous losses.

The problem of 2D measurements requires further study before the scientific community can agree upon a standard. Agreement on an international standard would allow producers of electrical sheets to supply rotational loss data to machine designers. This would expedite efforts by the machine community to incorporate rotational loss measurements into everyday design procedures. Furthermore, a standardized test will allow steel producers to develop steels optimized for use in motor cores.

Several authors have attempted to study the effects of rotational losses in machine cores. The work to date has not quantified the contribution of these losses to the overall core loss of a machine. More specifically, the question of how much accuracy is to be gained in the calculation of no-load core loss by including rigorous calculation of the rotational losses, remains unanswered. In Chapter 6, we will establish that the accuracy to be gained is small.

Chapter 4

Description of the Test Apparatus

4.0 Introduction

This chapter outlines some modifications and improvements made to the rotational core loss tester since the time of completion of earlier work described in [172]. These changes were made to facilitate the measurements of iron losses at higher flux density levels and with greater accuracy. The yoke of the apparatus remains unchanged from the version described in [172]. The yoke is a horizontal system that many other researchers have adopted as outlined in Section 3.2.5.2.1 and 3.2.5.2.2. Figure 4.1 illustrates the horizontal yoke system. Search coils through drilled holes are used to measure flux density values (as described in Section 3.3.2) and the field strengths are measured using the tangential H coil method (as described in Section 3.3.6.1). Square samples measuring 8cm x 8cm were used in this investigation.

4.1 Experimental Setup

The experimental setup is described in figure 4.2. A personal computer (PC) containing an arbitrary waveform generation (AWFG) card is used to generate the flux density signals in the x and y direction. If the two signals are in phase quadrature, a rotating magnetic field is created in the sample. By varying the magnitudes of the signals, an elliptical flux density locus is obtained if the flux density in the x direction is plotted against the flux density in the y direction. If the two signals are in phase, then an alternating field is created. The field can be made to alternate at any direction relative to the x axis of the sample by

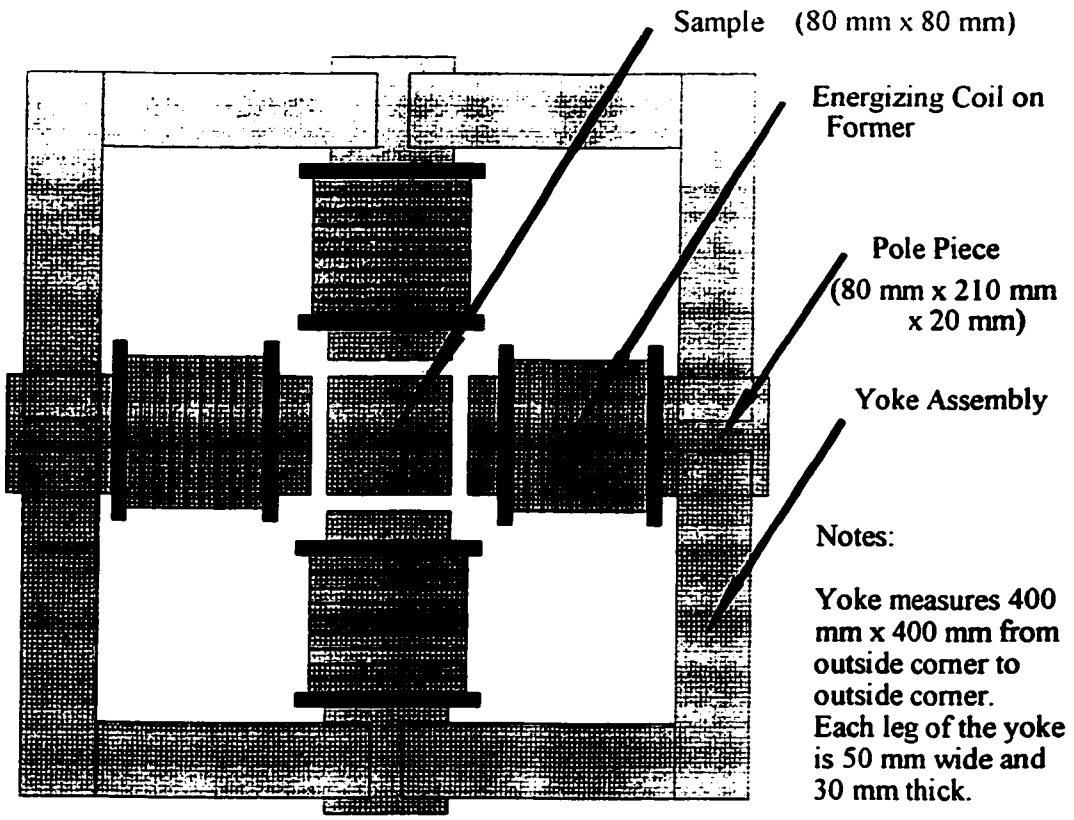

Figure 4.1 - Horizontal yoke system used in this investigation.

adjusting the magnitudes of the signal separately. A two channel, adjustable gain preamplifier is used to adjust the magnitude of the flux density signals. These signals are then amplified using a pair of power amplifiers. Magnetic field quantities are sampled, digitized, and stored in the PC with the aid of a Keithley DAS 16F analog to digital (A/D) converter. Losses in the electrical sheet sample are calculated from the digitized signals.

4.1.1 Power Supply Amplifiers

Two Tecron 7560 Power Supply Amplifiers (see figure 4.2) are now used (one amplifier in a monographic configuration for each set of series connected energizing coils). These amplifiers are much more powerful than the ones used in [172]. Each Tecron amplifier

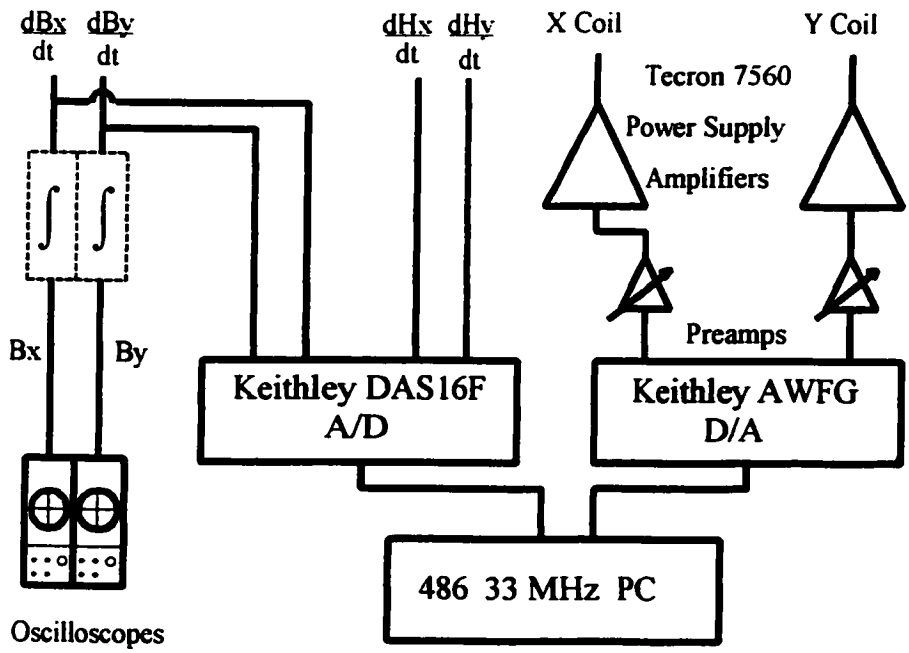

Figure 4.2 - Waveform generation, amplification and sampling.

can deliver up to 1 kW of continuous power into a 4 ohm load. A maximum current of 20 A can be drawn from each amplifier. These amplifiers have allowed loss measurements for flux density levels of 1.5 to 1.7T in comparison to 1.0 to 1.2T using the previous two channel Onkyo amplifier.

4.1.2 Signal Generation

A Keithley AWFG (Arbitrary Waveform Generator) Card is used to output two sinusoidal signals in phase quadrature. Each signal is derived from 1665 points (i.e. 1664 data panels) which are loaded from a data file. The sample points are output at a rate of 10 microseconds. This gives each signal a frequency of $1/(1664 \times 10^{-5}\ \text{sec}) = 60.09615$ Hz. The signals coming from the AWFG are then fed through two preamplifiers with adjustable gains.

This allows the flux density levels in the sample to be set. The preamplified signals are then passed into the Tecron 7560 Power Supply Amplifiers in order to provide the current required to drive the energizing coils.

4.1.3 Flux Density Signal Integration

In the old system the signals coming from the search coils were integrated to give voltages proportional to flux densities rather than the time derivatives of the flux densities. These integrator circuits have now been eliminated from the data collection circuits and are retained only for the purposes of outputting signals to oscilloscopes (see figure 4.2). The oscilloscope traces aid the operator in setting the required flux density.

To accurately calculate the power loss in a sample using the field-metric method described in Chapter 3, it is important to avoid phase shifts in the signals. By using a Fourier analysis of the incoming signals, and integrating for the flux density mathematically, errors associated with electronic phase shifts are easily avoided.

4.2 Formulation of Power Loss Using Fourier Analysis

The rotational power loss in the sample is found by evaluating the following expression:

$$P_t = \frac{1}{T\rho}\int_0^{2L}\left(B_x(t)\frac{dH_x(t)}{dt} + B_y(t)\frac{dH_y(t)}{dt}\right)dt \qquad \textbf{(4.1)}$$

The search coils in the sample and the tangential field sensing coils, give signals proportional to the time derivatives of B_x, B_y, H_x and H_y. These signals may be decomposed into separate harmonic components using Fourier series analysis. A function f(t) may be expressed by the Fourier series given by equations (4.2) to (4.6).

$$f(t) = c_0 + \sum_{n=1}^{\infty} c_n \cos\left(\frac{2n\pi t}{T} + \phi_n\right) \tag{4.2}$$

where

$$c_0 = \frac{a_0}{2} \qquad c_n = \sqrt{a_n^2 + b_n^2} \qquad \phi_n = \tan^{-1}\left(\frac{-b_n}{a_n}\right) \tag{4.3}$$

and

$$a_0 = \frac{1}{T}\int_0^T f(t)dt \tag{4.4}$$

$$a_n = \frac{2}{T}\int_0^T f(t)\cos\left(\frac{2n\pi}{T}t\right)dt \tag{4.5}$$

$$b_n = \frac{2}{T}\int_0^{2L} f(t)\sin\left(\frac{2n\pi}{T}t\right)dt \tag{4.6}$$

The function has a period of T. Recall that the signals coming from the flux density search coils and the tangential field sensing coils will have a frequency of 60.09615 Hz. Each signal is sampled at a rate of 25 kHz such that there are 416 panels (i.e. 417 data points) associated with each waveform. This allows the use of Simpson's rule for calculating the Fourier integrals. Note that none of the signals have dc components (a_0 and $c_0 = 0$).

Looking at the x and y components of equation (4.1) separately, we can write a Fourier series for each field quantity as follows:

$$\frac{dB(t)}{dt} = \sum_{n=1}^{\infty} \dot{B}_n \cos\left(\frac{2n\pi}{T}t + \phi_{Bn}\right) \tag{4.7}$$

$$\frac{dH(t)}{dt} = \sum_{m=1}^{\infty} \dot{H}_m \cos\left(\frac{2m\pi}{T}t + \phi_{Hm}\right) \tag{4.8}$$

Performing a term by term integration gives the expression for B(t)

$$B(t) = \sum_{n=1}^{\infty} \frac{T}{2n\pi}\dot{B}_n \sin\left(\frac{2n\pi}{T}t + \phi_{Bn}\right) \tag{4.9}$$

or alternatively,

$$B(t) = \sum_{n=1}^{\infty} \frac{T}{2n\pi}\dot{B}_n \cos\left(\frac{2n\pi}{T}t + \phi_{Bn} - \frac{\pi}{2}\right) \tag{4.10}$$

Now,

$$\begin{aligned} B(t)\frac{dH(t)}{dt} = &\left[\sum_{n=1}^{\infty} \frac{T}{2n\pi}\dot{B}_n \cos\left(\frac{2n\pi}{T}t + \phi_{Bn} - \frac{\pi}{2}\right)\right] \\ &\times\left[\sum_{m=1}^{\infty} \dot{H}_m \cos\left(\frac{2n\pi}{T}t + \phi_{Hm}\right)\right] \end{aligned} \tag{4.11}$$

Only the terms with the same frequency (m = n) will contribute average values to the power expression, so we can write

$$\int_0^T B(t)\frac{dH(t)}{dt}dt = \sum_{n=1}^{\infty} \int_0^T \frac{T}{2n\pi}\dot{B}_n\dot{H}_n \cos\left(\frac{2n\pi}{T}t + \phi_{Bn} - \frac{\pi}{2}\right)\cos\left(\frac{2n\pi}{T}t + \phi_{Hn}\right)dt \tag{4.12}$$

Using the trigonometric identity

$$\cos\alpha\cos\beta = \frac{1}{2}\cos(\alpha - \beta) + \frac{1}{2}\cos(\alpha + \beta)$$

we can write

$$\int_0^T B(t)\frac{dH(t)}{dt}dt = \sum_{n=1}^{\infty} \frac{T}{2n\pi}\dot{B}_n\dot{H}_n \times$$
$$\left[\int_0^T \frac{1}{2}\cos\left(\phi_{Bn} - \phi_{Hn} - \frac{\pi}{2}\right)dt + \int_0^T \frac{1}{2}\cos\left(\frac{4n\pi}{T}t + \phi_{Bn} + \phi_{Hn} - \frac{\pi}{2}\right)dt\right] \quad \textbf{(4.14)}$$

The second term of the equation above has an average value of zero over the integration interval so that

$$\int_0^T B(t)\frac{dH(t)}{dt}dt = \sum_{n=1}^{\infty} \frac{T^2}{4n\pi}\dot{B}_n\dot{H}_n\cos\left(\phi_{Bn} - \phi_{Hn} - \frac{\pi}{2}\right) \quad \textbf{(4.15)}$$

Finally we can express the rotational power loss as

$$P_{rot} = \sum_{n=1}^{\infty} \frac{T^2}{4n\pi}\left[\dot{B}_{xn}\dot{H}_{xn}\cos\left(\phi_{Bxn} - \phi_{Hxn} - \frac{\pi}{2}\right) + \dot{B}_{yn}\dot{H}_{yn}\cos\left(\phi_{Byn} - \phi_{Hyn} - \frac{\pi}{2}\right)\right] \quad \textbf{(4.16)}$$

The rotational power losses are calculated twice. In the first instance, the losses are calculated using the first 25 harmonics in each waveform. The losses are also calculated using the fundamental component only. In this way, the degree of error associated with any distortion in the flux density waveform can be determined.

4.3 Flux Density Waveform Distortion

4.3.1 Introduction

Maintaining a non-distorted sinusoidal waveform beyond 1.5 T in both the rd and td is the major difficulty of making power loss measurements in electrical steels. Many researchers have attempted to use feedback techniques or digital waveform control algorithms to help achieve this goal. Limited successes have been reported in the literature. There is

little quantitative data in the literature documenting significant reduction of flux density harmonics using any of the various techniques.

4.3.2 Waveform Control Techniques by Various Researchers

J. Sievert [101,102] describes a system whereby the flux density waveforms are obtained by integrating the signals coming from the search coils with analog integration circuits and then fed back into the input circuit in the form of negative feedback. In this scheme the input voltage and the fundamental output voltage will be phase shifted by 90°. The input voltage will be in phase (or 180° out of phase) with the search coil voltage, which is proportional to the time derivative of the flux density. Therefore, feeding back an integrated signal is not appropriate.

Zhu and Ramsden [135] have used a negative feedback technique using the signal from the search coil directly without integration. In other words a signal proportional to the time derivative of the flux density rather than the flux density is used as a feedback signal. A similar method has been used by Morino et al [139].

M. Enokizono et al [130,133] have used digital waveform control algorithms. In this scheme, the induced voltage waveforms in the rd and td search coils are sampled and compared with the objective induced voltage waveforms. An error signal is calculated as the difference between the two. The D/A converters are loaded with a new waveform that consists of the old input signal minus some portion of the error signal. This procedure is repeated iteratively until the desired waveform is achieved.

Tamura et al [140] have used essentially the same procedure to control the flux density waveform when making alternating loss measurements at arbitrary directions. They show a waveform diagram that indicates improvement in the waveform achieved for a sample of GO material although the maximum value of the flux density is limited to 1.0 T. In essence, this method is similar to the analog negative feedback system such as that used by

Zhu and Ramsden [135] the only difference being that the negative feedback is performed digitally rather than by using a difference amplifier.

Salz [147] reported a very elaborate control system that uses both analog and digital control algorithms. Unfortunately, even though a great deal of complexity was added to the measuring system, NO samples could only be measured under rotating flux conditions for values up to approximately 1.55 T.

4.3.3 Method Used in the Present Investigation

Presently, the tester is being run in the open loop configuration. Before upgrading to the Tecron power supply amplifiers, I tried to incorporate negative feedback loops of signals proportional to the induced voltage in the search coils. I could not improve the harmonic content of the waveforms and in fact I often found that the waveforms could become completely unstable (once resulting in the loss of the power transistors in the Onkyo amplifier)!

From what is available in the literature as described above it would appear that other researchers are encountering difficulties in achieving feasible waveform control. The problem lies in trying to apply linear control systems theory and methods to a highly nonlinear problem. Most researchers try to compensate for harmonics in the search coils of the samples using feedback systems that add compensating harmonics to the supply voltage (and therefore the current). These additional current harmonics will attenuate the original harmonics in the induced voltage (and therefore the sample flux density). The problem is that the compensating currents can create additional harmonics of their own.

Furthermore, power amplifiers can provide only limited current. By careful consideration of any typical BH curve (for instance, see figure 4.3) it is apparent that enormous additional harmonic currents are necessary to maintain sinusoidal flux density waveforms at levels much higher than the knee of the magnetization curve. Therefore the

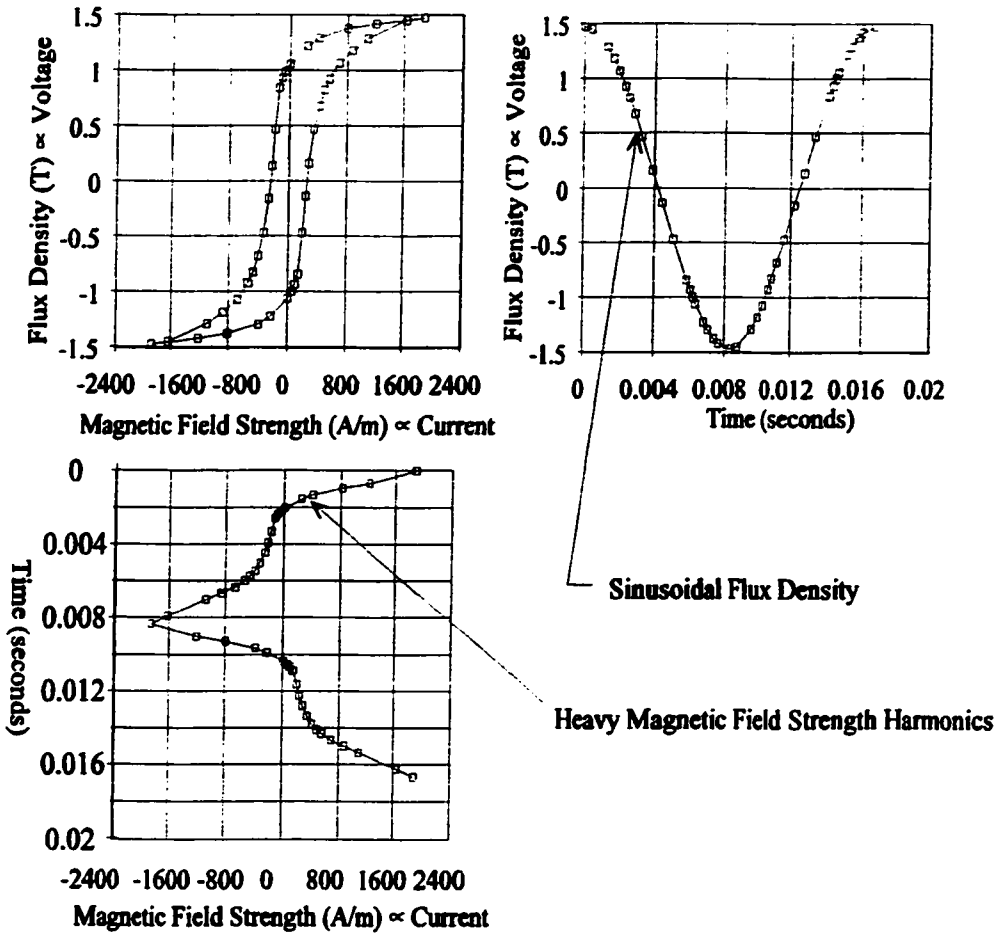

Figure 4.3 - Typical BH curve and heavily distorted magnetic field strength waveform necessary to maintain sinusoidal flux density waveform.

ability of the amplifier to supply these harmonic currents also limits the amount of harmonic reduction that can be achieved using negative feedback.

The above-mentioned points make the problem of waveform control difficult to solve, and although some researchers have incorporated these feedback techniques into their test apparatus, few if any of them have provided data that shows significant reductions of harmonic levels in the flux density waveforms. It appears that the practical limit for making loss measurements remains at approximately the 1.5T value, which incidentally, is standard

for NO steels tested using the Epstein Test.

With the Tecron Amplifiers I found that it was relatively easy to obtain higher flux density levels, even without feedback loops. Therefore I decided to run the tester in the open loop mode and concentrate instead on quantifying the distortion in the waveforms and reporting it with my measurements, rather than trying to eliminate it. Nakata et al [146] also used an open loop system in their investigations.

4.4 Measurement of Distortion

4.4.1 Form Factor Method

The form factor of a period function is defined [173-174] as the ratio of the root mean square value to the average absolute value, averaged over a full period of the function. For a sinusoidal wave form, the form factor will be

$$\frac{V_{rms}}{V_{ave}} = \frac{\frac{1}{\sqrt{2}}}{\frac{2}{\pi}} = 1.1107 \qquad \textbf{(4.17)}$$

ASTM A343 [98] states that the form factor should be maintained within a certain amount of 1.111. The form factor method is convenient to use with the Epstein test because the rms and average values of the flux density waveform are available from rms and average reading voltmeters.

4.4.2 Distortion Factor Method

The distortion factor (DF) of a distorted waveform is expressed [173-174] as the ratio of the root-mean-square of the harmonic content to the root-mean-square value of the fundamental quantity. Waveform DF is expressed as a percent of the fundamental as indicated in equation (4.18).

$$DF = \left[\frac{\text{(sum of the squares of amplitudes of all harmonics)}}{\text{(square of amplitude of fundamental)}}\right]^{\frac{1}{2}} \times 100 \qquad \textbf{(4.18)}$$

I have chosen to report the distortion in my flux density waveforms using this method since the information needed to calculate it is readily available.

4.5 Measurement Procedure

Two quadrature waveforms are set using the AWFG card. The fundamental flux density in the sample is manually set by adjusting the gain of the preamplifiers. A loss measurement is made by sampling the specimen field waveforms and executing the calculations described in Section 4.2. Once the losses are evaluated, the value of the fundamental flux density is output so that the operator can check the value. The flux density is reset and another measurement is made. This is repeated iteratively until the desired flux density levels are achieved. This task is aided by displaying the flux density signals on oscilloscopes so that the operator can see the shapes and sizes of the waveforms. When the required flux density levels are finally set, the losses are calculated and the operator records the values of the rotational loss, the loss component in the rd, the loss component in the td, and the distortion factors in the waveforms in the rd and td.

Loss measurements of rotating fields require two sets of measurements, once with a cw rotation of the field and once with a ccw rotation of the field. The results of these two measurements may then be averaged to mitigate any errors in the measurements due to small misalignments of the field sensing and flux density search coils [102,132].

Summary

We have improved the test apparatus in several ways. The analog integrator circuits that were used to measure the flux density levels have been removed, thereby eliminating any

errors due to phase shifting that may have arisen due to their presence. Sample loss can be determined under both alternating and rotational flux conditions. A numerical approach has been implemented that allows the loss in the sample to be determined based on a Fourier analysis of the flux density and magnetic field strength waveforms. Information on distortion levels in the flux density is also determined from the Fourier analysis.

A pair of Tecron amplifiers has replaced the Onkyo amplifier. The Tecron amplifiers can supply more current than the Onkyo amplifier. This has extended the flux density capability of the test apparatus into the level of those found in practical ac induction motors. The apparatus is run in an open loop configuration, but by recording the DF for each measurement, the distortion levels encountered during the measurements are recorded.

Chapter 5

Loss Measurement Results

5.0 Introduction

Loss curves were generated for seven grades of steel. Three grades of MLQ steel and four grades of NO silicon steel were characterized. The steels are described in table 5.1. Entries for 50/50 Epstein losses are guaranteed values furnished by suppliers. The entry for NO steel C is a typical value for that grade of steel as defined in [175]. For each grade, alternating losses were measured in the rd and td of the sample, as well as for purely rotational flux conditions. The results of these loss measurements are presented in the figures contained in the body of this chapter. Additional loss measurements were made for NO steel D. The cores of the five induction machines under study are made from this material. For this steel, a family of curves for various flux density polarizations were measured. Measurements at various angles to the rd were also made to ascertain the anisotropic behaviour of the material. The loss measurements on NO steel D were then mated with the results of a finite element study to determine the losses in the stator cores of the machines. These results are presented in Chapter 6.

To aid in the graphing of the data, third order polynomials obtained by a least squares fit [176], were applied to the data points. In Chapter 2, we saw that rotational losses can decrease at high flux density values. Second order polynomials cannot capture the inflection point that can occur due to rotational losses at high flux densities. If the order of the polynomial is increased beyond three, the curve may begin to oscillate through the data points; in other words, the curve fit may not be a smooth one. Usually, two third order polynomials were applied to each curve. One polynomial describes the first half of the data

Table 5.1 - Nominal Thickness, Composition and 50/50 Epstein Loss for Each Steel Under Investigation

Steel	Nominal Thickness (mm)	Si (%)	Al (%)	Mn (%)	50/50 Epstein losses at 1.5 T (W/kg)
MLQ A	0.635	0.01	0.04	0.35	8.6
MLQ B	0.635	0.60	0.04	0.35	NA
MLQ C	0.635	0.75	0.30	0.65	NA
NO A	0.635	1.75	NA	NA	6.25
NO B	0.48	2.70	NA	NA	4.71
NO C	0.635	2.75	0.35	0.17	4.81 (ASTM A677)
NO D	0.48	2.70	NA	0.15	3.86

and a second polynomial is used to describe the second half of the data. Graph markers show the values of measured points on the graphs of the rd and td alternating losses as well as those of rotational losses. The solid lines on the graphs show the polynomial fits. In the graphs that show loss comparisons, the markers are points on the polynomials, not data points. In all cases, the losses are plotted against the amplitude of the fundamental component of the flux density.

5.1 Loss Measurements for MLQ Grades

5.1.1 MLQ Steel A

Distortion levels in the flux density waveforms at the highest flux density level for each measurement are reported in table 5.2. Figures 5.1 through 5.4 show the results of the loss measurements for MLQ steel A. Figure 5.1 shows the data for rotational losses. Note that the losses obtained from the fundamental component of flux density are nearly exactly the same as those obtained when including the harmonics in the flux density waveform. This

result is expected due to the low distortion levels (≤2.0%) encountered during the rotational loss measurements.

Figures 5.2 and 5.3 show the losses in the rd and td of the sheet respectively. Harmonics in the waveform begin to have a small effect above 1.6 T as the flux density waveform begins to distort. Note that the distortion factor (DF) at 1.8 T exceed 8% in the rd and 9% in the td. Table 5.1 reveals that the alloy content of this steel is very small. As the alloy content of the steel is increased the saturation induction will drop (see Chapter 2, Section 2.3.1.1). The saturation induction of such a material will be nearly equal to that of pure iron. This explains why it is relatively easy to obtain flux density levels up to 1.8 T for the alternating case. Note that for the rotating case, it was possible to obtain flux density values up to only 1.6T. This suggests that the permeability of the steel is lower under rotating flux conditions than it is under alternating flux conditions.

Figure 5.4 shows a comparison of the losses for the three cases described above and also for the sum of the losses in the rd and td. The curves without the effects of the distortion harmonics are used in the comparison as is the case in the subsequent graphs for the other steels. Note that the sum of the losses in the rd and td does not accurately reflect the losses due to rotating flux. The alternating loss characteristics of the steel are very isotropic in the rd and td of the sample.

Table 5.2 - Distortion Factors for Measurements on MLQ Steel A

Loss Measurement	Distortion Factor (rd)	Distortion Factor (td)
Alternating	8.92% @ 1.8 T	9.41% @ 1.8 T
Alternating	2.76% @ 1.6T	3.13% @ 1.6 T
Rotational CW	1.67% @ 1.6 T	2.00% @ 1.6 T
Rotational CCW	1.67% @ 1.6 T	1.55% @ 1.6 T

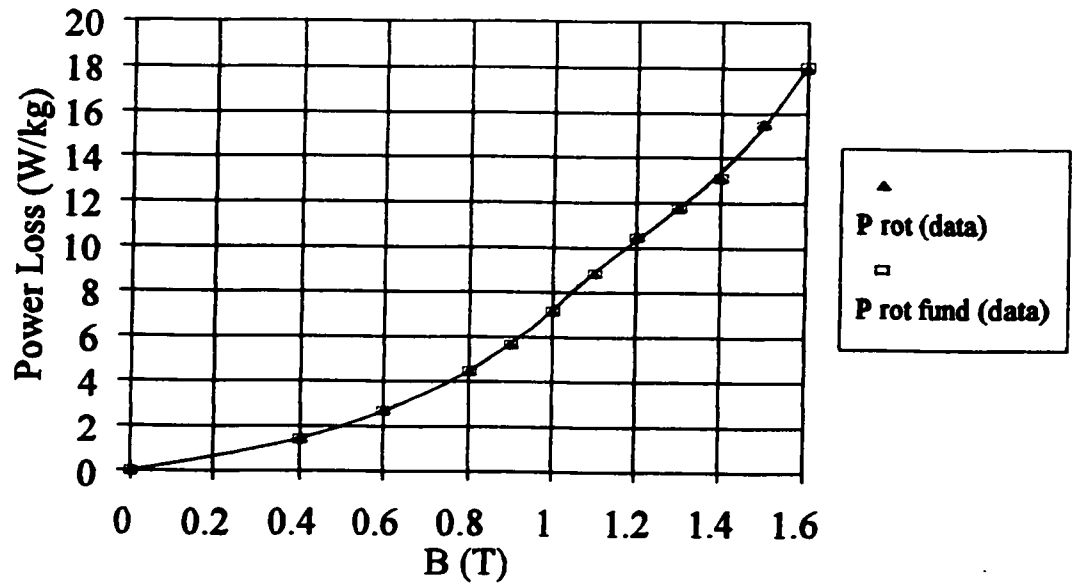

Figure 5.1 - MLQ Steel A - Rotational power losses with and without distortion harmonics.

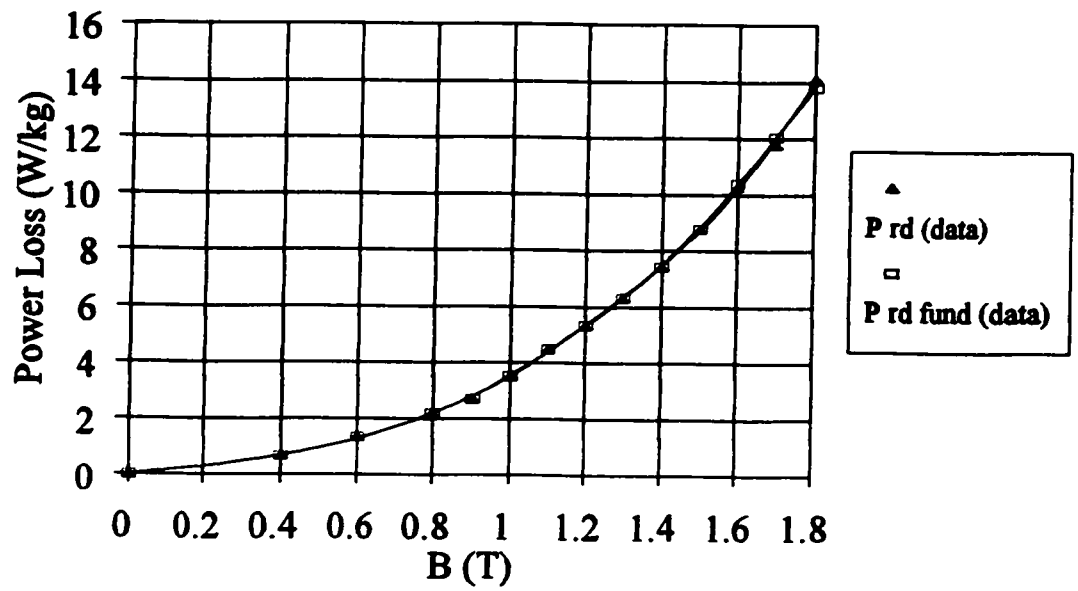

Figure 5.2 - MLQ Steel A - Power losses (rd) with and without distortion harmonics.

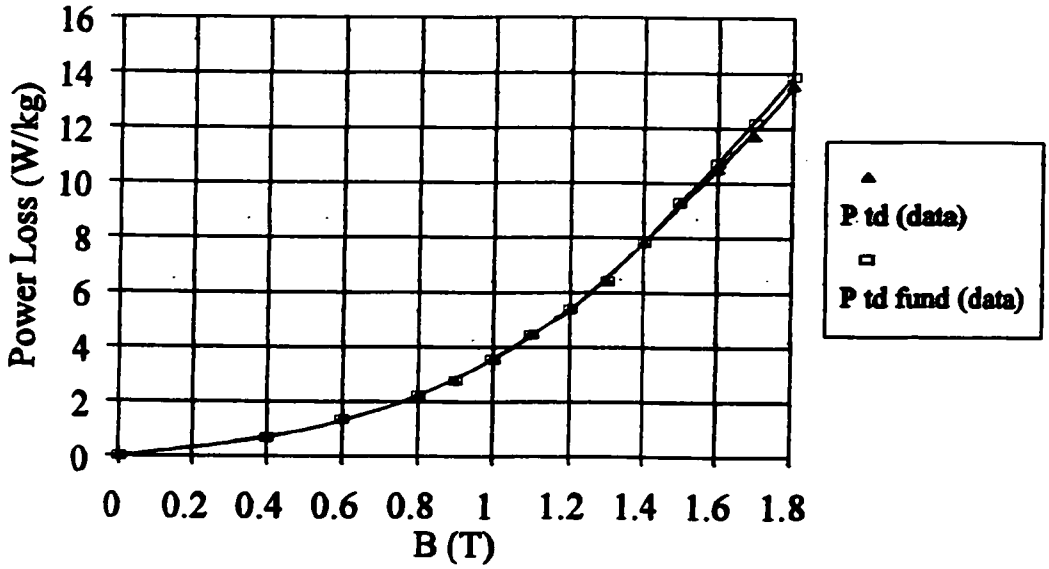

Figure 5.3 - MLQ Steel A - Power losses (td) with and without distortion harmonics.

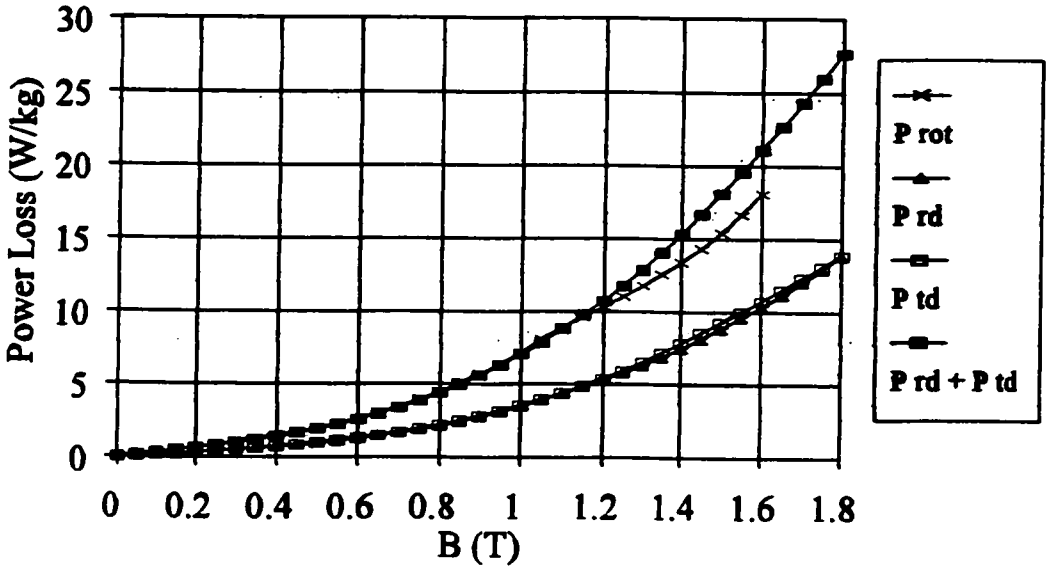

Figure 5.4 - MLQ Steel A - Comparison of alternating and rotational power losses.

5.1.2 MLQ Steel B

Figures 5.5 through 5.8 show the losses for MLQ steel B. Figure 5.5 shows the rotational losses in the material. Figures 5.6 and 5.7 show the alternating losses in the rd and td respectively. Table 5.3 gives the DF present during each measurement. It is interesting that the DFs for the flux densities in the td are more than twice as high as the DFs in the rd for the rotational loss measurements. Nevertheless, the power loss contained in the harmonics is small, as evidenced by the close agreement between the curves in figure 5.5.

MLQ steel B contains 0.60% silicon and is harder to magnetize than MLQ steel A, probably due to a lowering of the saturation induction value. Figure 5.8 shows a comparison of the losses (for curves without the distortion harmonics) for the alternating losses and rotational losses. The steel has nearly isotropic alternating loss characteristics. The losses in the td are only slightly higher than in the rd. Note the rotational losses are not defined by the sum of the rd and td losses. Differences in losses for the distorted and undistorted waveforms are more pronounced at 1.7 T for the td losses due to the higher DF. In the rd, the DF is less than 5% and the power loss in the harmonics is very small, as shown by the fact that the two curves in figure 5.6 are nearly exactly coincident. Distortion factors for the various measurements are reported in table 5.3.

Table 5.3 - Distortion Factors for Measurements on MLQ Steel B

Loss Measurement	Distortion Factor (rd)	Distortion Factor (td)
Alternating	4.79% @ 1.7 T	12.3% @ 1.7 T
Alternating	2.80% @ 1.6 T	7.37% @ 1.6 T
Rotational CW	3.22% @ 1.6 T	7.24% @ 1.6 T
Rotational CCW	3.25% @ 1.6 T	7.42% @ 1.6 T

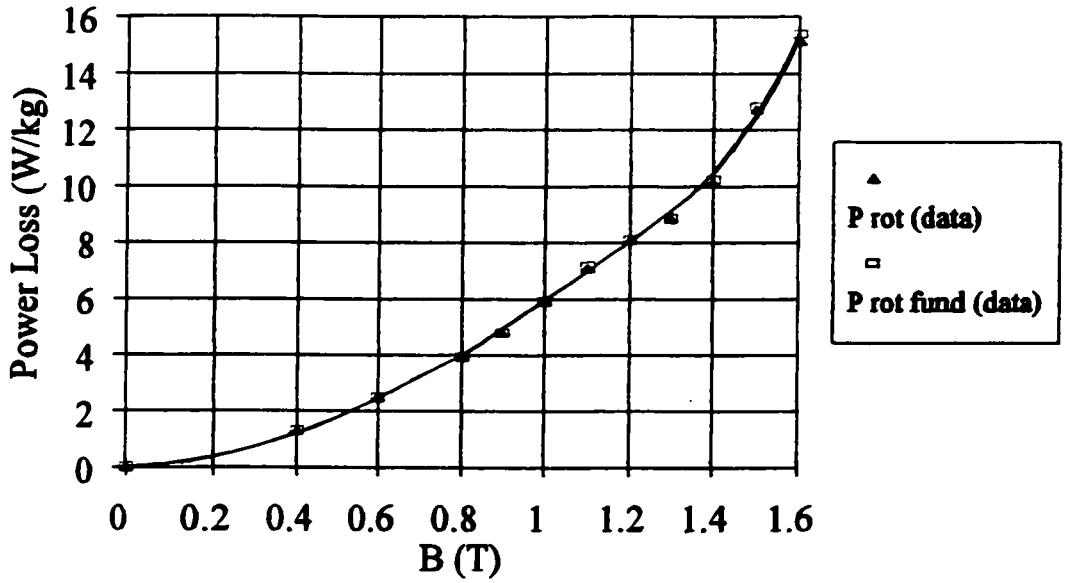

Figure 5.5 - MLQ Steel B - Rotational power losses with and without distortion harmonics.

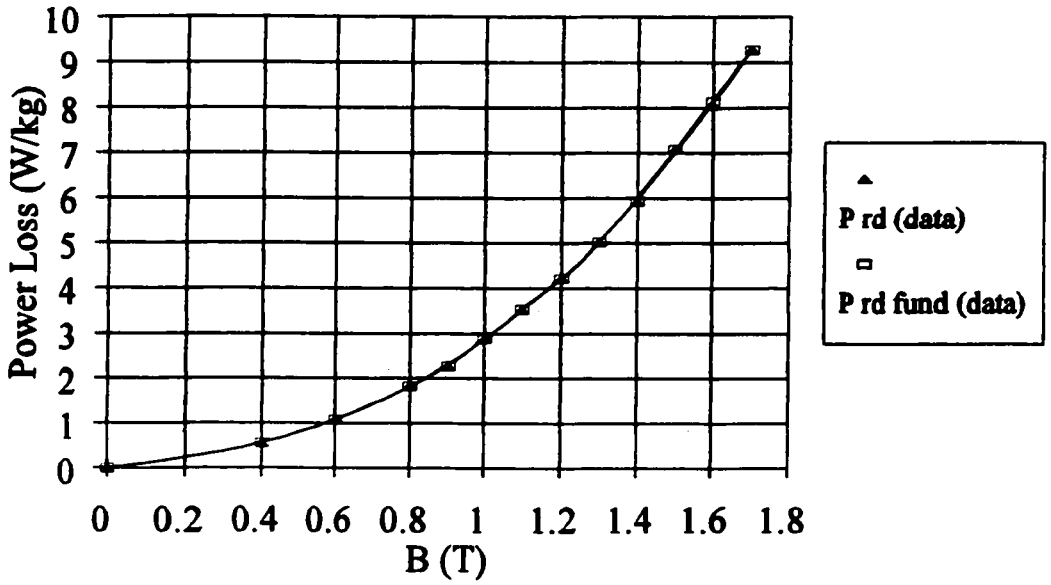

Figure 5.6 - MLQ Steel B - Power losses (rd) with and without distortion harmonics.

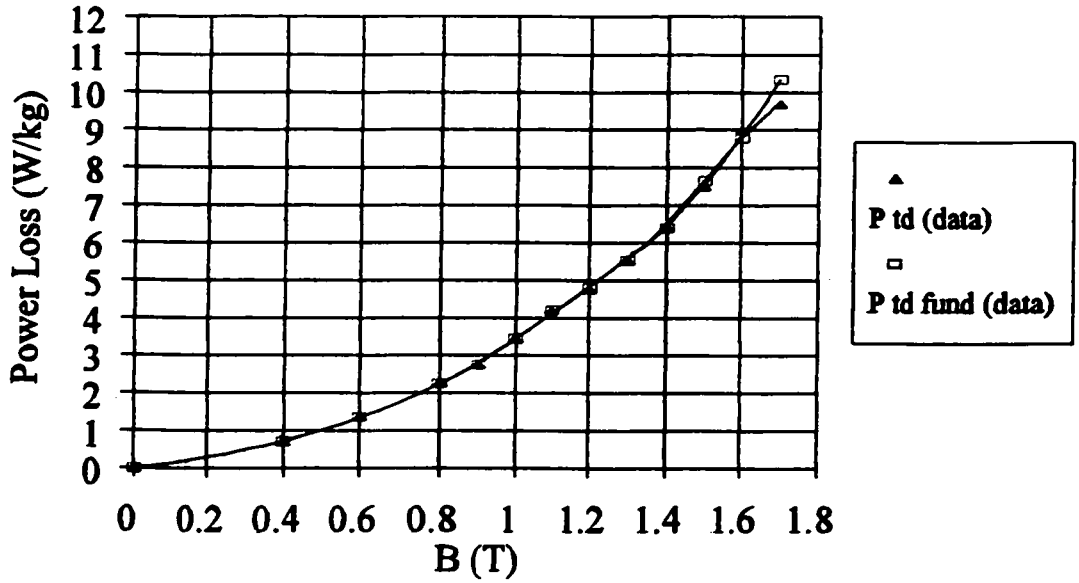

Figure 5.7 - MLQ Steel B - Power losses (td) with and without distortion harmonics.

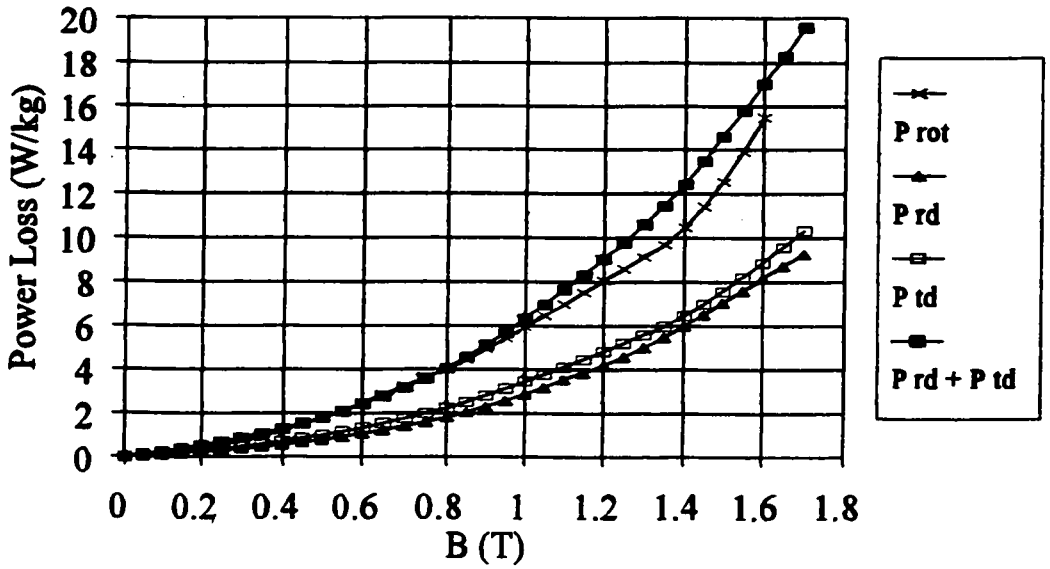

Figure 5.8 - MLQ Steel B - Comparison of alternating and rotational power losses.

5.1.3 MLQ Steel C

Figures 5.9 through 5.12 show the losses measured for MLQ steel C. The rotational power losses are shown in figure 5.9. Figures 5.10 and 5.11 show the losses in the rd and td of the sample respectively. Figure 5.12 shows a comparison of the losses (for curves without the distortion harmonics) for the alternating losses and rotational losses. MLQ steel C has higher Si, Al and Mn content than MLQ steels A and B. It will have a lower saturation induction value than either of the previous two steels. As the saturation induction of the steel is lowered, the "knee" of the magnetization curve will occur at a lower flux density value. In other words, the steel begins to saturate at a lower flux density value. This explains why alternating loss measurements could only be made to 1.6 T for MLQ steel C. Beyond 1.6 T, the sample became heavily saturated and the waveform began to distort excessively. MLQ steel C has very isotropic alternating loss properties in the rd and td.

The rotational losses are not accurately predicted by the sum of the alternating losses in the rd and td of the sample. Also note that the anisotropy of loss in the rd and td losses is very small for all three MLQ steels. Distortion factors for the measurements are noted in table 5.4. For all three MLQ steels, the distortion factors in the rd are lower than in the td. This suggests that the steels exhibit anisotropic permeability properties. Flux density levels are more easily obtained in the rd and the distortion is less in the rd.

Table 5.4 - Distortion Factors for Measurements on MLQ Steel C

Loss Measurement	Distortion Factor (rd)	Distortion Factor (td)
Alternating	2.68% @ 1.6 T	7.42% @ 1.6 T
Rotational CW	3.28% @ 1.6 T	7.34% @ 1.6 T
Rotational CCW	3.29% @ 1.6 T	7.36% @ 1.6 T

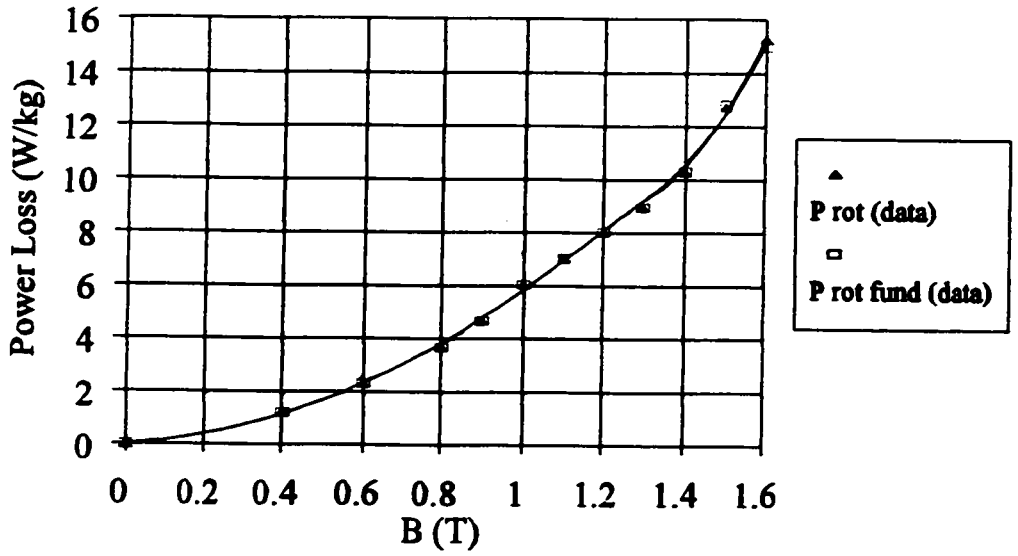

Figure 5.9 - MLQ Steel C - Rotational power losses with and without distortion harmonics.

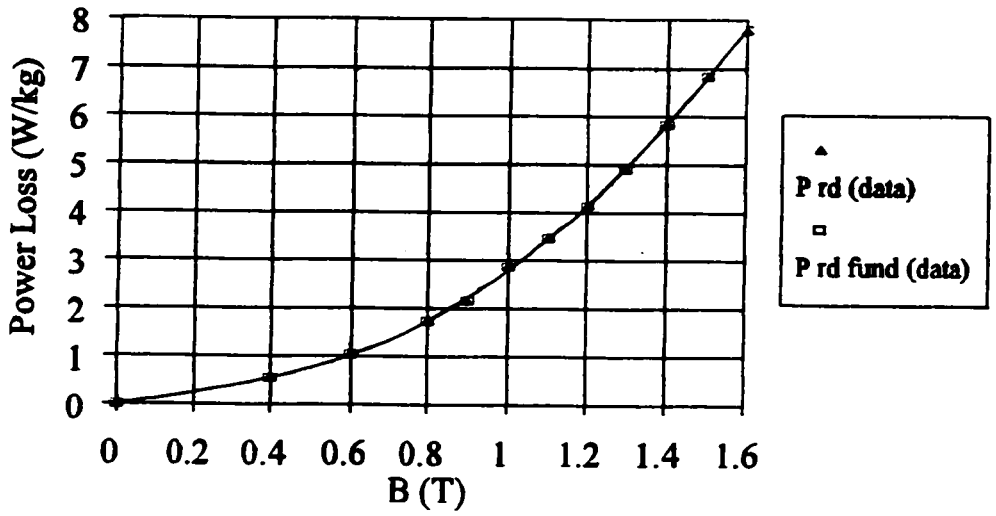

Figure 5.10 - MLQ Steel C - Power losses (rd) with and without distortion harmonics.

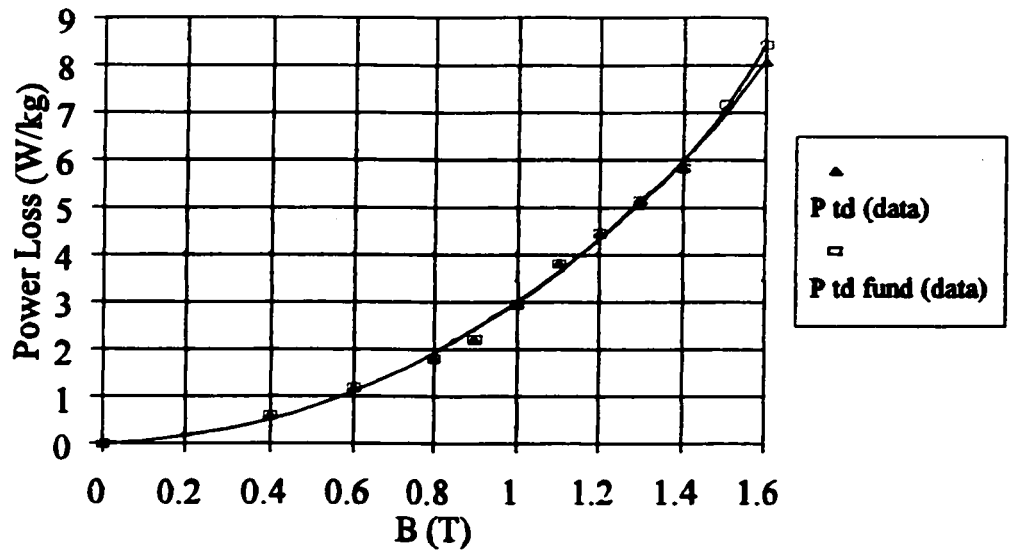

Figure 5.12 - MLQ Steel C - Power losses (td) with and without distortion harmonics.

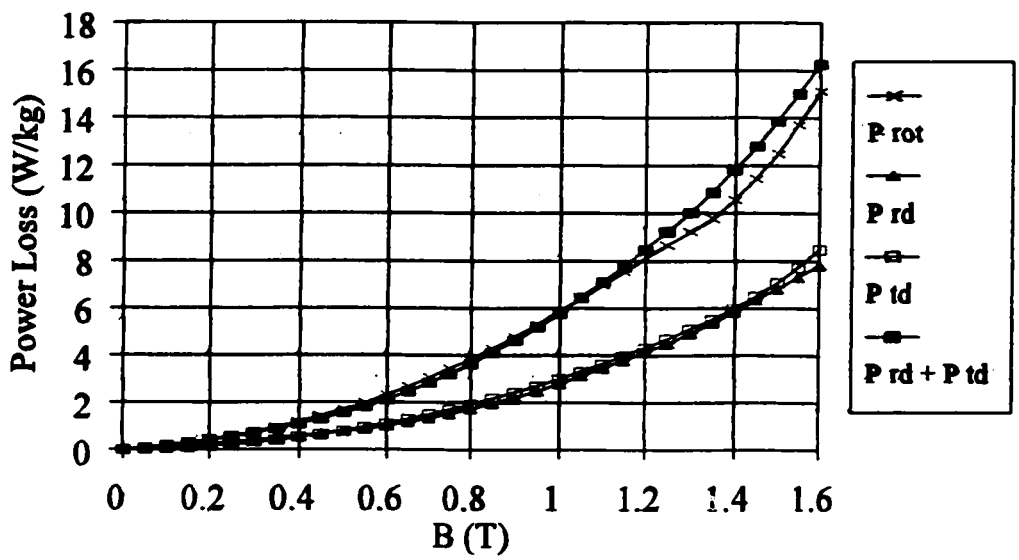

Figure 5.11 - MLQ Steel C - Comparison of alternating and rotational power losses.

5.2 Loss Measurements for NO Silicon Grades

5.2.1 NO Steel A

Figures 5.13 through 5.16 show the losses for NO steel A. Distortion levels for NO steel A are given in table 5.5. Note that the effect of the distortion harmonics on the rotational losses is very small as evidenced by the agreement between the two curves in figure 5.13. The distortion factor at 1.5 T was less than 5% for the case of the rotational losses. The effects of the distortion harmonics are slightly more pronounced in the alternating losses for the points taken at 1.6 T. Figure 5.16 shows a comparison of the alternating and rotational losses, and as with the MLQ steels, the sum of the rd and td alternating losses does not accurately predict the rotational losses. Note the increase in anisotropy of the losses in the rd and td when compared with the MLQ steels. This is typical of NO silicon steels. The higher silicon content of the material tends to encourage the development of preferred texture during cold rolling. This material has a silicon content of approximately 1.75% which is a much higher level than seen for the MLQ steels. The saturation induction level for this material will be lower than for the MLQ steels. This explains why measurements were only possible up to flux density levels of 1.5 T for the rotational case and 1.6 T for the alternating case.

Table 5.5 - Distortion Factors for Measurements on NO Steel A

Loss Measurement	Distortion Factor (rd)	Distortion Factor (td)
Alternating	4.43% @ 1.6 T	8.70% @ 1.6 T
Alternating	2.58% @ 1.5 T	5.03% @ 1.5 T
Rotational CW	2.74% @ 1.5 T	3.97% @ 1.5 T
Rotational CCW	2.88% @ 1.5 T	4.28% @ 1.5 T

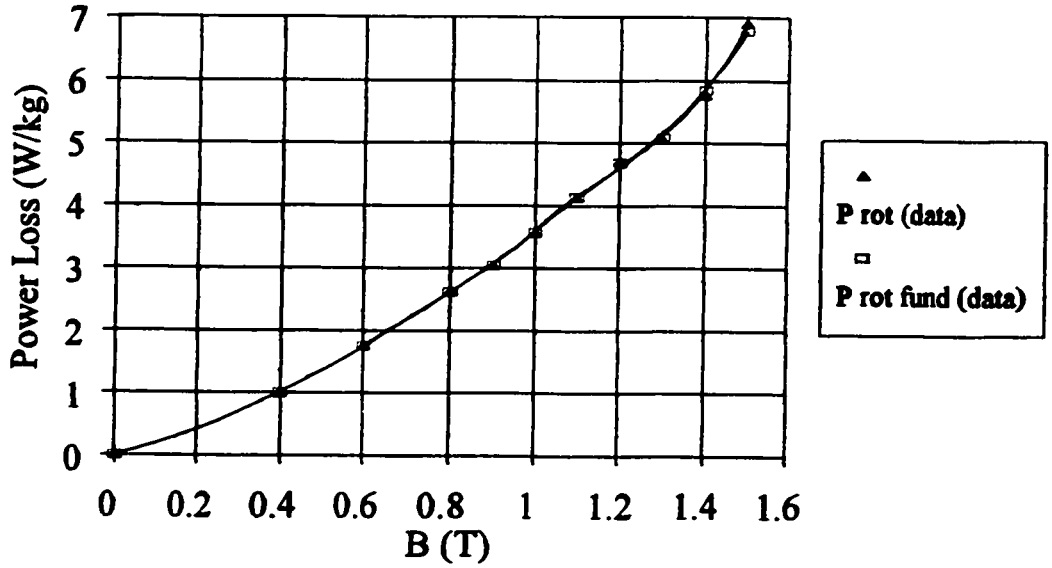

Figure 5.13 - NO Steel A - Rotational power losses with and without distortion harmonics.

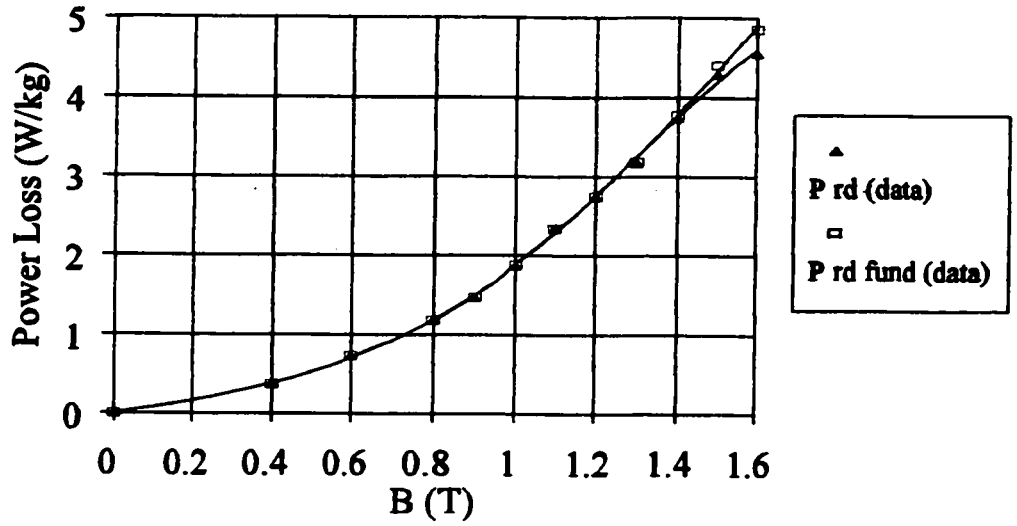

Figure 5.14 - NO Steel A - Power losses (rd) with and without distortion harmonics.

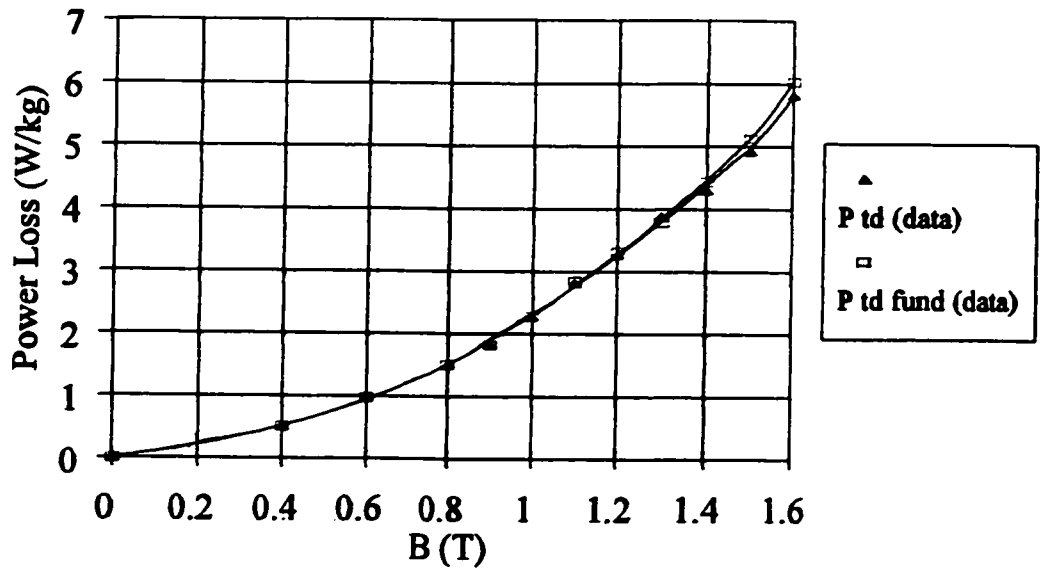

Figure 5.16 - NO Steel A - Power losses (td) with and without distortion harmonics.

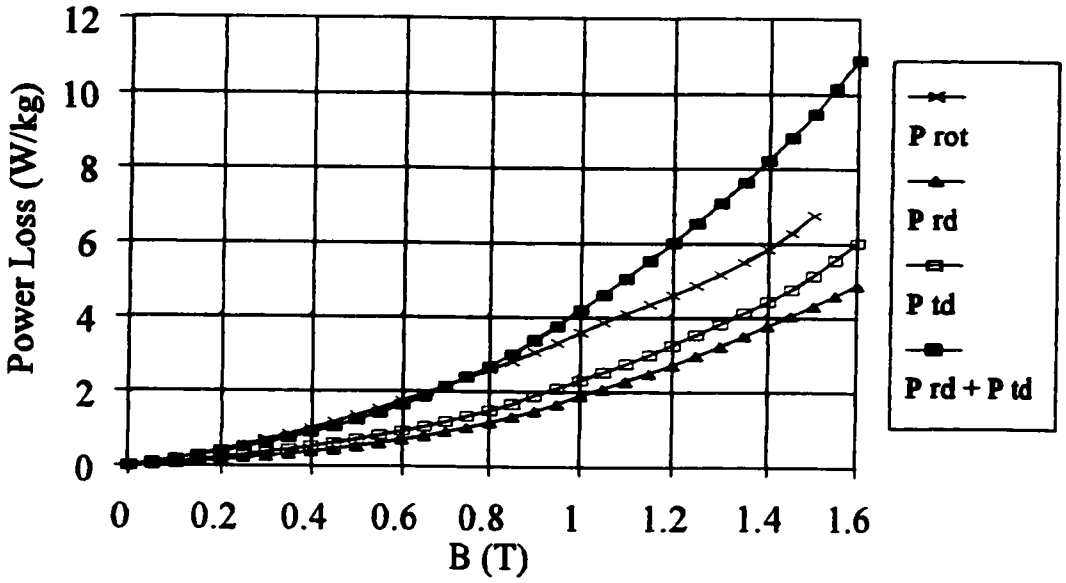

Figure 5.15 - NO Steel A - Comparison of alternating and rotational power losses.

5.2.2 NO Steel B

Figures 5.17 through 5.20 show the losses in NO steel B. Note that for all the loss curves, the effects of the distortion harmonics are very small. As seen in figure 5.20, the rotational losses in this steel are also not accurately given by the sum of the td and rd losses. The sum of the losses in the rd and td gives a somewhat reasonable estimate of the rotational losses at flux density values less than 1.0 T. Note that at the lower flux density values, the rotational losses are slightly greater than estimated by the assumption of superposition. As the flux density levels are increased, the assumption of superposition tends to over predict the rotational losses.

Note the level of anisotropy in the losses when comparing the rd and td losses. This is a general feature of typical "non-oriented" steels. The loss anisotropy is masked for the case of alternating loss measurements using the 50/50 Epstein square. The current test apparatus has the advantage of being able to measure losses in the rd and td of the same sample. Distortion levels for NO steel B are given in table 5.6. Note that it is much harder to maintain an undistorted waveform in the td as opposed to the rd. This is illustrated by the higher distortion factors in the td at 1.5 T and 1.6 T. NO steels exhibit anisotropy of permeability and loss. In the td, the permeability of the material tends to be lower than in the rd, hence the increased DF values in the td.

Table 5.6 - Distortion Factors for Measurements on NO Steel B

Loss Measurement	Distortion Factor (rd)	Distortion Factor (td)
Alternating	3.64% @ 1.6 T	9.13% @ 1.6 T
Alternating	2.39% @ 1.5 T	6.14% @ 1.5 T
Rotational CW	4.73% @ 1.5 T	3.25% @ 1.5 T
Rotational CCW	4.74% @ 1.5 T	2.86% @ 1.5 T

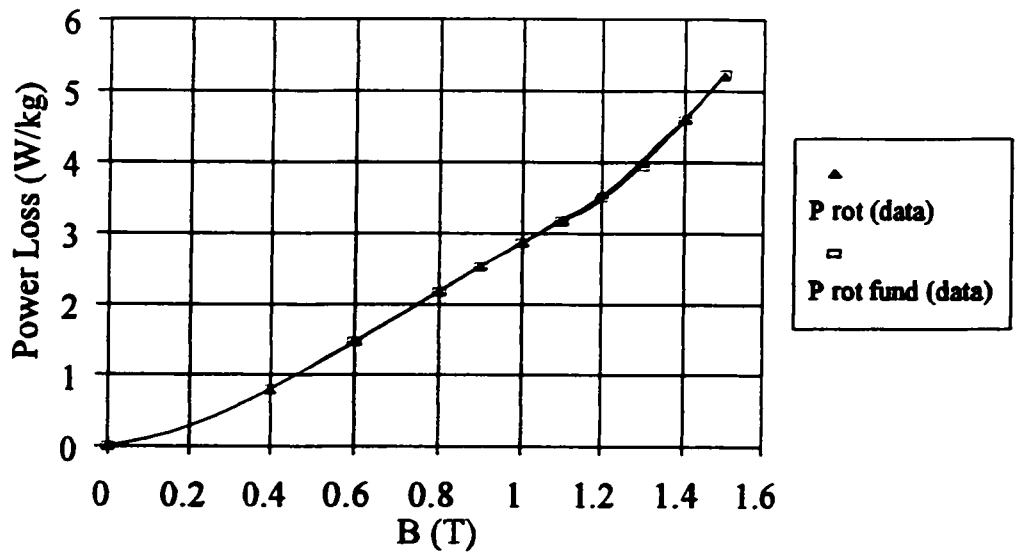

Figure 5.17 - NO Steel B - Rotational power losses with and without distortion harmonics.

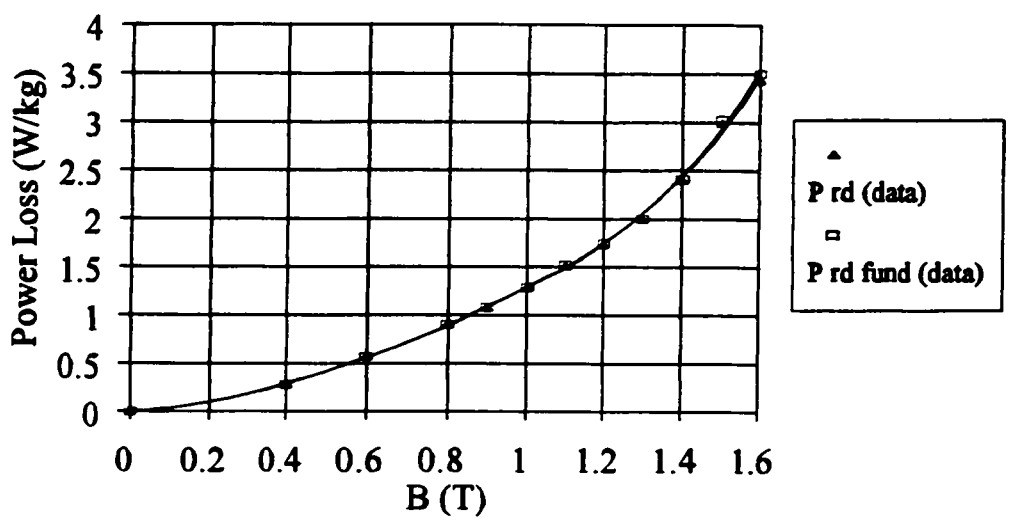

Figure 5.18 - NO Steel B - Power losses (rd) with and without distortion harmonics.

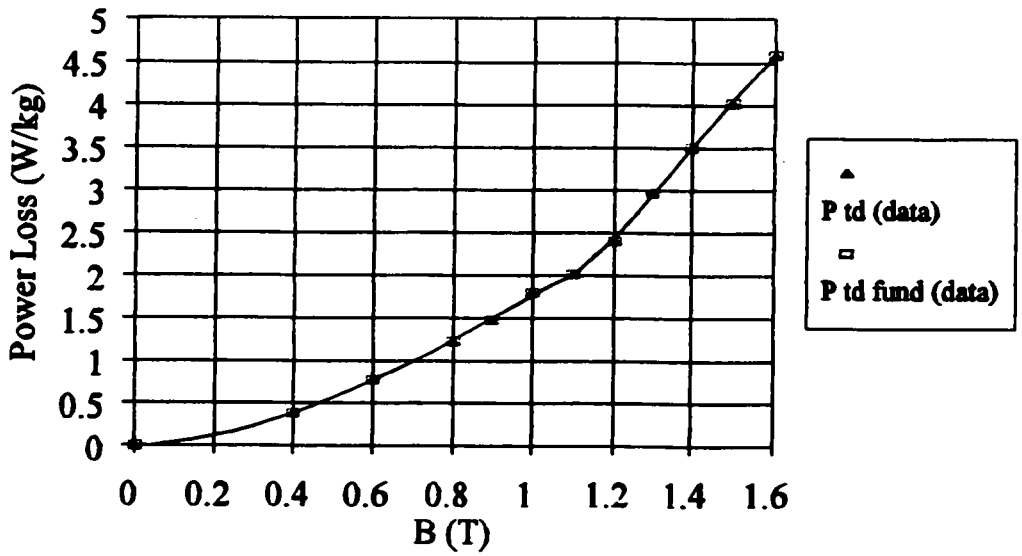

Figure 5.19 - NO Steel B - Power losses (td) with and without distortion harmonics.

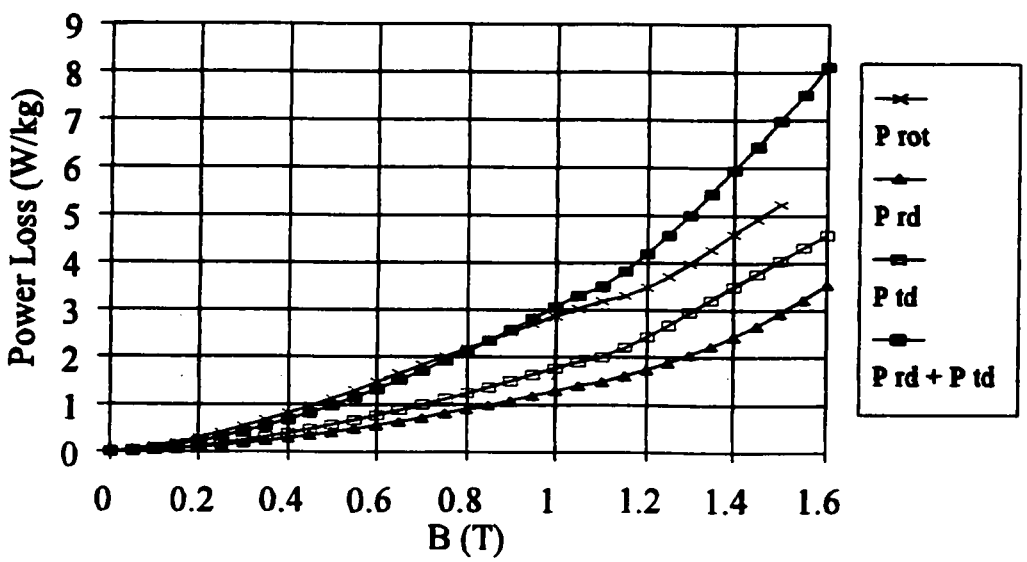

Figure 5.20 - NO Steel B - Comparison of alternating and rotational power losses.

5.2.3 NO Steel C

Figures 5.21 through 5.24 show the losses in NO steel C. Note that in all the curves, the effects of the distortion harmonics are slightly apparent for the last data point in each curve. Losses are slightly smaller for the case of the curves containing the distortion harmonics. This may seem counterintuitive at first, but is explained in section 2.3.5. For the alternating loss case, the distortion factor exceeded 5% when the rd and td losses were measured at 1.6 T. This steel has a silicon content of approximately 2.75% and small portions of aluminium and manganese (as shown in table 5.1). The increased alloy content in this steel makes it harder to magnetize than the MLQ steels at the highest flux density levels. Once again, this is due to a lowering of the saturation induction as discussed in Section 2.3.1.1.

Rotational losses in this steel are also not accurately given by the sum of the td and rd losses. Superposition gives a good estimate of the rotational losses to a flux density of approximately 0.9 T. At the higher flux density levels, the rotational losses are overestimated by the superposition approximation. The rotational losses reach a peak value at approximately 1.4 T and then begin to decrease. Note the level of anisotropy in the losses when comparing the rd and td losses in figure 5.24. Distortion levels for NO steel C are given in table 5.7.

Table 5.7 - Distortion Factors for Measurements on NO Steel C

Loss Measurement	Distortion Factor (rd)	Distortion Factor (td)
Alternating	6.12% @ 1.6 T	8.96% @ 1.6 T
Alternating	3.72% @ 1.5 T	5.42% @ 1.5 T
Rotational CW	1.84% @ 1.5 T	3.38% @ 1.5 T
Rotational CCW	1.79% @ 1.5 T	3.16% @ 1.5 T

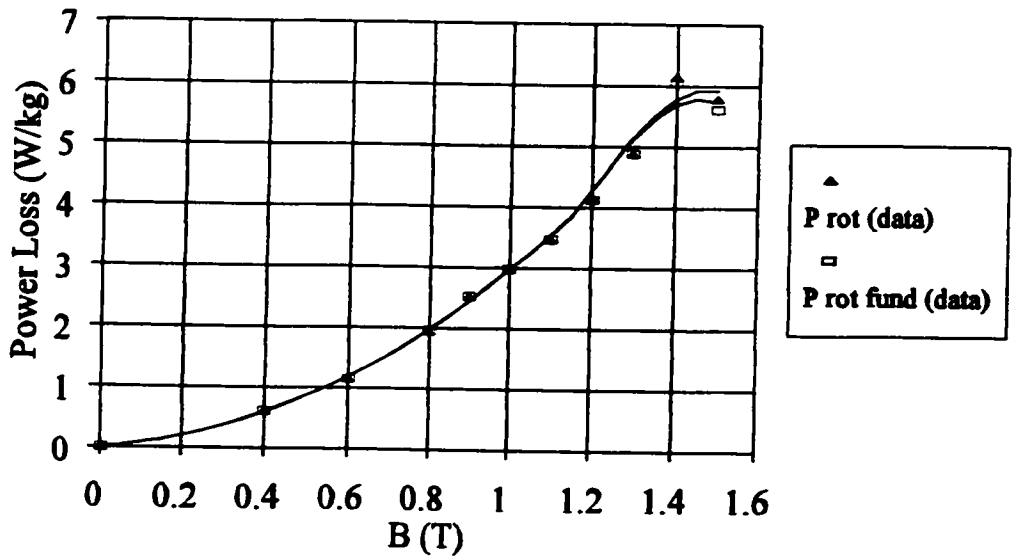

Figure 5.21 NO Steel C - Rotational power losses with and without distortion harmonics.

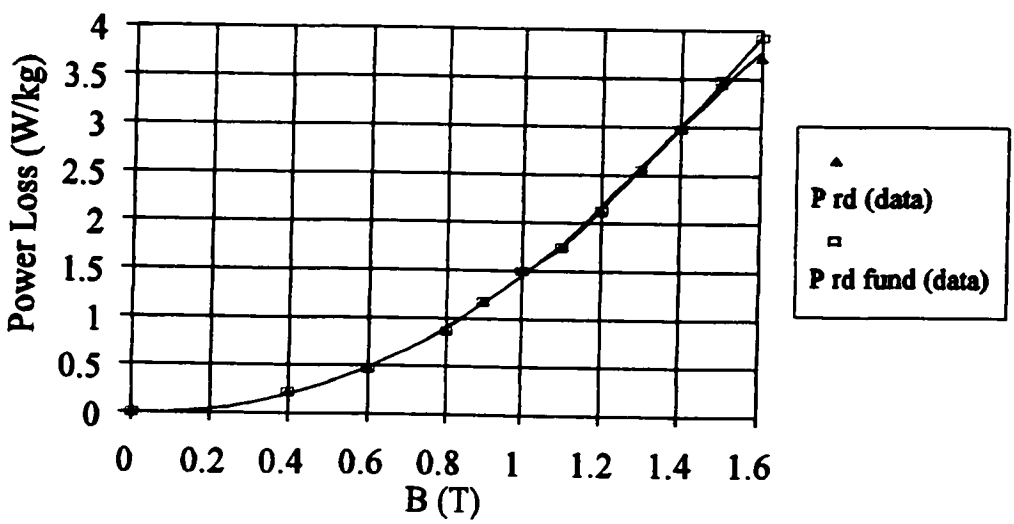

Figure 5.22 - NO Steel C - Power losses (rd) with and without distortion harmonics.

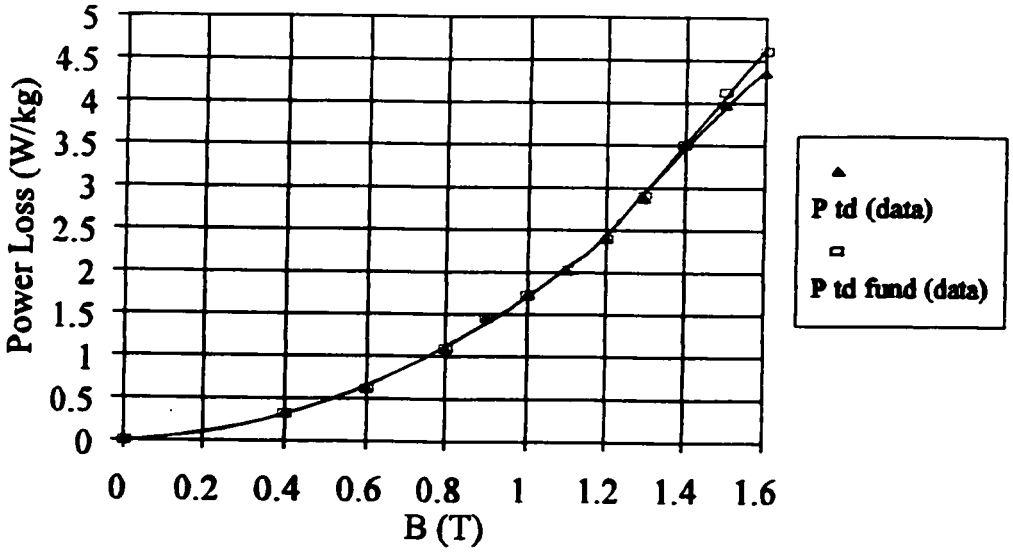

Figure 5.23 - NO Steel C - Power losses (td) with and without distortion harmonics.

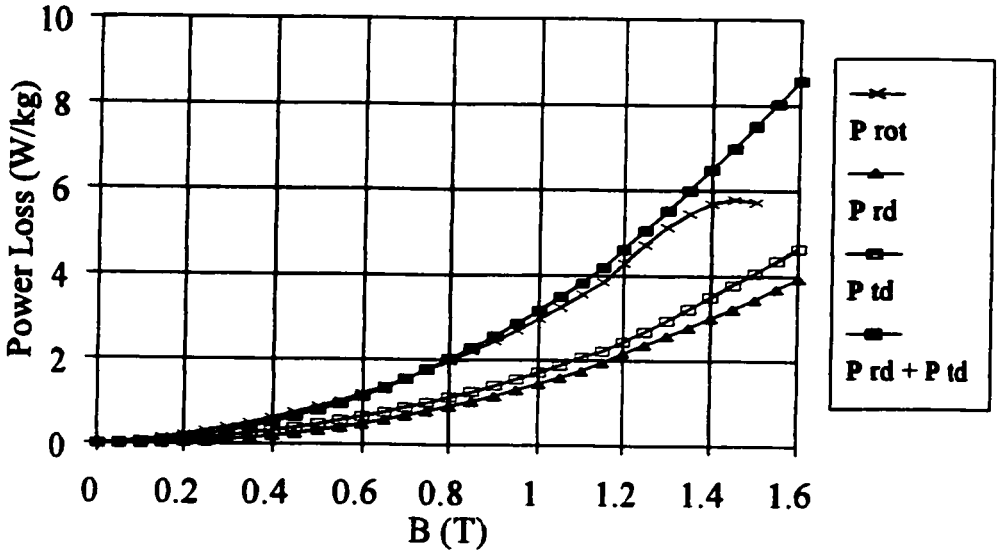

Figure 5.24 - NO Steel C - Comparison of alternating and rotational power losses.

5.2.4 NO Steel D

Figures 5.25 through 5.28 show the losses in NO steel D. Note that in figure 5.25, the effects of the distortion harmonics are apparent for the last two data points in the curve. This steel is the grade that was used in the cores of the five induction machines investigated as part of this research. Figure 5.28 shows a comparison of the losses for the alternating and rotational loss cases (curves without the distortion harmonics).

Rotational losses in this steel are also not accurately given by the sum of the td and rd losses. The estimate begins to break down at flux density levels above 0.8 T. This steel has a high alloy content and thin gage. In Section 2.3.1.1 we saw that alloying agents increase the resistivity of the steel. Classical eddy current losses are inversely proportional to the material resistivity and directly proportional to the thickness of the material (see Section 2.2.3). Therefore, the eddy current losses are very low, and more losses are attributable to hysteresis. Note the level of anisotropy in the losses when comparing the rd and td losses shown in figure 5.28. Distortion levels for NO steel D are given in table 5.8.

Table 5.8 - Distortion Factors for Measurements on NO Steel D

Loss Measurement	Distortion Factor (rd)	Distortion Factor (td)
Alternating	11.26% @ 1.6 T	9.94% @ 1.6 T
Alternating	6.76 @ 1.5 T	7.19 @ 1.5 T
Rotational CW	9.29% @ 1.575 T	6.09% @ 1.575 T
Rotational CW	8.90% @ 1.575 T	6.11% @ 1.575 T
Rotational CW	6.74% @ 1.5 T	4.89% @ 1.5 T
Rotational CCW	6.68% @ 1.5 T	4.96% @ 1.5 T

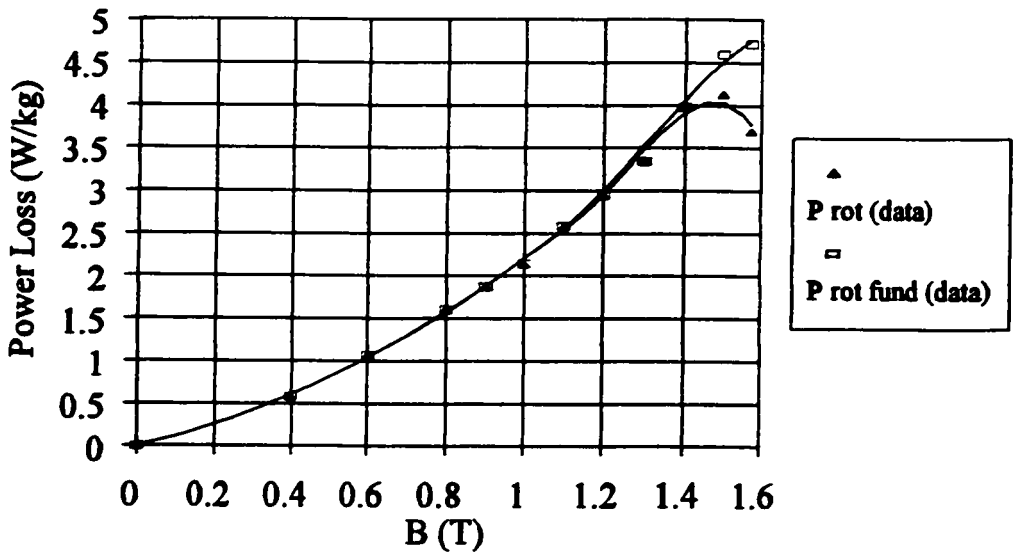

Figure 5.25 - NO Steel D - Rotational power losses with and without distortion harmonics.

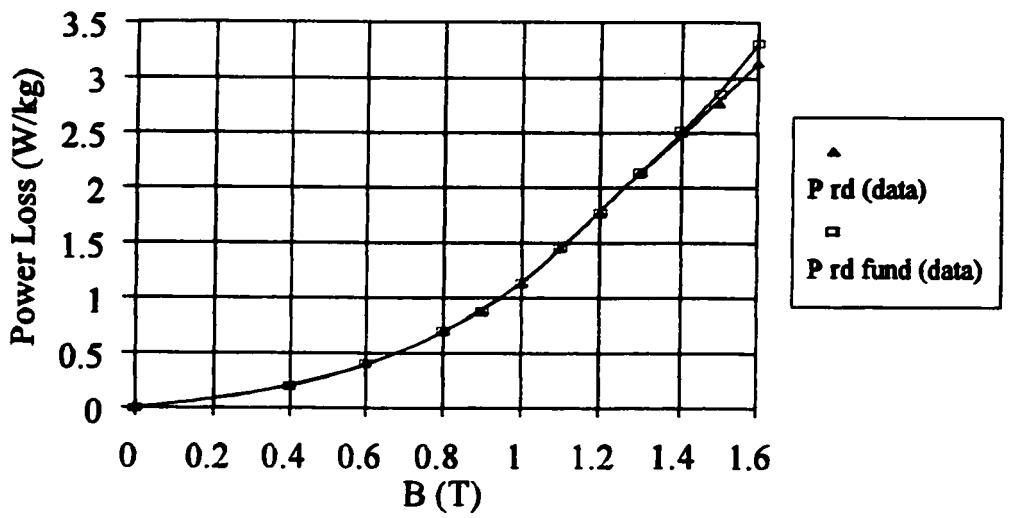

Figure 5.26 - NO Steel D - Power losses (rd) with and without distortion harmonics.

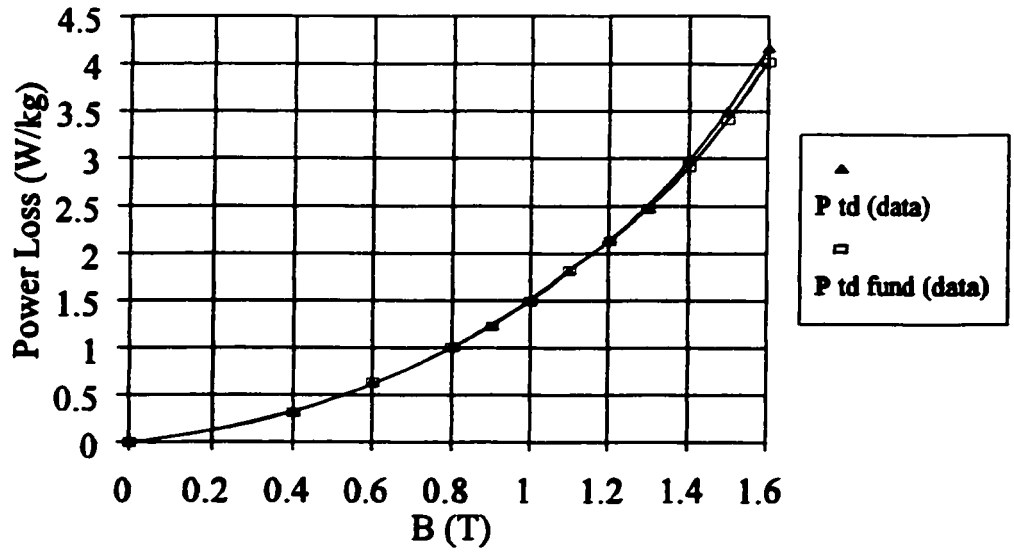

Figure 5.27 - NO Steel D - Power losses (td) with and without distortion harmonics.

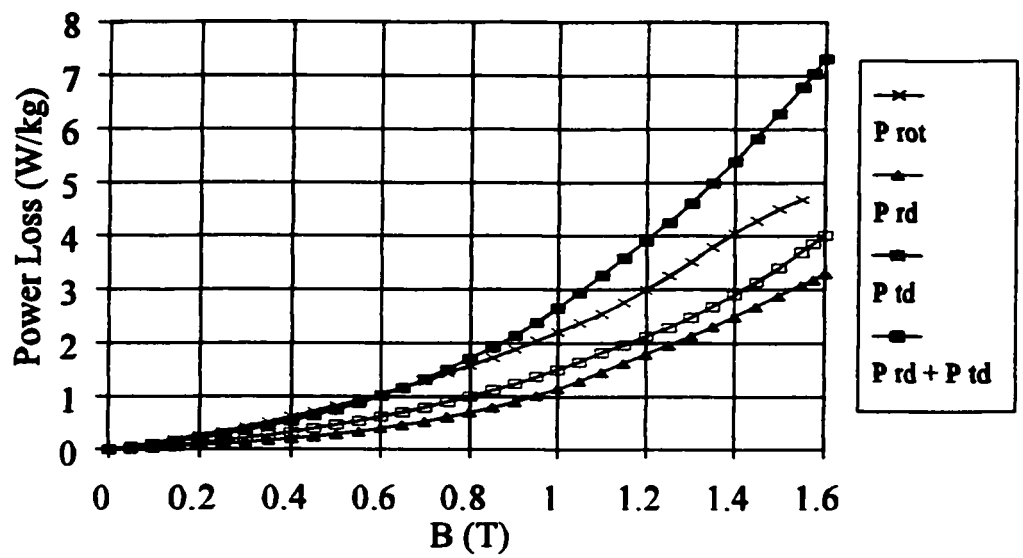

Figure 5.28 - NO Steel D - Comparison of alternating and rotational power losses.

5.3 Cross Grade Comparisons

The curves in this section are taken from the polynomial interpolations for the measurements without the distortion harmonics.

5.3.1 MLQ Steels

Figures 5.29 through 5.31 shows a comparison of the losses amongst the three grades of MLQ steels. MLQ steel A shows the highest losses for both the alternating and rotational cases. Referring to table 5.1, we see that MLQ steel A has the lowest alloy content of the three steels; therefore, it also has the lowest resistivity. We expect that MLQ steel A will exhibit the highest eddy current losses among the three steels due to its low resistivity (see Section 2.2.3). MLQ steel B has slightly higher alternating losses than MLQ steel C in the rd. The alternating losses in the td are markedly higher in MLQ steel B than MLQ steel C. MLQ steel B has a slightly lower alloy content than MLQ steel C, therefore, we would expect this result. Note the result in figure 5.29. Rotational losses for MLQ steel B and MLQ steel C are remarkably similar. This is a clear example of how only making loss measurements for the alternating flux case can be misleading in judging the overall performance of a steel in a motor core. MLQ steel C may be the better steel based on alternating loss measurements but steel B has similar rotational loss characteristics. When used in motor cores, MLQ steels B and C might yield similar core loss performance.

A general trend is found for the alternating loss measurements. An increase in alloy content leads to lower alternating losses in the steels. Alternating losses are lowered by increasing the resistivity of the steel through additions of alloys, as discussed in Section 2.3.1.1. Additions of silicon also have beneficial effects on alternating hysteresis, as discussed in Section 2.3.1.1.1. Due to their higher alloy contents, MLQ steels B and C have lower alternating losses than MLQ steel A, as shown in figures 5.30 and 5.31. As discussed in Section 2.2.3, an increase in alloy content will also lower the rotational eddy current losses.

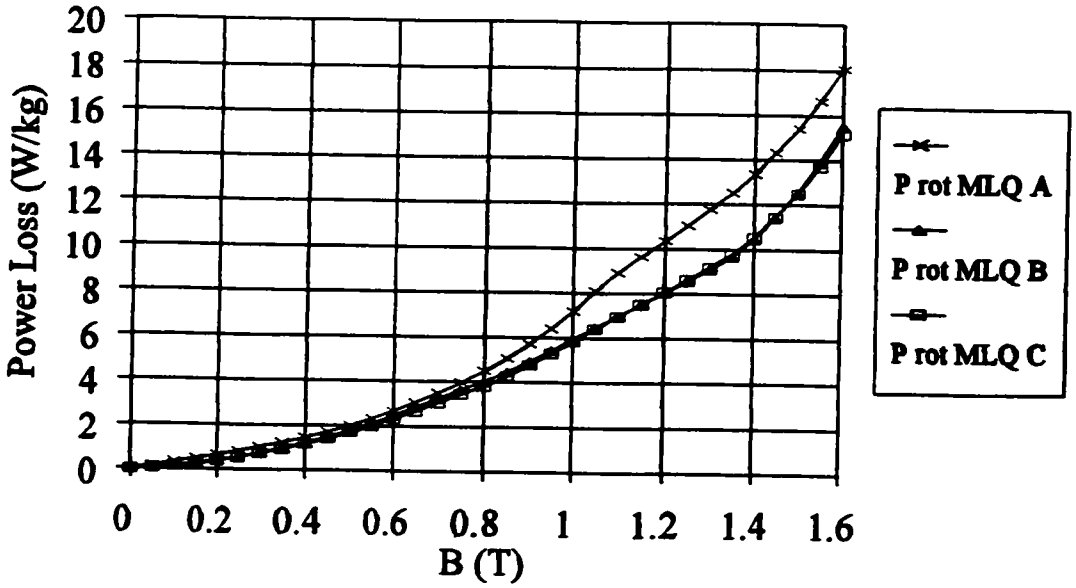

Figure 5.29 - Comparison of rotational power losses amongst MLQ steels.

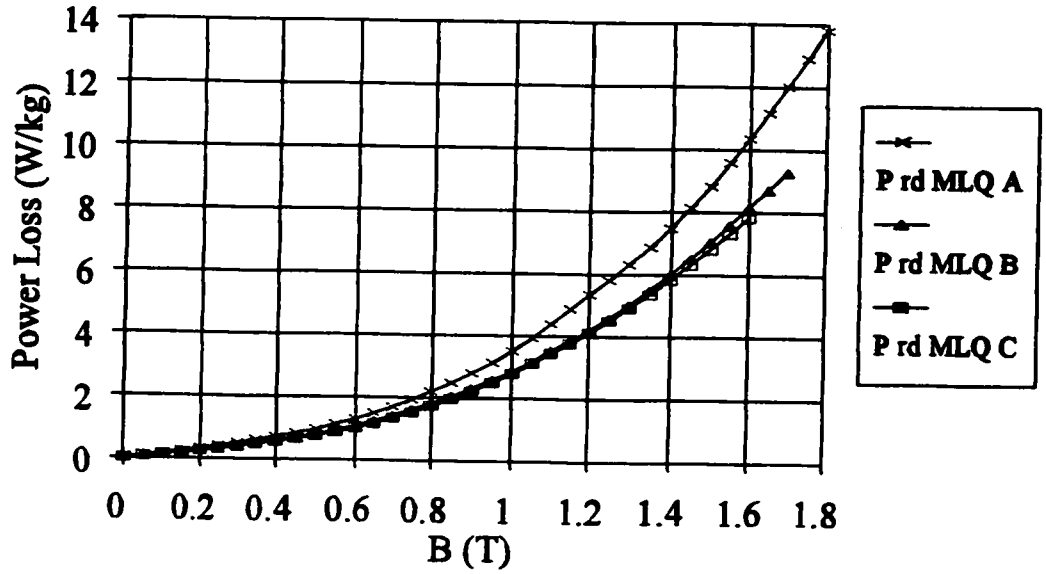

Figure 5.30 - Comparison of power losses (rd) amongst MLQ steels.

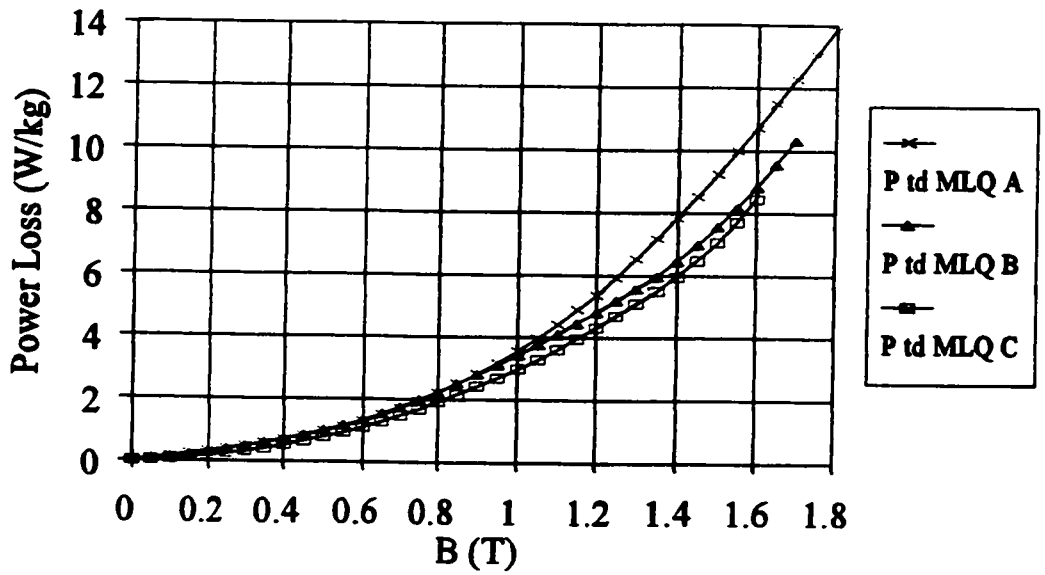

Figure 5.31 - Comparison of power losses (td) amongst MLQ steels.

5.3.2 NO Silicon Steels

Figures 5.32 to 5.34 show a comparison of losses for the four grades of NO silicon steel. Steel B and D have similar chemical compositions and thickness. Note that NO steels B and D have similar alternating losses in the rd. In the td, NO steel B exhibits higher losses than NO steel D. NO steel B also exhibits higher rotational losses than steel D as shown in figure 5.32. NO steel A exhibits rotational losses that are similar to those of steel C at 1.4 T, yet at the same flux density value, it has much higher alternating losses as shown in figures 5.33 and 5.34. NO steel A also has much higher rotational losses than NO steel C at flux density values above and below 1.4 T. NO steel A also exhibits higher alternating losses in both the rd and the td as shown in figures 5.33 and 5.34. NO steel B has higher rotational losses than steel C at flux density levels below about 0.9 T but lower losses at flux densities above 0.9 T. It also appears that at some point beyond 1.6 T another cross over point could

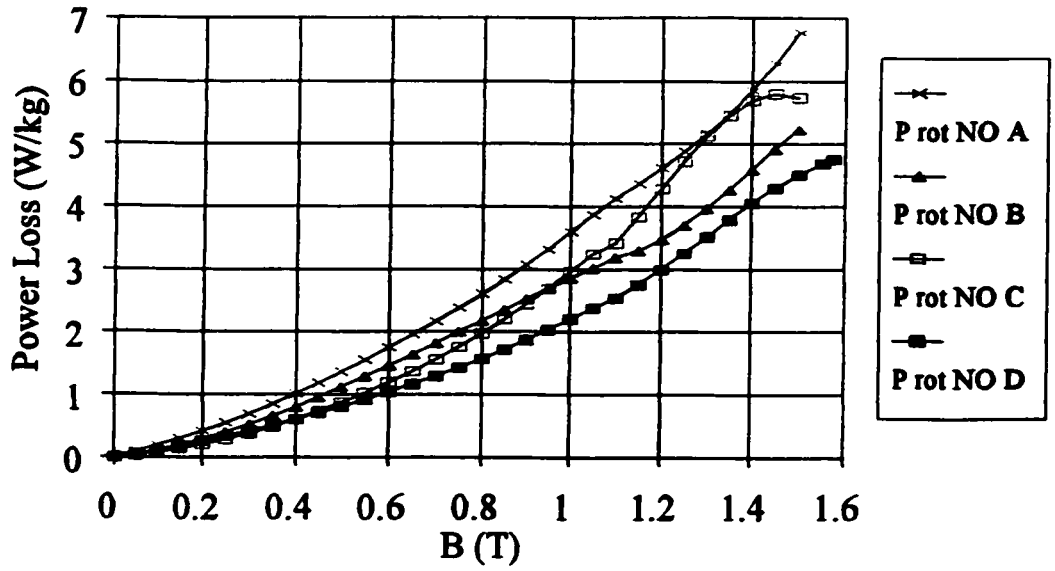

Figure 5.33 - Comparison of rotational power losses amongst NO steels.

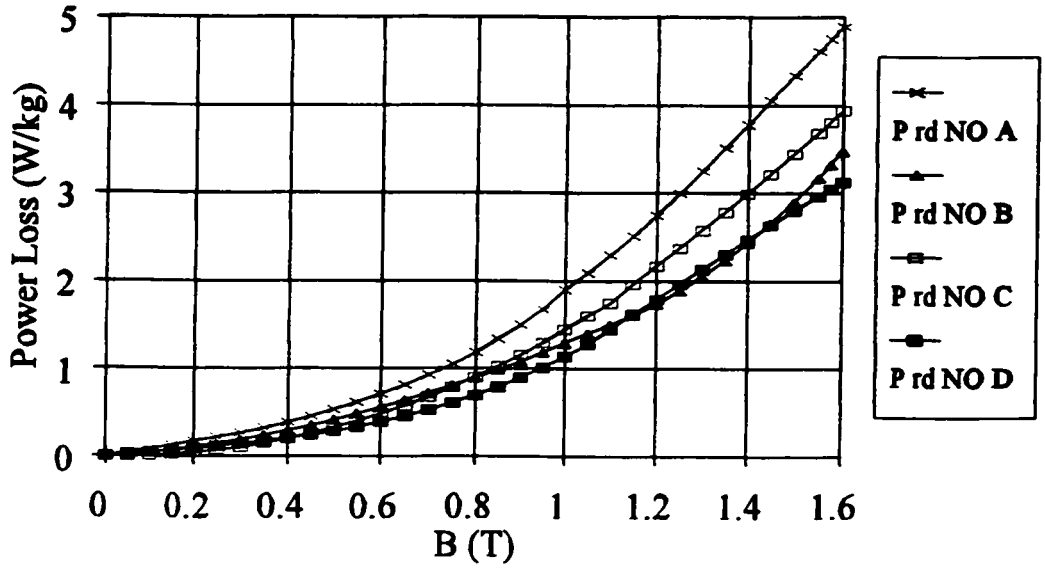

Figure 5.32 - Comparison of power losses (rd) amongst NO steels.

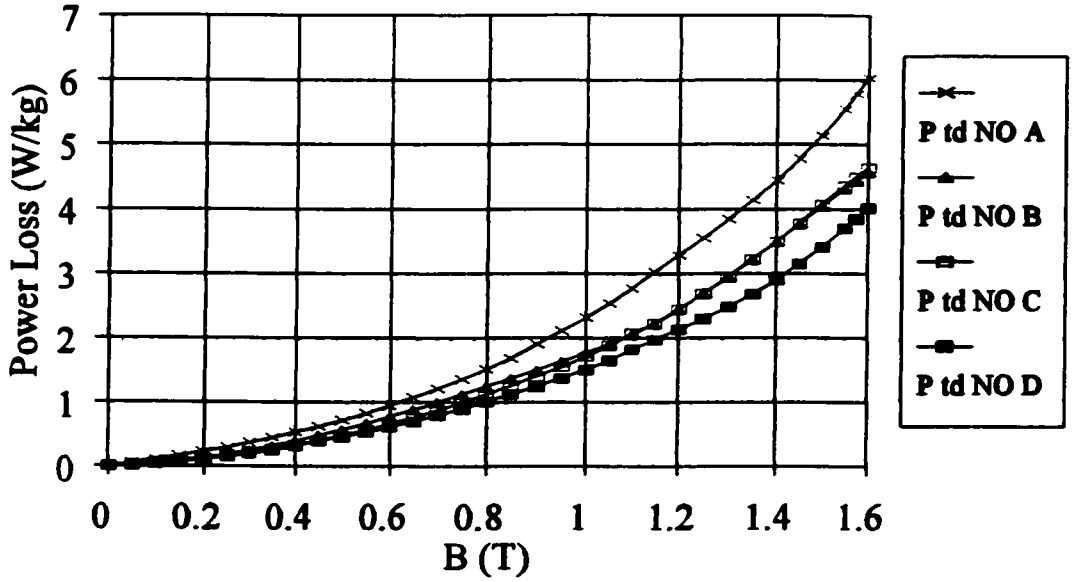

Figure 5.34 - Comparison of power losses (td) amongst NO steels.

occur. NO steels C and D exhibit maximum values of rotational losses at flux density values of approximately 1.45 and 1.6 T respectively. At these points, the rotational hysteresis losses in the samples have reached maximum values and at higher levels of saturation the rotational hysteresis values should begin to decrease as discussed in Section 2.2.2. NO steels A and B would likely exhibit the same behaviour at higher levels of saturation; although observing this with the present apparatus was not possible.

5.4 Family of Curves for a Range of Aspect Ratios

One goal of the current research, was to analyse the losses in the stator cores of five large induction motors rigorously. All the induction motor cores under investigation had cores constructed of NO steel D. To do this analysis, additional loss curves for NO steel D were measured for various aspect ratios. In figure 5.35, loss curves are shown for aspect ratios of 1.0, 0.8, 0.6 and 0.4 as well as curves for the rd and td alternating losses. In figure

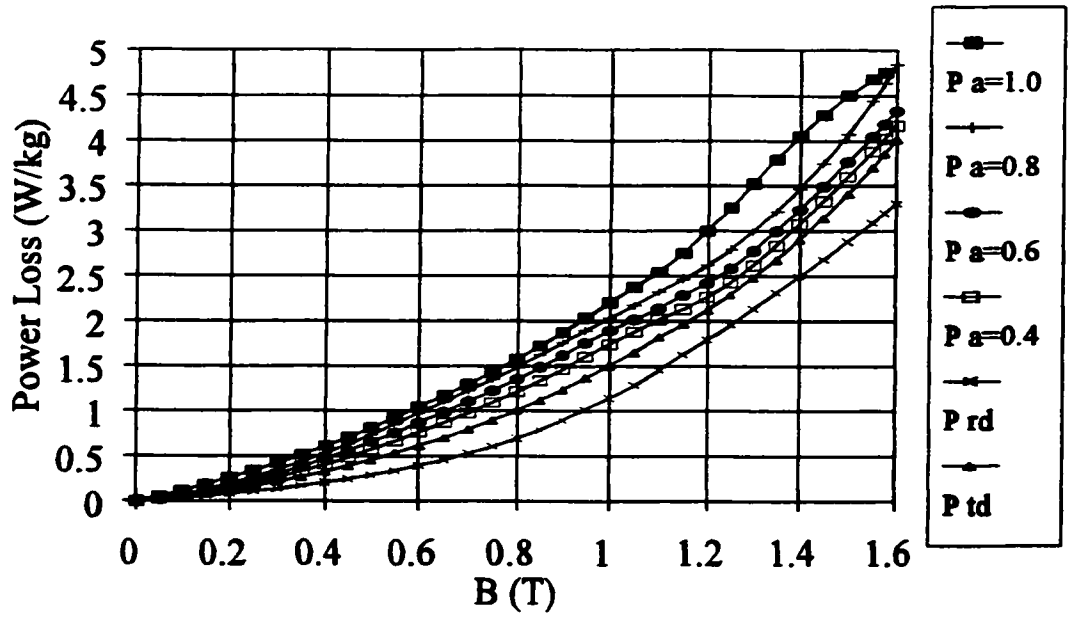

Figure 5.35 - NO Steel D - Power losses for a family of aspect ratios (a).

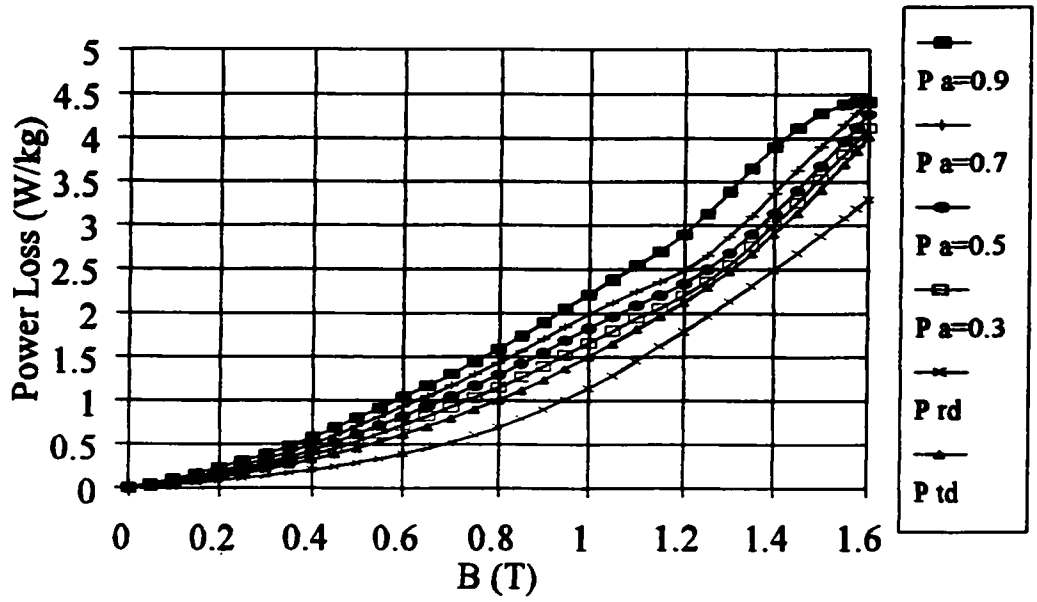

Figure 5.36 - NO Steel D - Power losses for a family of aspect ratios (a).

5.36, loss curves are shown for aspect rations of 0.9, 0.7, 0.5 and 0.3 as well as curves for the rd and td alternating losses. The aspect ratio is taken as the magnitude of the minor axis of the ellipse divided by the magnitude to the major ellipse. The major axis of the ellipse always lies along the td for reasons that will become clear in Chapter 6. For this reason the curve for the td losses forms a lower bound for the elliptically polarized loss curves. An aspect ratio of 1.0 gives a purely rotating flux and an aspect ratio of 0.0 gives a purely alternating flux.

5.5 Comparison of Loss Data With Standard Epstein Test Results

For NO steel D, guaranteed loss curves based on Epstein test results for the rd and td were available for comparison to the results made with the proposed test apparatus. The guaranteed curve is based on "as sheared" material (i.e. without a stress relief anneal). The guaranteed loss curve is based on a series of loss measurements for various batches of steel and represents the maximum loss that can be expected when considering variations in different batches of steel. Therefore it is not uncommon for specific batches of steel to exhibit losses that are below the guaranteed curve. Figure 5.37 shows a comparison of the losses as expected from the guaranteed Epstein loss curves in the rd and td and as obtained with the PRL test apparatus. Losses obtained with the PRL test apparatus are lower.

The difference between the guaranteed Epstein loss curve and the PRL test apparatus can be attributed to several factors. Samples tested using the PRL test apparatus were stress relief annealed. Before annealing, the samples were virtually impossible to test due to the cutting strains in the edges of the sample. The stress relief anneal will reduce the losses below the guaranteed value. The test sample had a thickness of only 0.0179 inches as opposed to the nominal 0.0185 inches specified for the material. Any reduction in thickness will reduce the classical eddy current losses in the sample as suggested by equation 2.3. A great deal of variation may exist from one batch of steel to the next. The sample used in this study had a

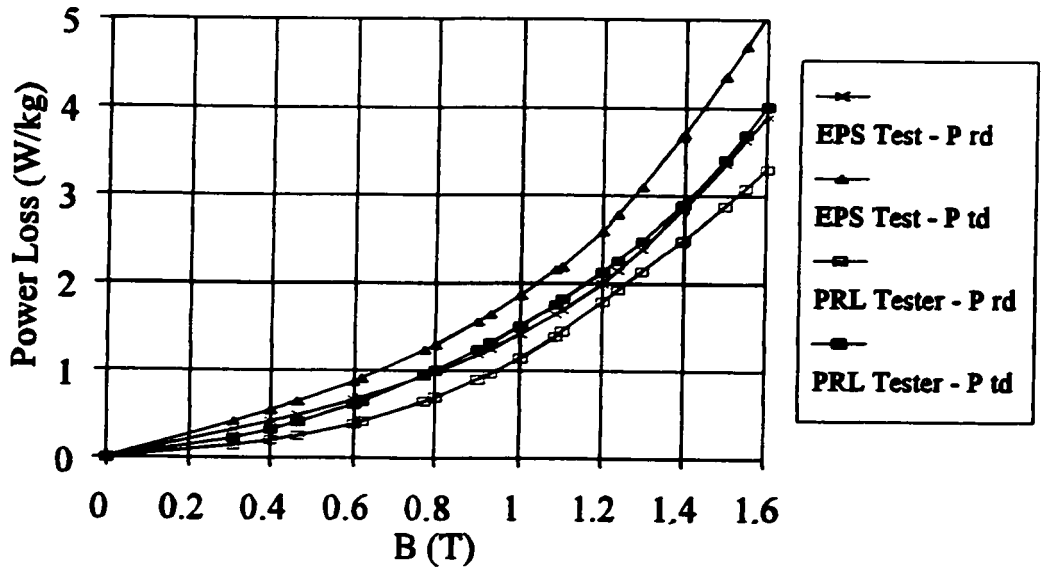

Figure 5.37 - Comparison of loss curves. Epstein Test (EPS) vs. PRL Tester (PRL).

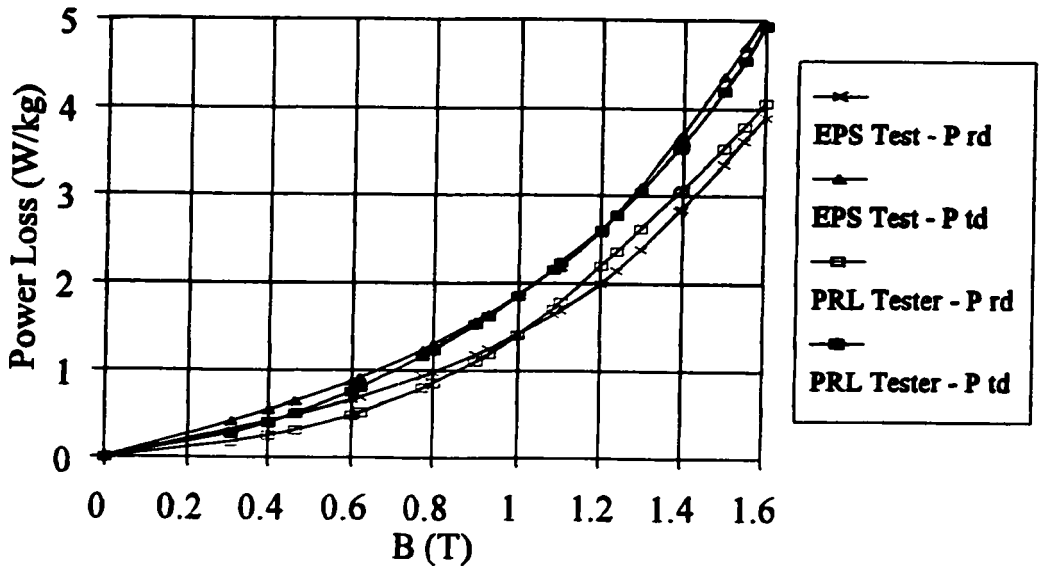

Figure 5.38 - Comparison of loss curves. Epstein Test (EPS) vs. PRL Tester (PRL) with factor of 1.23 applied to the results.

measured Epstein loss that was well below the guaranteed value. The specific sample used in this study had a measured "as sheared" Epstein loss of 3.47 W/kg @ 1.5 T when measured with half the samples cut in the rd and half in the td. Compare this with the guaranteed value of 3.86 W/kg @ 1.5 T specified by the steel manufacturer.

Now examine the curves in figure 5.38. The results taken using the PRL test apparatus have been multiplied by a factor of 1.23. The factor 1.23 is obtained by taking the guaranteed loss value of 3.86 W/kg @ 1.5 T and dividing by 3.14 W/kg that is the average of the rd and td loss measurements from my apparatus taken at 1.5 T. Notice that the curves coincide closely (especially the results for the td). Taking into account the variation between specific batches of steel, and the additional stress relief anneal, the results seem reasonable.

Table 5.8 shows a comparison of the measured values with Epstein results. The results for MLQ Steel A are in very close agreement with Epstein results obtained for a different batch of the same material. MLQ steels are shipped semi-processed and must have a decarburisation anneal before use. After shearing and drilling, the sample used in this investigation received the same type of anneal as the Epstein samples did. It is therefore not surprising that the results are in close agreement. Epstein data was not available for MLQ steels B and C.

The NO materials are all fully processed and should have been measured in the as sheared condition. As discussed in Chapter 4, this was impractical due to the cutting strains in the edges of the sample. In order to proceed with the measurements, a stress relief anneal was applied to the samples. The subsequent anneals may have lowered the losses of the fully processed materials. This helps to explain why the measurements in this investigation are lower than would be expected from the guaranteed Epstein values. In any case, further investigation is warranted. Comparing loss measurements for more semi-processed materials with Epstein test results for samples would be useful. By using samples cut from the same coil, any differences attributable to manufacturing variations would be avoided.

Table 5.9 - Comparison of Results With Epstein Values

Steel	Average of rd and td Losses Measured on PRL Tester (W/kg)	50/50 Epstein Loss (W/kg)	Comments on Epstein Values
MLQ Steel A	9.04 @1.5 T 5.36 @1.2 T 3.55 @1.0 T	8.6 @1.5 T 5.3 @1.2 T 3.7 @1.0 T	Typical value from Epstein curve for a different batch of the same material supplied by manufacturer.
NO Steel A	4.74 @1.5 T	6.25 @1.5 T	Guaranteed value for as sheared material.
NO Steel B	3.51 @1.5 T	4.71 @1.5 T	Guaranteed value for as sheared material.
NO Steel C	3.75 @1.5 T	4.81 @1.5 T	Guaranteed value from ASTM A677 for as sheared material.
NO Steel D	3.14 @1.5 T	3.47 @1.5 T 3.86 @ 1.5 T	Measured value for as sheared material cut from same coil. Guaranteed value for as sheared material.

5.6 Variation of Alternating Losses With Respect to Angle of Magnetization

As discussed in Chapter 4, rotational core loss testers can be used to make measurements of losses at arbitrary angles to the rd or td of the sample. Such a measurement has been make for NO steel D and is shown in figure 5.39. Note that the measurements were made for 15 degree increments of angle to the td. A third order polynomial interpolation was applied to each curve. The graphs in figure 5.39 show the results of the polynomial interpolation. Notice that at 0.9T and 1.2T the distortion harmonics had very little effect on the result. At 0.9T the two curves are nearly coincident, but at 1.5T the discrepancy is quit noticeable. It is very difficult to keep the flux density waveform from distorting when making arbitrary loss measurements in the open loop configuration at higher flux densities,

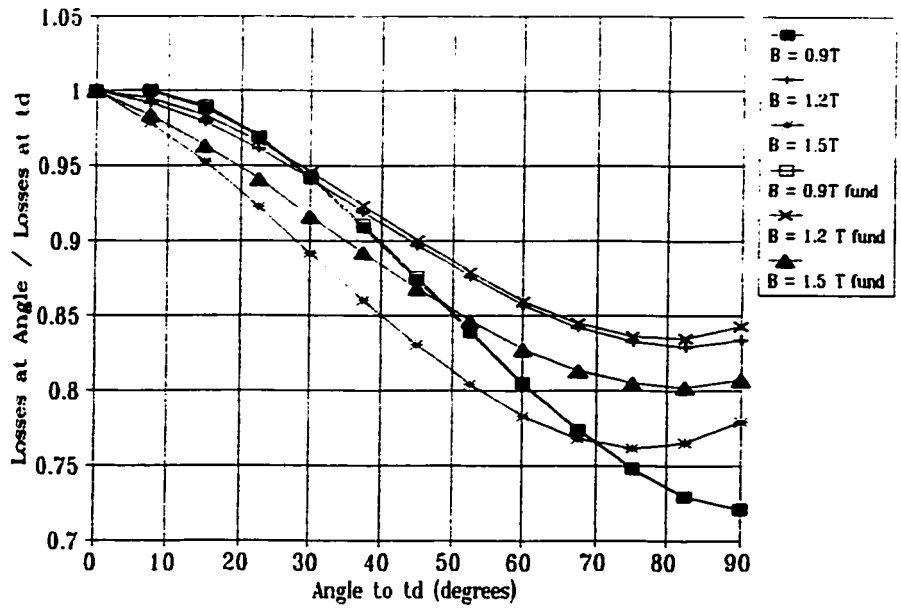

Figure 5.39 - Loss measurements at angles to the td with and without distortion harmonics.

hence the discrepancy.

5.7 Discussion of Results

5.7.1 Comparisons With Results of Other Researchers

Yamaguchi and Narita [41] reported rotational loss measurements for a 0.35 mm thick NO silicon iron. This steel exhibited approximately 2.1 W/kg loss @1.5T and 60 Hz when the losses in the rd and td were averaged. Curves for aspect ratios of 1.0, 0.75, 0.5 and 0.25 were reported in figure 10 on page 19 of the paper. Yamaguchi and Narita's curves are similar in shape and behaviour to the curves in figures 5.35 and 5.36. The rotational power loss curve for an aspect ratio of 1.0 is similar to that for NO steels C and D in that it reaches a maximum value and then begins to decrease. The maximum rotational loss on Yamaguchi and Narita's curve is at 1.6T whereas for NO steel C it is at 1.45 T and for NO steel D it is at about 1.6 T. Yamaguchi and Narita also concluded that rotational losses for an aspect ratio of 1.0 could be accurately estimated from alternating losses for flux density values up

to around 0.6 T and that beyond that point the losses would be overestimated. For aspect ratios of 0.75, 0.50, and 0.25, Yamaguchi and Narita estimated that the losses would be overestimated for flux density values beyond 0.8 T, 0.9 T, and 1.2 T respectively. Below the above mentioned points, they concluded that the superposition of alternating losses would underestimate the losses to a small degree. This seems reasonable, given the results in figures 5.8, 5.11, 5.16, 5.20, 5.24, and 5.28 that show that the rotational losses can be slightly larger than given by superposition of the alternating losses at low flux density values. The reader is cautioned that measurements were only made down to 0.4 T and 0.6 T and that the curves have been extended to the origin using a third order polynomial curve fit. In future studies it would be interesting to collect more data for the low flux density values.

Sasaki et al [2] made measurements of rotational losses for a 3% Si NO silicon sheet at 50 Hz. Their results are very similar to those obtained for NO steel D. The average of the alternating losses in the rd and td of the sample were about 2.9 W/kg at 1.5T. The curve for rotational loss crosses the curve for alternating losses in td and rd at about 1.6T. This result is very similar to that obtained for NO steel D as shown in figure 5.28 except that for the current measurement the curves would cross at a slightly higher flux density level.

Few results for measurements of rotational losses on MLQ steels are reported in the literature. Fiorello and Rietto [3] have reported results for a "soft Fe" that has characteristics similar to those of an MLQ steel. The peak loss occurred at 1.5 T and then fell as the flux density value was further increased. In the present investigation, a peak value of rotational loss was not encountered at the flux density values investigated. Fiorello and Rietto did not report alternating losses for the material. Measurements taken for a 3% Si NO steel showed a peak loss at about 1.6T and then a gradual reduction beyond that flux density value.

Looking at figures 5.29 and 5.32, we see that in the curves for rotational losses there occur points of flexure where the rate of increase of losses changes at some point between 1.1T and 1.4T. As was discussed in Chapter 3, Brailsford [17] reported a similar

phenomenon in his study of rotational hysteresis losses on four different materials.

Salz and Hempel [90] reported the magnetic properties of a (100)[001] textured material. They reported rotational losses for a 0.65mm sample and a 0.50mm sample. For 50 Hz measurements, both samples exhibit maximum loss around 1.55 T. Rotational losses then dropped off rapidly as the flux density levels were further increased. The shape of the curve was very similar to that observed in figures 5.8 and 5.25 for MLQ steel B and NO steel D. The main difference was that the rate at which the losses decreased after 1.55 T was very much greater. Neither the alternating loss values nor the nominal chemistry of the material was reported.

Alinejad-Beromi, Moses and Meydan [138] reported the rotational losses in a 2.7% NO silicon iron sample. The measurements were made at 50 Hz, but the thickness of the sample was not reported. The shape of their curve is very similar to that found for NO steel C. At a flux density of approximately 1.2T, there occurred a rapid flexure in the curve. The losses rose rapidly reaching a maximum at about 1.5T. Alternating losses were not reported by these authors.

In a subsequent paper, Moses [177] reported a new set of curves for a 2.7% NO silicon steel. The rotational loss curve was the same as reported in the previous paper, but this time the rotational losses were compared with the sum of the losses in the rd and td of the sample. For flux densities below 0.6 T the rotational losses were very nearly equal to the sum of the losses in the rd and td of the sample. As the flux density increased the approximation was no longer valid. The sum of the losses in the rd and td of the sample consistently gave losses that were higher than the rotational losses. This behaviour is observed in the curves presented in this study as well, although for the steels currently investigated the approximation based on superposition of alternating losses seems valid to flux densities of 0.8 to 1.0 T.

Kedous-Lebouc et al [136] reported rotational losses at 50 Hz for a 0.50 mm thick,

3% silicon NO steel. Measurements were taken up to flux density levels of 1.5T. The results of their measurements agree with those presented in this study on two points. First, the authors found that for the sample under investigation, the principle of superposition of alternating losses was only valid for flux densities up to about 0.8 T. Above this flux density level the approximation overestimated the rotational losses. This agrees with the results obtained for three of the NO steels currently under investigation. For NO steel B superposition of losses was approximately valid up to 0.9 T. For MLQ steel A the point of departure was around 1.2T and around 0.9T and 1.0 T for MLQ steels B and C respectively. This observation was noted for both circular polarization and various degrees of elliptical polarization. The authors' results agree with those presented here on a second point. The shape of the loss curve for purely rotating flux density was similar in shape to the curves for MLQ steels A and C (figures 5.1and 5.9) and NO steels A and B (figures 5.14 and 5.17). Although the rotational losses above 0.8T were smaller than the sum of the alternating losses in the rd and td, a maximum was not reached and a decrease in the losses was not observed.

Results similar to those shown in figure 5.39 were observed by Page [178], for a 0.35 mm 3% Si NO material. His figure 1 shows a continuous decrease of alternating power loss as the angle of magnetization is changed from 0° to the td to 90° to the td (i.e. the rd). His measurements were carried out for a flux density level of 1.5 T and a frequency of 50 Hz.

5.7.2 The Effect of Distortion Harmonics on the Losses

Note that in general, the loss curves obtained by considering only the fundamental component of flux density, are higher than those that include the harmonics. Examples of this are found in figures 5.3, 5.7, 5.11, 5.14, 5.16, 5.22, 5.23 and 5.26. The saturation harmonics encountered during magnetic testing under alternating flux conditions always occur in a way that reduces the peak flux density of the waveform. We saw an example of this type of waveform earlier in Section 2.2.5, figure 2.5. When the peak flux density of the waveform

is reduced, the hysteresis losses in the material are also lower as discussed in Section 2.2.5. No minor loops exist in the waveform and the hysteresis losses can be approximated by taking the equivalent sinusoidal hysteresis losses at the reduced peak flux density (for instance, as in equation 2.6). Also in equation 2.4, note that the eddy current losses due to a distorted waveform are approximately proportional to the eddy current losses for a sinusoidal waveform at the same peak flux density. Therefore, if the peak flux density of the waveform is lowered due to saturation harmonics, it is completely reasonable to encounter lower losses than obtained by considering the losses in the fundamental component only.

In some figures, the losses including the distortion harmonics are higher than the losses contained in the fundamental component alone. Examples of this are shown in figures 5.2, 5.9, 5.13, 5.21, and 5.27. When this is the case, the additional eddy current losses caused by the distortion harmonics (for instance, as given by the constant in equation 2.5), outweigh the reduction of the hysteresis losses due to the reduction of peak flux density.

Summary

We have compared rotational and alternating loss curves for a variety of materials. A comparative set of data using a single apparatus for all the materials was unavailable in the literature prior to this study. The method of superposition of alternating losses works best for materials in which the eddy current component of the losses form a large portion of the total losses. This occurs in low resistivity materials with the larger sheet thicknesses (for instance the three MLQ steels). For thinner materials with higher values of resistivity (for instance NO Steel D) the hysteresis losses form a larger portion of the total losses and the effects of rotational hysteresis become more pronounced. The method of superposition of alternating losses is least applicable to these types of materials.

Chapter 6

Description of Core Loss Analysis in Induction Motor Stators

6.0 Introduction

A general description of induction machines is provided to give a general understanding of their construction. Core loss calculations by conventional design equations are compared with the proposed analysis. The equations presented are slight variations of those presented in Alger's [179] classic reference on induction motors. The proposed analysis is based on a time-harmonic finite element (FE) analysis of the flux density in the stator core of the machine. This method is becoming increasingly popular as a design tool for induction motors. The time-harmonic formulation yields all the information required to account for the fundamental frequency rotational losses in the stator. A second method of analysis is based on a series of magnetostatic solutions. This method is computationally more expensive. Losses presented in Chapter 5 are easily coupled with the FE analysis, thereby avoiding the need for empirical formulas. FE solutions were obtained using a commercial FEA package (MagNet 2D version 5.1a from Infolytica Corporation).

6.1 General Description of Machines

A typical cross section of the type of machine under investigation is shown in figure 6.1. The rotor of the machine is made of ring punchings that are then shrink fitted onto the spider arms and shaft. The four, six, eight and ten pole machines are constructed in this manner. The two pole machine is slightly different. Rotor laminations are shrink fitted directly onto the shaft as shown in figure 6.2. All the machines have non-skewed rotor bars.

The stator is built up from 60°segmental punchings that are piled into the stator frame. At specific intervals a space block assembly is included. Space blocks are used to create radial cooling vents in the core of the machine. The radial cooling vents are shown in figure 6.3. A space block assembly is a stator segment with mild steel beams welded to it at certain intervals (figure 6.4). Table 6.1 summarizes some basic features of the machines. All the machines are designed to run from balanced, three phase, 60 Hz ac power supplies.

Table 6.1 - General Description of Induction Motors in Study

Machine	Voltage (kV)	Power Rating (kW)	Stator Slots	Rotor Slots	Rated Speed (rpm)
2 Pole	4.0	3728.5	54	46	3573.3
4 Pole	4.0	3728.5	84	68	1785.4
6 Pole	4.16	5965.6	90	104	1183.8
8 Pole	4.0	2610.0	120	142	890.4
10 Pole	6.6	4474.2	120	142	713.5

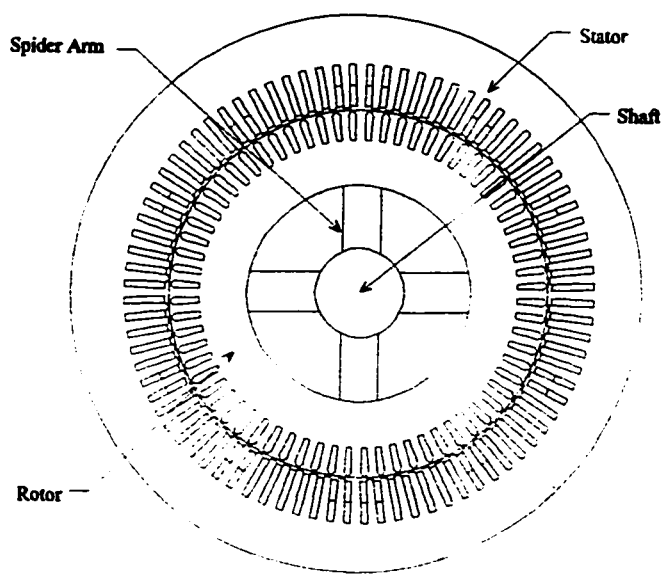

Figure 6.1 - General features of industrial induction motor with spider arm construction.

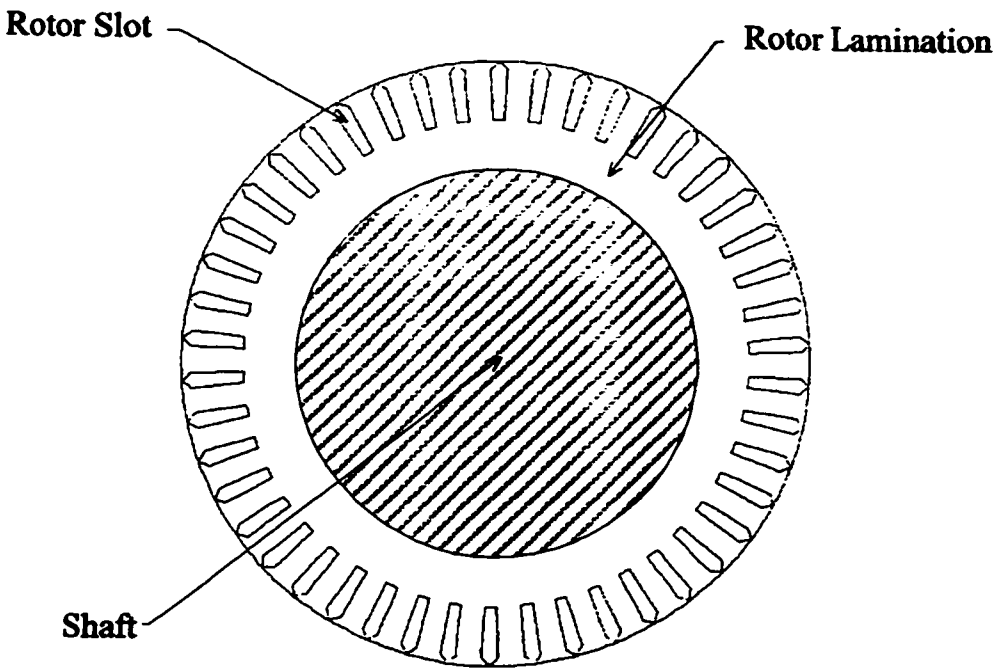

Figure 6.2 - Two pole rotor lamination shrink fitted onto shaft.

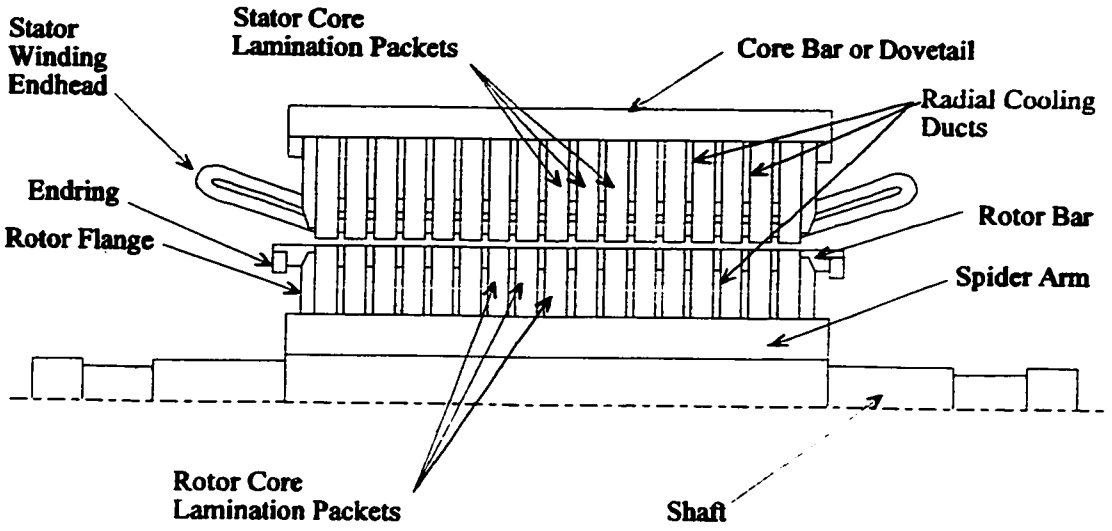

Figure 6.3 - Axial cross section through induction motor with radial ventilating ducts.

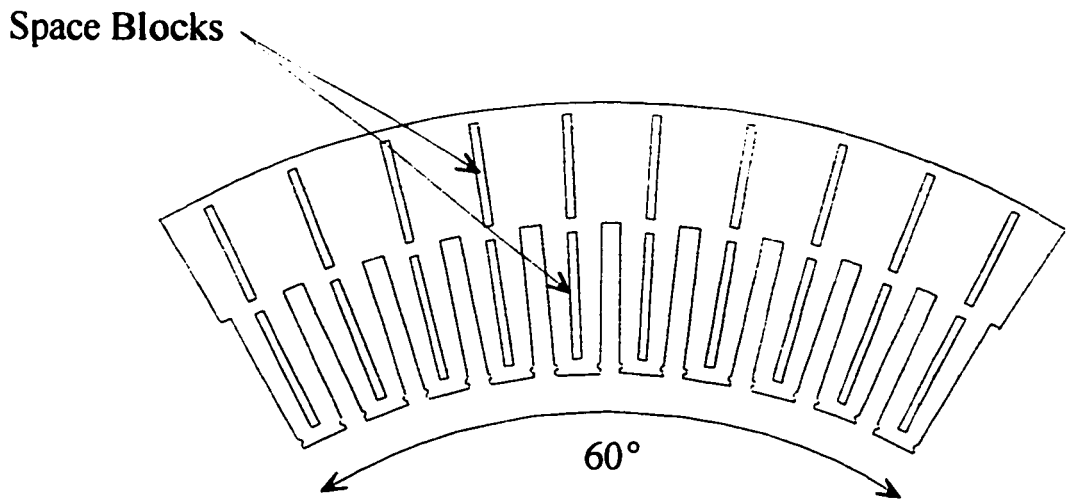

Figure 6.4 - Segmental punching and space block assembly.

6.2 Calculation of Core Loss by Design Equations for the Machines Under Study

The equations presented are modified versions of those described by Alger [179]. In order to begin the analysis, the flux density values in the core must be determined. This begins with a calculation of the flux per pole across the air gap of the machine.

6.2.1 Calculation of Air Gap Flux per Pole

The peak value of the flux per pole in the machines is calculated using Faraday's Law of induction:

$$V = -N\frac{d\phi}{dt} \tag{6.1}$$

Given a flux ϕ, that varies sinusoidally in time and links an N-turn coil at a frequency f:

$$\phi = \phi_p \sin 2\pi ft \qquad \text{Wb} \tag{6.2}$$

the rms value of the voltage induced in the coil is given by the equation:

$$V_{rms} = 2\pi f N \frac{\Phi_p}{\sqrt{2}} \qquad V \tag{6.3}$$

For a rotating electric machine, the rms value of the induced terminal voltage per phase is given by the equation:

$$V_{rms} = 2\pi f K_p K_d N_c \frac{\Phi_p}{\sqrt{2}} \qquad V \tag{6.4}$$

where,

Nc is the number of conductor turns in series per phase.
K_p is the winding pitch factor.
K_d is the winding distribution factor.
f is the stator frequency in (Hz).
Φ_p is the peak value of the air gap flux per pole (Wb).

By including the factors K_p and K_d in equation 6.4, we can replace a short pitched, distributed phase winding by an equivalent concentrated winding as depicted in figure 6.5. The two sides of this equivalent winding encompass the entire span of the pole. This allows the peak flux in the air gap to be calculated by analogy to the peak flux in the core of a single phase transformer. The magnitude of the flux is assumed to alternate through the pole and across the air gap, giving a flux that varies sinusoidally with time. Rearranging gives the expression for the peak value of the air gap flux per pole:

$$\Phi_p = \frac{\sqrt{2}V_{rms}}{2\pi f K_p K_d N_c} \qquad Wb \tag{6.5}$$

Note that the result of equation 6.5 gives no indication of the spatial distribution of the flux within the pole and ignores the effects of the stator teeth. It only gives the peak amount of flux linking a coil with the equivalent of $K_d K_p N_c$ turns.

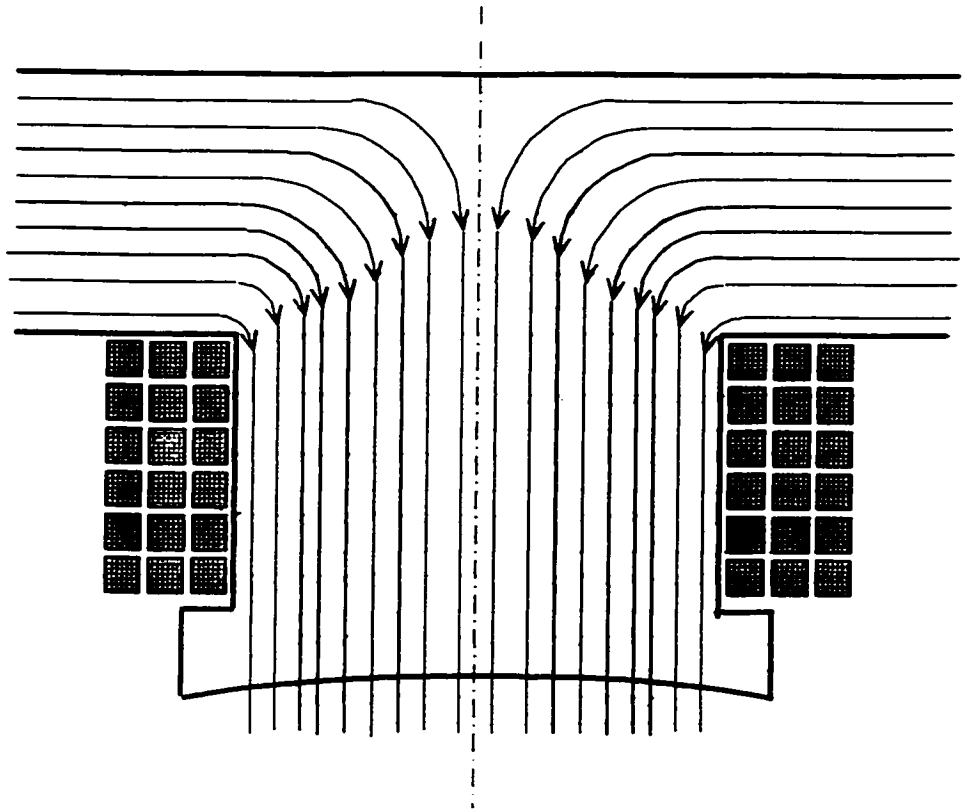

Figure 6.5 - Magnetic circuit used for calculation of air gap flux per pole.

6.2.2 Calculation of Flux Densities

6.2.2.1 Calculation of the Average Air Gap Flux Density

The average air gap flux density is given as:

$$B_{gap} = \frac{\Phi_p}{A_{gap}} \qquad T \tag{6.6}$$

The air gap sectional area per pole is approximated as:

$$A_{gap} = \left(\frac{\pi Bore}{S_1} - W_{slot} + gap \right) \times \left(L_{stack} - N_{ducts} \times W_{duct} \right) \times \frac{S_1}{poles} \tag{6.7}$$

where,

Bore is the inside punching diameter or bore of the stator (m).
S_1 is the number of stator slots.

W_{slot} is the width of the stator slot at top of the slot (closest to air gap) (m).
gap is the radial length of the air gap (m). This term increases the effective area to approximate the effects of fringing.
L_{stack} is the stack length of the machine (m).
N_{ducts} is the number of radial cooling ducts in the stack.
W_{ducts} is the width of the radial cooling ducts (m)
poles is the number of machine poles.

6.2.2.2 Peak Stator Yoke Flux Density

The peak stator yoke flux density is found from:

$$B_{yoke} = \frac{\Phi_p}{A_{yoke}} \quad T \tag{6.8}$$

where the cross sectional area of the stator yoke is given as:

$$A_{yoke} = (OD - Bore - 2\times DT)\times(L_{stack} - N_{ducts}\times W_{duct})\times SFS \tag{6.9}$$

where,

OD is the outside diameter of the stator (m)
DT is the depth of the stator slot (m), and
SFS is the stator stacking factor to account for lamination coating.

6.2.2.3 Average Stator Tooth Flux Density

The average flux density for the entire tooth is found from:

$$B_{tooth} = \frac{\Phi_p}{A_{tooth}} \quad T \tag{6.10}$$

where the average stator tooth sectional area per pole is taken as:

$$A_{tooth} = T_{avg}\times(L_{stack} - N_{ducts}\times W_{duct}) \times SFS\times\frac{S_1}{poles} \tag{6.11}$$

where the average stator tooth width is found from

$$T_{avg} = \frac{1}{3}W_{TY} + \frac{2}{3}W_{TB} \tag{6.12}$$

In equation 6.12,

W_{TY} is the width of the tooth at the yoke (m), and

W_{TB} is the width of the stator tooth at the bore (m).

The average flux density for the top half of the tooth is:

$$B_{tooth\ top} = \frac{\Phi_p}{A_{tooth\ top}} \quad T \tag{6.13}$$

where the average stator tooth sectional area per pole at the top half of the tooth is:

$$A_{tooth\ top} = \left(\frac{W_{TM} + W_{TB}}{2} \times\right)\left(L_{stack} - N_{ducts} \times W_{duct}\right) \times SFS \times \frac{S_1}{poles} \tag{6.14}$$

where W_{TM} is the stator tooth width at the middle of the tooth length (m).

The average flux density for the bottom half of the tooth is:

$$B_{tooth\ bottom} = \frac{\Phi_p}{A_{tooth\ bottom}} \quad T \tag{6.15}$$

where the average stator tooth sectional area per pole at the bottom half of the tooth is:

$$A_{tooth\ bottom} = \left(\frac{W_{TM} + W_{TY}}{2} \times\right)\left(L_{stack} - N_{ducts} \times W_{duct}\right) \times SFS \times \frac{S_1}{poles} \tag{6.16}$$

Examination of equations 6.8, 6.13 and 6.15 leads to the question of why the resulting flux density in the yoke is considered a peak quantity, while those in the teeth and air gap are considered average quantities; all three flux densities are calculated using the peak value of flux given by equation 6.5. Since a peak value of flux is used in the calculations, it would appear that the resulting flux densities should all be peak values. Equation 6.5 yields an estimate of the peak number of lines of flux (recall the obsolete unit "lines" of flux, where 1 Wb = 10^8 lines). It gives no information about the spatial distribution of the flux in the air gap; therefore, the lines of flux are assumed to be uniformly distributed in the teeth of the machine. To help explain this point, it is helpful to refer to figures 6.6 and 6.7. Both figures

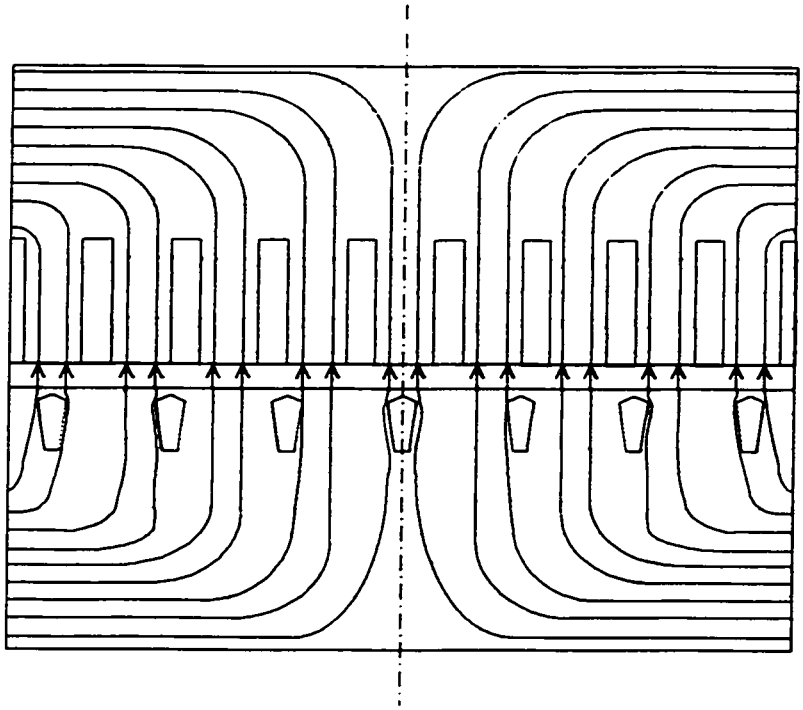

Figure 6.6 - Uniform distribution of flux density in the teeth of the machine.

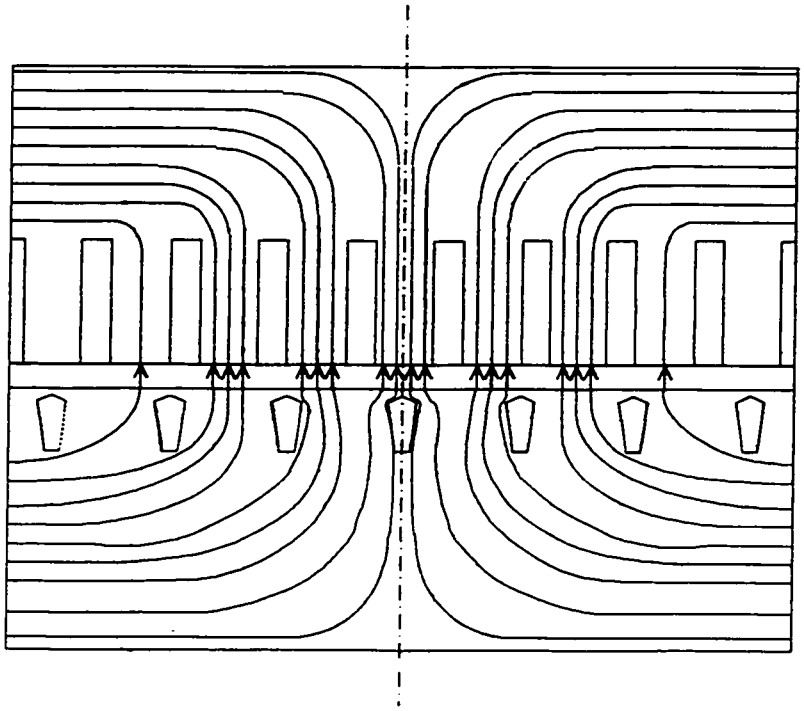

Figure 6.7 - Flux density in machine teeth approximately sinusoidally distributed.

show the same number of lines of flux per pole. In figure 6.6, the lines of flux are distributed uniformly; each tooth has the same flux density. The flux density in the air gap below each tooth is also the same. Figure 6.7 illustrates an approximately sinusoidal distribution of the flux lines in the air gap that is more typical of the situation in an induction motor. Note that in both figures, the peak flux density in the yoke of the machine occurs at the pole edges. It makes no difference whether the flux in the teeth is distributed uniformly or sinusoidally in the air gap because all the lines of flux must close through the yoke. This explains why we take the flux density given by equation 6.8 to be a peak value. Figure 6.6 illustrates the distribution of the lines of flux that corresponds to the peak flux calculated by equation 6.5 and the magnetic circuit of figure 6.5. This distribution is used to find the tooth and air gap flux densities. Since the lines of flux are divided uniformly in the teeth of the machine the flux densities in the teeth given by equations 6.13 and 6.15 are considered average flux density values. The flux density in the air gap of the machine given by equation 6.6 is also an average value. It represents the flux density in the air gap below each stator tooth. Iron losses can now be calculated using the values of flux densities.

6.2.3 Iron Losses

Yoke losses are approximated by:

$$P_{yoke} = K_{iron} \times (\text{yoke mass}) \times \left(\frac{B_{yoke}}{1.55} \right)^2 \quad \text{W} \tag{6.17}$$

where K_{iron} is a core loss coefficient in W/kg for the steel at 1.55 T while the yoke mass is given in kg. The motor manufacturer uses a coefficient of 6.36 W/kg for design calculations.

Tooth losses in the top and bottom portions of the teeth are approximated by:

$$P_{tooth\ top} = K_{iron} \times (\text{mass of tooth tops}) \times \left(\frac{\frac{\pi}{2} B_{tooth\ top}}{1.55} \right)^2 \quad \text{W} \tag{6.18}$$

$$P_{tooth\ bottom} = K_{iron} \times (\text{mass of tooth bottoms}) \times \left(\frac{\frac{\pi}{2} B_{tooth\ bottom}}{1.55} \right)^2 \quad W \qquad \textbf{(6.19)}$$

Note that in equations 6.17 to 6.19, the flux density is normalized to a value of 1.55 T. The manufacturer uses a loss coefficient of 6.36W/kg at 1.55 T. The losses in the machine are therefore assumed to vary with the square of the flux density. For instance, if the flux density is 1.7 T, the loss coefficient is multiplied by:

$$\left(\frac{1.7}{1.55} \right)^2 = 1.20 \qquad \textbf{(6.20)}$$

In equations 6.18 and 6.19, the flux density in the teeth is multiplied by $\pi/2$ as prescribed by Alger [179]. This converts the average value of flux density in the teeth to a peak value. The factor $\pi/2$ is used as an approximate method of accounting for the sinusoidal distribution of the flux in the air gap (illustrated in figure 6.7) that was ignored when calculating the air gap flux per pole using equation 6.5.

6.2.4 Tooth Pulsation and Surface Losses

Spooner's descriptions [180-183] of high frequency losses in induction motors serves as a good overview of the subject as does Walker's paper [184]. Spooner and Kinnard [181] define surface losses as "those hysteresis and eddy-current losses which occur just below the surface of a magnetized smooth-core laminated material which is adjacent to a slotted member having a relative motion with respect to the first member." Spooner and Kincaid [183] gave a series of empirically derived curves that could be used to estimate the surface losses in an induction motor.

Synchronous machine designers generally refer to these losses as pole face losses rather than surface losses, although both are caused by the slotting of the stator core. Pole face losses were studied early on by Adams et al [185] and Carter [186]. Pole face losses

have also been investigated by Gibbs [187], Bondi and Mukherji [188], Grieg and Freeman [189], Findlay and Briggs [190] and Karmaker [191] to name only a few.

Tooth pulsation losses are those losses caused by the high frequency pulsations of flux extending the whole length of the tooth and a little way into the core. They are caused by the rotational reluctance variations to the fundamental component of the air gap flux as the slots of one member pass the teeth of the other. Skewed rotors may be used to control the effects of pulsation losses. None of the machines in this investigation has skewed rotors.

Surface losses occur on the rotor due to the stator flux variations and on the stator due to rotor flux variations. All the machines investigated in this study have closed rotor slots and therefore smooth rotor surfaces. If the rotor bridge is saturated, the permeability of the bridge is very low and the rotor magnetic circuit will behave not unlike a rotor with open slots. The bridge will become heavily saturated when the machine is operating at full load and rated rotor current. Consequently, pulsation losses contribute to the stray load loss to a much greater extent than the no-load core loss. Although not strictly correct, designers often assume that the contribution of tooth pulsation loss to the no load core loss can be ignored for machines with closed rotor slots. Furthermore, the surface losses on the stator side are assumed negligible compared to the surface losses on the rotor when dealing with induction machines with closed rotor slots. As evidence of the validity of this assumption, the reader is referred to the work of Gyselinck et al [192]. The authors used a 2D time-stepping FEM with full rotor motion to analyse the no-load flux density distribution in a three phase, 3 kW, 4 pole induction motor. They modelled the machine with both open and closed rotor slots. A flux density plot in figure 4 of that reference clearly shows that the rotor permeance harmonics are only appreciable for the machine with the open rotor slots. In the machine with the closed rotor slots, the flux density variations in the stator tooth is virtually sinusoidal. In section 3.5 we also saw that Jamil et al [164] reported very small flux density pulsations in the stator tooth of an induction motor that was modelled using time-stepping

with full rotor motion.

Stator slot permeance harmonics can cause additional losses by inducing harmonic currents in the rotor bars. The phenomenon is described by Alger [179][193]. For machines with open rotor slots, these additional rotor losses will manifest themselves under no-load conditions. For machines with closed rotor slots, the losses at no-load are less apparent. Alger [179] explains that, "...if the rotor slots are closed, with a bridge sufficiently deep to carry one-half the flux per pole of the permeance ripple without saturation ...the induced rotor currents will be very small. In this way, the no-load stray loss may be held to a low value...However, when the load comes on, the rotor slot bridges will become magnetically saturated, and the effective reactance for the harmonics will be reduced, so that the full amount of the permeance wave loss, W_p, will appear." Based on Alger's argument, we can expect that harmonic rotor bar losses will be small at the no-load condition for the machines in this study.

The surface losses on an induction motor rotor are dependant on the average air gap flux density, the slot passing frequency, the slot width of the stator slots, and the length of the air gap. Other factors affecting the surface losses are the resistivity of the rotor laminations, the lamination thickness, rotor slot pitch, peak flux density, stacking factor and the permeability of the material at harmonic frequencies. Surface loss calculations are described by Alger et al [194] and also in an internal report by Wray [195].

The slot passing frequency is given by:

$$f_{slot} = \frac{2fS_1}{poles} \quad \text{Hz} \tag{6.21}$$

Wray's formula [195] for estimating surface losses is given by

$$P_{surface} = 0.785 \times D_{gap} \times L_{stack} K_{pf} \left(\frac{\frac{\pi}{2} B_{gap}}{1.55} \right)^2 C_{s2} \lambda_1 \quad \text{W} \tag{6.22}$$

where,

D_{gap} is the air gap diameter (m),
K_{pf} is a pole face loss coefficient as a function of slot width divided by air gap length, given in figure 3 on page 351 of the classic paper on stray load losses by Alger, Angst and Davies [194].
C_{s2} is the rotor iron loss coefficient at 1.55 T in W/m^3 , for slot passing frequency. The coefficient is given in W/inch^3 by the curve in figure 4 on page 351. The curve is derived from Birnstingl's internal report [196], that is referenced simply as an acknowledgement of his original work.
λ_1 is the stator slot pitch (m).

The factor $\pi/2$ is introduced to convert the average air gap flux density into a peak value. Equation 6.22 is entirely equivalent to equation (2) given by Alger et al [194] with the exception that the term $\left(\frac{\pi}{2}\right)^2$ is moved to the front of the equation. When multiplied with the empirical factor 0.785 this results in a value of 1.94. Alger takes this value and rounds it up to 2. Wray's formula is referenced as an acknowledgement of his original work. The factor 0.785 (or 2 in the case of the equation given by Alger) is empirical as explained by Alger in [194]. He states that the equation, "is to some extent empirical, but it is dimensionally correct, and it is based on a long record of earlier investigations".

The surface loss estimates presented in table 6.2, were provided courtesy of the machine manufacturer. These estimates are based on a formulation that is very similar to equation 6.22, with some minor modifications based on design experience. Yoke and tooth loss estimates are found from equations 6.17, 6.18 and 6.19. Total tested losses (by the method described in Section 6.3) are also included. For the six pole machine entry, the tested loss is the average from two duplicate machines. One machine tested with 22.08 kW and the second with 21.07 kW. The variation between the two results is due to variations in the manufacturing process and test procedures.

Some interesting observations can be made when examining table 6.2. Note that for some machines, the total calculated loss is much closer to the tested value than for others.

Table 6.2 - Summary of Flux Densities, Calculated Component Losses by Design Equations, and Tested Core Loss Values for Five Induction Machines Under Study

Motor (by # of Poles)	Yoke (eq. 6.6 & 6.15)		Tooth Top (eq. 6.6 & 6.15)		Tooth Bottom (eq. 6.6 & 6.15)		Surface Losses (eq. 6.20) (kW)	Total Calc. (kW)	Total Tested (Section 6.3) (kW)
	B (T)	Loss (kW)	B (T)	Loss (kW)	B (T)	Loss (kW)			
Two	1.69	16.92	1.02	2.58	0.71	1.81	3.86	25.17	32.4
Four	1.71	9.88	1.00	1.75	0.83	1.45	3.15	16.23	22.1
Six	1.38	12.20	1.04	3.27	0.90	2.83	12.29	30.60	21.58
Eight	1.55	6.59	0.97	1.92	0.84	1.67	5.34	15.53	13.63
Ten	1.42	12.62	1.02	5.47	0.90	4.82	7.91	30.83	23.5

For the eight pole machine a test to calculated (T/C) ratio of 13.63/15.53 or approximately 0.88 is found. One might conclude that this is a reasonable value for engineering purposes. The ratio is reasonably close to one and the error is on the conservative side. For the six pole machine the T/C ratio is 21.58/30.60 or 0.71 and for the ten pole machine we have 23.5/30.83 or 0.76. If we were to look at these two machines in isolation from the others, we might conclude that the manufacturer's equations are too conservative. Now look at the results for the two and four pole machines. The T/C ratios are 32.4/25.17 or 1.29 and 22.1/16.23 or 1.36 respectively. Looking at these two machines in isolation from the others, one might conclude that the manufacturer's equations underestimate the losses. The observation drawn from this exercise is that when trying to devise a method of predicting core losses, researchers should be aware that several machines should be analysed with any new proposed method. A methodology that may work for a particular machine may yield totally inadequate results for other machines. It is for this reason, that in the present study, all five machines have been

Table 6.3 - Total Calculated Fundamental Frequency Losses as a Percentage of Calculated Total and Total Tested Core Loss Values

Motor	Total Calculated Fundamental Frequency Yoke and Tooth Losses (kW)	As a % of Total Calculated Losses	As a % of Total Tested Losses
2 Pole	21.31	84.7	65.8
4 Pole	13.08	80.6	59.2
6 Pole	18.30	59.8	84.8
8 Pole	10.18	66.4	74.7
10 Pole	22.91	74.3	97.5

analysed.

In table 6.3, the calculated values of the fundamental frequency losses (by the manufacturer's method) are tabulated as a percentage of the total calculated losses (by the manufacturer's method) and as a percentage of the total tested losses. Based on the manufacturer values, one would expect that the fundamental frequency loss in each machine would comprise a major portion of the total loss.

6.3 Core Loss and Friction and Windage Loss Testing (No-Load Test)

The total tested no-load core losses in table 6.2 were determined by the method described in IEEE Std. 112 [197]. Measurement instruments have a full scale error no greater than ±0.5%. Initially, the stator winding resistance of the machine is measured. The machine is operated at full speed, no-load conditions. Line currents are measured, and the average value is taken as the no-load current. At the same time, the total input power to the machine is measured. If the stator I^2R losses (at the temperature of the test) are subtracted from the total input power, the remaining power is attributable to the friction, windage, and core

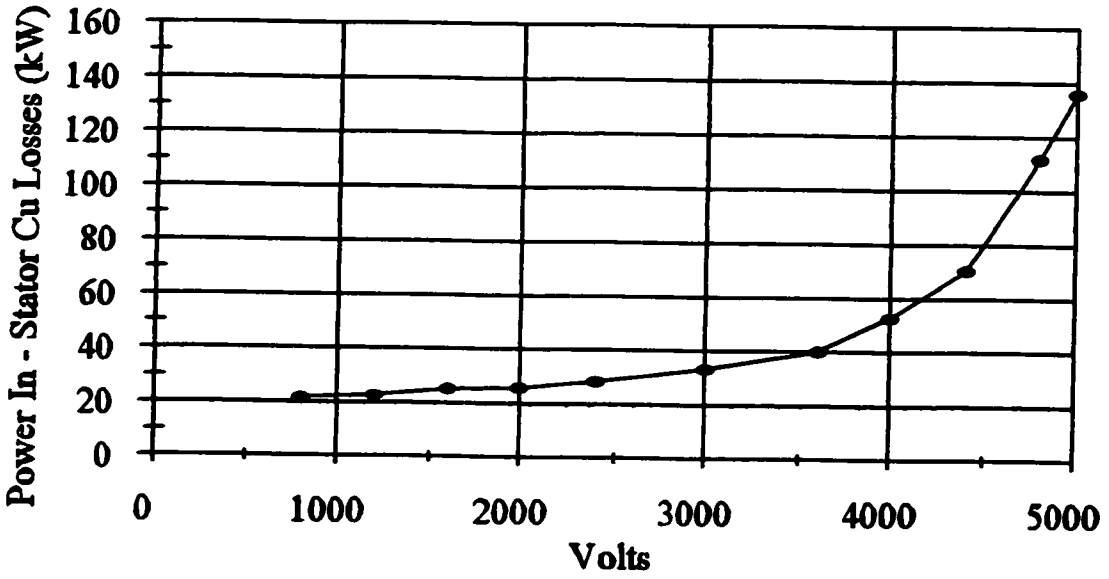

Figure 6.8 - Two pole machine. No-load power minus stator copper loss vs. voltage.

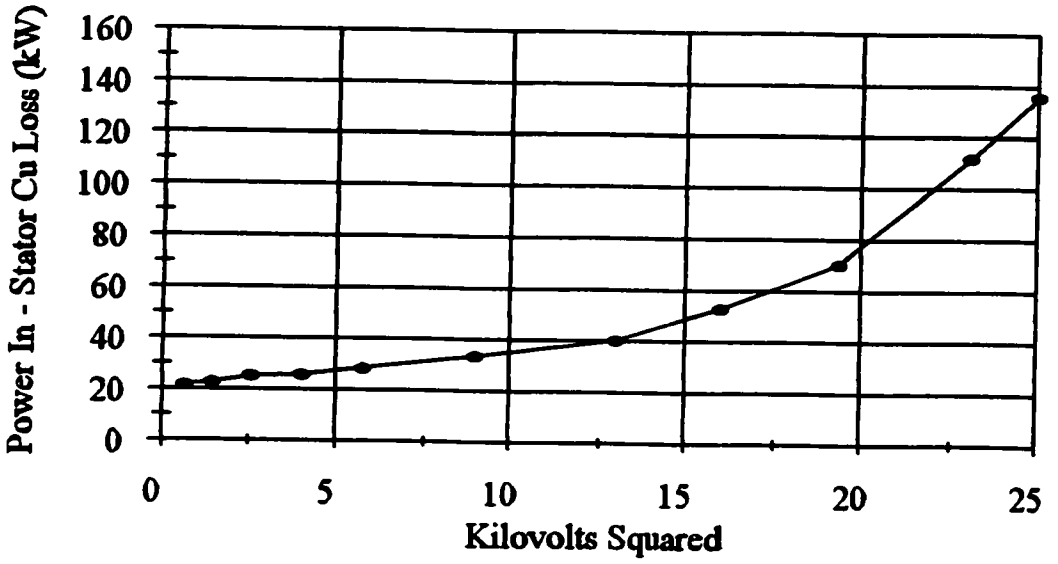

Figure 6.9 - Two pole machine. No-load power minus stator copper loss vs. voltage squared.

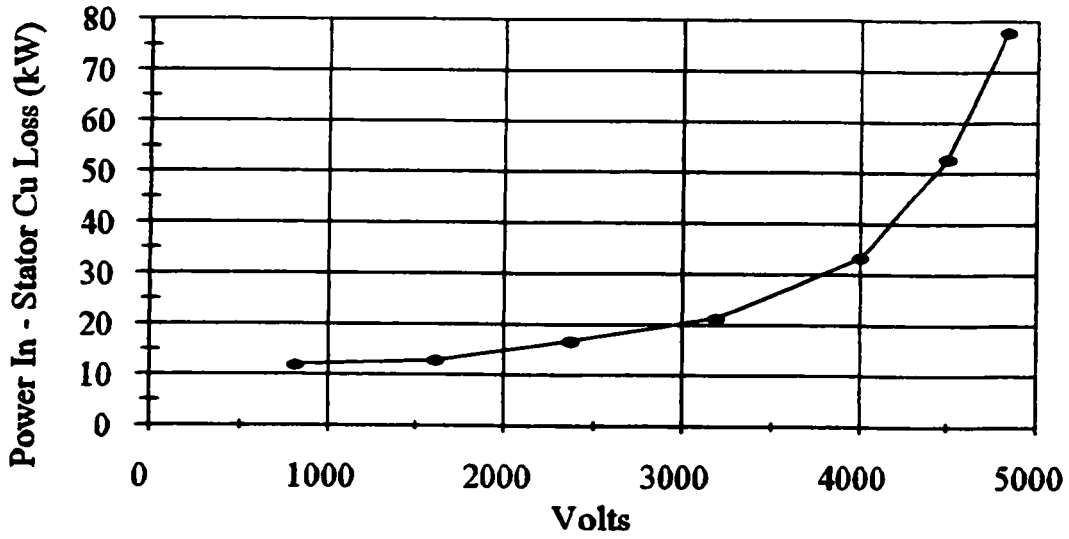

Figure 6.10 - Four pole machine. No-load power minus stator copper loss vs. voltage.

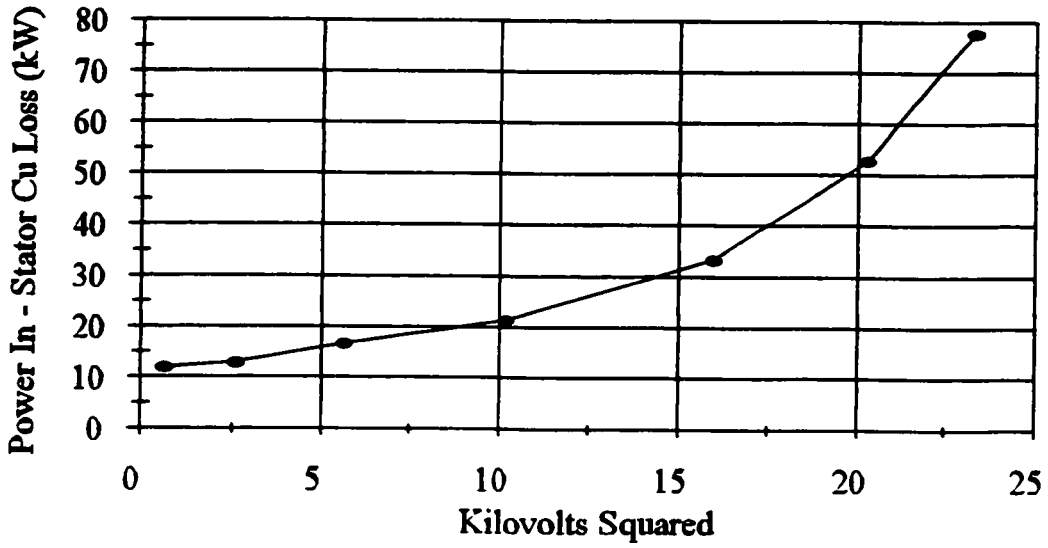

Figure 6.11 - Four pole machine. No-load power minus stator copper loss vs. voltage squared.

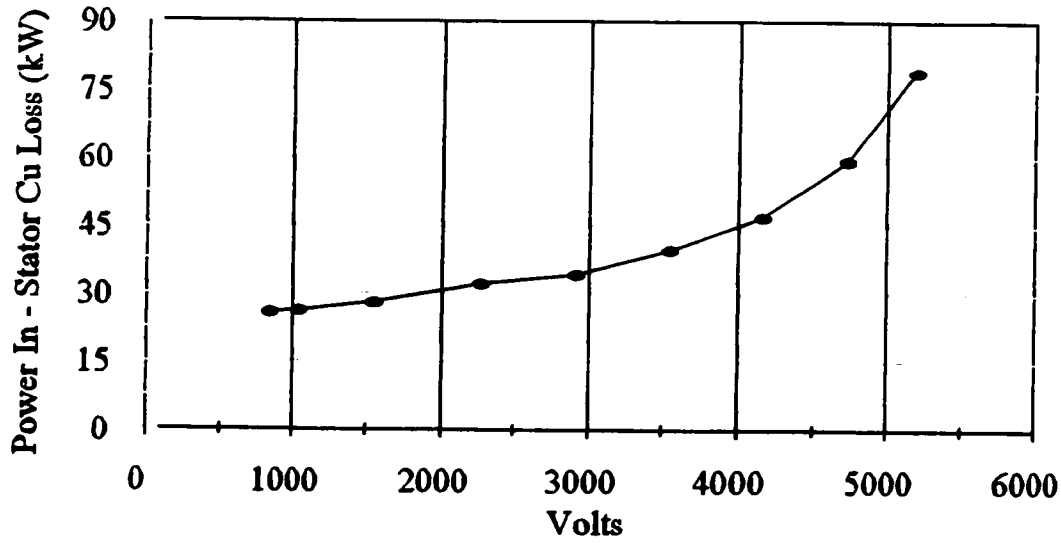

Figure 6.12 - Six pole machine #1. No-load power minus stator copper vs. voltage.

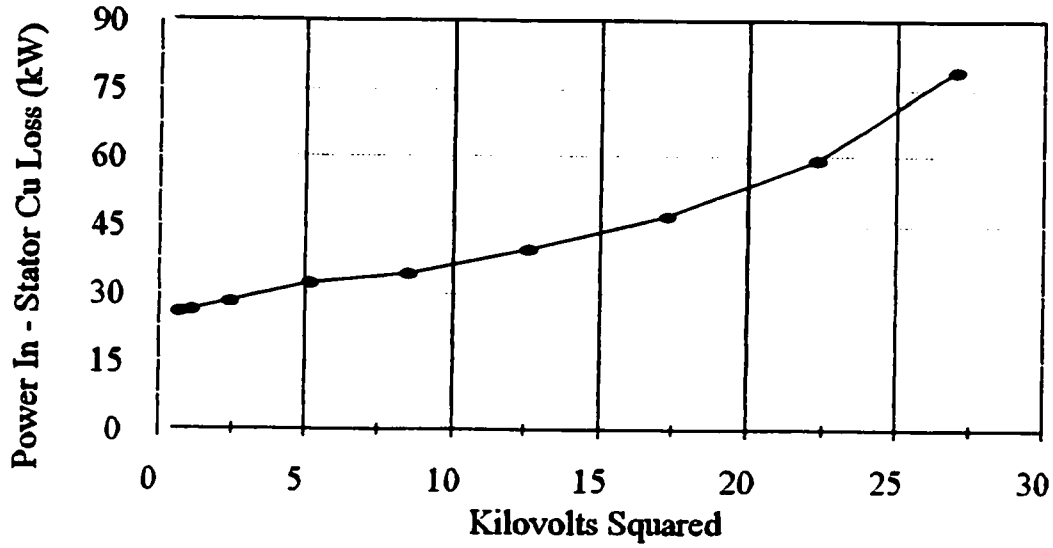

Figure 6.13 - Six pole machine #1. No-load power minus stator copper loss vs. voltage squared.

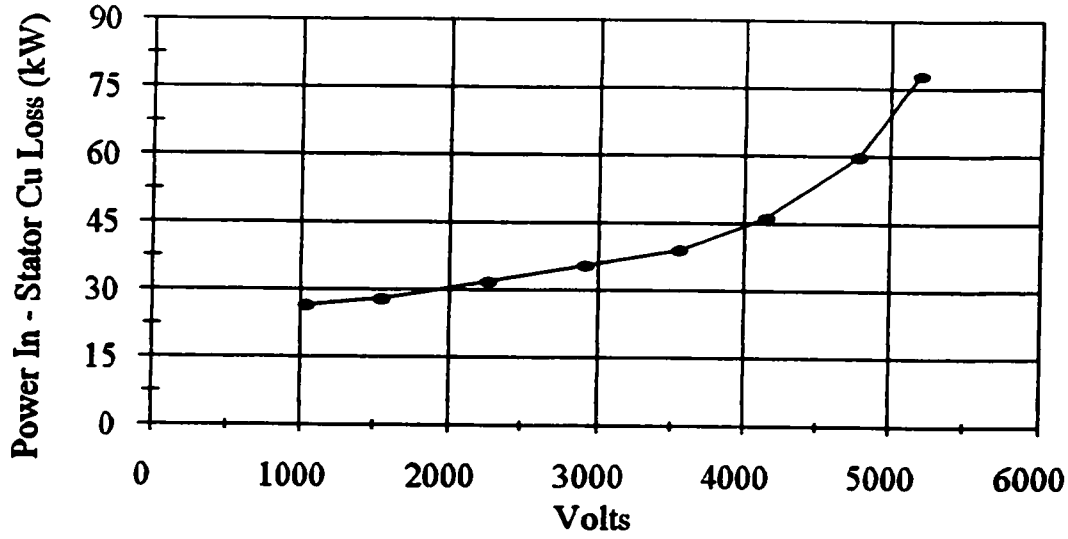

Figure 6.14 - Six pole machine #2. No-load power minus stator copper loss vs. voltage.

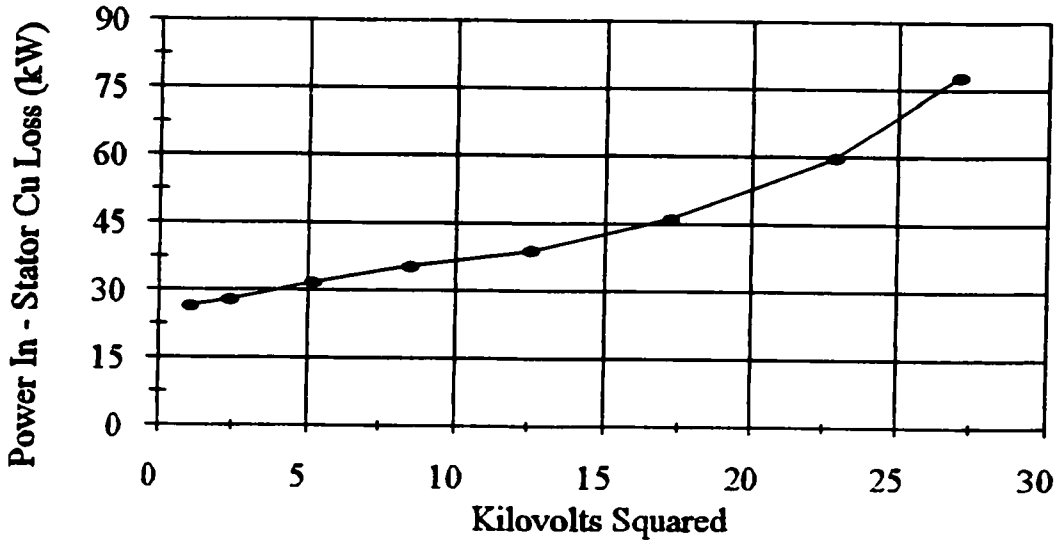

Figure 6.15 - Six pole machine #2. No-load power minus stator copper loss vs. voltage squared.

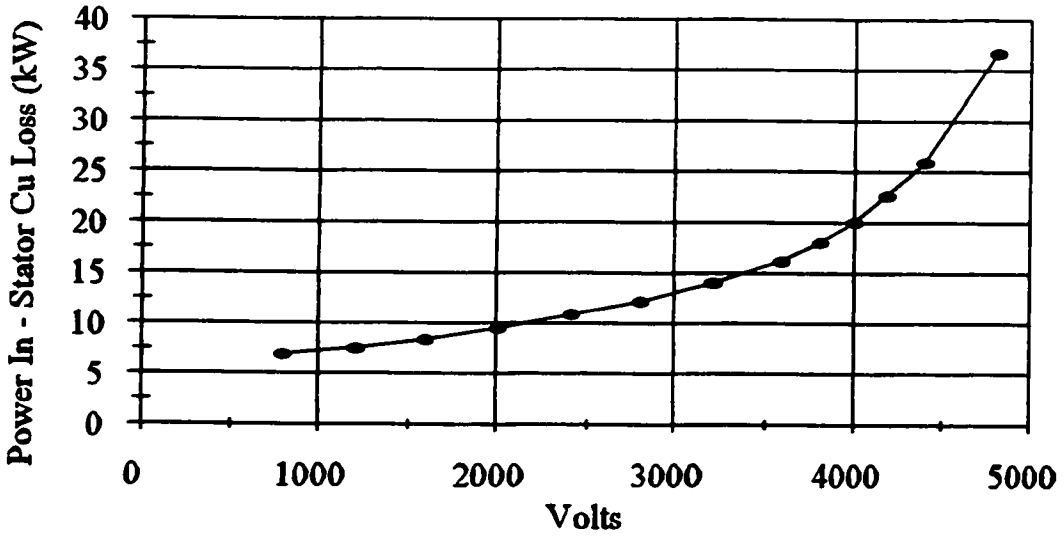

Figure 6.16 - Eight pole machine. No-load power minus stator copper loss vs. voltage.

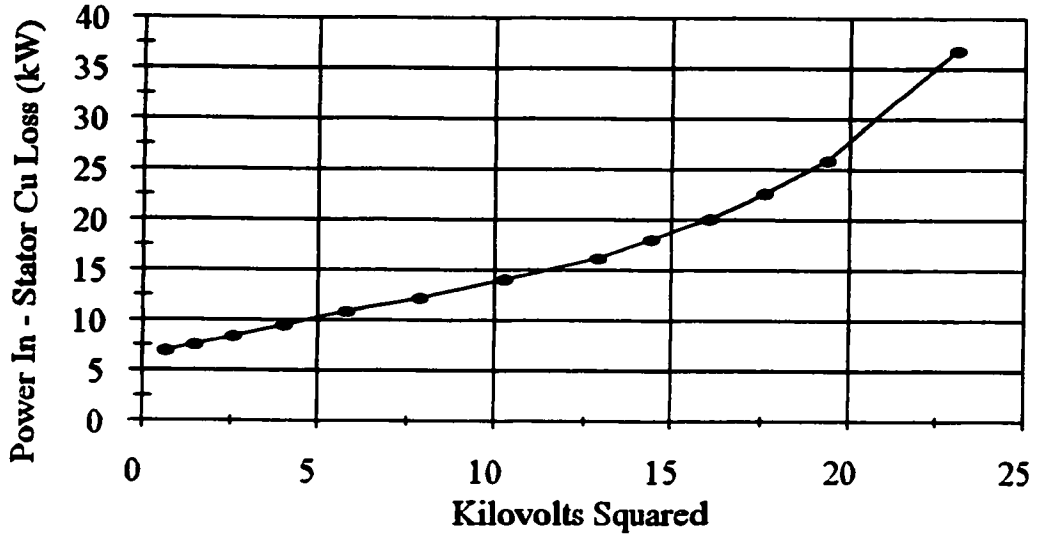

Figure 6.17 - Eight pole machine. No-load power minus stator copper loss vs. voltage squared.

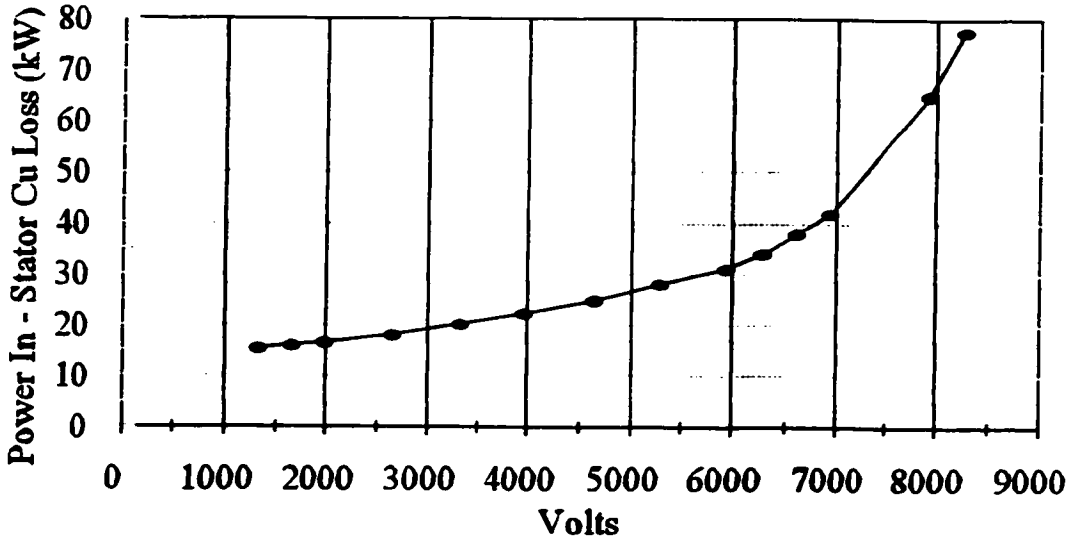

Figure 6.18 - Ten pole machine. No-load power minus stator copper loss vs. voltage.

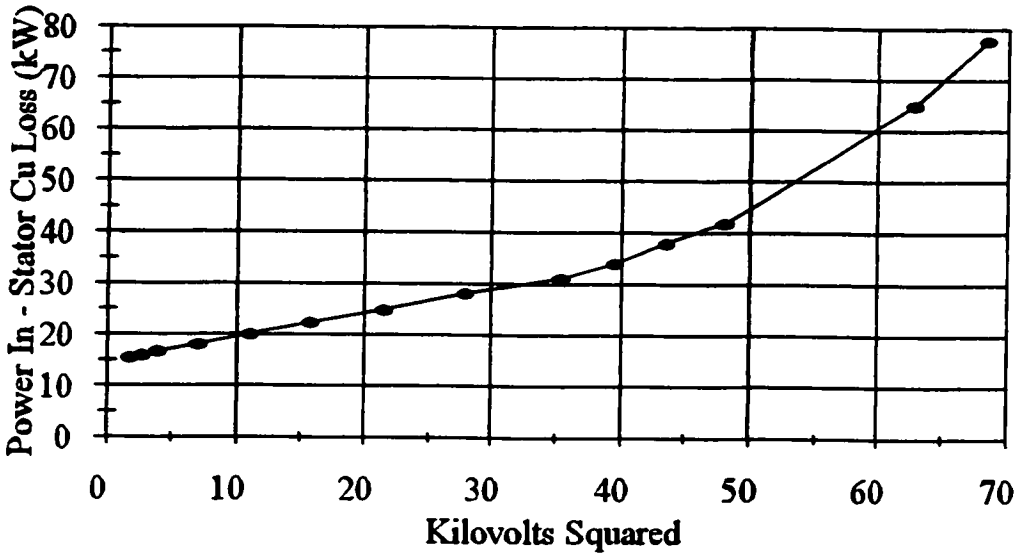

Figure 6.19 - Ten pole machine. No-load power minus stator copper loss vs. voltage squared.

Table 6.4 - Summary of No-Load Loss Measurements at Rated Voltage and Frequency

Machine	No-Load Stator Copper Loss (kW)	No-Load Core Loss (kW)	Friction and Windage Loss (kW)	Total No-Load Loss (kW)
Two Pole	1.46	32.4	20.35	54.2
Four Pole	1.59	22.1	11.4	35.1
Six Pole #1	1.02	22.08	24.9	48.0
Six Pole #2	0.98	21.07	25.25	47.3
Eight Pole	1.39	13.63	6.47	21.5
Ten Pole	2.56	23.5	14.5	40.6

losses. Measurements of voltage, current and input power at rated frequency are repeated at voltages ranging from approximately 125% of rated voltage down to the point where further voltage reduction increases the current. Power input minus the stator I^2R loss is plotted vs. voltage. The curves in figures 6.8, 6.10, 6.12, 6.14, 6.16 and 6.18 are those taken for the machines investigated during the course of this work. If each curve is extrapolated to zero volts, the intercept of the curve with the wattage axis gives the friction and windage loss. To aid in the determination of the intercept, the input power minus stator I^2R loss may be plotted against the voltage squared. This will result in a fairly linear plot if the values in the lower voltage range are used. For the machines under investigation, the curves plotted against the voltage squared are shown in figures 6.9, 6.11, 6.13, 6.15, 6.17 and 6.19. The friction and windage loss and the stator no-load I^2R loss, adjusted to the temperature during test, is then subtracted from the total power inputted to the machine at rated voltage. This result is taken as the no-load core loss of the machine. Note that by this method, the assumption is made that the rotor I^2R losses are negligible at no-load. Therefore, the measurement of no-load core loss includes rotor I^2R losses, no matter how large they may be. Table 6.4 summarizes the no-load loss tests for the machine under investigation. The results

are presented to the precision supplied by the manufacturer of the machine. Some values are quoted to two decimal places while others are quoted only to one.

6.4 Finite Element Analysis

Those readers who are unfamiliar with the finite element method (FEM) are referred to a brief overview of the topic in Appendix B. The stator flux distributions for no-load conditions were modelled using two variations of the FEM. The first method used a series of time stepped magnetostatic (TSM) solutions. Flux density polarization was ascertained by plotting the loci of the fundamental components of B_x vs. B_y obtained from the set of magnetostatic solutions. This is similar to the approach used by Shirkoohi [198] and was used as a basis of comparison for the second method.

The flux density polarization was also modelled using a time-harmonic (TH) formulation. The TH formulation yields a solution for the fundamental flux density only. It is very commonly used for analysing induction motor problems [199-207]. The main advantage that the TH FEM offers over the TSM FEM is speed. It offers the design engineer, working in an industrial setting, the capability of iteratively applying the FEM during the design process. A designer can run a TH analysis, study the results, and then change the design to improve it. This can be done repeatedly, until a final design is arrived at. With the TSM (particularly if rotor motion and induced rotor currents are included in the analysis), solution times quickly escalate and it becomes impractical to apply the analysis in a design office environment. Time stepped solutions give the harmonic content of the flux density, but take much longer to solve. Use of the time-harmonic method for predicting rotational flux density distributions in induction motor cores was initially explored in [208-210].

The following assumptions were made for both methods:

1. The rotor currents are not modelled by FEM. In the no-load situation the motor only has to deliver enough torque to overcome the friction and windage losses of the machine. If

these losses are ignored, the machine can be assumed to operate at synchronous speed. Under these conditions, no rotor currents are induced in the rotor bars. This assumption has been used by Belmans et al [205]. The no-load slip for large induction motors is very small (for the machines under investigation it is less than 0.01%) and the reaction field generated by the rotor currents is very small. This assumption may not apply to small motors (<5 hp) which often have larger slip values at no load.

2. The rotor motion is not modelled (MagNet 2D has no provision for such analysis) and therefore the effects of rotor permeance variations are ignored. The machines under investigation have closed rotor slots, so the effect of rotor permeance variations is less important than in machines with open rotor slots. The rotor is treated as a stationary object to serve as a flux closure path. The rotor slots are modelled, however, to give a more realistic representation of the rotor reluctance path.

6.5 Time-Stepped Magnetostatic (TSM) Simulation

The 2D magnetostatic formulation of the FEM using a Newton iteration yields a solution to the nonlinear partial differential equation

$$\frac{\partial}{\partial x}\left(\nu\frac{\partial A_z}{\partial x}\right) + \frac{\partial}{\partial y}\left(\nu\frac{\partial A_z}{\partial y}\right) = -J_z \qquad \textbf{(6.23)}$$

where,

ν is the field dependent reluctivity (m/H),
A_z is the z directed component of the magnetic vector potential (Wb/m), and
J_z is the z directed component of the current density (A/m^2).

The flux density is found from:

$$\nabla x\overline{A} = \overline{B} \qquad \textbf{(6.24)}$$

Taking the curl of the vector potential reduces the order of the flux density solution. A first order triangular mesh results in a first order approximation to the vector potential but a constant value for the flux density in each element.

The boundary conditions used for the FE simulations are illustrated in figures 6.22, 6.28, 6.34, 6.40 and 6.46. The outer edges of the stators and the inner edges of the rotors are constrained by a unary condition (a Dirichlet or constant flux constraint). A binary constraint is imposed on the left and right edges of the machines. This constraint forces the vector potentials on one side of a pole span to equal the negative of the values on the opposite side. In other words, the amount of flux entering one pole edge must equal the amount of flux leaving the opposite pole edge.

The two pole machine differs from the slower speed machines in that the rotor laminations are shrink-fitted around the shaft of the machine. Because of this, the shaft becomes an integral part of the magnetic structure of the machine rotor. The four, six, eight and ten pole machines have shaft spider constructions (a shaft with radial "spider" arms extending to the inside diameter of the rotor punching). We assume further that the flux in the rotor is confined to the laminations.

A series of solutions for each machine were obtained by time stepping the stator currents in increments of 10° electrical. No-load values of current were available from test results and were used in this study. The value of current assigned to each coil was found from:

$$I_{coil} = \sqrt{2} \times \frac{I_{NL}}{\text{number of circuits}} \times \text{turns per coil} \qquad \textbf{(6.25)}$$

where I_{NL} is the rms no-load or running light current obtained by test. Table 6.5 summarizes the values of currents used in this study.

At the design stage, a method will be required to predict the no load current drawn

Table 6.5 - No-Load Currents and Coil Currents for Machines Used in Study

Machine	No-Load Current (rms A)	Circuits	Turns/Coil	Coil Current (peak A)	Winding Pattern Figure #
Two Pole	174.8	2	4	494.4	6.22
Four Pole	147.2	4	6	312.26	6.34
Six Pole	176.7	6	9	374.84	6.43
Eight Pole	102.2	4	7	252.9	6.52
Ten Pole	150.2	5	10	424.8	6.61

by the machine accurately. The input current waveforms were modelled as sinusoids with only the first half of the waveforms used (the second half of the solution was obtained by symmetry). This required a total of 18 magnetostatic solutions for each machine.

Winding patterns for each machine are also shown in figures indicated in table 6.5. Note that the two pole machine has an "interspersed" winding, described by Chalmers [211]. Interspersed windings help control air gap harmonics that arise as consequence of short coil pitches. The short pitch coils are required to ease the winding of two pole machines.

6.6 Time-Harmonic (TH) Formulation

The same discretization used for time stepped magnetostatic simulations was also used for the time-harmonic case. A magnetic vector potential varying sinusoidally with time is assumed. Root mean square (rms) values are used for the time harmonic formulation. This yields rms values of flux densities which must be multiplied by the square root of 2 in order to yield peak values. First order elements were used. The time harmonic FEM yields a solution to the equation

$$\nabla^2 \hat{A}_z - j\mu\omega\sigma\hat{A}_z = -\mu\hat{J}_z \qquad \textbf{(6.26)}$$

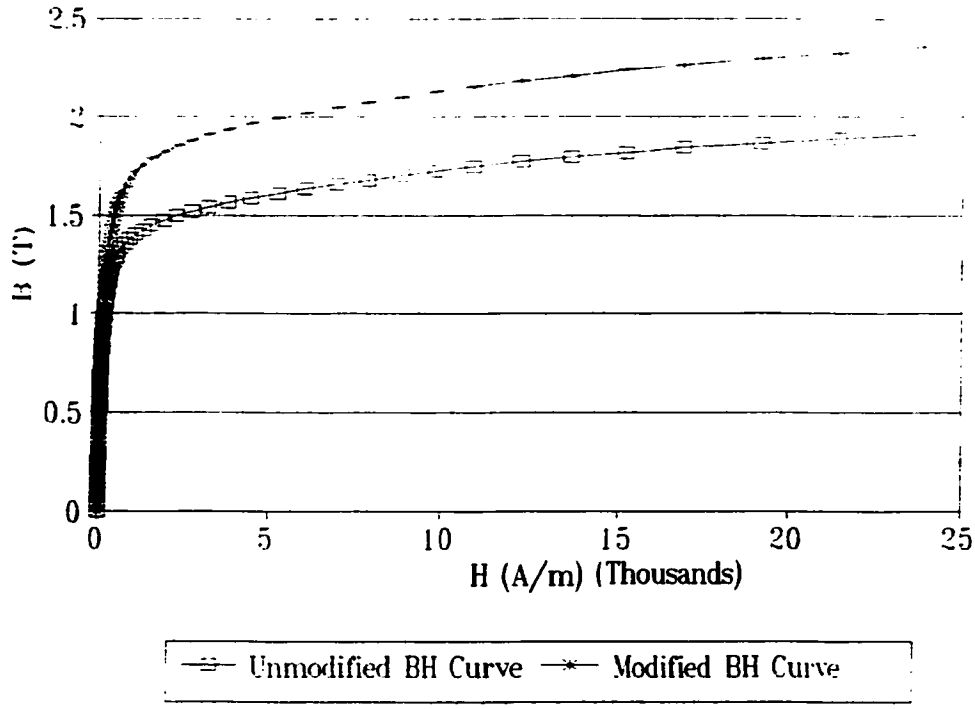

Figure 6.20 - Normal magnetization curve and effective BH curve for electrical steel used in this investigation.

where,

$\hat{A}_z$ is the z directed component of the magnetic vector potential expressed in complex phasor notation, i.e. $Re[A_z e^{j\omega t - \theta}]$ (Wb/m).
$\hat{J}_z$ is the z directed component of the source current density expressed in complex phasor notation, i.e. $Re[J_z e^{j\omega t - \theta}]$ (A/m^2)
ω is the angular frequency (rad/s)
μ is the material permeability (H/m)
σ is the material conductivity (S).

The finite element formulation based on equation 6.26 is called time-harmonic because the currents and magnetic vector potentials are expressed in complex phasor notation. Magnet 2D allows the magnetic state of the core to be modelled. The permeability of each element is allowed to vary. Initially, two nonlinear magnetostatic problems are solved. One problem corresponds to the real component of the no load stator current and the second corresponds to the imaginary component. A reluctivity vector is extracted from each

magnetostatic solution. The two results are averaged, and a reluctivity value is assigned to each element.

6.6.1 Time-Harmonic Method With Effective Permeability

The B-H curves of magnetic materials are given by manufacturers for peak values of B and H (see for instance the unmodified curve in figure 6.20). These curves can be used directly when solving magnetostatic problems. In time-harmonic problems, the H waveform will be sinusoidal (for current driven problems). The corresponding B waveform will contain harmonics. Unfortunately, the time-harmonic finite element method cannot model these additional harmonics very easily. I have chosen to use the fundamental value of the flux density in each element to look up the corresponding loss on the loss curves. An effective B-H curve is required which will yield the fundamental value of the flux density for a given peak value of H. I have used sinusoidal H waveforms and the normal magnetization curve to derive corresponding nonsinusoidal B waveforms. A Fourier analysis of each of the resulting B waveforms is performed to get the fundamental flux density for each value of peak H. The plot of fundamental B vs. peak H yields the effective B vs. H curve. Modified and unmodified curves for the material used in this investigation are shown in figure 6.20.

One accepted method of deriving an effective B-H curve is based on energy considerations [206-207]. The method consists of finding an equivalent sinusoid B_e, which produces the same stored energy for one period as the exact nonsinusoidal B. According to Vassent et al [206-207], this is achieved by finding a value of B_e which satisfies the following expression:

$$\frac{1}{2}\int_0^{B_e} H_m dB_e = \frac{1}{T}\int_0^T\int_0^B HdBdt \qquad \textbf{(6.27)}$$

To build the equivalent B-H curve, a sinusoidal function of magnetic field strength is assumed

such that

$$H = H_m \sin(\omega t) \tag{6.28}$$

The electromagnetic energy for one value of H_m over one period of time T, is computed for several different values of H_m. This approach yields good results for integral quantities such as torque.

The fundamental component of the resulting flux density waveform was computed using Simpson's rule to numerically evaluate the Fourier integral

$$B_1 = \frac{1}{\pi}\int_0^{2\pi} B(t)\sin(t)dt \tag{6.29}$$

The flux density wave consists of 128 data panels (i.e. 129 data points). According to Lowther and Forghani of the Infolytica Corporation, the source currents must be input as rms values and the BH curve is provided as peak values of H and B[1]. The use of effective BH curves with the time-harmonic solver, is also discussed in [212]. The Fourier method yields the same result as the equivalent energy method discussed above. If we consider the energy over one period of time, it becomes apparent that all the energy is contained in the fundamental frequency component of the energy waveform. For a sinusoidal H, only the product of the fundamental H and B waveforms will yield an average value for the energy once an integration is performed over one period of time.

The nodal vector potentials resulting from equation 6.26 are complex numbers. Taking the curl of the real and imaginary components of the first order magnetic vector potential gives a zero order flux density solution. There is no spatial variation of the flux density in any individual element but the flux density can vary with time. If a point of interest

---

[1] Private Communication.

lies on the boundary of two elements the result on either side of that point will differ according to the flux density value for each element on either side of the element boundary.

The flux density polarization can be obtained by plotting the variation of the flux density according to

$$B_x(t) = Re[B_x]\cos(\omega t) + Im[B_x]\sin(\omega t)$$
$$B_y(t) = Re[B_y]\cos(\omega t) + Im[B_y]\sin(\omega t) \quad \textbf{(6.30)}$$

6.6.2 Determining Elliptical Loci from Time-Harmonic and Time-Stepped Magnetostatic Solutions

An expression for the instantaneous magnitude of an elliptical locus (see figure 6.21) is written as:

$$R(\omega t) = \sqrt{B_x^2(\omega t) + B_y^2(\omega t)} \quad \textbf{(6.31)}$$

This can be rewritten in the form:

$$R(\omega t) = \sqrt{\alpha\cos^2(\omega t) + 2\beta\sin(\omega t)\cos(\omega t) + \gamma\sin^2(\omega t)} \quad \textbf{(6.32)}$$

where,

$$\alpha = Re[B_x]^2 + Re[B_y]^2 \quad \textbf{(6.33)}$$

$$\beta = Re[B_x]Im[B_x] + Re[B_y]Im[B_y] \quad \textbf{(6.34)}$$

and,

$$\gamma = Im[B_x]^2 + Im[B_y]^2 \quad \textbf{(6.35)}$$

To find the maximum and minimum values of R (and therefore the magnitudes of the major

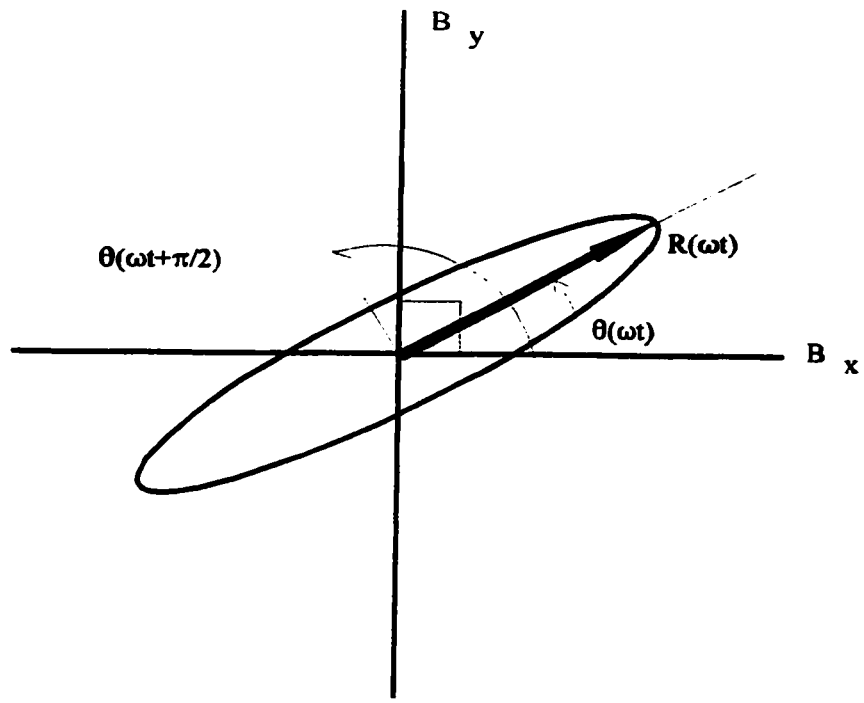

Figure 6.21 - Elliptical flux density loci.

and minor axes of the ellipse), the derivative of equation 6.32 with respect to ωt must be set to zero. It can easily be shown that the maximum or minimum occurs when:

$$\omega t = \frac{1}{2}\arctan\left(\frac{2\beta}{\alpha - \gamma}\right) \tag{6.36}$$

or,

$$\omega t = \frac{1}{2}\arctan\left(\frac{2\beta}{\alpha - \gamma}\right) + \frac{\pi}{2} \tag{6.37}$$

The angle of inclination for the ellipse is given by:

$$\theta(\omega t) = \arctan\left(\frac{B_y(\omega t)}{B_x(\omega t)}\right) \tag{6.38}$$

where ωt is chosen from equation 6.36 or 6.37 depending on which value gives the maximum for $R(\omega t)$.

The approach is similar if the data for the time-stepped magnetostatic solutions is used. First, a Fourier analysis is done on the data for the x and y components of the flux density. The fundamental component of B_x is decomposed into a cosine and sine function. The coefficient in front of the cosine is $Re[B_x(\omega t)]$ and the coefficient in front of the sine is $Re[B_x(\omega t)]$. The procedure is then repeated for the B_y waveform. For each element, the coefficients of the Fourier analysis yield an equation of the same form as 6.30.

6.7 Methods of Analysis

The iron losses due to the fundamental frequency variation of the flux density in the core were analysed in six different ways. From these results, the effects of various assumptions on the fundamental frequency losses in the yoke and teeth of the machine can be quantified. Calculations for each method are made from both the time-harmonic finite element analysis and the analysis using the time-stepped magnetostatic solutions. The first two methods take into account the losses due to rotational fluxes in the machine, while the others treat the losses as if the flux were purely alternating. The third method uses the 50:50 Epstein test results and uses the assumption that the flux in the yoke and teeth of the machine is purely alternating.

Recall that for the machines under investigation, the stator cores are constructed from segmental punchings. Due to this construction, the yokes of the machines are essentially oriented along the td of the electrical sheet. The stator teeth are oriented approximately along the rd of the electrical sheet. For machines constructed from 60° segments, these assumptions hold within a maximum error of ±30°. The fourth method attempts to quantify the effects of this construction with respect to the fundamental frequency iron losses in the machine.

The last two methods allow for the rotational losses in the stator in only an approximate way. Rotational losses are estimated from the alternating losses in the rd and td of the electrical sheets. The six methods are outlined further in the following sections.

6.7.1 Method I - Rotational Losses With Partial Correction for Anisotropy

Losses in the stator were calculated using the rotational loss curves in figures 5.35 and 5.36. The iron loss curves obtained using the 2D tester were analysed to result in a polynomial fit for each curve. Each curve was split into two sections such that the portion from 0 to 1.1T was represented by a third order least mean square fit polynomial and the section from 1.1T and higher was approximated by a second polynomial. Iron loss values were then assigned to each element according to the flux density levels and aspect ratios obtained using the time harmonic method. The expressions presented in equations 6.30 through 6.38 were used to determine the characteristics of the flux locus in each element. For aspect ratios falling between two measured curve values, a linear interpolation between the two curves of measured values was performed. In the case of the magnetostatic solutions the fundamental harmonic was obtained using Fourier analysis of the resulting waveforms. The loss was assigned on a per kg basis and the loss due to each element was integrated over the entire volume of the stator. To accomplish this, the area of each element was multiplied by the active stack length of the core (the actual length of the core minus the axial length occupied by the radial cooling ducts) and the density of the steel to approximate the mass. The results obtained by the time-harmonic method were compared with the results obtained using the fundamental harmonics from the magnetostatic solutions.

The major axis of each ellipse does not always lie on the tangential axis of the machine. An approximate correction for the anisotropy with respect to the td was made using the curves in figure 5.39 and the flux density in the major axis of the ellipse. The inclination angle from the ellipse with respect to the td is used to determine the correction factor. If the

flux density in the major axis of the ellipse had a value between the curves in figure 5.39, the correction factor was found by a linear interpolation between two curves. When the flux density in the major axis of the ellipse was greater than 1.5 T, then the curve for 1.5 T was used. When the flux density in the major axis was less than 0.9T, the curve for 0.9 T was used to correct for anisotropy (this situation does not typically occur at the working flux densities of the machines under investigation).

6.7.2 Method II - Rotational Losses With No Correction for Anisotropy

Losses in the stator yokes were calculated using the rotational loss curves in figures 5.35 and 5.36. No corrections were made for anisotropy. In order to apply the values in figures 5.35 and 5.36, the major axis of each ellipse was assumed to lie in the td and the minor axis of each ellipse was assumed to lie in the rd. Using this assumption, any losses calculated in the teeth would obviously be non-applicable (since the teeth tend to be oriented along the rolling direction of the sheet). The losses were calculated using time harmonic (TH) solutions and the fundamental components of the magnetostatic solutions as described in the preceding section.

6.7.3 Method III - Alternating Losses Using 50:50 Epstein Test Results

This method is what could be thought of as a traditional iron loss calculation using the FE method. Losses were calculated using the 50:50 Epstein test loss curves presented in figure 5.37 (average of the rd and td curves). No allowance was made for the rotational nature of the flux density and the rotational losses. The magnitude of the flux density in the major and minor axis was obtained from the expressions in equations 6.30 through 6.38. In each element, the flux density was modelled as purely alternating in nature. The expressions for B_{major} and B_{minor} were individually squared and summed. The magnitude of the flux density was then obtained by taking the square root of this sum on an element by element basis. The

magnitude of the flux density in each element was then used to attribute a loss value to each element that was then integrated over the volume of the machine.

6.7.4 Method IV - Yoke Losses Treated as Alternating in the TD and Tooth Losses Treated as Alternating in the RD

This is the traditional FE method similar to method III. Once again the flux density is assumed to alternate with time and the effects of the rotational flux is ignored. The flux density in each element was determined by the procedure outlined in the previous section. The td loss curve in figure 5.37 was used in the iron loss calculation in yokes of the machines. In the machine teeth, the rd loss curve was used in the iron loss calculation. This method gives some insight into the anisotropy effects caused by the construction of the machine from segmental stator punchings.

6.7.5 Method V -Rotational Losses Approximated Using the Superposition Principle and Epstein Results

In this method, the rotational losses were estimated as the sum of the losses in the td and rd of the sheet. In each element, the flux density was calculated according to equation 6.30 through 6.37 and the inclination angle is ignored. The major axis of each ellipse is assumed to be oriented along the td of the sheet. Epstein test results presented in figure 5.37 were used to calculate the losses.

6.7.6 Method VI -Rotational Losses Approximated Using the Superposition Principle and Results From Current Apparatus

This method is identical to the previous method except that the losses in the rd and td of the sheet were obtained from the PRL test apparatus.

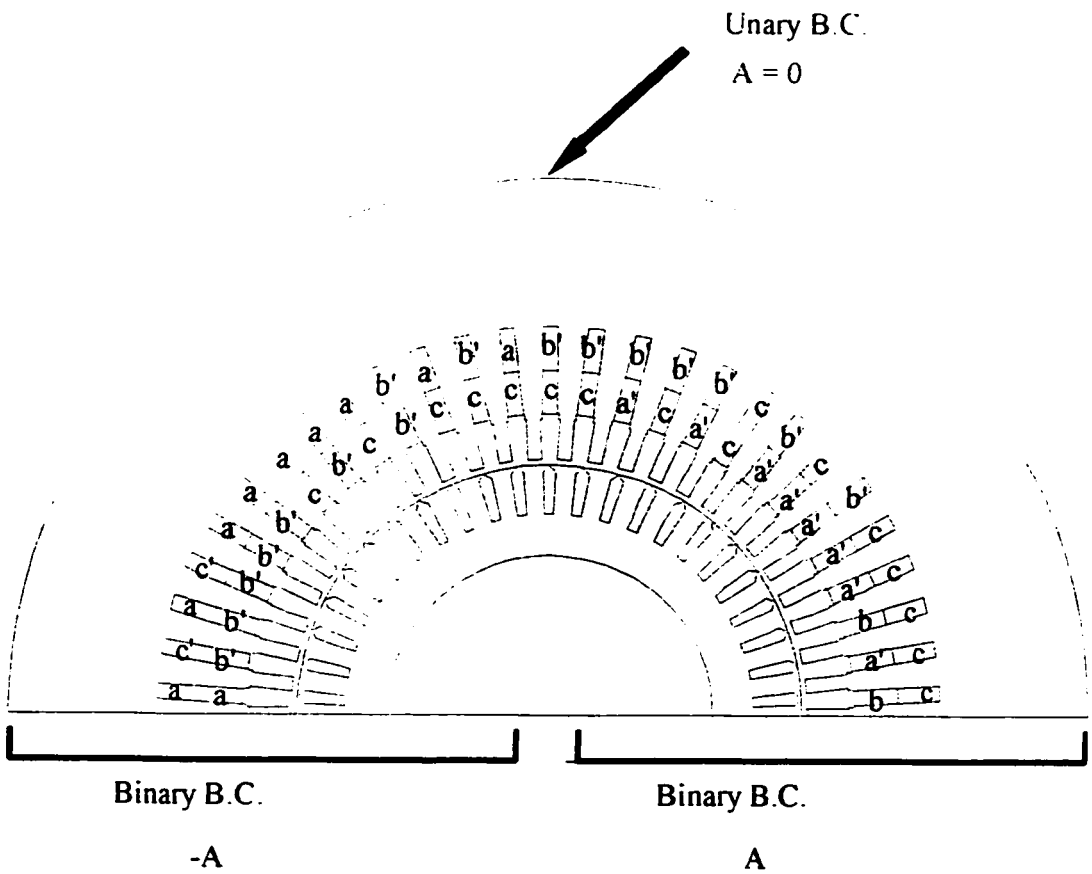

Figure 6.22 - Winding pattern and boundary conditions for two pole machine.

6.8 Results of Analysis

6.8.1 Results for Two Pole Machine

The two pole machine under investigation is a 5000 hp (3729 kW), 4 kV machine with 54 stator slots (27 slots/pole) and 46 rotor slots (23 slots/pole). Note that for this machine, the number of stator and rotor slots may be modelled exactly with one pole pitch, because the machine has an integral number of slots per pole for both the stator and rotor. The mesh used to model this machine has 4703 nodes, 9289 elements, and 85 constraints. Figure 6.22 shows the winding pattern and boundary conditions for this model. An unary or constant flux line boundary condition (BC) is applied to the outside diameter of the stator yoke. Flux

lines are confined to the inside of the machine by setting the value of the magnetic vector potential to zero on every point along the outside diameter of the machine. The two edges of the pole pitch are modelled with a binary or anti-periodic BC. Here, the vector potential on each node on one side of the pole pitch is specified as the negative value of the corresponding node on the opposite pole pitch. Imposition of boundary conditions with the FEM is discussed in greater detail in Appendix B, Section B4.3. Figure 6.23 shows the no load flux distribution for the machine from one of the magnetostatic solutions. Note that the machine shaft is magnetic and carries flux.

Figures 6.24 and 6.25 show respectively, the real and imaginary components of the flux distribution at no load as given by the TH simulation. The real component of the solution may be thought of as the flux distribution at an electrical angle of 0°. The imaginary component may be thought of as the flux distribution at an electrical angle of 90°. In other words, the two solutions are in phase quadrature. Note that the real component of the flux distribution (figure 6.24) happens to correspond to the approximate instant in time at which the flux density is at a maximum in this particular tooth. The imaginary component (figure 6.25) corresponds to the approximate instant in time at which the flux density reaches a maximum in the stator yoke. These two figures can aid one to envision the mechanism by which rotational fields are produced in the stator yoke. Imagine that figure 6.24 represents a north pole in the stator. For this condition, the flux lines exit the tooth and enter the rotor. This will occur at an electrical angle of 0°. When the flux distribution has shifted another 90°, the condition in figure 6.25 will exist. In the yoke, the flux lines have now rotated clockwise. At an electrical angle of 180°, the flux lines will look similar to the situation in figure 6.24 but the flux will now be leaving the rotor and enter the stator teeth. The flux lines in the yoke will have rotated correspondingly from their initial orientation by 180°. At an electrical angle of 270°, the flux lines will be oriented as in figure 6.25 but in the opposite direction. The flux lines in the yoke will have rotated 270° from their initial orientation. The

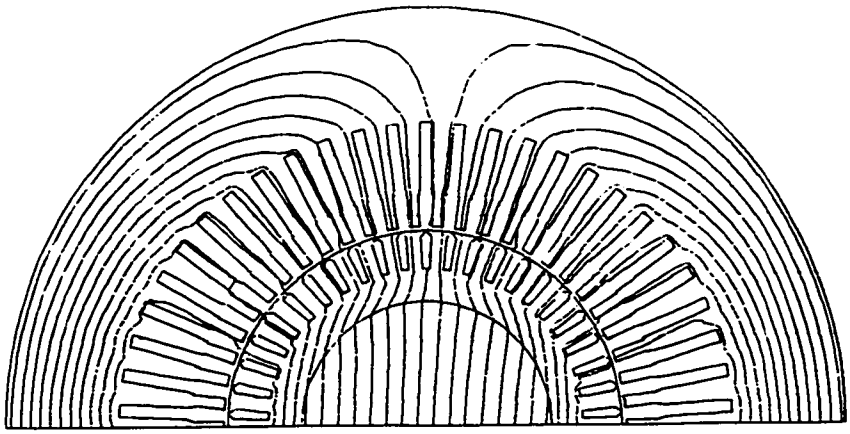

Figure 6.23 - No-load flux distribution in two pole induction motor.

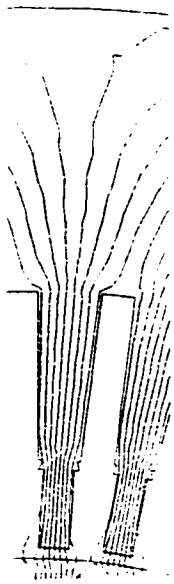

Figure 6.24 - Plot of Re[A] in two pole induction motor.

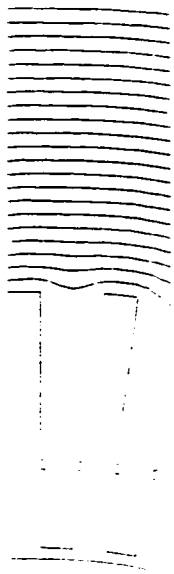

Figure 6.25 - Plot of Im[A] in two pole induction motor.

cycle is completed when the flux lines return to the original orientation at 360°. By picking a particular point on the yoke and following this line of thought, it is possible to imagine that the flux density at that point will approximate an elliptical locus.

Figures 6.26 and 6.27 show, in respective order, the distribution of the tangential and radial components of the flux density in the machine yoke taken along the radial centre line of a tooth and a slot. The tangential and radial components of the flux density were calculated taking into account the rotational nature of the flux density by applying equations 6.30 through 6.37. Flux densities are plotted against the normalized radial distance from the inside diameter of the stator yoke (corresponding to the bottom of the stator slots) to the outside diameter of the yoke (see figures 6.28 and 6.29). Figures similar to 6.26 and 6.27 were made for the results of each machine and are presented in the sections that follow. In each case, the results were taken along line contours similar to those defined in figures 6.28 and 6.29. In figure 6.26, note that the distribution of flux density in the radial direction is strongest directly behind the root of the stator tooth and gradually declines to zero at the very back of the stator yoke. Behind the tooth, the tangential component of the flux density is approximately constant along the stator yoke for about 80% of the distance along the stator yoke. The tangential flux density is lower from the root of the stator tooth to approximately 20% of the distance into the yoke. This is caused by some tangential flux leaking into the stator tooth root (as shown by the curvature of the flux lines into the tooth root in figure 6.25).

Behind the stator slot, the distribution of the tangential component of the flux is nearly constant along the entire radial length of the yoke as indicated in figure 6.27. Very little flux will leak into the slot, because it is filled with nonmagnetic materials (for instance, copper and insulation). Consequently, the tangential flux density behind the slot (shown in figure 6.27) does not exhibit the weakening effect at the inner portion of the yoke, an effect that is clearly evident behind the stator tooth (shown in figure 6.26).

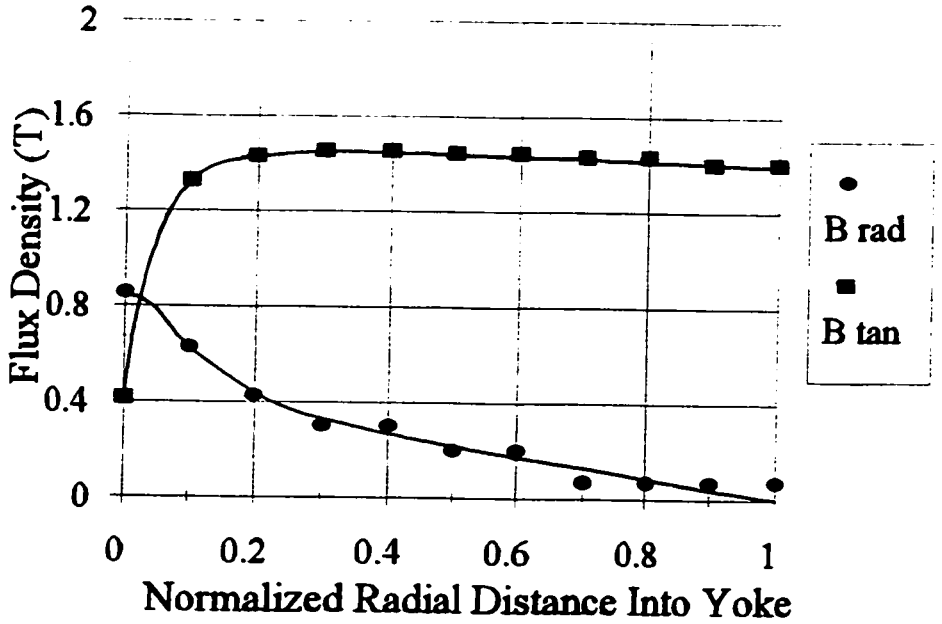

Figure 6.26 - Radial and tangential flux density. Two pole yoke behind stator tooth.

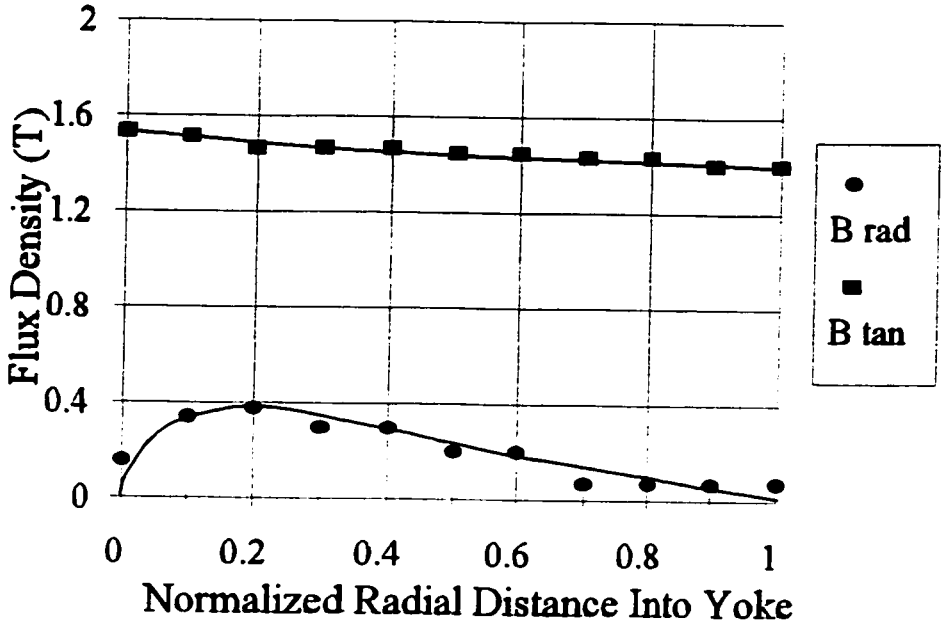

Figure 6.27 - Radial and tangential flux density. Two pole yoke behind stator slot.

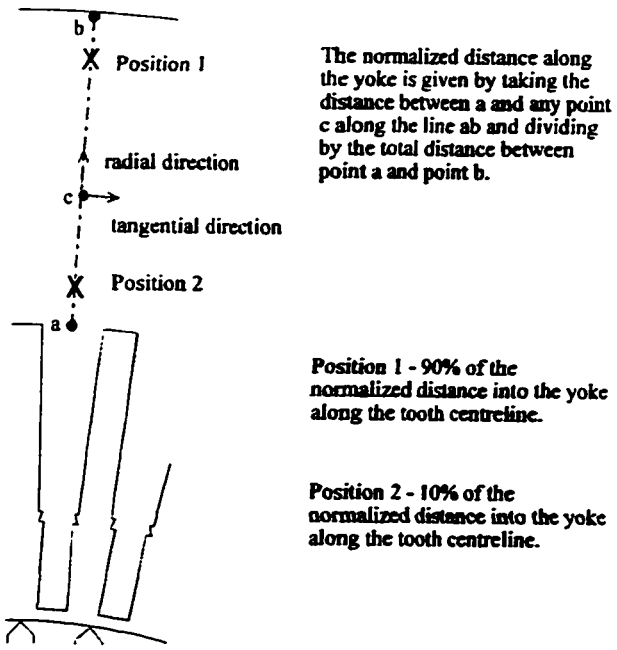

Figure 6.28 - Definition of normalized distance along the yoke behind stator tooth.

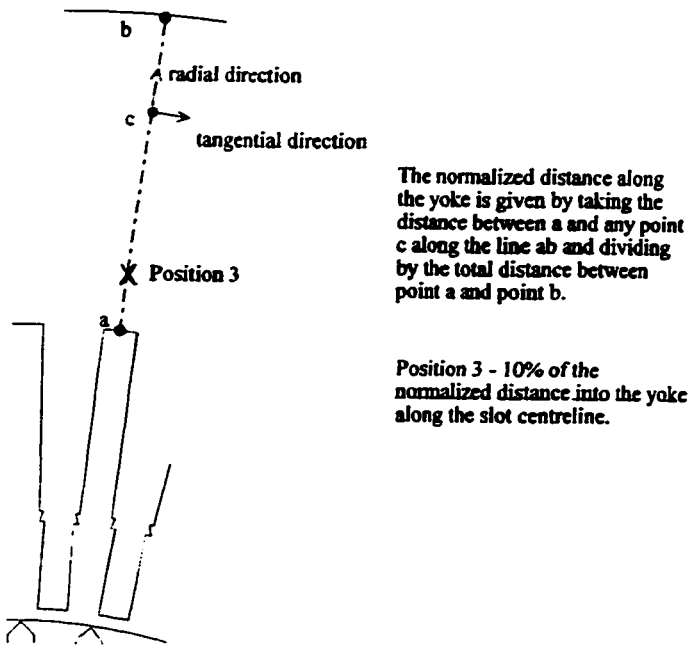

Figure 6.29 - Definition of normalized distance along the yoke behind stator slot.

An indication of the flux density polarization is given by the ratio of the radial flux density value to the tangential flux density value all along the yoke. For an elliptical locus, this is the aspect ratio of the ellipse. Note that the polarization is much stronger behind the tooth than behind the slot. In figure 6.26, a circular flux density polarization of approximately 0.8T is evident at approximately 5% of the radial distance into the yoke. In physical terms, the radial component of the flux density "pours" into the yoke from the tooth. Behind the stator slot, only the radial component of tooth flux that leaks into the area behind the slot will manifest itself as a radial component of flux density (for instance, see figure 6.24). Behind the stator slot, a maximum aspect ratio of approximately 0.3 is found at about 20% of the radial distance into the yoke.

Note that the data points for the curves in figures 6.26 and 6.27 exhibit a stepped behaviour (for instance points at distance 0.3 & 0.4, 0.5 & 0.6, 0.7 & 0.8, 0.9 & 1.0). This occurs because some points lie on the same finite element. Since the flux density is constant over the entire area of a first order element (see Appendix B - equation B3), the two points must have the same value. This is a form of discretization error caused by the mesh and does not represent a physical phenomenon. The situation could be improved by adding more elements to the model, but the commercial software package used in this investigation limits the number of nodes to approximately 5000. Consequently, a greater portion of the total elements was budgeted for the inner portions of the yoke where the strongest flux density polarization was expected. Most of the models presented in the following sections exhibit this discretization phenomenon to some extent.

Figure 6.30 shows a plot of the radial and tangential flux densities along the centerline of a stator tooth as defined in figure 6.31. Note that there is very little tangential component of flux density in the tooth other than in the root (i.e., the transition area between the stator tooth and the stator yoke at a normalized distance of one).

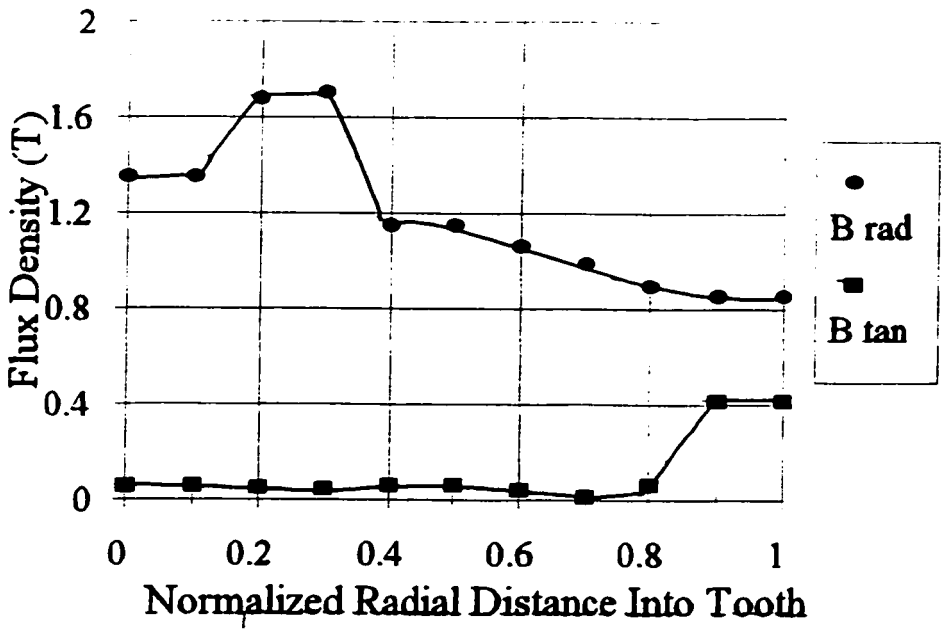

Figure 6.30 - Radial and tangential flux density. Two pole stator tooth.

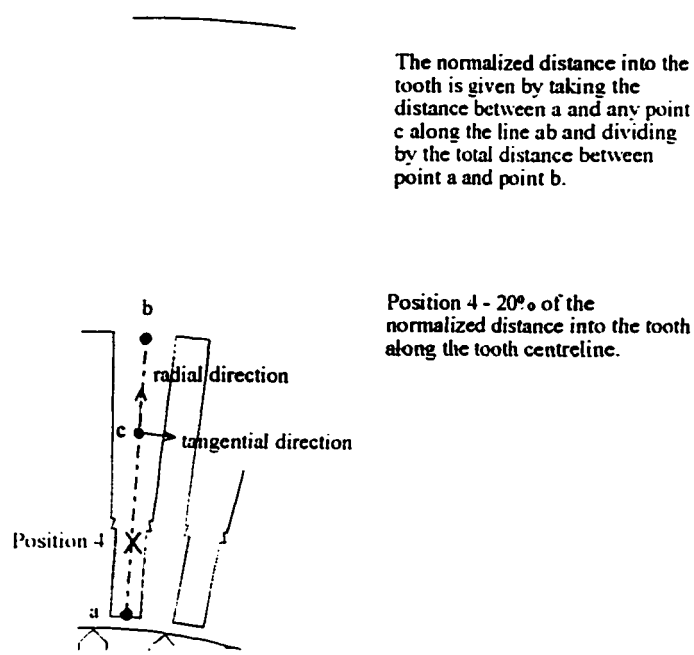

Figure 6.31 - Definition of normalized distance into tooth.

Note that the points at 90% and 100% of the normalized distance into the tooth belong to the same element, thus the flat portion on the curve of the tangential flux density. The radial component of the flux density is dominant and shows that the flux density is nearly purely alternating in nature along the tooth centerline. A sharp increase in the magnitude of the radial flux density is evident in the region corresponding to 0.20 to 0.30 of the normalized distance into the tooth. This is caused by the narrowing of the tooth near the recessed stator slot wedge (see for instance figure 6.24, the grooves for the wedges are shown, but the wedges are not). The flux lines are crowded in this area but spread out further into the tooth. The flux density is lower at the tooth tip because some flux leaks out of the tooth tip into the surrounding air (also indicated in figure 6.24).

Figures 6.32 and 6.33 show some flux density loci for various positions in the stator tooth and yoke. The four positions of interest are shown in figures 6.28, 6.29 and 6.31. Position 1 is located at the back of the stator yoke at 90% of the normalized radial distance into the yoke along the tooth centerline. Position 2 is located near the tooth root at 10% of the normalized distance into the yoke along the tooth centerline. Position 3 is located behind the stator slot at 10% of the normalized distance into the yoke at the slot centerline. Position 4 is located near the stator tooth tip, 20% of the distance into the tooth along the tooth centerline. The loci are given for three different methods of flux density analysis. In this way the results obtained from the TH simulations, the fundamental component of the time-stepped magnetostatic (TSM) simulations and the TSM solutions proper can all be compared. Similar figures, corresponding to similar positions within the machine stators were prepared and are shown in the sections that follow.

Note that all three analyses yield similar peak magnitudes for the flux densities along the major and minor axes of the loci. The results for the TSM solutions at positions 2 and 3 indicate that the loci are not purely elliptical and that the waveforms have some harmonic content.

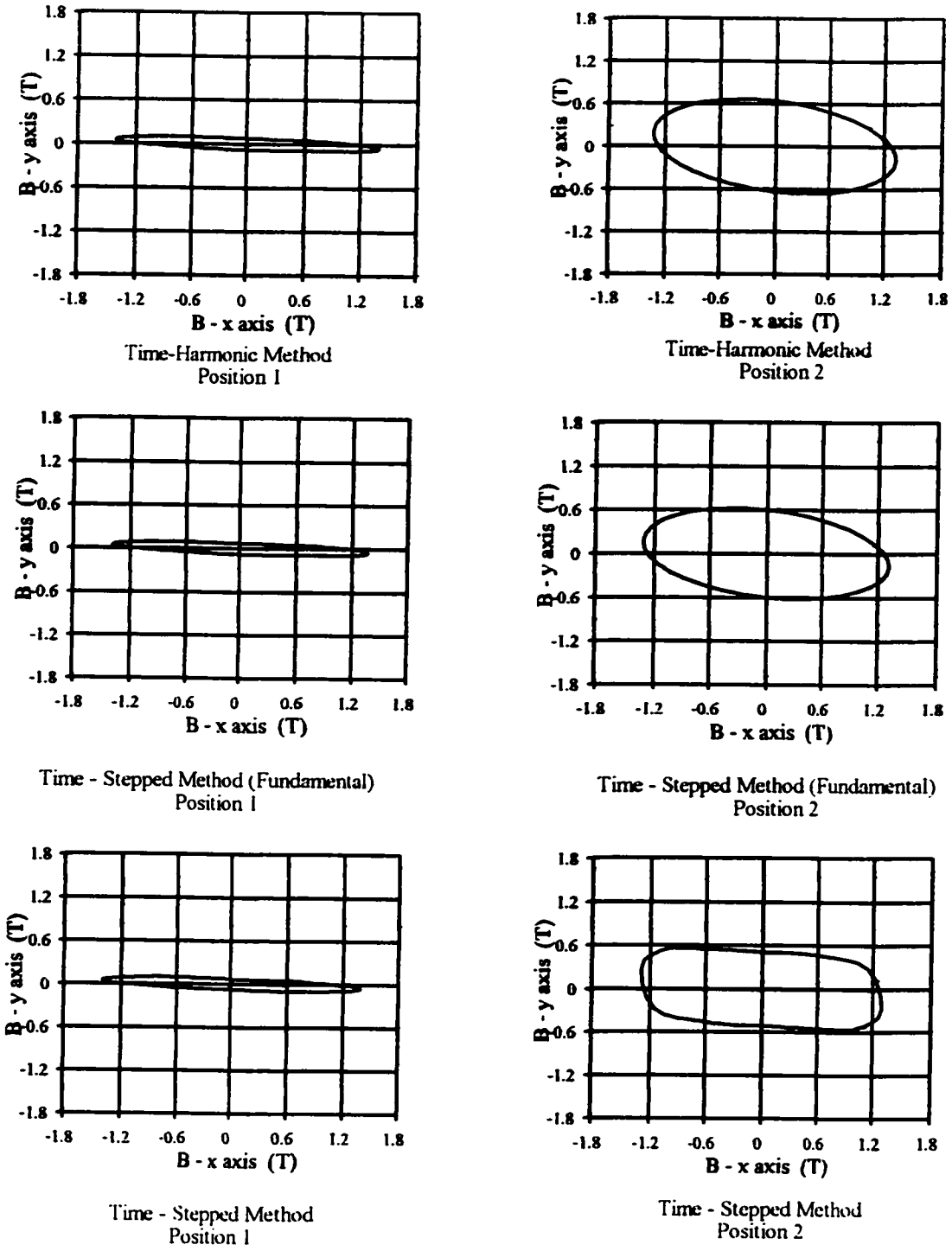

Figure 6.32 - Flux density loci for two pole machine at positions 1 and 2.

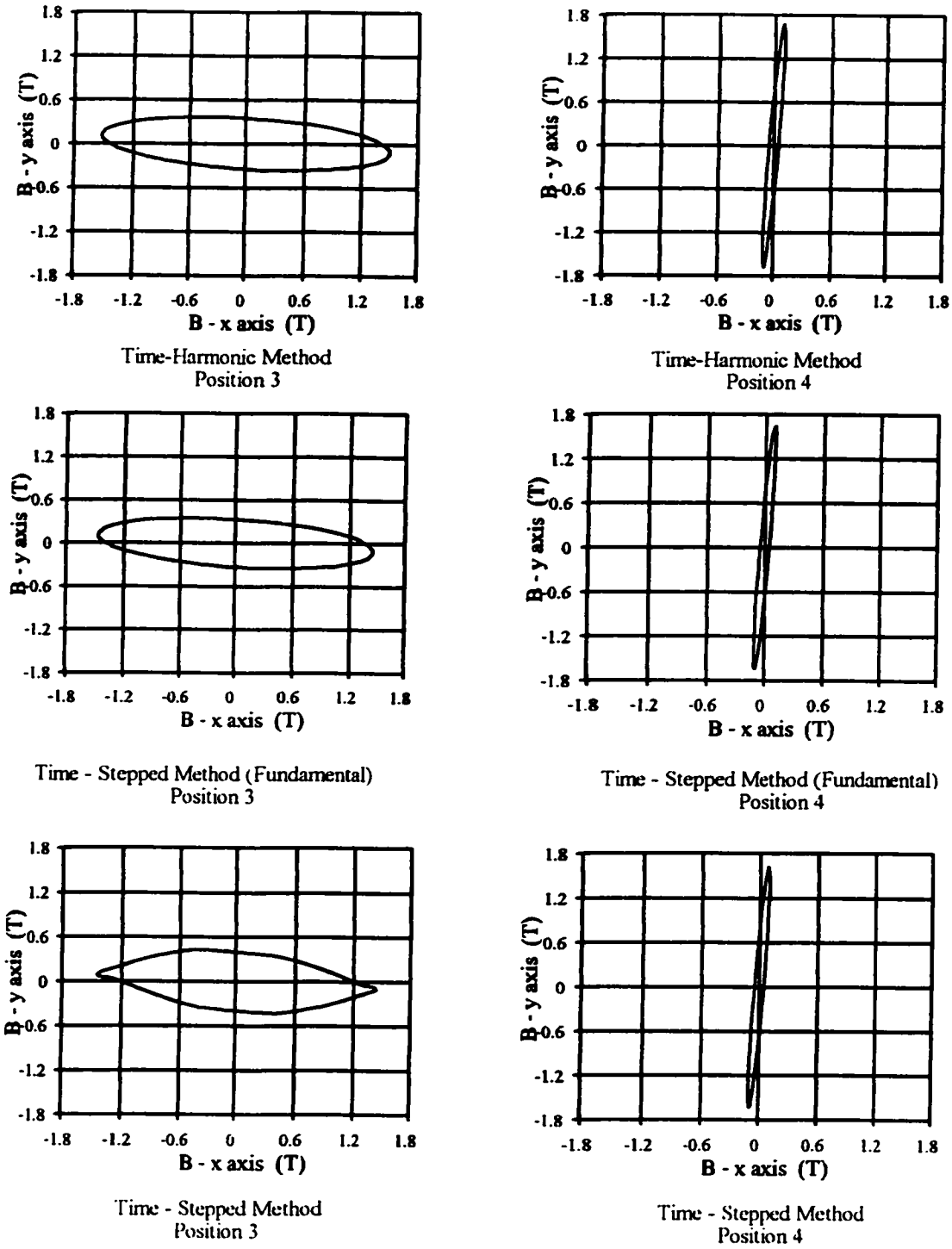

Figure 6.33 - Flux density loci for two pole machine at positions 3 and 4.

Table 6.6 - Loss Estimates for Two Pole Machine

Method	Yoke Loss TH (Δ% from I)	Yoke Loss TSM (Δ% from I)	Tooth Loss TH (Δ% from I)	Tooth Loss TSM (Δ% from I)
I	9.37 kW (0.0)	8.91 kW (0.0)	1.71 kW (0.0)	1.63 kW (0.0)
II	9.48 kW (1.2)	9.01 kW (1.1)	NA	NA
III	8.88 kW (-5.2)	8.42 kW (-5.4)	1.92 kW (12.5)	1.84 kW (13.3)
IV	10.04 kW (7.1)	9.53 kW (6.9)	1.67 kW (-2.3)	1.60 kW (-1.8)
V	10.21 kW (9.0)	9.71 kW (8.9)	NA	NA
VI	9.76 kW (4.2)	9.28 kW (4.1)	NA	NA

Table 6.6 shows the loss estimates by the six methods outlined in Section 6.7. Losses are for the entire yoke and all the stator teeth. Method I is the most rigorous method, since it takes account of the rotational losses and estimates the effect of the sheet anisotropy. Method II gives a slightly higher estimate of the losses in the stator yoke, because the effect of the sheet anisotropy is ignored. The lowest estimate in the yoke is given by using the 50:50 Epstein test curve (Method III) which is the method usually used in industry. The direction of sheet orientation is predominately in the transverse direction. By using the 50:50 Epstein test data, an inherent assumption is made that the yoke of the machine is oriented equally in the td and rd of the sheet. This may be a better method for use in small machines using ring punchings in the yoke. Method V gives the highest estimate. As we saw in Chapter 5, the method of superposition tends to overestimate the rotational losses in the sheet. Method VI is identical to method V with the exception that rd and td alternating loss curves were obtained using the PRL tester. Method VI gives a slightly lower estimate than method V due to the small disagreement between the Epstein test measurements and the PRL apparatus (previously discussed in Section 5.5). Loss estimates obtained by the magnetostatic solutions are slightly lower than those given by the time-harmonic method because the estimates of the flux density values in the machine are slightly lower. As an

example of this refer to figures 6.32 and 6.33. A comparison of the ellipses obtained from the TH method and the fundamental of the TSM method shows that the flux density in the major axis of each ellipse is slightly lower in the latter. At position 2, the flux density in the minor axis of the ellipse is also slightly smaller. This will be discussed in greater detail in Section 6.8. We can estimate the differences in the calculation of yoke loss when using the 50:50 Epstein test curve, and the method of superposition based on the PRL curves if we consider method I to be the basis for comparison. Method III differs by -5.2 and method VI differs by 4.2% when using the TH solutions. Method III differs by -5.4 and method VI differs by 4.1% when using the TH solutions. We can estimate the differences in the calculation of the tooth loss when using the 50:50 Epstein test curve, and the results obtained when using the Epstein curve for the TD losses for the yoke and the RD curve for the losses in the teeth. Again, these two results are compared with method 1, which takes account of the rotational losses more rigorously. When using the TH simulations, the results from method III differ from the results from method I by 12.5% and the results from method IV differ the results from method I by -2.3%. From the TSM simulations, the results of method III differ from the results of method I by 13.3% and the results from method IV differ the results from method I by -1.8%.

6.8.2 Results for Four Pole Machine

The four pole machine under investigation is a 5000 hp (3729 kW), 4 kV machine with 84 stator slots (21 slots/pole) and 68 rotor slots (17 slots/pole). The mesh used to model this machine has 4330 nodes, 8528 elements, and 104 constraints. The number of stator and rotor slots can be modelled exactly by the single pole pitch model because the machine has an integral number of stator and rotor slots per pole. The winding pattern and boundary conditions for the model are shown in figure 6.34. As in the two pole model, the outside diameter of the machine is constrained with a unary BC and the edges of the pole pitch are

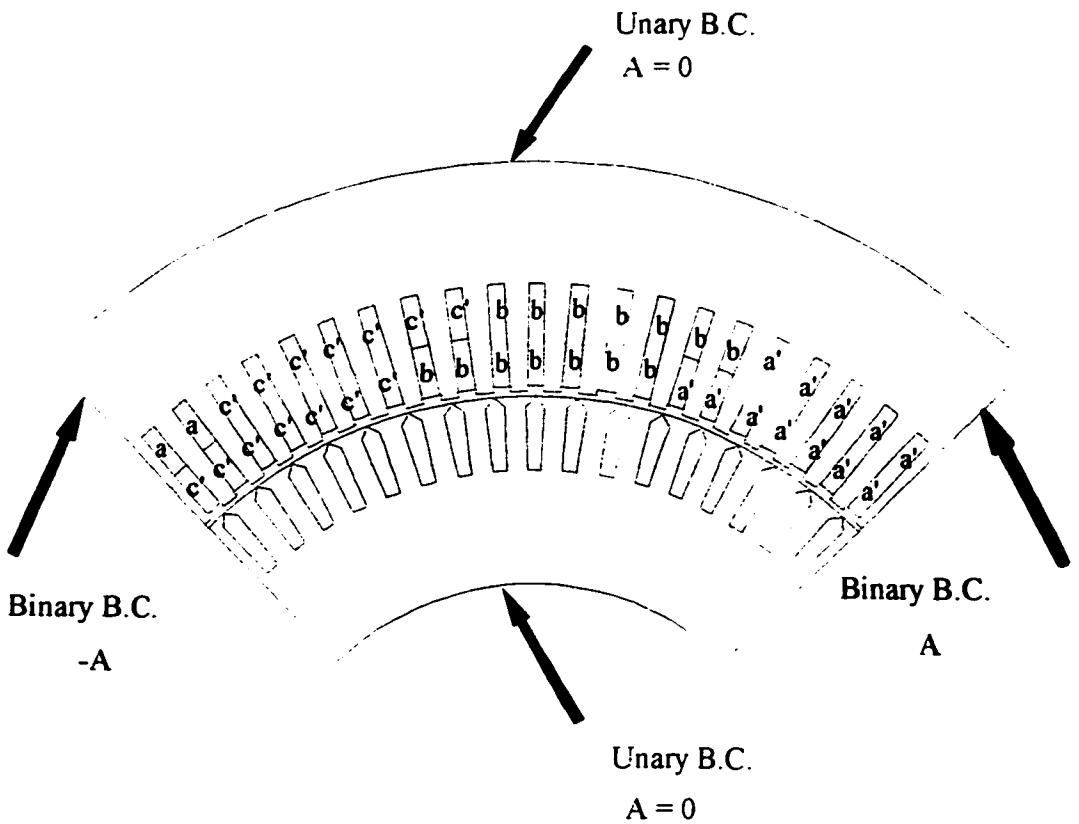

Figure 6.34 - Winding pattern and boundary conditions for four pole machine.

constrained with the anti-periodic BC. The inside diameter of the machine is also constrained with a unary BC in order to simulate the spider arm construction of the machine. Figure 6.35 shows the no load flux distribution of the machine from one of the magnetostatic solutions.

Figures 6.36 and 6.37 show the real and imaginary components of the flux density distribution obtained from the TH simulation at no load. Note for the previous machine, in figure 6.24, the real component of the flux happened to coincide very closely to the instant in time at which the flux density in the shown tooth was a maximum. Figure 6.25 coincided with the instant in time at which the flux density in the yoke was at a maximum. In figures 6.36 and 6.37 the flux densities in the teeth and yoke are at a more intermediate flux density

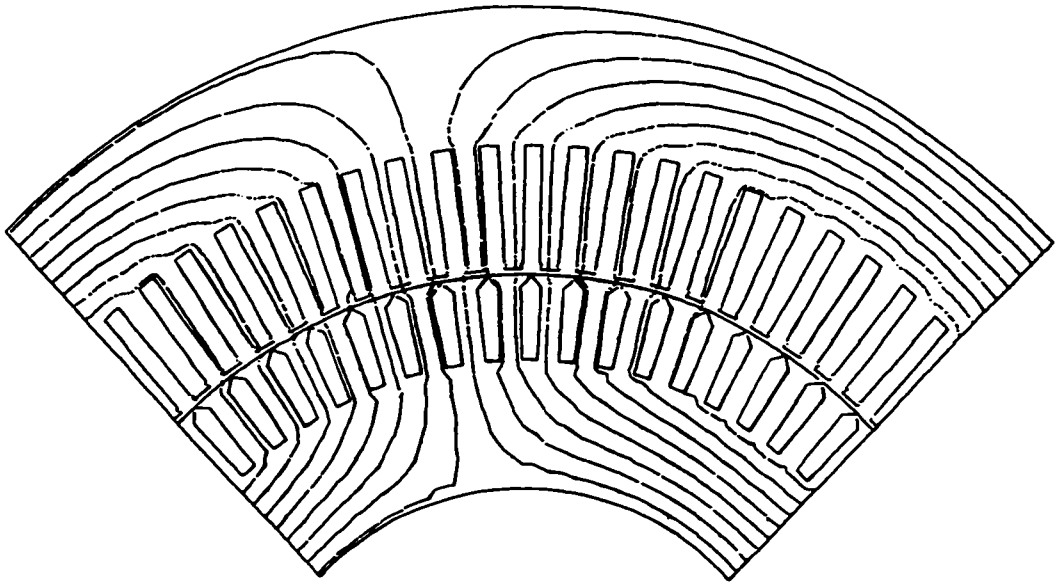

Figure 6.35 - No-load flux distribution in four pole induction motor.

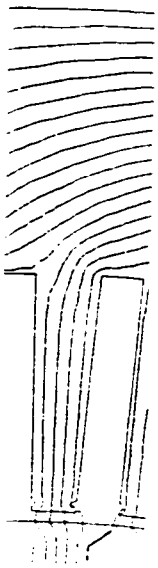

Figure 6.36 - Plot of Re[A] in four pole induction motor.

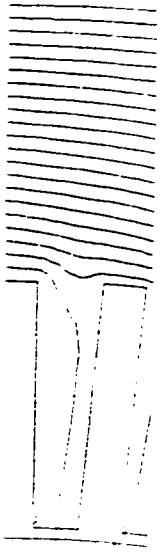

Figure 6.37 - Plot of Im[A] in four pole induction motor.

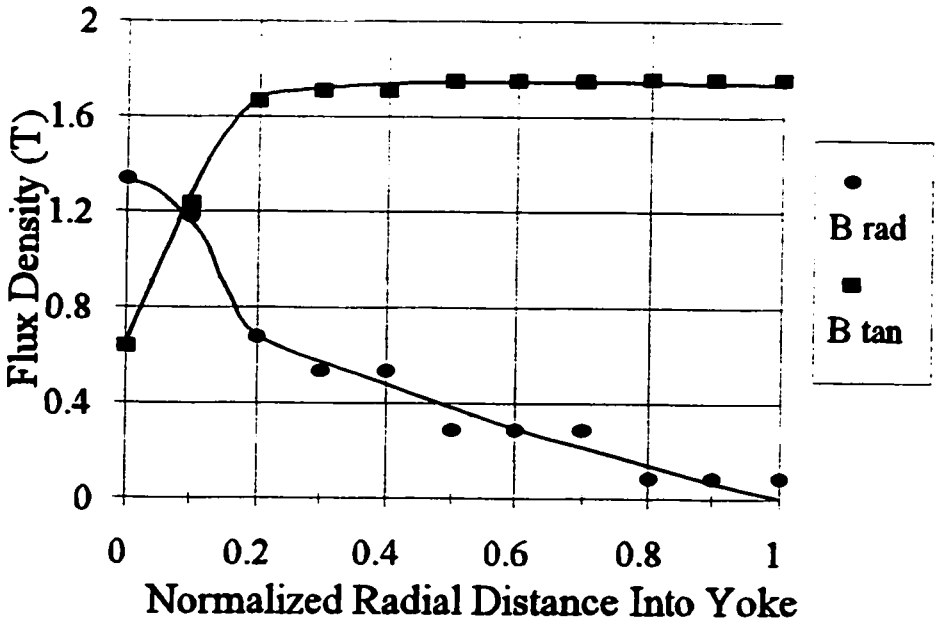

Figure 6.38 - Radial and tangential flux density. Four pole yoke behind stator tooth.

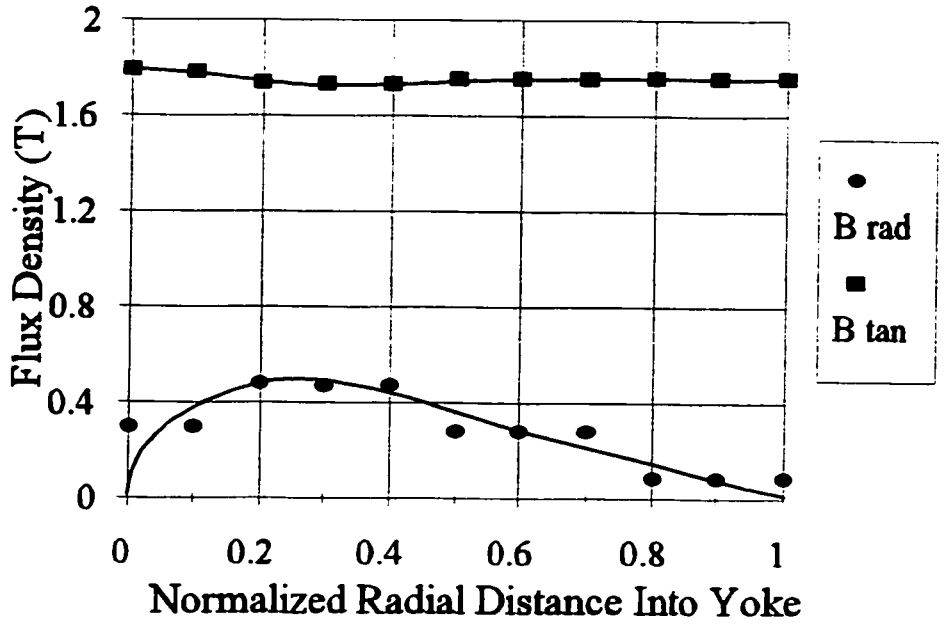

Figure 6.39 - Radial and tangential flux density. Four pole yoke behind stator slot.

level, nevertheless, the flux densities shown are still in phase quadrature.

Figures 6.38 and 6.39 show, in respective order, the distribution of the tangential and radial components of the flux density in the machine yoke taken along the radial centre line of a tooth and a slot. The tangential and radial components of the flux density were calculated taking into account the rotational nature of the flux density by applying equations 6.30 through 6.37. Flux densities are plotted against the normalized radial distance from the inside diameter of the stator yoke (corresponding to the bottom of the stator slots) to the outside diameter of the yoke as was previously described for the previous machine.

The distribution of the radial component of the flux density is strongest directly behind the stator tooth. The tangential component of the flux density is weakened due to leakage into the tooth root. This leakage phenomenon into the stator tooth is similar to that already discussed for the two pole machine and is evident in figure 6.37. Behind the stator slot, the tangential component of the flux density is nearly constant along the radial depth of the yoke. Note that, as with the two pole machine, the flux density polarization is much stronger behind the stator tooth than behind the slot. Behind the stator tooth (see figure 6.38), a circular polarization at a flux density of approximately 1.2T is evident at about 10% of the normalized radial distance into the yoke and gradually declines to zero at the back of the stator yoke. A more elliptical pattern is found behind the stator slot. From about 20 to 40% of the radial distance into the yoke, the aspect ratio is approximately 0.3.

Figure 6.40 shows a plot of the radial and tangential flux densities along the centerline of a stator tooth. There is very little tangential component of flux density in the tooth except for the vicinity of the stator tooth root. Here, the tangential component of the flux density in the stator yoke is leaking into the tooth. Starting at about 70% of the radial distance into the tooth, the tangential component begins to increase as the inside diameter of the stator yoke is approached. Along the rest of the tooth, the radial component of the flux density is dominant and the flux density in the stator tooth is nearly purely alternating in most of the

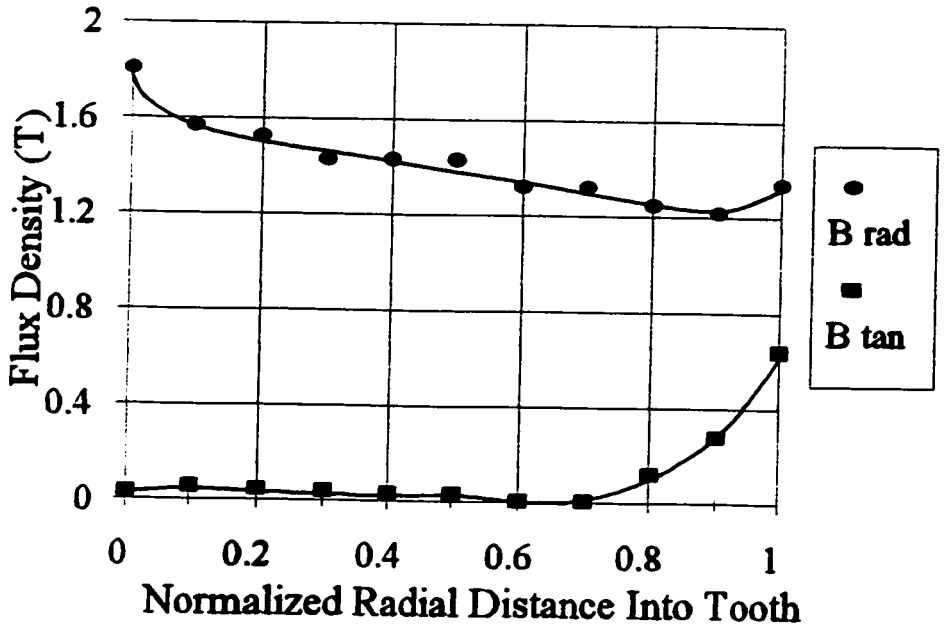

Figure 6.40 - Radial and tangential flux density. Four pole tooth.

tooth. The maximum flux density is found near the tooth tip where the tooth is narrowest, apart from the narrow area between the slot wedge grooves. An inspection of figures 6.36 reveals that the grooves for the stator slot wedges are very close to the tips of the stator teeth. The narrowing of the stator teeth caused by these wedges helps explain the sharp increase in the flux density at the tooth tips.

Figures 6.41 and 6.42 show some flux density loci for positions similar to those described in the previous case of the two pole machine. Note that for all four positions, the flux densities obtained by the TH simulations are slightly larger than those obtained by plotting the fundamental of the TSM solutions. The results for the TSM solutions at positions 2 and 3 show that the loci are not purely elliptical and that the waveforms have some harmonic content.

Table 6.7 summarizes the loss estimates for the four pole machine by the six methods outlined in Section 6.7. Method II gives a slightly higher estimate of the losses than method I. This is similar to the result obtained for the two pole machine. The effect of the sheet

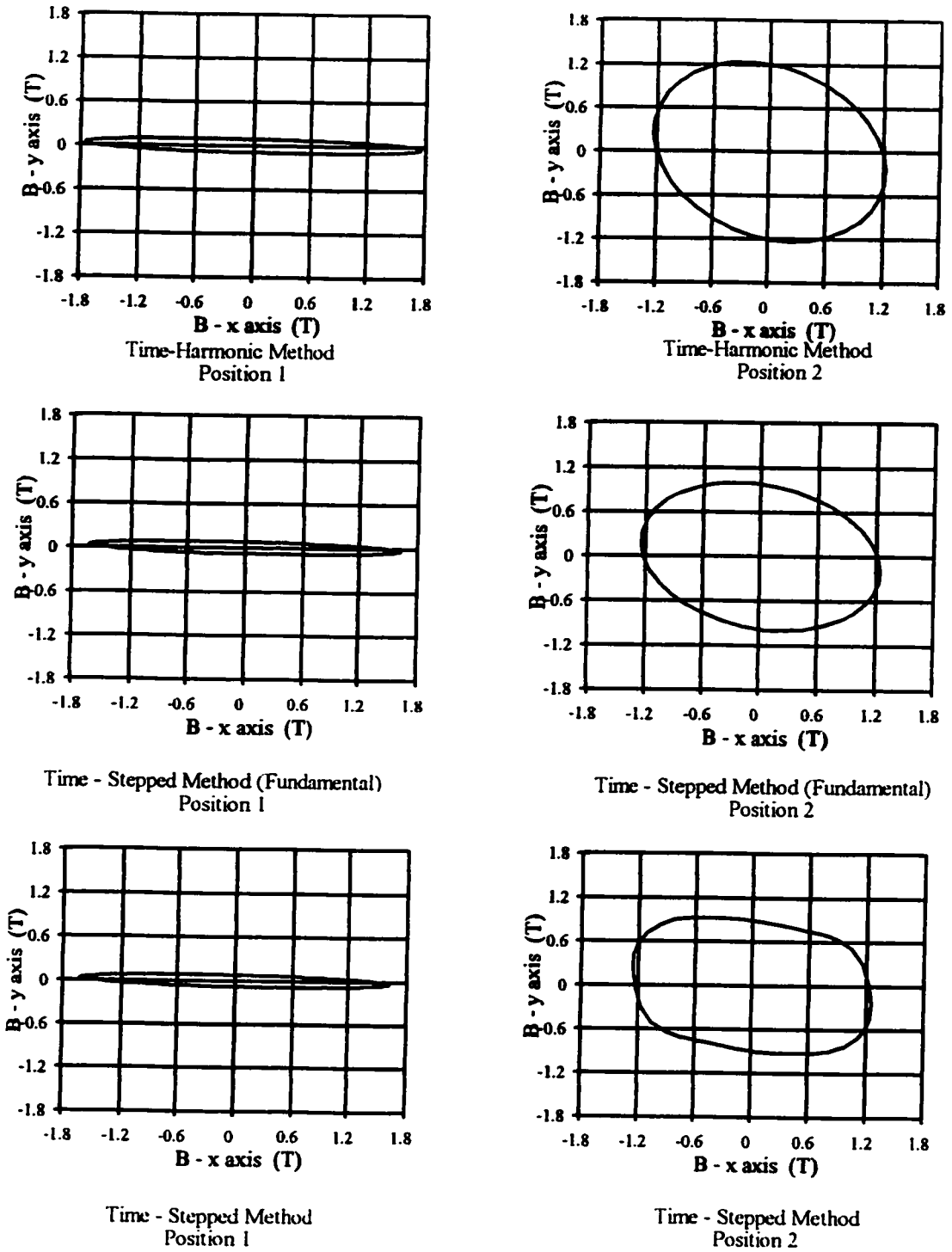

Figure 6.41 - Flux density loci for four pole machine at positions 1 and 2.

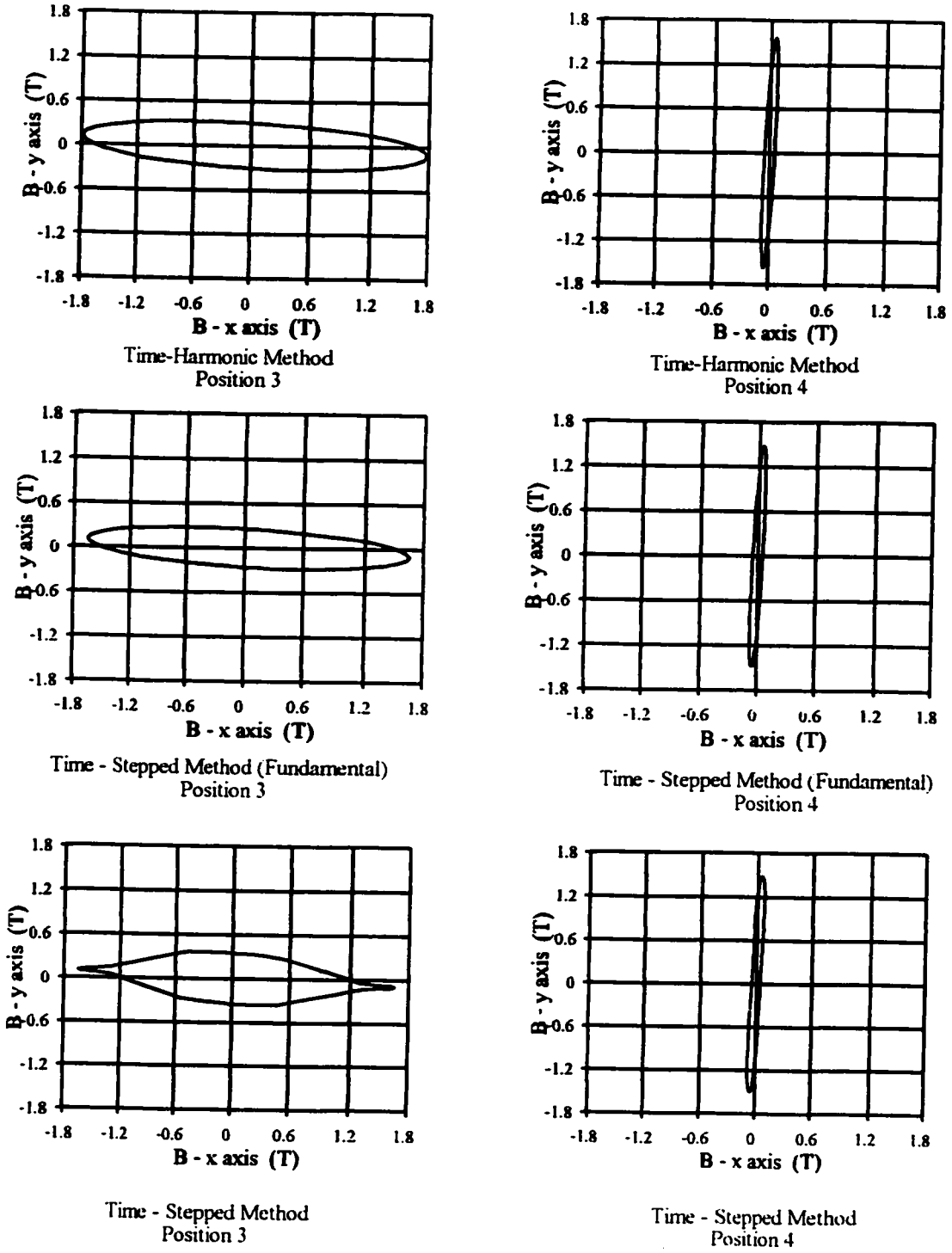

Figure 6.42 - Flux density loci for four pole machine at positions 3 and 4.

Table 6.7 - Loss Estimates for Four Pole Machine

Method	Yoke Loss TH (Δ% from I)	Yoke Loss TSM (Δ% from I)	Tooth Loss TH (Δ% from I)	Tooth Loss TSM (Δ% from I)
I	8.30 kW (0.0)	7.09 kW (0.0)	1.62 kW (0.0)	1.41 kW (0.0)
II	8.39 kW (1.1)	7.16 kW (1.0)	NA	NA
III	7.76 kW (-6.5)	6.70 kW (-5.5)	1.80 kW (11.1)	1.54 kW (9.3)
IV	8.77 kW (5.7)	7.57 kW (6.8)	1.56 kW (-3.4)	1.34 kW (-5.0)
V	8.84 kW (6.5)	7.63 kW (7.6)	NA	NA
VI	9.07 kW (9.3)	7.48 kW (5.4)	NA	NA

anisotropy is slightly evident in this result. Method III again gives the lowest result due to the assumption that a large portion of the yoke is oriented along the rolling direction of the sheet. Using method IV, the flux density in each element is assumed to be alternating. The td loss curve from the Epstein test is used in the yoke and the rd loss curve from the Epstein test is used in the teeth. Method IV and V yield similar yoke losses for this machine. Methods V and VI give higher estimates of the losses than methods I and II, indicating that the superposition method of estimating rotational losses tends to give a value that is too high. Methods I and II give results that are higher than method III but lower than methods IV, V and VI. Loss estimates obtained by the TSM solutions are slightly lower than those given by the time-harmonic method because the estimates of the flux density values in the machine are slightly lower as indicated in figures 6.41 and 6.42.

We can estimate the differences in the calculation of yoke loss when using the 50:50 Epstein test curve, and the method of superposition based on the PRL curves if we consider method I to be the basis for comparison. Method III differs by -6.5 and method VI differs by 9.3% when using the TH solutions. Method III differs by -5.5 and method VI differs by 5.4% when using the TSM solutions. For the calculation of the tooth losses we can estimate

the differences in the calculation of the tooth loss when using the 50:50 Epstein test curve, and the results obtained when using the td Epstein curve for the losses for the yoke and the rd curve for the losses in the teeth. Again, these two results are compared with method I, which takes account of the rotational losses more rigorously. From the results of the TH simulations, the losses from method III differ from the results from method I by 11.1% and the results from method IV differ from the results from method I by -3.4%. From the results of the TSM simulations, the tooth losses using method III differ from the results from method I by 9.3% and the results from method IV differ from the results from method I by -5.0%.

6.8.3 Results for Six Pole Machine

The six pole machine under investigation is an 8000 hp (5966 kW), 4.16 kV machine with 90 stator slots (15 slots/pole) and 104 rotor slots (17.33 slots/pole). The mesh used to model this machine has 4761 nodes, 9398 elements, and 94 constraints. Note that this machine is modelled with 17 rotor slots/pole which is not strictly correct. To model the machine exactly, three pole spans (i.e., half the machine geometry) should be modelled. As previously mentioned, the software package used in this investigation limits models to approximately 5000 nodes. To model half the machine geometry, the number of elements in each pole span would be roughly one third of that used in the model described above. This coarser mesh would have greatly reduced the accuracy of the field calculation in the stator. The small error in the stator flux density caused by this simplification in rotor geometry does not justify a three pole pitch model. Figure 6.43 shows the winding pattern of the machine and the boundary conditions used to model the problem. Boundary conditions similar to the ones used for the four pole machine were used; the outer and inner diameters of the machine were constrained with the unary condition and the sides of the model were constrained with the anti-period condition. Figure 6.44 shows the no load flux distribution resulting from one

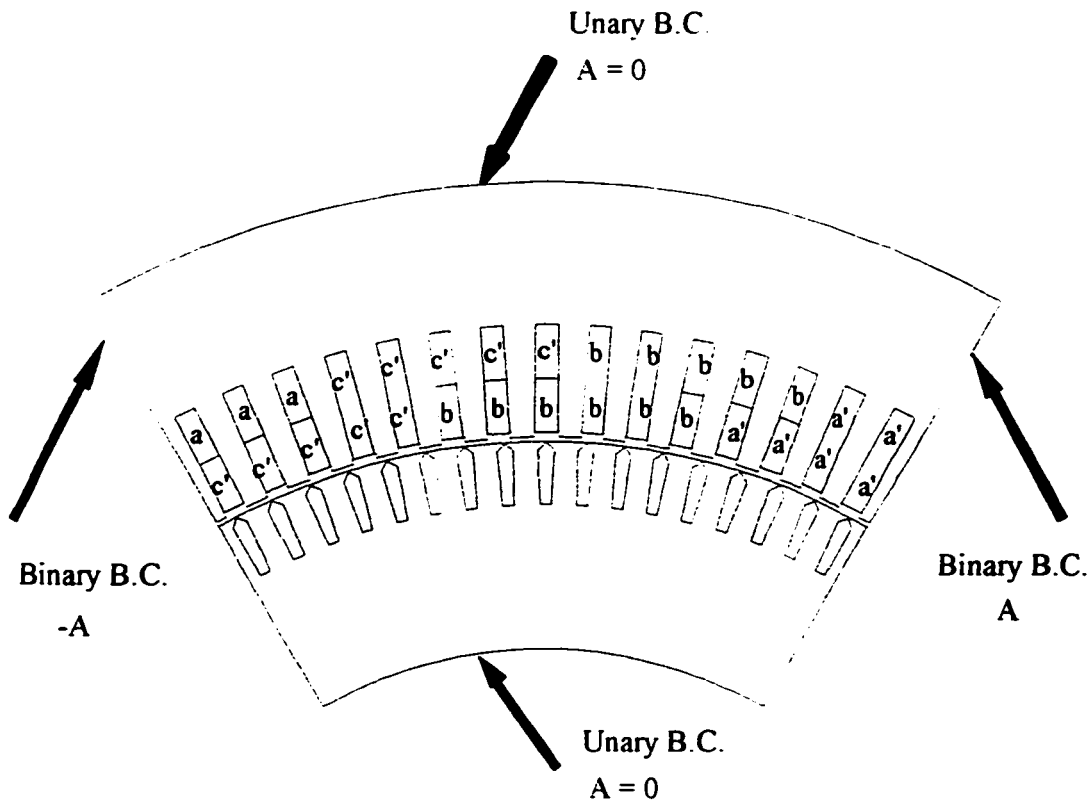

Figure 6.43 - Winding pattern and boundary conditions for six pole machine.

of the magnetostatic solutions.

Figures 6.45 and 6.46 respectively show the real and imaginary components of the flux distribution for one tooth pitch of the machine. Figures 6.47 and 6.48 show the distribution of the radial and tangential flux density in the machine yoke taken along the radial centre lines of a machine tooth and slot in similar fashion to that already described for the previous two machines. The flux density polarization is much stronger along the radial line behind the stator tooth as was noted for the previous two machines. In figure 6.47, a circular flux density polarization of 1T is found at approximately 10% of the radial distance into the yoke. Behind the stator slot (figure 6.48), the strongest flux density polarization exhibits an aspect

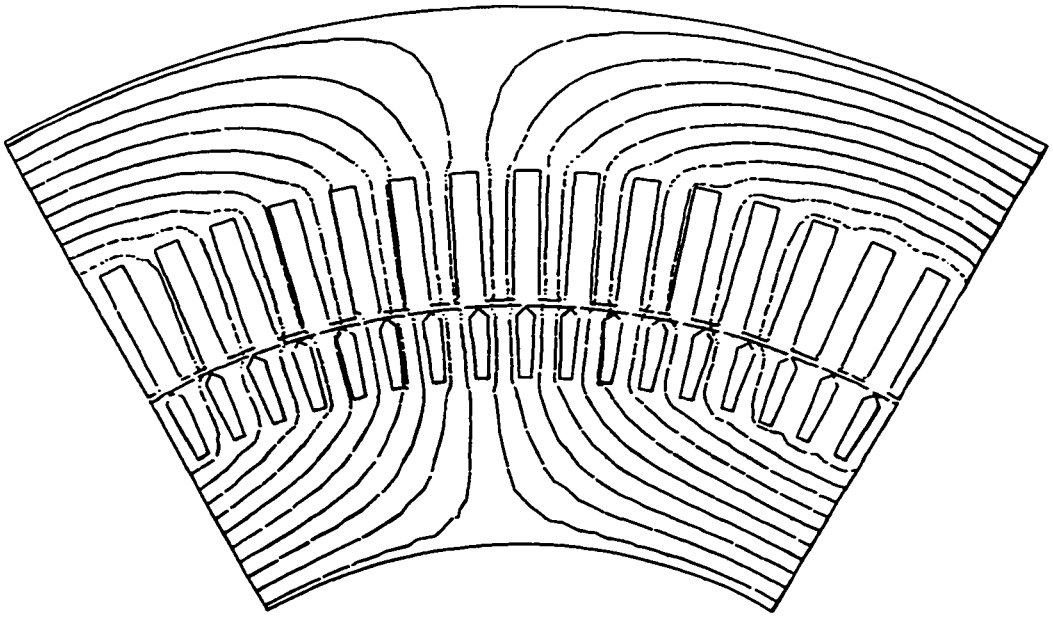

Figure 6.44 - No-load flux distribution in six pole induction motor.

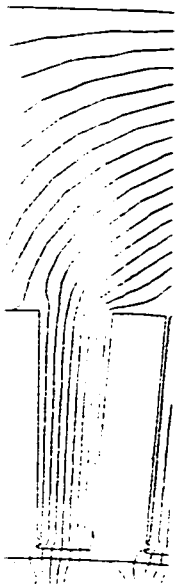

Figure 6.45 - Plot of Re[A] in six pole induction motor.

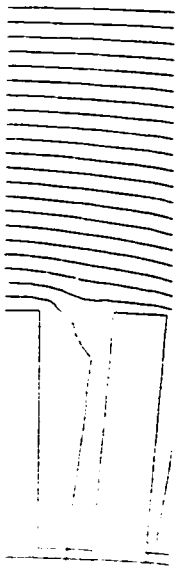

Figure 6.46 - Plot of Im[A] in six pole induction motor.

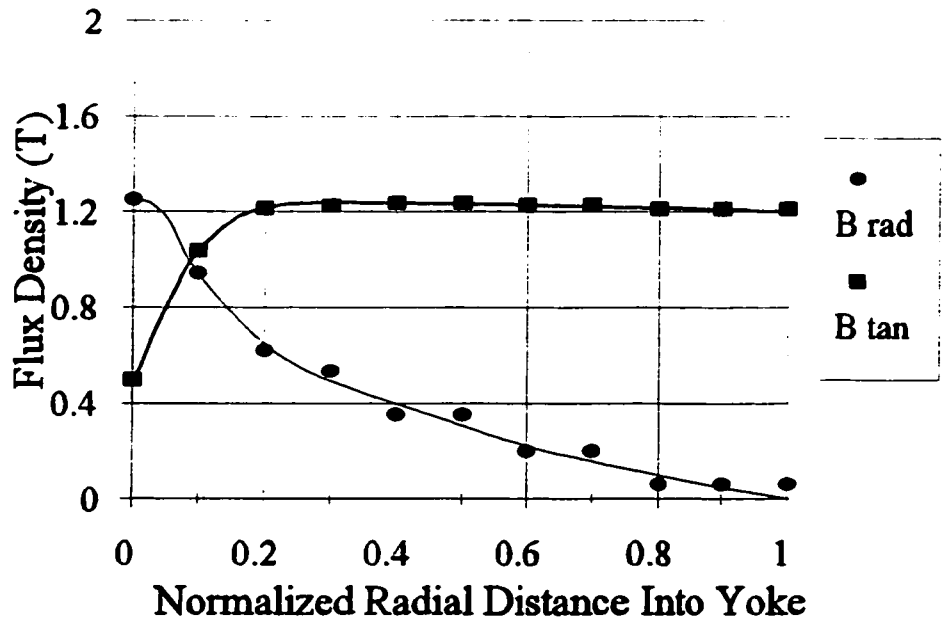

Figure 6.47 - Radial and tangential flux density. Six pole yoke behind stator tooth.

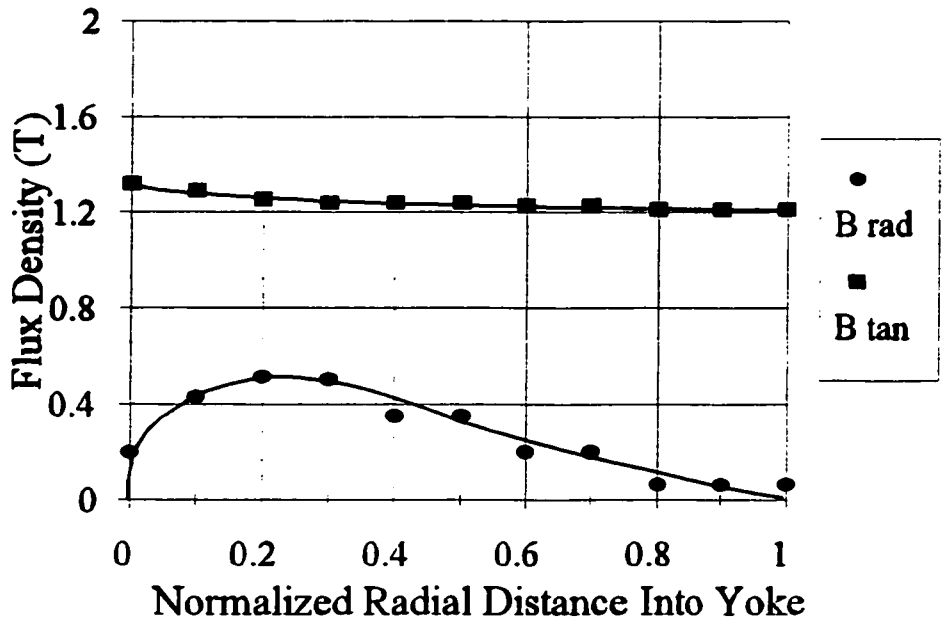

Figure 6.48 - Radial and tangential flux density. Six pole yoke behind stator slot.

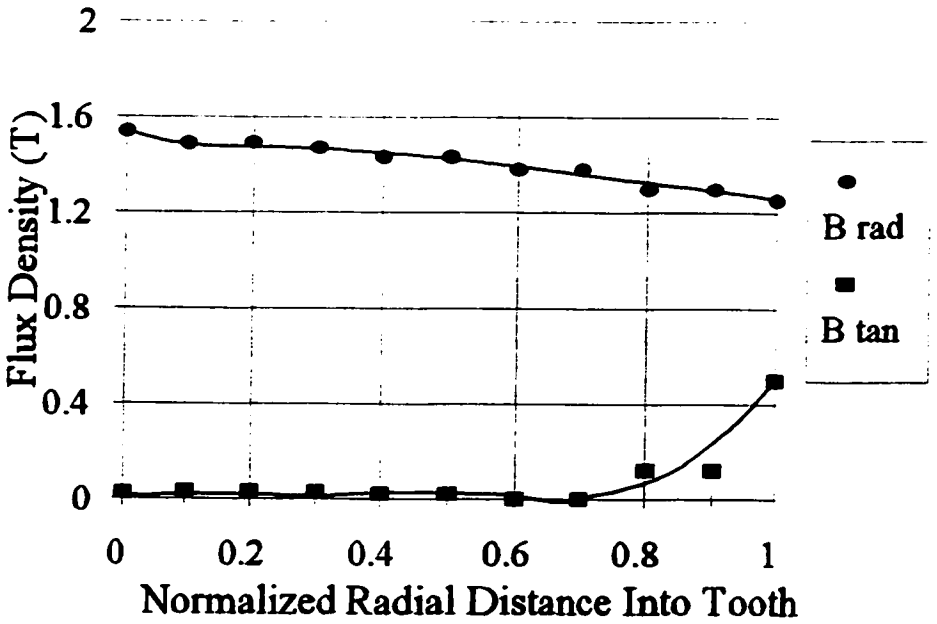

Figure 6.49 - Radial and tangential flux density. Six pole stator tooth.

ratio of approximately 0.4. This occurs at approximately 20% of the radial distance into the yoke.

Figure 6.49 shows a plot of the radial and tangential flux densities along the centerline of one of the stator teeth. There is very little tangential component of flux density in the tooth except for the vicinity of the stator tooth root. Here, the tangential component of the flux density in the stator yoke is leaking into the tooth. Starting at about 70% of the radial distance into the tooth, the tangential component begins to increase as the inside diameter of the stator yoke is approached. Along the rest of the tooth, the radial component of the flux density is dominant and the flux density in the stator tooth is nearly purely alternating in most of the tooth. The maximum flux density is found near the tooth tip which is the narrowest portion of the tooth aside from the area in which the slot wedge groove is found. An inspection of figures 6.45 and 6.46 reveals the grooves for the stator slot wedges that are very close to the tips of the stator teeth. The narrowing of the stator teeth caused by these wedges also helps explain the increase in the flux density at the tooth tips.

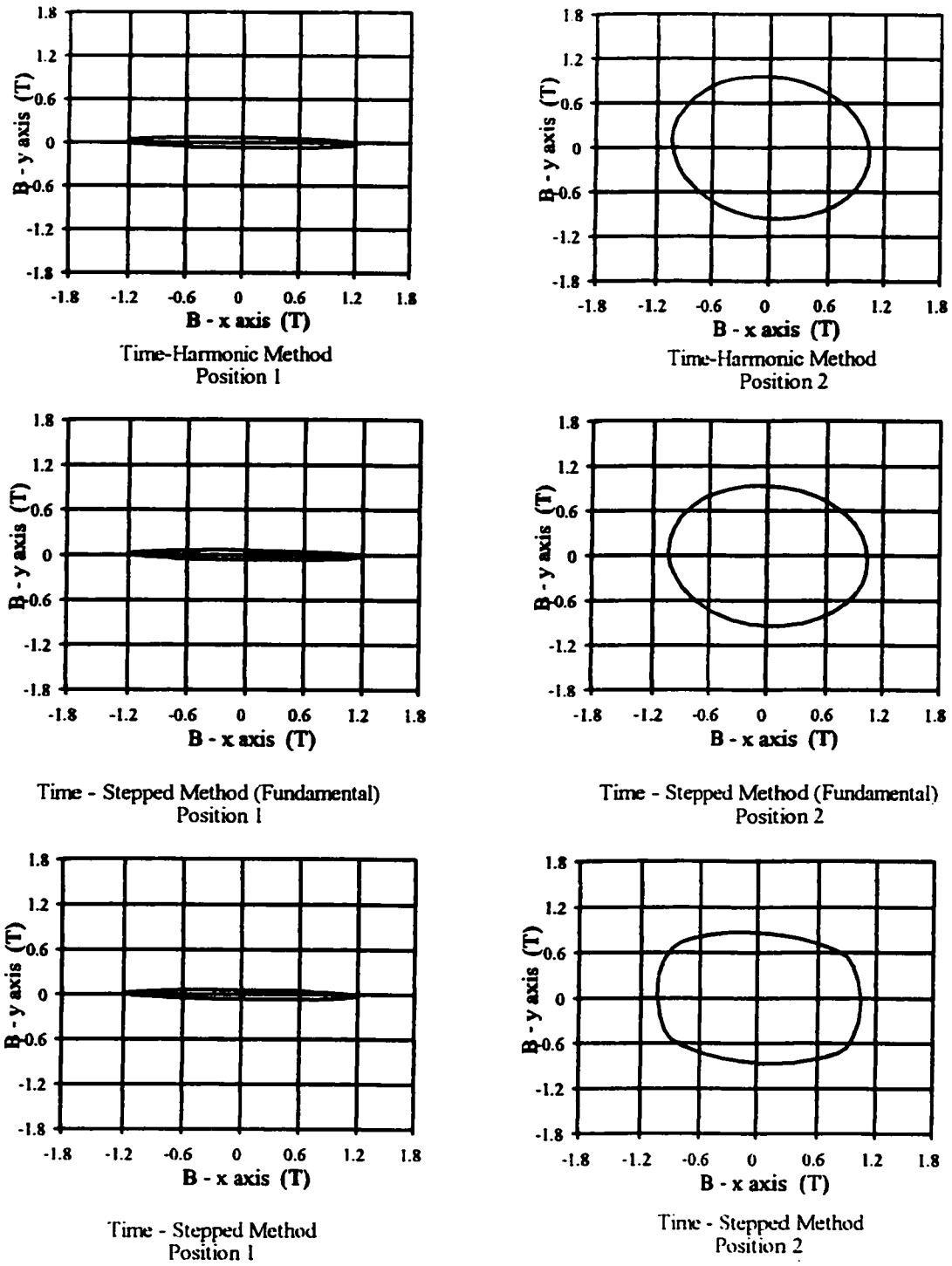

Figure 6.50 - Flux density loci for six pole machine. Positions 1 and 2.

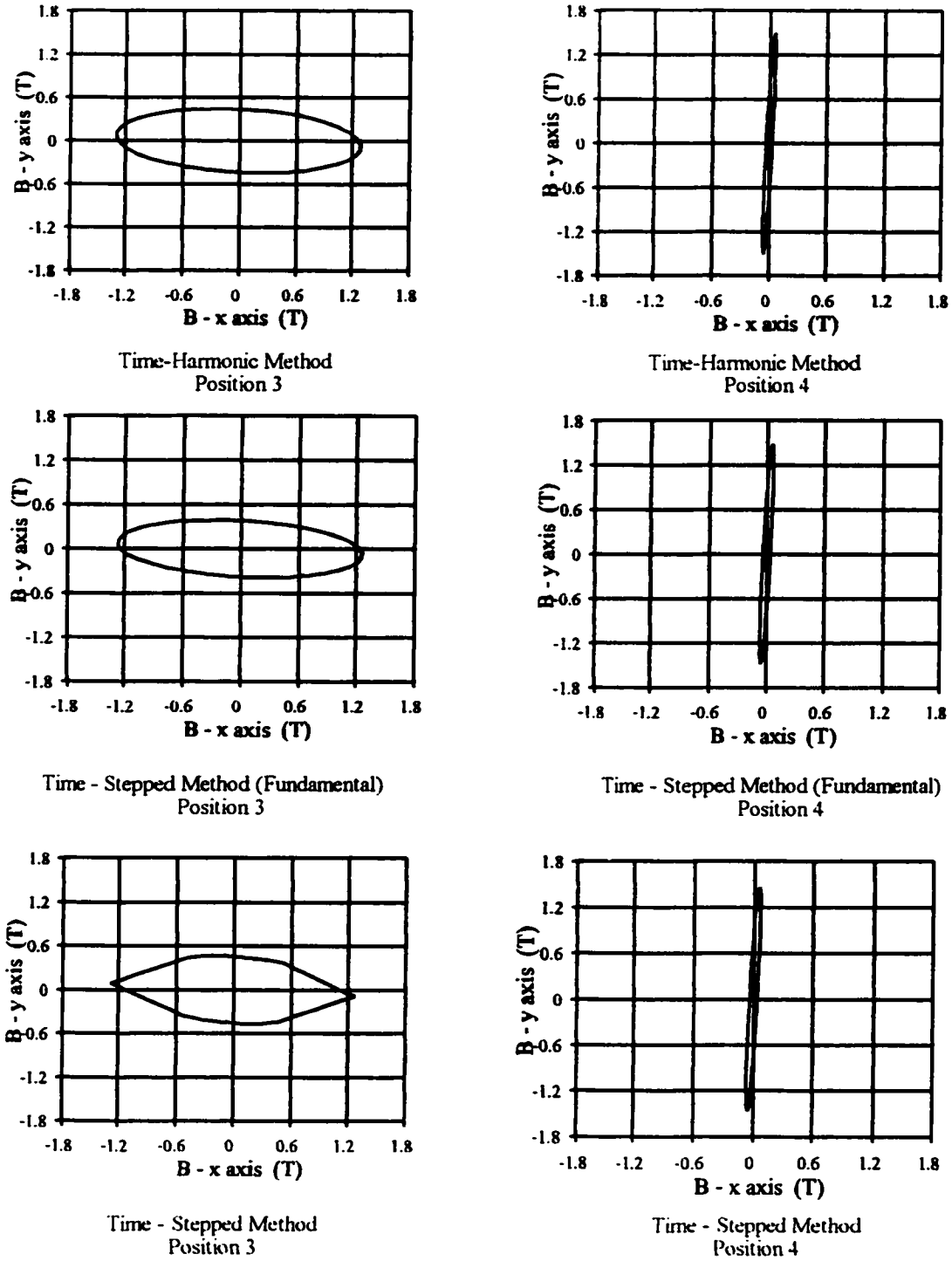

Figure 6.51 - Flux density loci for six pole machine. Positions 3 and 4.

Table 6.8 - Loss Estimates for Six Pole Machine

Method	Yoke Loss TH (Δ% from I)	Yoke Loss TSM (Δ% from I)	Tooth Loss TH (Δ% from I)	Tooth Loss TSM (Δ% from I)
I	7.42 kW (0.0)	7.32 kW (0.0)	2.75 kW (0.0)	2.68 kW (0.0)
II	7.49 kW (1.0)	7.38 kW (0.9)	NA	NA
III	7.07 kW (-4.7)	6.96 kW (-4.9)	3.07 kW (11.8)	2.75 kW (2.8)
IV	7.99 kW (7.2)	7.87 kW (7.5)	2.68 kW (-2.7)	2.60 kW (-3.1)
V	8.11 kW (9.4)	7.99 kW (9.2)	NA	NA
VI	7.90 kW (6.5)	7.79 kW (6.5)	NA	NA

Figures 6.50 and 6.51 show some flux density loci for positions similar to those described in the previous two cases. Note that for positions 3 and 4, the flux densities obtained by the TH simulations are slightly larger than those obtained by plotting the fundamental of the TSM solutions. At positions 1 and 2, the results are in much closer agreement. The results for the TSM solutions at positions 2 and 3 show that the loci are not purely elliptical and that the waveforms have some harmonic content.

Table 6.8 summarizes the loss estimates by the six methods of analysis. The results for this machine are similar to those found for the previous two cases. Method III gives losses that are lower than methods I and II. The yoke losses given by methods V and VI are greater than those given by methods I and II. Once again, this suggests that the method of superposition over estimates the losses caused by the rotational fields, while using the 50:50 Epstein test data underestimates the losses. We can estimate the difference incurred in the calculation of yoke loss when using the 50:50 Epstein test curve, and the method of superposition based on the PRL curves if we consider method I to be the most rigorous method. With the results of the TH simulation, method III gives a difference of -4.7% and method VI gives a difference of 6.5%. Using the results of the TSM simulations, method III

gives a difference of -4.9% and method VI gives a difference of 6.5 %. If we turn to the tooth losses, we see from the results of the TH simulations, that the losses given by method III differ from those given by method I by 11.8%. The losses given by method IV differ from those given by method I by -2.7%. If we use the results of the TSM simulation, we see that method III differs from method I by 2.8% and method IV differs from method I by -3.1%.

6.8.4 Results for Eight Pole Machine

The eight pole machine under investigation is a 3500 hp (2610 kW), 4 kV machine with 120 stator slots (15 slots/pole) and 142 rotor slots (17.75 slots/pole). The mesh used to model this machine has 4152 nodes, 8178 elements, and 96 constraints. Note that this machine was modelled with 18 rotor slots/pole. A four pole pitch model (i.e., half the machine geometry) would be necessary to model the number of rotor slots in the machine exactly. To model half the machine geometry, the number of elements in each pole span would be roughly one fourth of that used in the model described above. A coarser mesh would have resulted and greatly reduced the accuracy of the field calculation in the stator. The machine was modelled with the simplified rotor geometry to avoid using a very coarse mesh. Figure 6.52 shows the winding pattern of the machine and the boundary conditions used to model the problem. Boundary conditions similar the ones used for the four and six pole machines were utilized; the outer and inner diameters of the machine were constrained with the unary condition and the sides of the model were constrained with the anti-period condition. Figure 6.53 shows the no load flux distribution resulting from one of the magnetostatic solutions.

Figures 6.54 and 6.55 show, in respective order, the real and imaginary components of the flux distribution for one tooth pitch of the machine. Note that for this machine, the real component corresponds very closely to the instant at which the flux density in the tooth is at a maximum and the imaginary component corresponds very closely to the instant in time

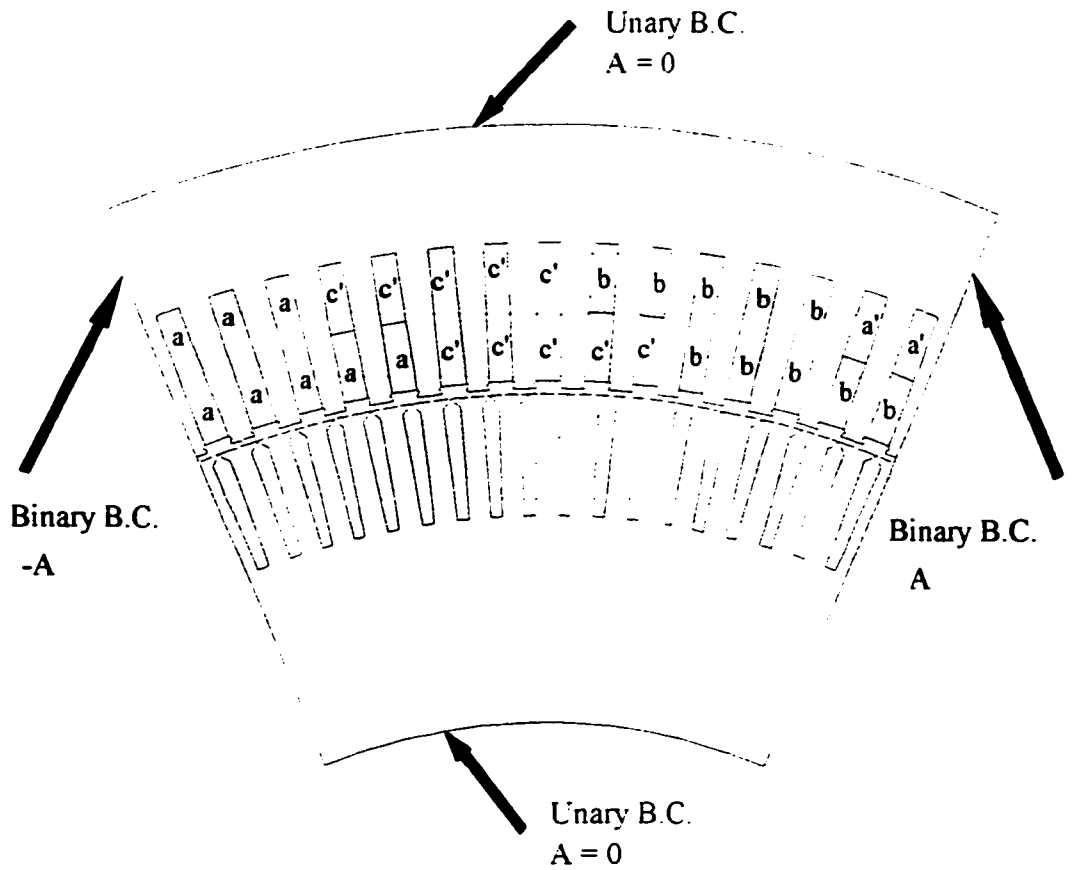

Figure 6.52 - Winding pattern and boundary conditions for eight pole machine.

at which the flux density in the yoke is at a maximum. Figures 6.56 and 6.57 show the distribution of the radial and tangential flux density in the machine yoke taken along the radial centre lines of a machine tooth and slot. The flux density polarization is much stronger along the radial line behind the stator tooth as was noted for the previous two machines. In figure 6.56, a circular flux density polarization of 1.1T is found at approximately 8% of the radial distance into the yoke. Behind the stator slot (figure 6.57), the strongest flux density polarization exhibits an aspect ratio of approximately 0.33. This occurs at approximately 20% of the radial distance into the yoke.

Figure 6.58 shows a plot of the radial and tangential flux densities along the centerline

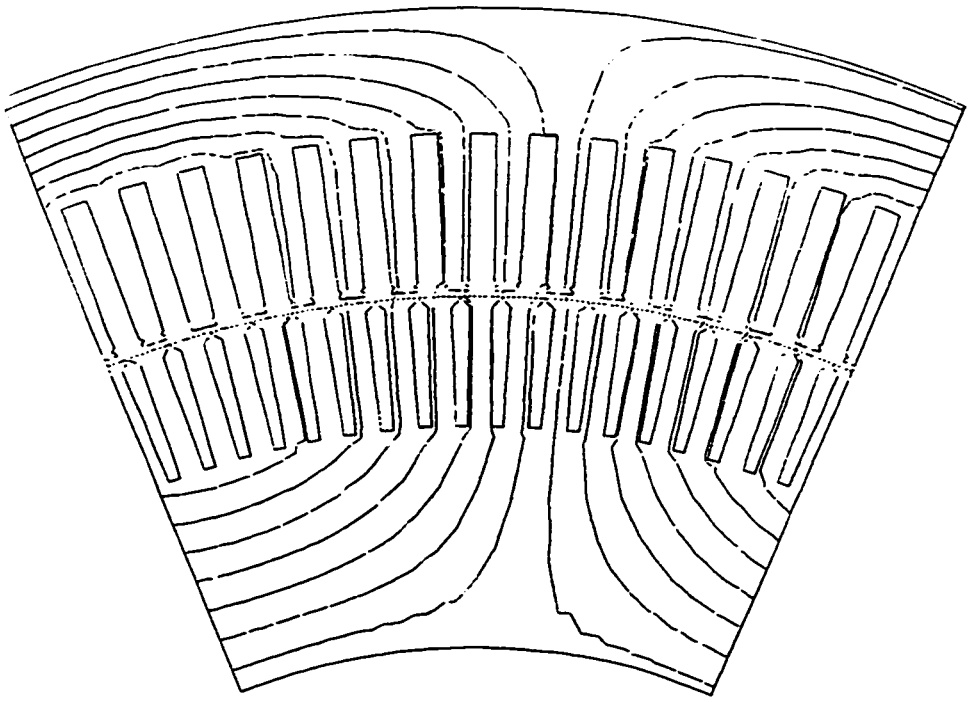

Figure 6.53 - No-load flux distribution in eight pole induction motor.

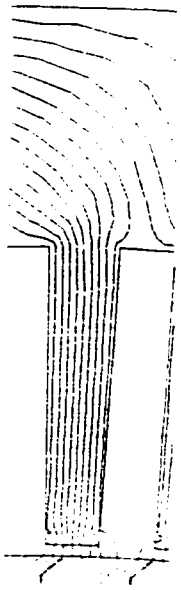

Figure 6.54 - Plot of Re[A] in eight pole induction motor.

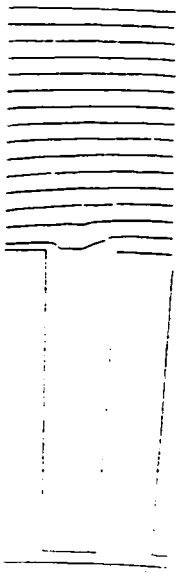

Figure 6.55 - Plot of Im[A] in eight pole induction motor.

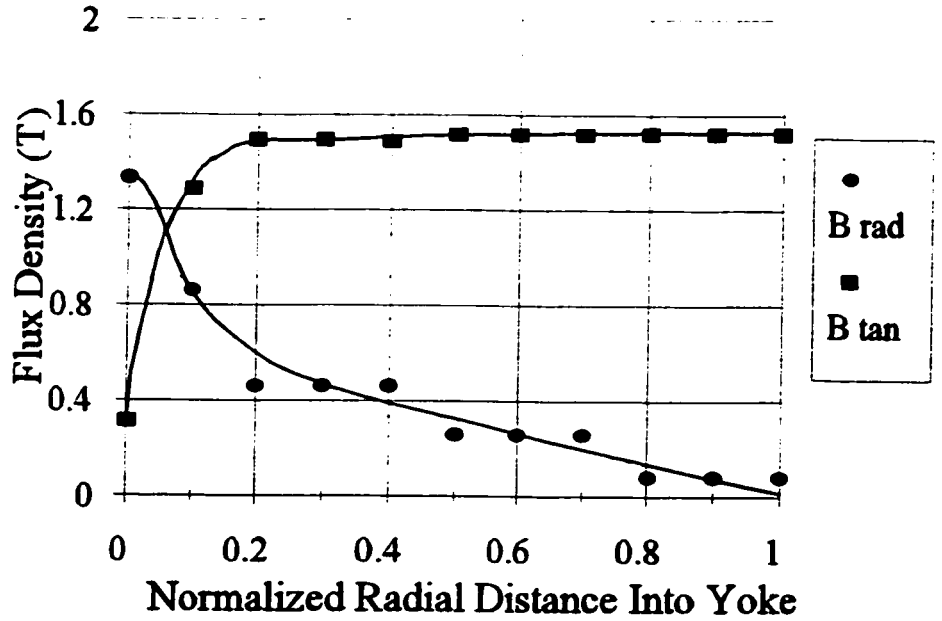

Figure 6.56 - Radial and tangential flux density. Eight pole yoke behind stator tooth.

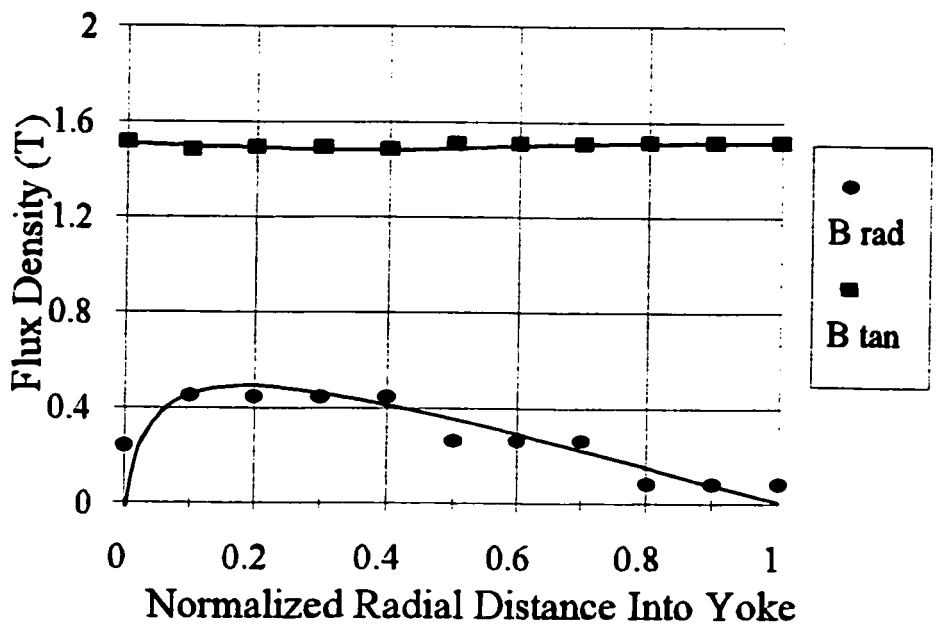

Figure 6.57 - Radial and tangential flux density. Eight pole yoke behind stator slot.

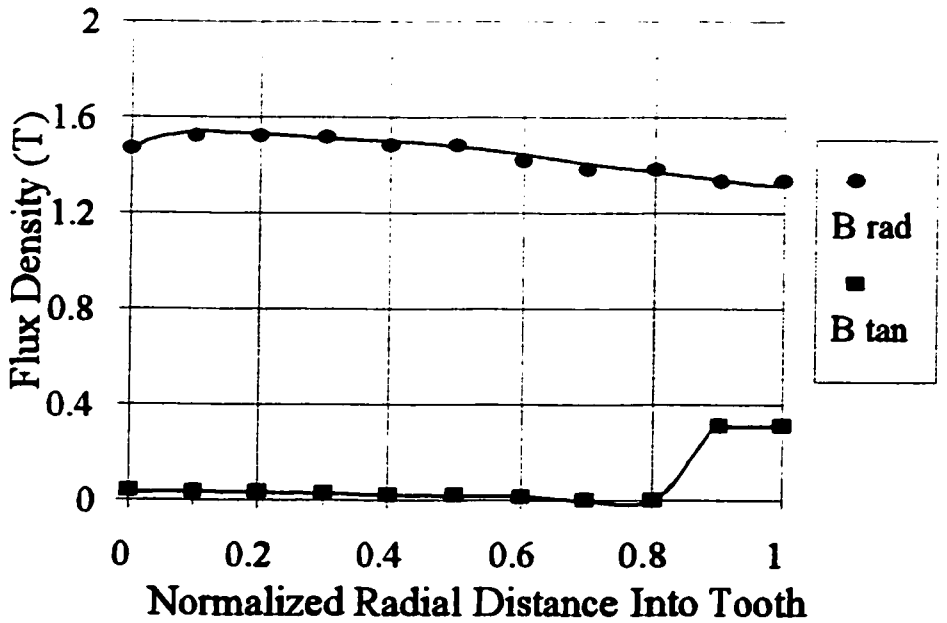

Figure 6.58 - Radial and tangential flux density. Eight pole stator tooth.

of one of the stator teeth. There is very little tangential component of flux density in the tooth except for the vicinity of the stator tooth root. Note that the curve for the tangential flux is flat near the tooth root. This occurred because the points at 90% and 100% of the radial distances into the tooth both lie on the same element. Since the flux density is constant over the entire area of a first order element, the two points must have the same value. The radial flux density is generally higher towards the tooth tip than gradually lessens towards the root of the tooth due to the taper of the tooth. At the very tip of the tooth, the radial flux density is slightly lower than the value obtained at 10% of the distance into the tooth. This is caused by a slight increase in the radial flux density caused by the narrowing of the tooth by the grooves for the slot wedges (see figures 6.54 and 6.55). Also note the leakage flux in figure 6.54 which tends to lower the radial flux density at the very tip of the tooth.

Figures 6.59 and 6.60 show some flux density loci for positions similar to those described in the previous three cases. Note that for all four positions, the flux densities

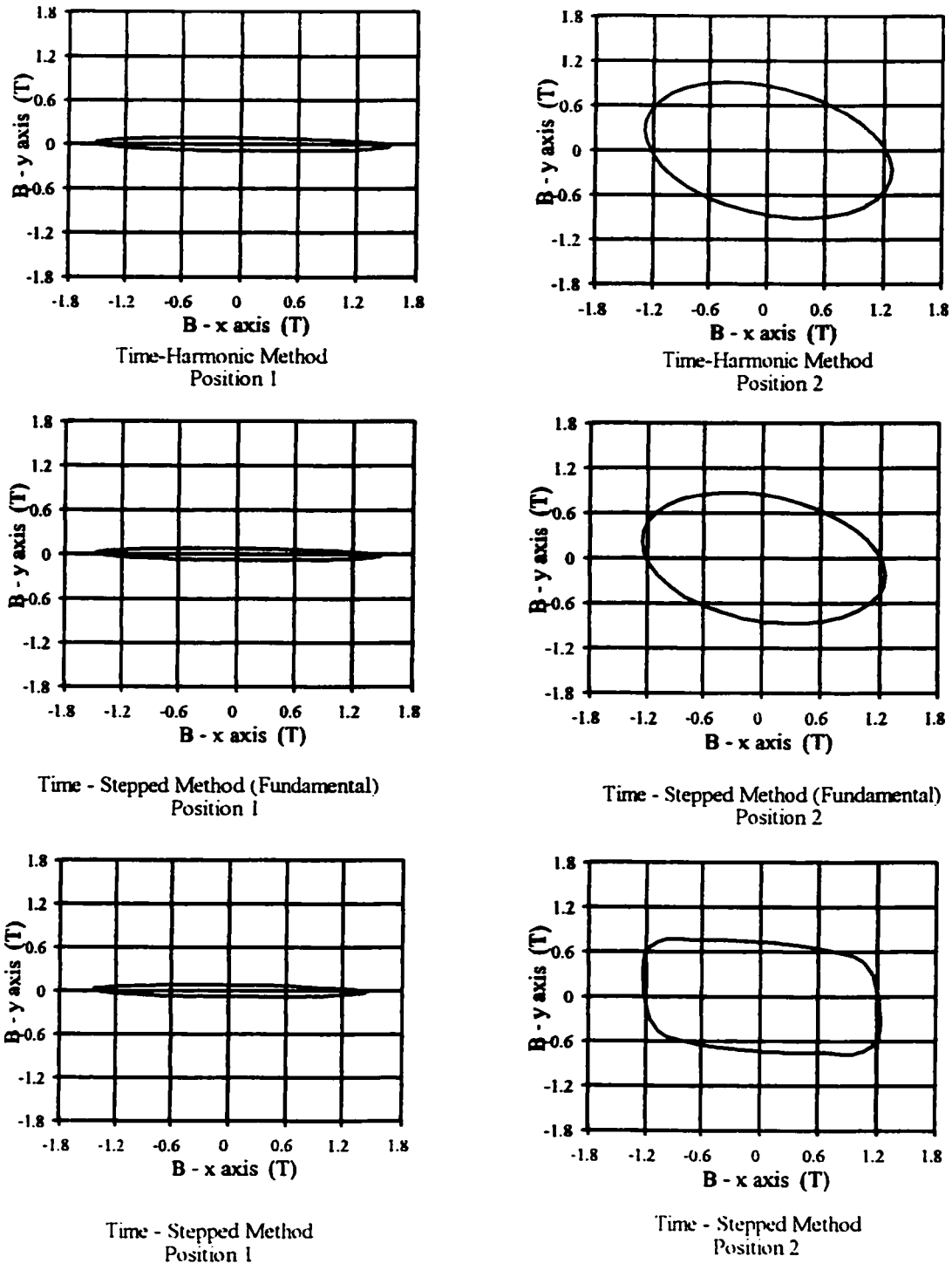

Figure 6.59 - Flux density loci for eight pole machine. Positions 1 and 2.

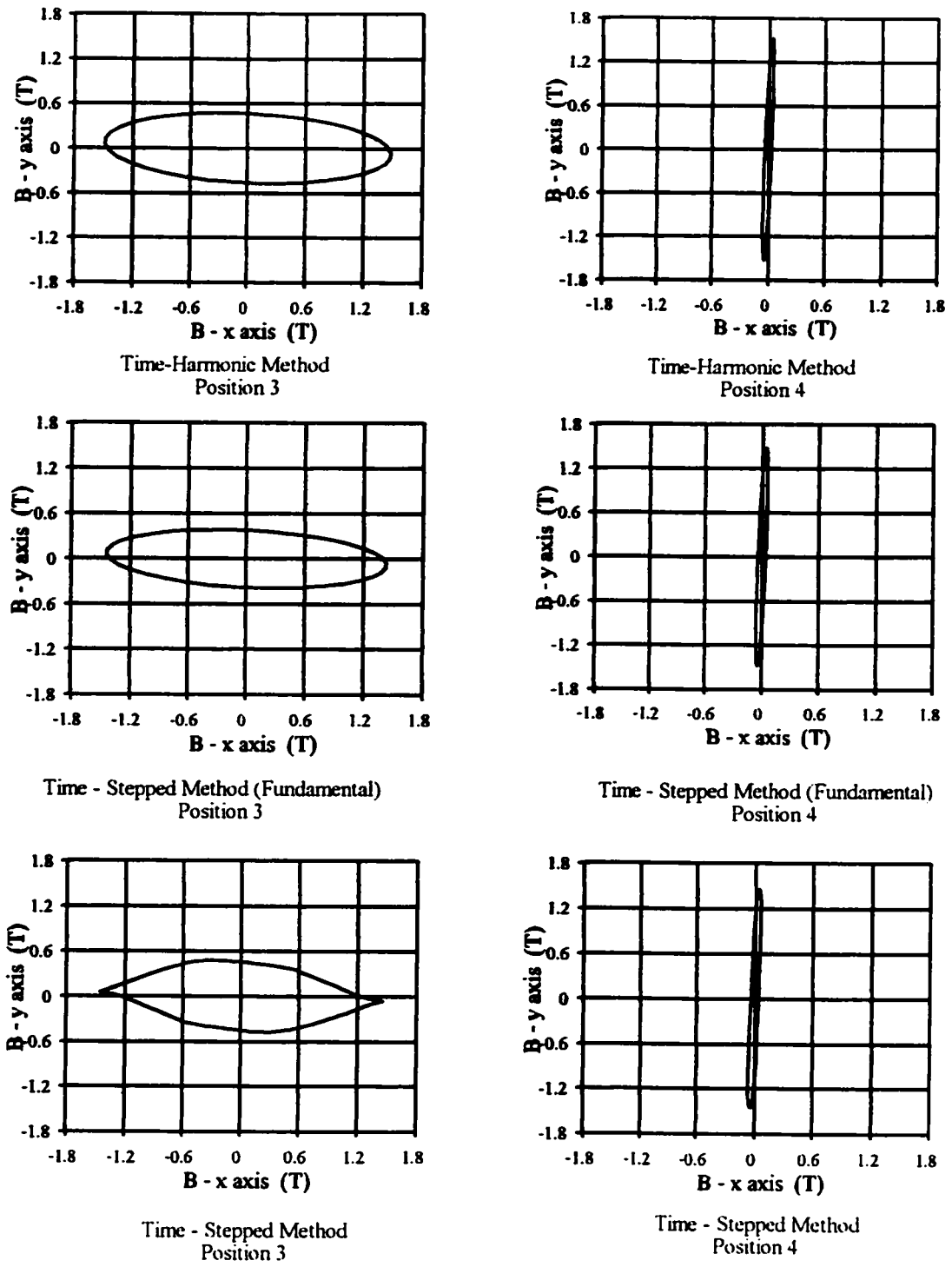

Figure 6.60 - Flux density loci for eight pole machine. Positions 3 and 4.

Table 6.9 - Loss Estimates for Eight Pole Machine

Method	Yoke Loss TH (Δ% from I)	Yoke Loss TSM (Δ% from I)	Tooth Loss TH (Δ% from I)	Tooth Loss TSM (Δ% from I)
I	4.79 kW (0.0)	4.49 kW (0.0)	2.05 kW (0.0)	1.91 kW (0.0)
II	4.84 kW (1.0)	4.53 kW (0.8)	NA	NA
III	4.64 kW (-3.1)	4.36 kW (-2.8)	2.31 kW (12.8)	2.14 kW (11.8)
IV	5.24 kW (9.4)	4.93 kW (9.8)	2.01 kW (-1.9)	1.86 kW (-2.7)
V	5.27 kW (9.9)	4.95 kW (10.3)	NA	NA
VI	5.04 kW (5.1)	4.72 kW (4.9)	NA	NA

obtained by the TH simulations are slightly larger than the those obtained by plotting the fundamental of the TSM solutions. The results for the TSM solutions at positions 2 and 3 show that the loci are not purely elliptical and that the waveforms have some harmonic content. Note that, as has been the case in the previous results, the flux densities at the back of the yoke (position 1) and the lower portion of the tooth (position 4) are nearly purely alternating.

Table 6.9 shows a summary of the loss estimates by the six methods of analysis. The results are similar to those in the previous three cases. Method III gives losses that are lower than methods I and II. The results given by methods V and VI are greater than those given by methods I and II. Once again, this suggests that the method of superposition over estimates the losses caused by the rotational fields. We can estimate the difference incurred in the calculation of yoke loss when using the 50:50 Epstein test curve, and the method of superposition based on the PRL curves if we consider method I to be the most rigorous result. Looking at the results of the TH simulation, method III gives a difference of -3.1% and method VI gives a difference of 5.1%. From the results of the TSM simulation, method III differs from method I by -2.8% and method VI gives a difference of 5.1%. In the teeth,

using the TH simulation, method III differs from method I by 10.8% and method IV differs from method I by -1.9%. Using the TSM simulation, method III differs from method I by 11.8% and method IV differs from method I by -2.7%.

6.8.5 Results for Ten Pole Machine

The ten pole machine under investigation is a 6000 hp (4474 kW), 6.6 kV machine with 120 stator slots (12 slots/pole) and 142 rotor slots (14.2 slots/pole). The mesh used to model this machine has 4382 nodes, 8636 elements, and 90 constraints. Note that this machine was modelled with 14 rotor slots/pole. A five pole pitch model (i.e. half the machine) would be required to model the number of rotor slots exactly.

To model half the machine geometry, the number of elements in each pole span would be roughly one fifth of that used in the model described above. To avoid the coarser mesh, the single pole pitch model was used. The small error in the stator flux density caused by this simplification in rotor geometry does not justify the use of a five pole pitch model. Figure 6.61 shows the winding pattern of the machine and the boundary conditions used to model the problem. The boundary conditions are similar the ones used for the four, six, and eight pole machines discussed in the previous sections of this chapter. Figure 6.62 shows the no load flux distribution resulting from one of the magnetostatic solutions.

Figures 6.63 and 6.64 respectively show the real and imaginary components of the flux distribution for one tooth pitch of the machine. Figures 6.65 and 6.66 show the distribution of the radial and tangential flux density in the machine yoke taken along radial centre lines of a machine tooth and slot. The flux density polarization is much stronger along the radial line behind the stator tooth as was noted for the previous two machines. A circular flux density polarization of about 1T is found at approximately 8% of the radial distance into the yoke. Behind the stator slot, the strongest flux density polarization exhibits an aspect ratio of just over 0.4. This occurs at approximately 20% of the radial distance into the yoke.

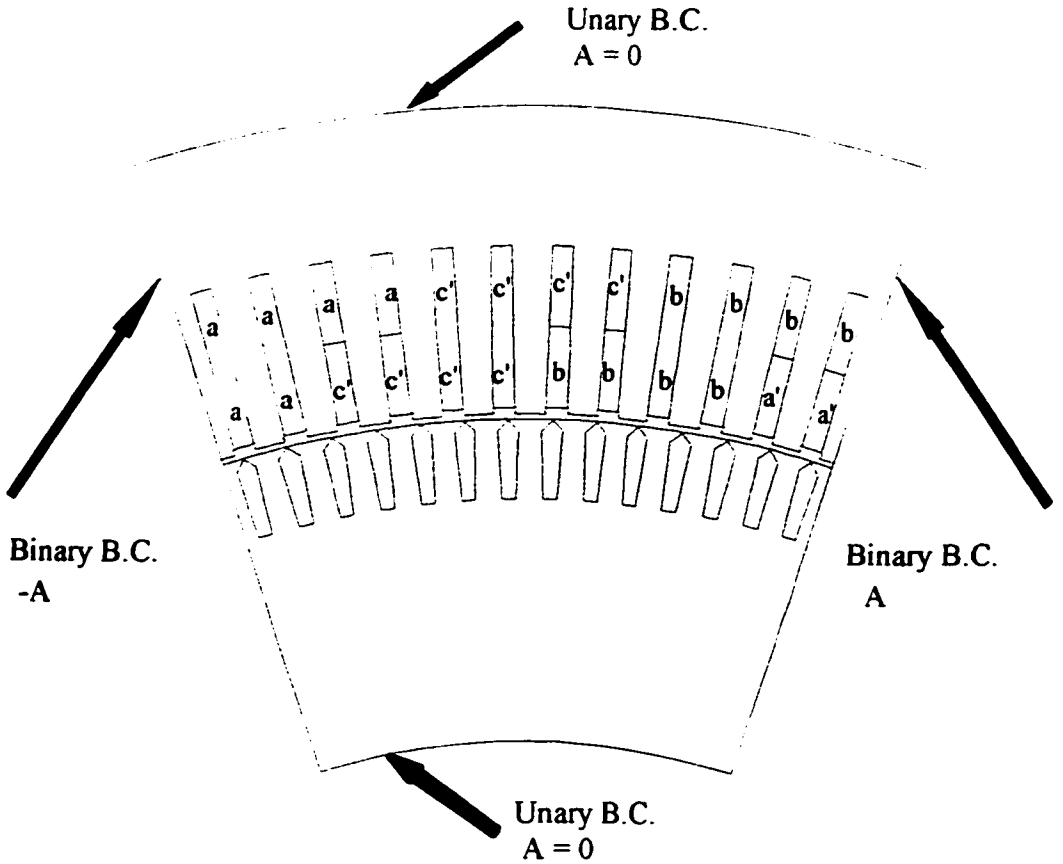

Figure 6.61 - Winding pattern and boundary conditions for ten pole machine.

Figure 6.67 shows a plot of the radial and tangential flux densities along the centerline of one of the stator teeth. There is very little tangential component of flux density in the tooth except for the vicinity of the stator tooth root, where the tangential component of the flux density rises sharply as the inner periphery of the yoke is approached. This is attributable to some of the tangential flux in the yoke leaking into the tooth root. The radial component of the flux density is greatest at the tooth tip and gradually weakens at the tooth root. This is attributable to the tooth taper; the tooth is narrower at the tip than at the root.

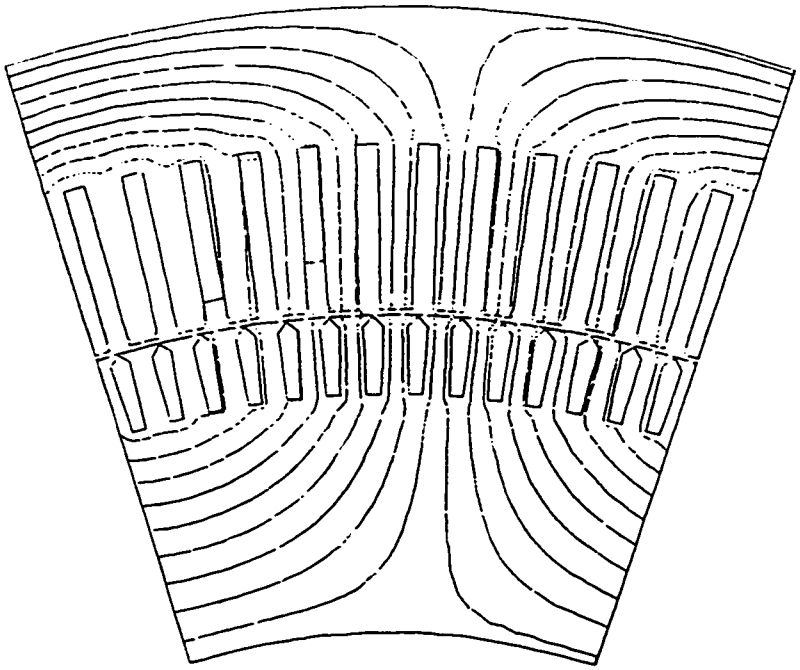

Figure 6.62 - No-load flux distribution in ten pole induction motor.

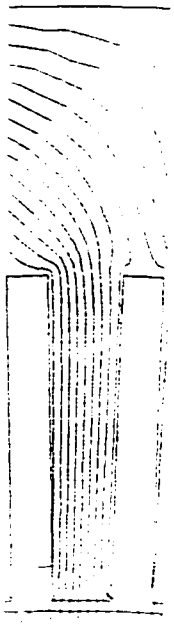

Figure 6.63 - Plot of Re[A] in ten pole induction motor.

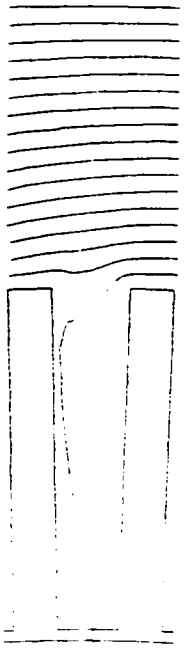

Figure 6.64 - Plot of Im[A] for ten pole induction motor.

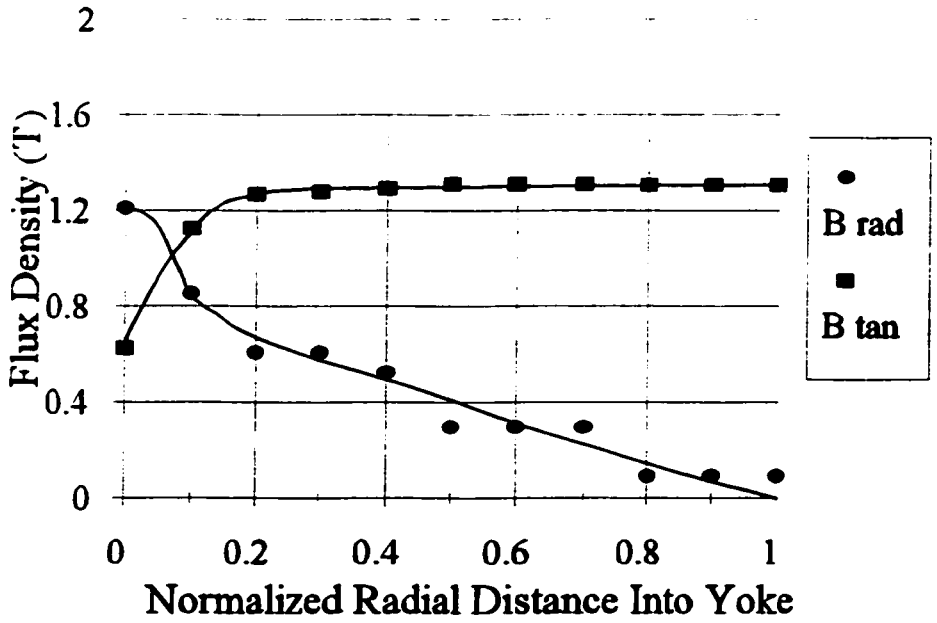

Figure 6.65 - Radial and tangential flux density. Ten pole yoke behind stator tooth.

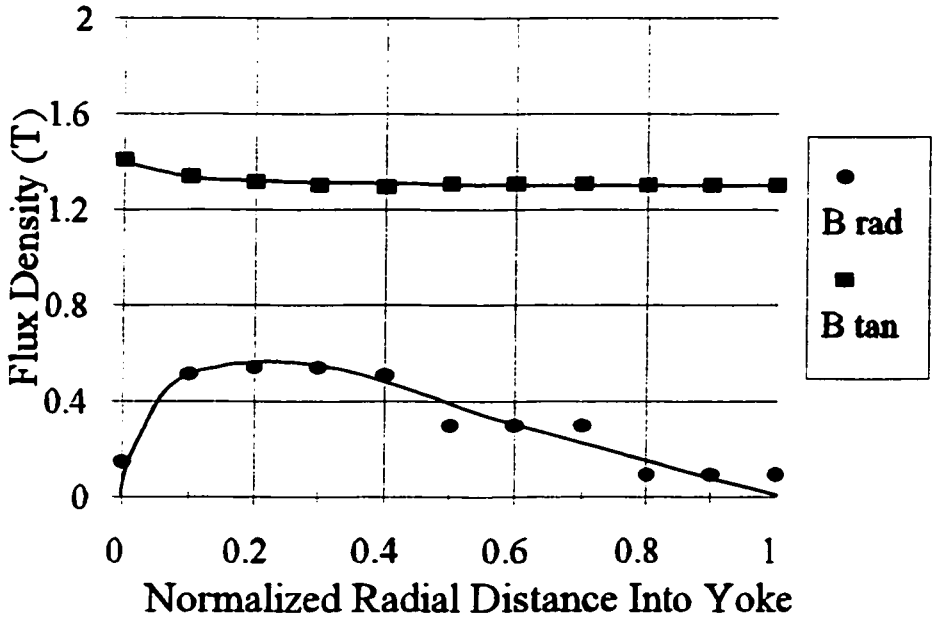

Figure 6.66 - Radial and tangential flux density. Ten pole yoke behind stator slot.

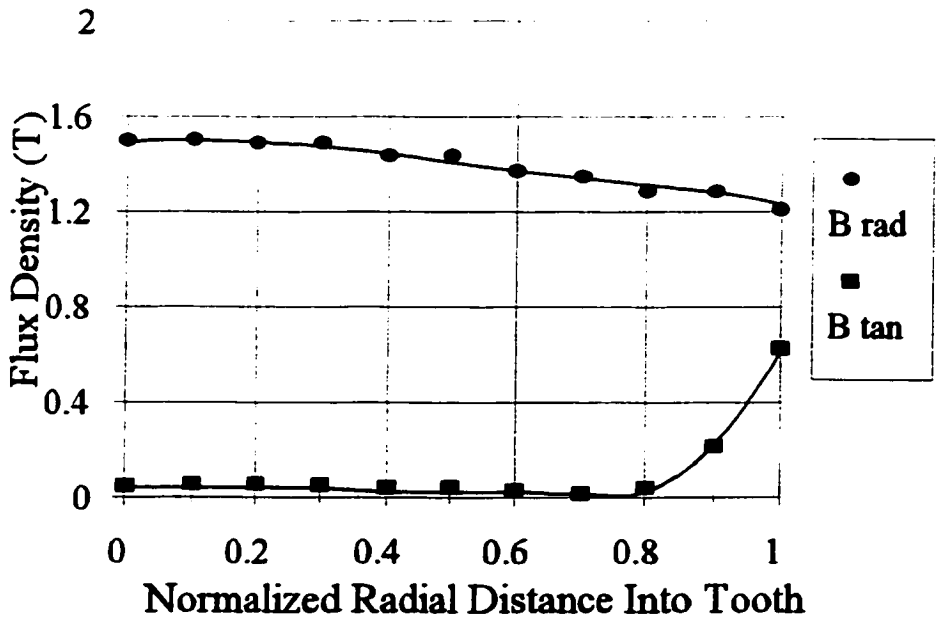

Figure 6.67 - Radial and tangential flux density. Ten pole yoke stator tooth.

Figures 6.68 and 6.69 show some flux density loci for positions similar to those described in the previous four cases. Note that for position 2, the flux densities in the tangential and radial directions obtained by the TH simulation are slightly larger than those obtained by plotting the fundamental of the TSM solutions. For the remaining positions, the flux densities but the two methods are very similar. The results for the TSM solutions at positions 2 and 3 indicate that the loci are not purely elliptical and that the waveforms have some harmonic content. Note that, as in the previous results, the flux densities at the back of the yoke (position 1) and the lower portion of the tooth (position 4) are nearly purely alternating.

Table 6.10 shows a summary of the loss estimates by the six methods of analysis. The results are similar to those in the previous four cases. Method III gives losses that are lower than methods I and II. The results given by methods V and VI are greater than those given by methods I and II. Once again, this suggests that the method of superposition over estimates the losses caused by the rotational fields. We can estimate the difference incurred

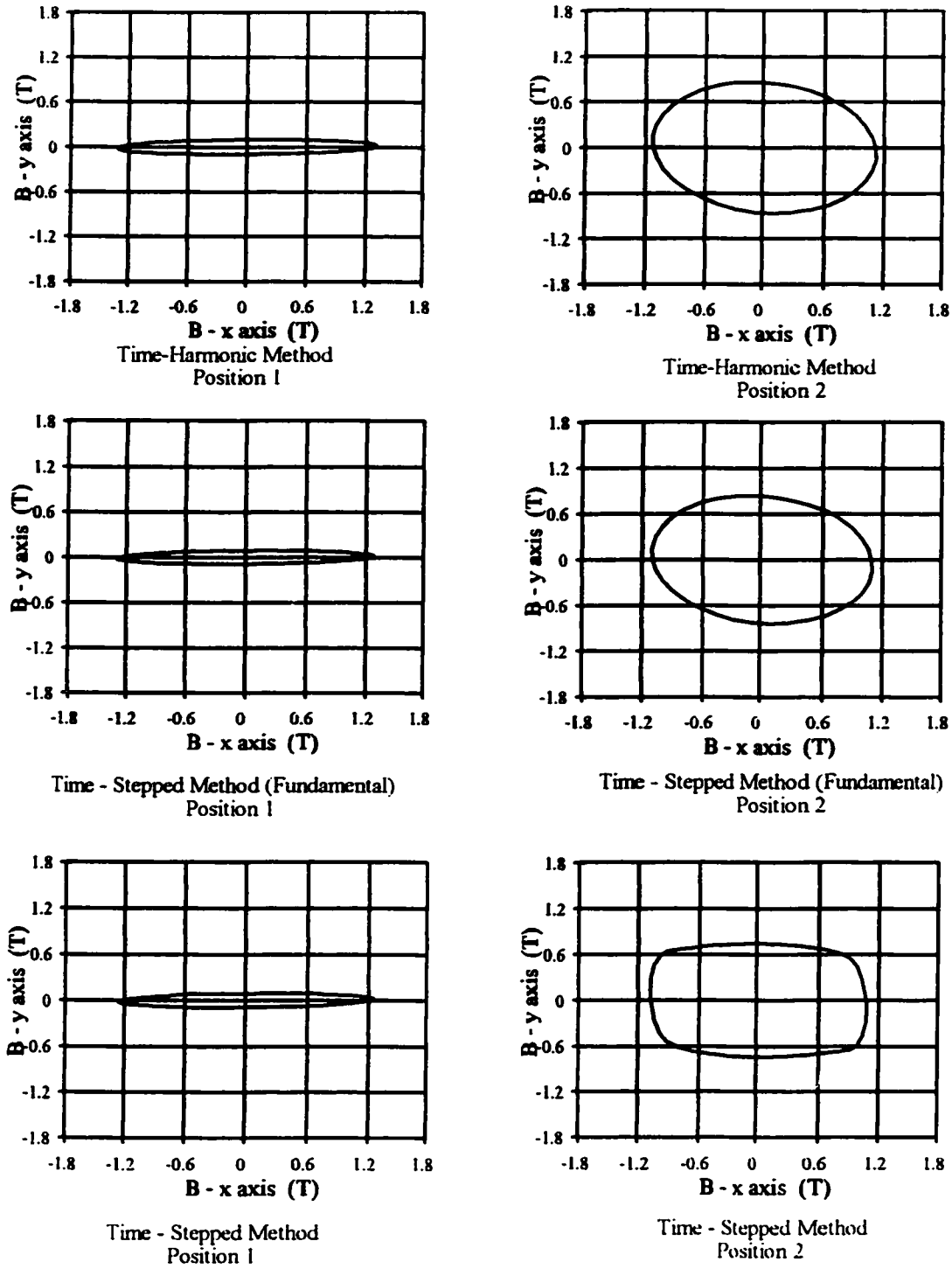

Figure 6.68 - Flux density loci for ten pole machine. Positions 1 and 2.

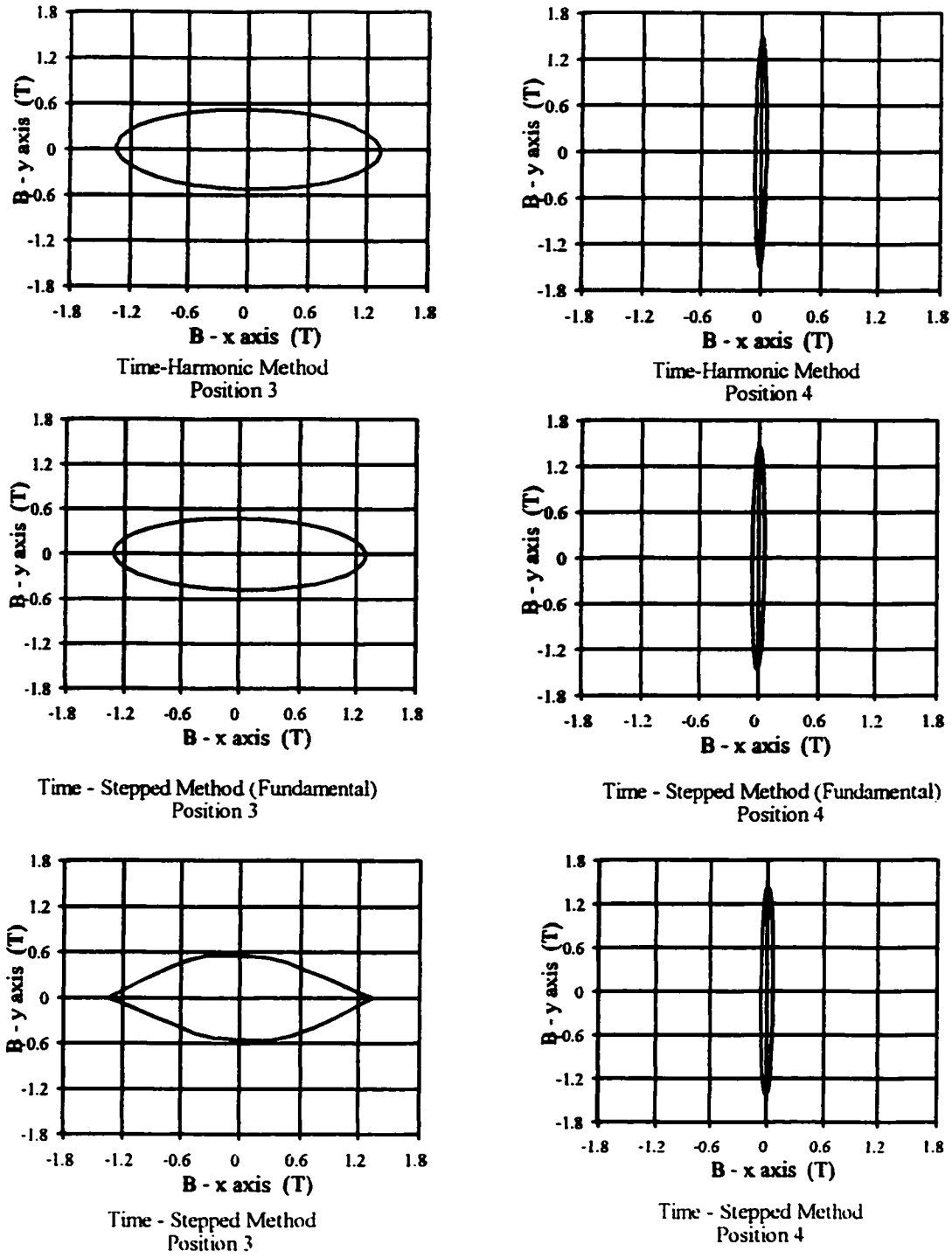

Figure 6.69 - Flux density loci for ten pole machine. Positions 3 and 4.

Table 6.10 - Loss Estimates for Ten Pole Machine

Method	Yoke Loss TH (Δ% from I)	Yoke Loss TSM (Δ% from I)	Tooth Loss TH (Δ% from I)	Tooth Loss TSM (Δ% from I)
I	8.02 kW (0.0)	7.74 kW (0.0)	4.87 kW (0.0)	4.62 kW (0.0)
II	8.10 kW (0.9)	7.81 kW (0.9)	NA	NA
III	7.86 kW (-1.9)	7.55 kW (-2.4)	5.44 kW (11.8)	5.12 kW (10.8)
IV	8.88 kW (10.8)	8.53 kW (10.2)	4.73 kW (-2.7)	4.45 kW (-3.6)
V	8.91 kW (11.1)	8.57 kW (10.7)	NA	NA
VI	8.56 kW (6.8)	8.27 kW (6.8)	NA	NA

in the calculation of yoke loss when using the 50:50 Epstein test curve, and the method of superposition based on the PRL curves if we consider method I to be the most rigorous result. Comparing the results obtained from the TH simulation, method III gives a difference of -1.9% and method VI gives a difference of 6.8%. Comparing the results obtained from the fundamentals of the TSM solutions, method III gives a difference of -2.4% and method VI gives a difference of 6.8%. In the stator teeth, for the TH simulation, method III gives a difference of 11.8% and method IV gives a difference of -2.7%. For the TSM simulation, method III gives a difference of 10.8% and method IV gives a difference of -3.6%.

6.9 Summary of Iron Loss Calculations and Discussion of Results

The results of the preceding sections show that the effects of rotational losses are small but consistently noticeable. For each of the five machines analysed, method I (which takes account of the rotational losses most rigorously), consistently gives loss values that are intermediate to those given using the 50:50 Epstein test results (method III) and those using the method of superposition of alternating losses (methods V and VI). Method I also gives lower estimates of loss when compared with method IV (for which the flux in each finite

element is assumed to alternate and the td losses are used in the yoke). Losses in the yoke are underestimated by using the 50:50 Epstein test results and assuming that the flux is alternating in each element of the model. The yoke losses are underestimated because the laminations in the yoke are predominantly arranged such that they lie in the td of the sheet. When the 50:50 Epstein losses are used to make the estimate of yoke losses, half the laminations in the yoke are assumed to lie in the rd of the sheet (the rd exhibits lower losses as shown in Chapter 5). The losses in the yoke are overestimated if the rotational losses are approximated by using the superposition of alternating losses in the rd and td of the sample. As we saw in Chapter 5, the method of superposition tends to overestimate the rotational losses. This is especially noticeable at higher flux densities. When using method IV, the losses are over estimated because the decrease in rotational losses at higher flux densities (shown in Chapter 5) is not accounted for.

When 50:50 Epstein test results are used to estimate the losses in the teeth, the losses are generally overestimated. The teeth lie in a direction that most closely corresponds to the rolling direction of the sheet. When alternating losses are measured using a 50:50 Epstein square, half the strips are cut in the rd and half are cut in the td. The losses in the td are larger than those in the rd and lead to a higher estimate of the tooth losses when compared with method I. The higher losses in the teeth do not necessarily cancel the lower loss estimate in the yoke. Conceptually, this would only occur if the mass of the teeth were exactly the same as the mass of the yoke and both members were operated at the same flux density level. Method I captures the effects of the rotational losses in the tooth root caused by the polarization of the flux density evident in figures 6.30, 6.40, 6.49, 6.58 and 6.65. Method IV gives less difference in the estimate of the tooth losses. This result suggests that the effect of rotational losses in the tooth root are not very strong. Examination of the figures mentioned above shows that the flux density is only weakly polarized (aspect ratios of the ellipses are small).

Method I only gives an approximate estimate of the anisotropy effects of the sheet. The losses are adjusted according to the direction of the major axis of the ellipse based on alternating loss measurements under alternating flux conditions. As such, the method tends to overestimate the effects of the anisotropy due to the inclination angle of the ellipse. In reality, the decrease in losses caused by the major axis lying at some angle from the td is partially offset by the increase in losses caused by the minor axis lying at some angle from the rd closer to the td. Despite this, the proposed method may offer a practical, if approximate, estimate of the anisotropy effects. To model the effect more accurately, a family of curves such as the ones presented in figures 5.35 and 5.36, would have to be produced for various arbitrary angles to the rolling direction. The time required to do this would be excessive and perhaps impractical in an industrial setting. Also note, that we may expect the effects of anisotropy to be small as suggested by only the small differences in results obtained by methods I and II.

As shown in tables 6.6 through 6.10, the TSM results consistently give losses that are slightly lower than the results obtained from the TH solutions. This occurs because for a given value of no load or magnetizing current, the TH solutions yield higher flux density values than the magnetostatic solutions. To understand how this can happen, we refer to figure 6.4. From this graph, we can see that for a given value of magnetizing field strength (proportional to magnetizing current), the modified curve used in the TH simulation will yield a higher flux density. As was discussed in section 6.5, the no load currents used in the simulation were taken from measured results. It was felt that using tested values of no load current would give the most accurate estimate of the flux density in the machine. In fact, it may have been more appropriate to derive an estimated value of no load current from the finite element solutions based on the flux density required to produce the rated voltage at the machine terminals. Using this approach, the working flux densities in the machines could be

Table 6.11 - Average Differences From Method I

Method	Yoke Loss TH (avg. Δ% from I)	Yoke Loss TSM (avg. Δ% from I)	Tooth Loss TH (avg. Δ% from I)	Tooth Loss TSM (avg. Δ% from I)
I	0.0	0.0	0.0	0.0
II	1.0	0.9	NA	NA
III	-4.3	-4.2	12.0	9.6
IV	8.0	8.2	-2.6	-3.2
V	9.2	9.3	NA	NA
VI	6.4	5.5	NA	NA

determined more accurately for both methods of simulation. The machines in this investigation were also modelled using the design values for the air gaps. If the machines were built with air gaps that were slightly off the design value, the manufacturing error would manifest itself in the amount of magnetizing current drawn by the machine. This in turn would lead to some error in the flux density values yielded by the simulations.

Table 6.11 summarizes the results of the fundamental frequency loss calculations in the stator yoke and teeth of the five machines under investigation. In the table, method I is used as a reference with which to compare the remaining five methods. The values in the table are expressed as the average percentage difference obtained by the method in the first column when compared with method I.

Refer to table 6.12. Note that the manufacturer's estimates of yoke losses are much larger than those obtained from using method I in conjunction with the TH and TSM finite element simulations. An examination of equation 6.17 reveals that a coefficient (K_{iron}) is used by the manufacturer to estimate the yoke losses. This loss value corresponds to a flux density value of 1.55T. Based on the results of Epstein tests, this value should be approximately 4.17 W/kg @1.55T (see figure 5.38 and average the value for the rd curve and td curve at 1.55T). As discussed in Section 6.2.3, the manufacturer uses a coefficient of 6.36

Table 6.12 - Comparison of Manufacturer's Estimates of Yoke Losses With Estimates by TH and TSM Method I

Machine	Manufacturer's Estimate of Yoke Losses		Estimate of Yoke Losses - Method I	
	With Empirical Calibration Factor (kW)	Without Empirical Calibration Factor (kW)	TH (kW)	TSM (kW)
Two Pole	16.92	11.06	9.37	8.91
Four Pole	9.88	6.46	8.30	7.09
Six Pole #1	12.20	7.98	7.42	7.32
Six Pole #2	12.20	7.98	7.42	7.32
Eight Pole	6.59	4.31	4.79	4.49
Ten Pole	12.62	8.25	8.02	7.74

W/kg at 1.55 T; therefore the losses in the yoke are scaled by a factor of 1.53. This is a clear example of what is often referred to in the machine industry as an "empirical calibration factor." The reason for using such a factor lies in the fact that simple design equations are often not detailed enough to model all the electromagnetic phenomena occurring in the machine rigorously. Table 6.12 gives the manufacturer's estimate both with and without the empirical calibration factor. Note that the manufacturer's results without the calibration factor agree more closely with the results of TH and TSM method I.

Now refer to table 6.13. Note that the manufacturer's estimates of tooth losses are much larger than those obtained from using method I in conjunction with the TH and TSM finite element simulations. An examination of equations 6.18 and 6.19 reveals that a coefficient (K_{iron}) is used by the manufacturer to estimate the losses in the tops and bottoms of the stator teeth. This loss value corresponds to a flux density value of 1.55T. The manufacturer uses a coefficient of 6.36 W/kg at 1.55 T for the teeth just as with the yoke. This means that the losses in the teeth are also scaled by a factor of 1.53. Note that the

Table 6.13 - Comparison of Manufacturer's Estimate of Tooth Losses With Estimates by TH and TSM Method I

Machine	Manufacturer's Estimate of Total Tooth Losses		Estimate of Tooth Losses - Method I	
	With Empirical Calibration Factor	Without Empirical Calibration Factor	TH (kW)	TSM (kW)
Two Pole	4.39	2.87	1.71	1.63
Four Pole	3.20	2.09	1.62	1.41
Six Pole #1	6.10	3.99	2.75	2.68
Six Pole #2	6.10	3.99	2.75	2.68
Eight Pole	3.59	2.35	2.05	1.91
Ten Pole	10.29	6.73	4.87	4.62

manufacturer's results without the calibration factor agree more closely with the results of TH and TSM method I, but still results in larger loss estimates for every case. In equations 6.18 and 6.19 the flux density in the teeth is multiplied by $\pi/2$ to convert it from an average value to a peak value. Perhaps this leads to a higher estimate of the tooth flux density than the more rigorous FE methods. Method I also takes into account the anisotropy of the material and since the teeth are oriented approximately along the rd, we would expect a lower estimate of the losses.

The reader is now referred to table 6.14. A comparison of the fundamental frequency losses in the stator yoke and teeth, with the total core losses measured by the manufacturer, yields an interesting point. The total iron losses in an induction motor are much larger than can be accounted for by estimating the fundamental frequency losses in the yoke and teeth, regardless of whether or not the rotational iron losses are accounted for. Comparing the sum of the fundamental frequency losses found in the yoke and teeth with the total no-load iron loss values (measured by the method discussed in Section 6.3, we find test to calculated (T/C) ratios ranging from 1.57 to 3.07. The manufacturer's estimates of the fundamental frequency

Table 6.14 - Comparison of Calculated Values of Yoke and Tooth Losses With Total Measured Losses

Machine	Total Tested Losses (kW)	Yoke and Tooth Losses					
		Design Equations*		TH Method I		TSM Method I	
		Calc. (kW)	T/C	Calc. (kW)	T/C	Calc. (kW)	T/C
2 Pole	32.4	13.93	2.33	11.08	2.92	10.54	3.07
4 Pole	22.1	8.55	2.58	9.92	2.23	8.50	2.60
6 Pole #1	22.08	11.97	1.84	10.17	2.17	10.00	2.21
6 Pole #2	21.07	11.97	1.76	10.17	2.07	10.00	2.11
8 Pole	13.63	6.66	2.05	6.84	1.99	6.40	2.13
10 Pole	23.5	14.98	1.57	12.89	1.82	12.36	1.90

* i.e the manufacturer's method without any scaling factors.

losses (see table 6.3) overemphasized their contribution to the overall losses. From this we must conclude that additional sources of core loss exist in the machines that require quantification. The losses measured by the method described in Section 6.3 yield the total no-load iron losses that include the high frequency (surface and pulsation) losses, losses in the stator space blocks, additional losses due to saturation, and losses in the frame of the machine caused by flux leakage. As a first step, we can include an estimate for the surface losses by the analytical approach used by the manufacturer.

We will investigate the correlation of test to calculated ratios when we include the manufacturer's estimate of the surface loss for each machine. This method of estimating surface losses was discussed in Section 6.2.4 and is given by equation 6.22. For machines with closed rotor slots, the manufacturer assumes that the pulsation losses in the machine can be ignored and they make no effort to estimate them. If we take the sum of the fundamental frequency losses in the yoke and teeth and add the manufacturers estimate of the surface

Table 6.15 - Comparison of Calculated Values of Yoke, Tooth, and Surface Losses With Total Measured Losses

Machine	Total Tested Losses (kW)	Surface Losses† (kW)	Total of Calculated Yoke, Tooth and Surface Losses					
			Design Equations* + Surface Losses		TH Method I + Surface Losses		TSM Method I + Surface Losses	
			Calc. (kW)	T/C	Calc. (kW)	T/C	Calc. (kW)	T/C
2 Pole	32.4	3.86	17.79	1.82	14.94	2.17	14.40	2.25
4 Pole	22.1	3.15	11.70	1.89	13.07	1.69	11.65	1.90
6 Pole #1	22.08	12.29	24.26	0.91	22.46	0.98	22.29	0.99
6 Pole #2	21.07	12.29	24.26	0.87	22.46	0.94	22.29	0.95
8 Pole	13.63	5.34	12.00	1.14	12.10	1.13	11.74	1.16
10 Pole	23.5	7.91	22.89	1.03	20.80	1.13	20.27	1.16

* i.e the manufacturer's method without any scaling factors.

† Surface losses calculated using the manufacturer's method as described in Section 6.2.4.

losses, the T/C ratios are much improved. The results are presented in table 6.15. Note that the discrepancy in the test to calculated ratios for the six, eight and ten pole machines is dramatically improved. The test to calculated ratios for the two and four pole machines are still rather large. Also note that a similar trend is apparent with all three methods. The calculated results are too low for the two and four pole machines, nearly equal or slightly larger than the tested values for the six pole machines, and slightly lower for the eight and ten pole machines. This result, suggests that the surface losses may constitute a major portion of the total no load losses in an induction machine. A major portion of the losses for the two and four pole machines remain unaccounted for.

As a further check, the surface losses were calculated using the formulation presented by Grieg and Freeman [189]. Bondi and Mukherji [188], presented a very comprehensive

Table 6.16 - Comparison of Calculated Values of Yoke, Tooth, and Surface Losses (Calculated by Grieg-Freeman Formulation) With Total Measured Losses

Machine	Total Tested Losses (kW)	Surface Losses† (kW)	Total of Calculated Yoke, Tooth and Surface Losses					
			Design Equations* + Surface Losses		TH Method I + Surface Losses		TSM Method I + Surface Losses	
			Calc. (kW)	T/C	Calc. (kW)	T/C	Calc. (kW)	T/C
2 Pole	32.4	4.68	18.61	1.74	15.76	2.06	15.22	2.13
4 Pole	22.1	3.67	12.22	1.81	13.59	1.63	12.17	1.81
6 Pole #1	22.08	10.03	22.00	1.00	20.20	1.09	20.03	1.10
6 Pole #2	21.07	10.03	22.00	0.96	20.20	1.04	20.03	1.05
8 Pole	13.63	4.53	11.19	1.22	11.37	1.20	10.93	1.25
10 Pole	23.5	6.27	21.25	1.11	19.16	1.22	18.63	1.26

* i.e the manufacturer's method without any scaling factors.
† Surface losses calculated using Grieg-Freeman formulation..

treatment of the tooth ripple phenomenon in smooth laminated pole shoes. They showed that apart from the notion of classical skin effect, there exists a second mode that penetrates deeply in the radial direction of the lamination. This second mode has a non-uniform distribution across the thickness of the lamination and the maximum value is found at the interface between the laminations. The equations presented by Bondi and Mukerji are quite complicated. Fortunately, Grieg and Freeman undertook the task of finding the most relevant terms of the equations and presented a simplified set of equations. They claim that their formulation under estimates the formulation of Bondi and Mukherji by no more than 10%.

Findlay and Briggs [190] described a test machine built to investigate pole face losses. In this apparatus, the rotor was slotted and rotated between two poles excited with a dc field. Rotor movement caused cyclic changes in reluctance below the poles and by that pole face

losses. The stationary poles were instrumented with thermistors and search coils and the authors measured the pole face losses by a calorimetric technique. Findlay [213] investigated the applicability of the Grieg-Freeman formulation using this test apparatus. He found that "...the results tend to be very conservative. That is that the values found in most cases tend to exceed the experimental values by a comfortable margin."

To undertake the Grieg-Freeman analysis, the first four air gap harmonics caused by the stator slotting had to be calculated. These were calculated using the method described by Freeman [214] and the estimate of the peak air gap flux density given by equation 6.6 multiplied by $\pi/2$. The results of the analysis are presented in table 6.16. A comparison of tables 6.15 and 6.16 reveals that the calculation procedure used by the manufacturer results in surface loss estimates that are similar to the results obtained by the Grieg-Freeman equations. For the two and four pole machines, the manufacturer's method yields a slightly lower estimate of the surface losses than the Grieg-Freeman formulation. For the six, eight, and ten pole machines, the Grieg-Freeman formulation yields a slightly lower estimate than the manufacturer's.

To calculate surface losses using the Grieg-Freeman formulation, a value of relative permeability must be assigned to the laminations. For all the cases presented in table 6.16, a relative permeability of 800 was used. This corresponds to the same value used by Birnstignl [196] in his derivation of the losses curve used by the manufacturer and presented in the paper by Alger et al [194]. This value was chosen to give a fair comparison of the two methods. The assignment of a permeability value is one difficulty associated with the calculation of surface losses. To check the effect of this parameter on the behaviour of the Grieg-Freeman formulation, the surface loss calculations presented in table 6.16 were repeated with different values of permeability. Relative permeability values of between 200 and 2000 were used and represent a variation in the parameter over an entire order of magnitude. The results for the upper and lower values are presented in tables 6.17 - 6.21

Table 6.17 - Sensitivity to μ_r Grieg-Freeman Equations - Two Pole Machine

Harmonic	Surface Losses (kW) $\mu_r = 200$	Surface Losses (kW) $\mu_r = 800$	Surface Losses (kW) $\mu_r = 2000$
Fundamental	4.10	3.97	3.43
Second	0.42	0.30	0.19
Third	0.52	0.28	0.18
Fourth	0.25	0.12	0.08
Total	5.29	4.68	3.87

Table 6.18 - Sensitivity to μ_r Grieg-Freeman Equations - Four Pole Machine

Harmonic	Surface Losses (kW) $\mu_r = 200$	Surface Losses (kW) $\mu_r = 800$	Surface Losses (kW) $\mu_r = 2000$
Fundamental	2.33	2.28	2.07
Second	1.19	0.92	0.59
Third	0.29	0.17	0.10
Fourth	0.59	0.29	0.19
Total	4.40	3.67	2.95

Table 6.19 - Sensitivity to μ_r Grieg-Freeman Equations - Six Pole Machine

Harmonic	Surface Losses (kW) $\mu_r = 200$	Surface Losses (kW) $\mu_r = 800$	Surface Losses (kW) $\mu_r = 2000$
Fundamental	6.19	6.12	5.80
Second	3.12	2.69	1.85
Third	1.24	0.78	0.48
Fourth	0.83	0.44	0.28
Total	11.38	10.03	9.79

Table 6.20 - Sensitivity to μ_r Grieg-Freeman Equations - Eight Pole Machine

Harmonic	Surface Losses (kW) $\mu_r = 200$	Surface Losses (kW) $\mu_r = 800$	Surface Losses (kW) $\mu_r = 2000$
Fundamental	3.32	3.28	3.11
Second	0.82	0.71	0.49
Third	0.61	0.38	0.24
Fourth	0.30	0.16	0.10
Total	5.04	4.53	3.93

Table 6.21 - Sensitivity to μ_r Grieg-Freeman Equations - Ten Pole Machine

Harmonic	Surface Losses (kW) $\mu_r = 200$	Surface Losses (kW) $\mu_r = 800$	Surface Losses (kW) $\mu_r = 2000$
Fundamental	2.85	2.83	2.73
Second	3.06	2.77	2.03
Third	0.03	0.02	0.01
Fourth	1.14	0.65	0.41
Total	7.08	6.27	5.18

along with the value obtained with the relative permeability set to 800. Examination of the results presented in these tables leads us to the conclusion that the discrepancy in the calculated and measured total losses in the two and four pole machines is not likely caused by a poor choice of μ_r.

Since the cores are constructed from fully processed steels, they are not annealed after punching. We may suspect that the punching strains are responsible for some additional losses in the stator core. Although a limited amount of data is available for the characterization of this effect, equation 2.12 may provide a rough estimate of the additional losses caused by punching strains. Results of calculations based on equation 2.12 are

tabulated in table 6.22. The larger value of k=356 is used since it will lead to the most conservative estimate of the effect. For the same reason, the minimum tooth width is used when calculating the factor for the teeth. New total calculated losses with the punching strain factors applied to the yoke and tooth losses are presented in table 6.23. Also, shown in table 6.23 are the updated T/C ratios. Note that although the T/C ratios are always smaller, a large discrepancy remains for the two and four pole machines. Results obtained for the six, eight, and ten pole machines are suitable for engineering purposes.

The author hypothesized that additional losses might be caused by saturation harmonics in the stator. To test this hypothesis, the TSM field solutions were decomposed into the fundamental, third, fifth, and seventh harmonics. Additional eddy current losses caused by these harmonics were estimated using equation 2.3. In each case the total power loss due to these harmonics was less than 100W. The discrepancy between the calculated and measured losses is not likely caused by saturation harmonics.

Although the saturation harmonics may not be responsible for the additional losses in the machines, saturation may still play some role in the discrepancy. The reader is referred to figures 6.67 to 6.73. The graphs show the test results of stator input power minus the I^2R losses vs the stator voltage squared as was described in Section 6.3. A straight line is also drawn to help show that the power loss in the machine does not follow a square law at the highest voltages. At the point that corresponds to the rated voltage of the machine, the difference between the two curves is noted. The results are summarized in table 6.24 and the difference between the two curves is given both in absolute values and as a percentage of the measured core loss at rated voltage. Although saturation harmonics may not be responsible for the additional losses in the core, one cannot rule out the possibility that as the machine is saturated, some flux will leak into the frame of the machine. This leakage flux will induce eddy current and hysteresis losses into the mild steel structure that comprises the frame of the machine. Frame losses will manifest themselves in the core loss measurement but they

Table 6.22 - Loss Factors (%) Due to Punching Strains Calculated by Equation 2.12

Machine	% Loss Increase Yoke	% Loss Increase Tooth
Two Pole	2.6	25.0
Four Pole	4.4	30.2
Six Pole Machine #1	3.3	20.0
Six Pole Machine #2	3.3	20.0
Eight Pole	6.6	33.8
Ten Pole	4.3	20.0

Table 6.23 - Comparison of Calculated‡ Values of Yoke, Tooth, and Surface Losses (Calculated by Grieg-Freeman Formulation) With Total Measured Losses

Machine	Total Tested Losses (kW)	Surface Losses† (kW)	Total of Calculated Yoke, Tooth and Surface Losses					
			Design Equations* + Surface Losses		TH Method I + Surface Losses		TSM Method I + Surface Losses	
			Calc. (kW)	T/C	Calc. (kW)	T/C	Calc. (kW)	T/C
2 Pole	32.4	4.68	19.62	1.65	16.43	1.97	15.86	2.04
4 Pole	22.1	3.67	13.13	1.68	14.45	1.53	12.91	1.71
6 Pole #1	22.08	10.03	23.06	0.96	20.99	1.05	20.81	1.06
6 Pole #2	21.07	10.03	23.06	0.91	20.99	1.00	20.81	1.01
8 Pole	13.63	4.53	12.27	1.11	12.38	1.10	11.87	1.15
10 Pole	23.5	6.27	22.95	1.02	20.48	1.15	19.89	1.18

‡ Including punching strain loss factors from Table 6.22.

* i.e the manufacturer's method without any scaling factors.

† Surface losses calculated using Grieg-Freeman formulation..

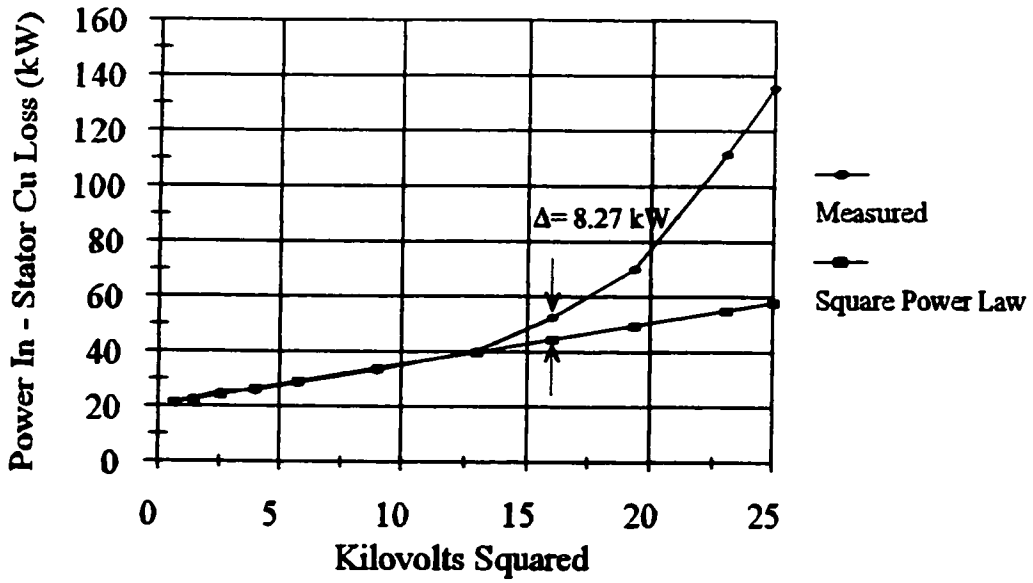

Figure 6.71 - Difference between square law assumption and measured losses for two pole machine.

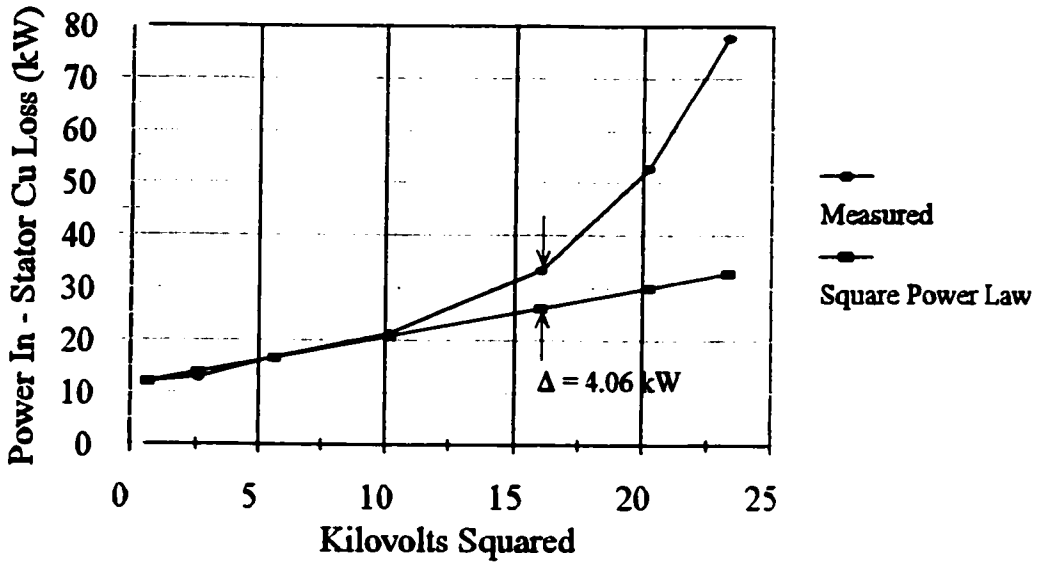

Figure 6.70 - Difference between square law assumption and measured losses for four pole machine.

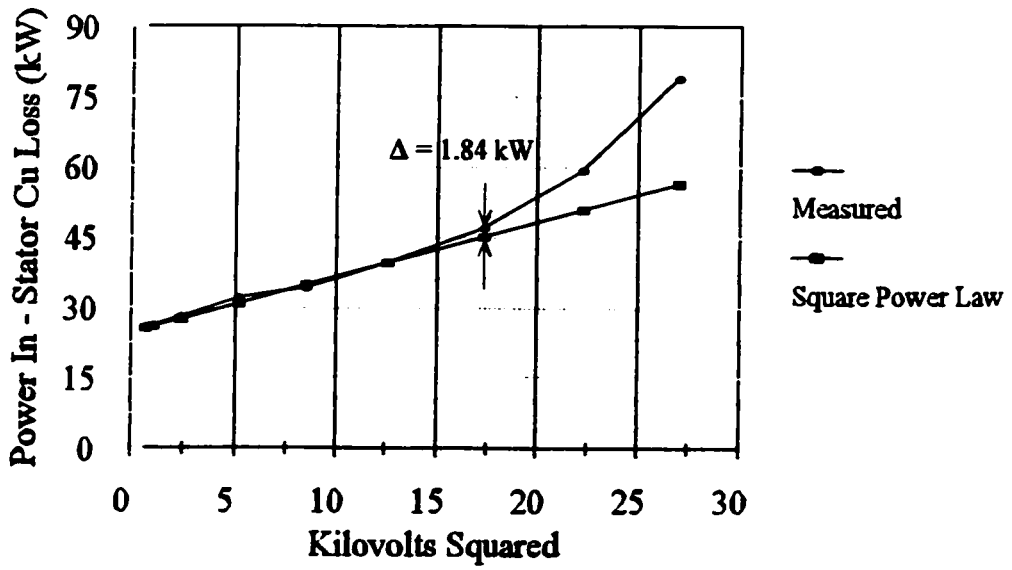

Figure 6.72 - Difference between square law assumption and measured losses for six pole machine #1.

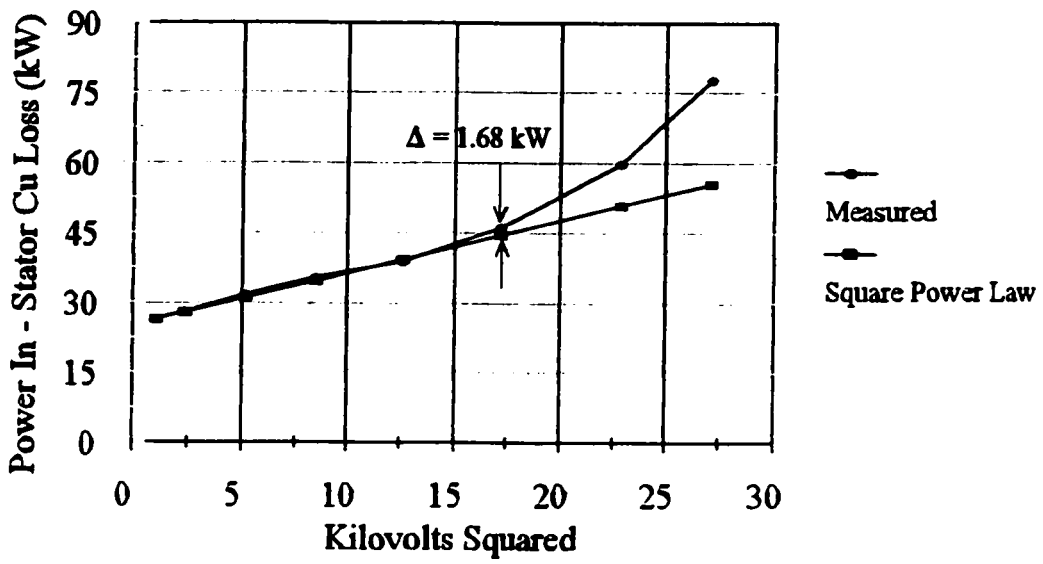

Figure 6.73 - Difference between square law assumption and measured losses for six pole machine #2.

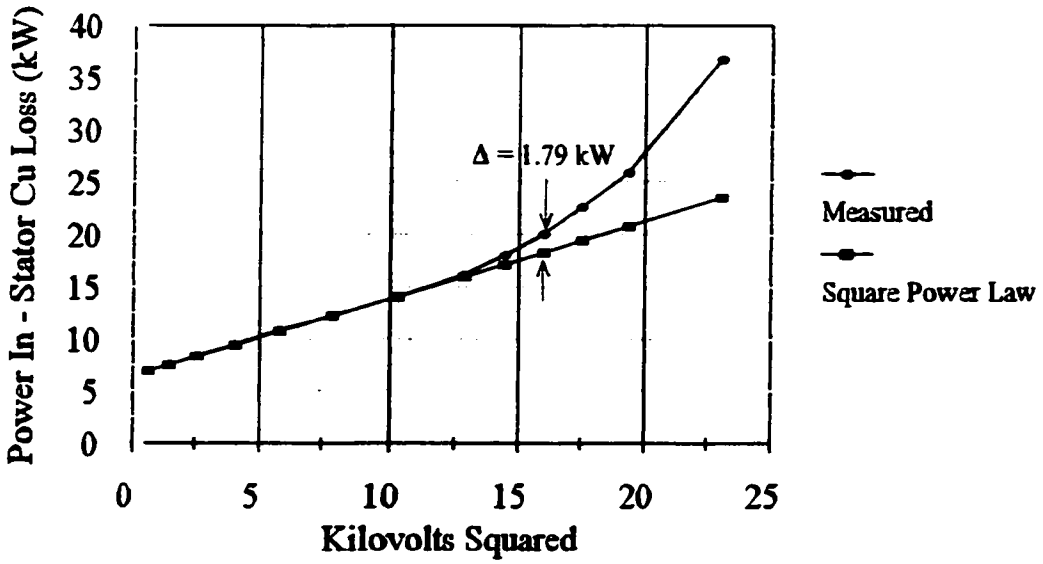

Figure 6.74- Difference between square law assumption and measured losses for eight pole machine.

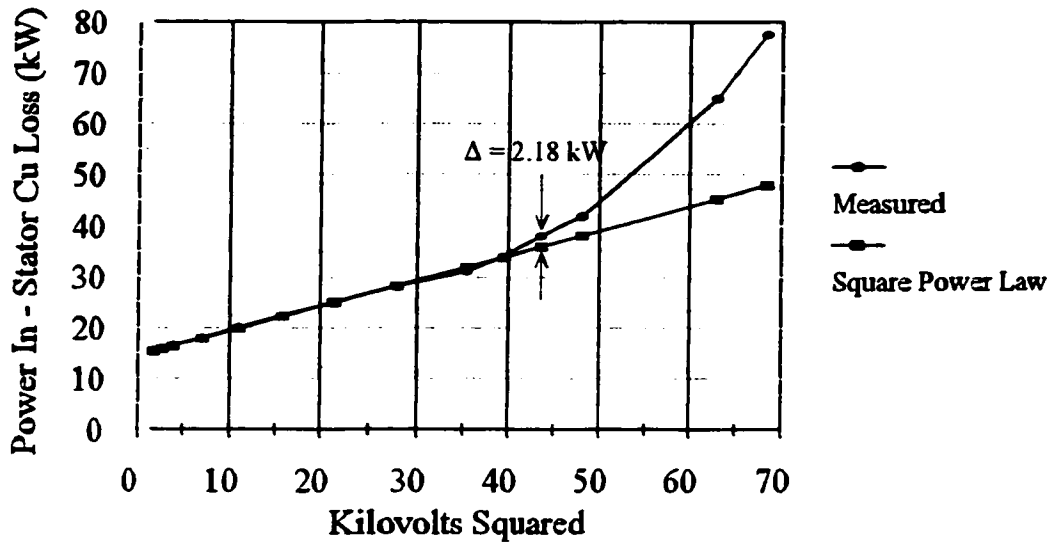

Figure 6.75 - Difference between square law assumption and measured losses for ten pole machine.

Table 6.24 - Difference Between Curve of Stator Input Power Minus I^2R Losses and Curve Assuming Squared Power Law

Machine	Δ (kW)	%Δ
Two Pole	8.27	25.5
Four Pole	4.06	18.4
Six Pole Machine #1	1.84	8.3
Six Pole Machine #2	2.20	10.4
Eight Pole	1.79	13.1
Ten Pole	2.18	9.3

are not included in the present calculation scheme. It is interesting to note that the results of table 6.24 show that biggest difference for the two and four pole machines which are precisely the same machines that show the biggest discrepancies in test to calculated ratios.

Besides frame losses due to leakage flux, the author suspects that some portion of the additional losses occur in the mild steel space blocks used to create the radial cooling vents throughout the length of a machine. As the machine becomes more heavily saturated, more flux will leak into the space blocks. In the stator teeth, the space blocks are oriented along the teeth and the flux carried in the space block is approximately alternating in nature. In the stator yoke, the space blocks are placed such that they lie radially in the yoke. With the space blocks in the yoke, the flux does not alternate through the length of the block. The flux will enter the length of the block nearly perpendicularly when the yoke flux is at a peak value. When the flux density is a maximum in the tooth, the flux enters the space block along its length. The flux density in the yoke space blocks is polarized in a manner similar to what we encounter for the yoke behind the stator slots and teeth. Figure 6.76 may help illustrate this point. Space blocks are typically made of mild steel. The resistivity of mild steel is very low and the space blocks are not laminated. We can expect that the eddy current losses induced

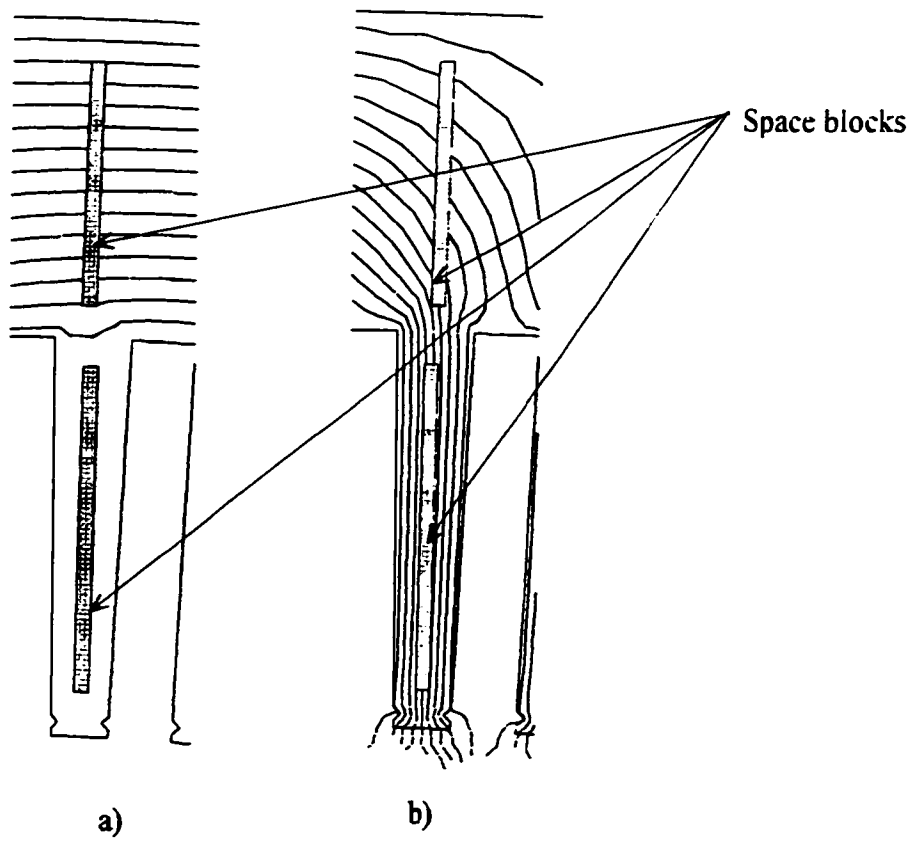

Figure 6.76 - a) Magnetization of radial space blocks at instant of peak value of yoke flux. b) Magnetization of radial space blocks at instant of peak value of tooth flux.

in the space blocks will be relatively high for these two reasons. In addition to the eddy current losses, the space blocks will also exhibit hysteresis losses. Estimating the losses in the space blocks is difficult for two reasons:

a) The flux density levels in the space blocks are not easily estimated
b) Loss data on mild steel is not readily available.

The results of this chapter show that for the steel used in these machines, the proposed calculation of rotational losses does not account for any large portion of the discrepancy between calculated and tested values of no-load core loss. Additional sources of core loss

are likely involved in addition to sources of manufacturing and test variation. Some topics will require further investigation and study. They are listed and discussed below.

a) **Surface Losses** - The manufacturer's method of calculation yields similar results to those found using the Grieg-Freeman formulation. Further study of the effects of rotor slotting on surface losses may be required. Studying surface losses using time-stepping finite element analysis may also be possible. At harmonic frequencies, the depth of penetration is very small and it is good practice to use several layers of elements to model the penetration depth. This would require an extremely fine mesh on the surface of the rotor and the resulting computation times might be excessive. The question of how to model conducting laminations arises since magnetic structures are usually assumed to be nonconducting and not laminated with FE studies.

b) **Pulsation Losses** - These losses occur in open slot rotors and closed slot rotors with heavily saturated rotor slot bridges. The latter is an area that requires further investigation. With closed slot rotors, the manufacturer assumes that pulsation losses are negligible under no-load conditions and that the bridge only saturates when the machine is heavily loaded (as discussed in Section 6.2.4). This assumption may not be correct if the machine is heavily saturated under no-load conditions. A time-stepping finite element package capable of modelling rotor motion will be required to pursue this area of study. MagNet 2D has no such capability.

c) **Additional Copper Losses in Rotor Bars** - These losses can occur at no load due to bridge saturation. This loss mechanism is related to the previous

point. With closed rotor slots, the manufacturer assumes that all harmonic fluxes are shunted through the bridge and that the harmonic flux linkage with the rotor bars is minimal (according to Alger [179] as discussed in Section 6.2.4) . When the slot bridge is heavily saturated, this may not be the case. Once again, to investigate this phenomenon a time-stepping finite element package capable of modelling rotor motion will be required. The harmonic currents flowing in the rotor bars could be quantified and an estimate of the rotor bars losses could be made.

d) **Normal Flux** - Some additional losses may be caused by flux entering normal to the direction of the laminations in the ducts and end structures. Flux leakage in the duct structure may result in large amounts of flux that enter the laminations in a normal direction. This phenomenon may be especially pronounced in the case of the two pole machine because the stator has radial ventilating ducts but the rotor does not.

e) **Core pressures** - The literature search has uncovered very little information on this topic. Perhaps losses increase as pressure on the core is increased. Two and four pole machines often have long stack lengths compared with the outside diameters of the machines. As such, the core pressures tend to be higher in these machines and this may further explain some of the discrepancy between the tested and calculated losses in these machines.

f) **Space Block Losses** - The space blocks in these machines are made of mild magnetic steel and therefore carry flux. Therefore, we can expect eddy current and hysteresis losses in the space blocks. The space block material

has a very low resistivity and therefore we can expect the eddy current losses to be rather large.

g) **Flux Leakage** - Some portion of the fundamental frequency flux carried by the machine core may leak into the frame and core bars at higher saturation levels. We have seen that the assumption of the square power law breaks down at higher saturation levels. This may be partly caused by flux leaking into the frame and core bars of the machine.

h) **Interlaminar Losses** - Interlaminar losses are increased when laminations are shorted together. The laminations may be shorted at the back of the stator yoke if the manufacturer chooses to apply a bead of weld to help hold the core together. Other shorting paths include the dove tail core bars onto which the laminations are piled and through burrs on the stator punchings.

i) **Punching Strains** - We have seen that for the machines in this study, the effect of punching strains is largest in the teeth since they form a narrower magnetic structure than the relatively deep yokes. The losses in the tooth are smaller than in the yoke and this mitigates the effect somewhat. A study similar to the one conducted by Cole [97] should be repeated with more modern materials to update the coefficients used in equation 2.12.

j) **Variability in Manufacture and Test** - We saw earlier that two identical machines had core loss test values that differed by approximately 1 kW or approximately 5% of the average measured value. This variation in the measured losses is partly due to manufacturing variations caused by part

tolerances, differences in worker skill levels, and variations in material quality. It is also partly due to variations in test procedures. These variations arise when different measuring instruments are used, and different operators do the tests. Also two identical machines progress through the manufacturing process at different times in the year such that changes in temperature may influence the test results. Understanding and controlling variations in manufacturing and test are significant. Even if the electromagnetic phenomena in the machine were perfectly understood and predictable by analytical techniques, some amount of uncertainty in the final test value would remain due to these sources of variation.

Chapter 7

Conclusions and Additional Considerations

7.1 Conclusions

A proper understanding of the magnetic phenomenon within the core of an induction machine is imperative to the designer for the purposes of: a) synthesizing a low loss machine b) accurately predicting the no-load core losses in the machine in order to specify efficiency to the customer c) effectively choosing core materials to synthesize the lowest cost machine that still meets the customer's expectations of efficiency.

Iron losses in rotating electric machines have been the subject of scholarly study for well over a century, yet the ability to predict the no-load core losses in induction motors remains a difficult task for the machine designer. The prediction of no-load iron losses is difficult for a number of reasons:

a) The problem is highly nonlinear.

b) The materials involved can be highly saturated.

c) A number of harmonic effects may be present.

d) The problem is highly dependent on material property variations.

e) Manufacturing variations and difficulties associated with testing often confound the task.

f) The machine designer often has only a limited amount of material data at his or her disposal.

This thesis has dealt with a major aspect of point f) that has concerned machine designers for many years; that is, the question of how best to model rotational losses in machine yokes. Rotational losses are a component of the no-load core losses that have

received a great deal of attention in the literature over the years. Work to date has been mainly concerned with the development of a standardized test apparatus for making rotational loss measurements in lamination steels. Researchers have been working towards a standardized test based on the belief that: a) rotational loss data would help machine designers to increase the accuracy of no-load core loss predictions, and b) the data would help steel producers to develop lower loss steels for use in motor cores.

The major goals of this thesis have been to determine how, and to what effect, machine designers may actually put rotational iron loss data to use. We have investigated analytical methods that can be conveniently used to incorporate rotational loss data into the design process. We also attempted to answer the following question: If rotational loss data were readily available, would it dramatically improve the accuracy of no-load iron loss predictions as various researchers have long suspected? It is an important question to raise. The investment in effort required to develop a standard test needs to be weighed against the likely benefits of having rotational loss data. Several induction motor designs have been analysed in order to answer this question. A further goal has been to investigate the likelihood that steel producers can put rotational loss data to use to create electrical sheet optimized for use in rotating machine cores. The conclusions that may be drawn from this work are outlined in the following sections.

7.1.1 The Hypothesis is False

It was hypothesized that part of the discrepancy between tested and calculated values of no-load core loss in induction motors is caused by the failure to account for rotational losses rigorously. Based on the results of the analysis of five induction machines, we must conclude that the hypothesis is false. We have seen that small differences will arise in the predicted core loss values of induction motors if the rotational losses are modelled using rotational loss measurements, as opposed to alternating loss data. The method of

superposition consistently over predicts the losses in the yokes of the machines. Yoke losses are consistently underestimated, if the flux density in each finite element is taken as alternating and the losses are assigned based on the 50:50 Epstein test. Various methods have been evaluated; however, the differences caused by including the effects of rotational losses are small compared with the overall measured core losses. The scientific community has been motivated to develop a standardized test for rotational losses based on the belief that data from such a test would aid machine designers to predict core losses with greater accuracy. Results of the current research show that this belief is perhaps overstated. Incorporation of rotational loss data into the design process will result in a refinement of the iron loss estimates for the yoke of the machine, especially near the tooth roots. The impact on the overall no-load core losses is less remarkable.

7.1.2 The Time-Harmonic Finite Element Method Can be Used to Predict the Flux Density Polarization in an Induction Motor Stator

The finite element method has come into widespread use in industry for predicting magnetic flux distributions in induction machines. One form of the finite element method known as the time-harmonic formulation, is particularly popular for analysing induction motor designs. The time-harmonic method lends itself naturally to the study of rotational losses. With one time-harmonic simulation, the distribution of the fundamental frequency flux density polarization is approximated throughout the stator of an induction machine. The applicability of using a series of magnetostatic solutions for quantifying the fundamental frequency rotational flux at no-load conditions has also been studied. Both methods yield comparable results. Rotational losses are easily looked up against a set of measured curves once the flux density polarization has been established. We can conclude that if rotational loss data were available to the design engineer, it could be quickly and conveniently put to use via the method herein presented.

7.1.3 Rotational Losses Are Not Accurately Predicted By Superposition of Alternating Losses

Results presented in Chapter 5 clearly show that rotational losses are not accurately accounted for by the method of superposition of alternating losses in the rd and td of the sheet. This is especially true at higher flux density levels. Classical eddy current losses can be estimated by the superposition method (according to analytical work available in the literature) but rotational hysteresis losses cannot. Anomalous losses are less understood but a greater understanding of this phenomenon is not very important when making loss estimates for fixed frequency machines. The method of superposition works well at lower flux density levels, but as the material begins to saturate the approximation is less satisfactory. The primary reason for this lies in the fact that the decrease in rotational hysteresis loss at higher flux density levels cannot be accounted for based on loss measurements made under alternating flux conditions. For materials with higher alloy contents and thinner gages, the eddy current losses are greatly reduced and most of the total loss in the material is attributable to hysteresis effects. The same can also be said for power frequencies below 60 Hz. For these situations, the method of superposition can lead to larger errors in the estimate of rotational losses when compared with materials with higher eddy current losses.

7.1.4 Rotational Losses Occur at Lower Than Expected Flux Density Levels

To achieve an economical design, modern induction machine cores are usually operated at or above the knee of the saturation curve. In Chapter 5, we saw that rotational losses are not accurately predicted by the method of superposition of losses for these very same flux density levels; therefore, we may have expected that the rotational losses could not be modelled accurately with only alternating loss data. In chapter 6, we established that at the roots of the stator teeth the rotational losses occur at flux density levels of approximately 0.9 to 1.2 T. This is much less than the 1.3 to 1.7 T flux density levels found in other areas

of the core. The magnitude of the rotational flux density polarization at the stator tooth roots is lowered because the tangential component of the flux density can leak into the root of the stator tooth. This lowers the magnitude of the rotational flux in the tooth root, though the average value of the flux density in the yoke of the machine may be much higher. At these lower flux density values, the error incurred by using the method of superposition of alternating losses to calculate the rotational losses, is mitigated.

For the machines under investigation, the errors incurred by ignoring the rotational losses are small (about ±10% in the yoke). The differences in calculated yoke losses are small when compared with the total measured core losses in the machines. The regions with the strongest polarization levels occur over a small percentage of the total yoke volume. Behind the stator slot the degree of rotational flux distribution is weak. Behind the stator teeth, the rotational flux density is much stronger but decays quickly as we move towards the back of the stator yoke. In the tooth roots, where the strongest flux density polarization is found, the flux density polarization is only at a level of 0.9 to 1.2 T.

7.1.5 The Hypothesis is Likely to Remain Null Even With Different Conventional Core Materials

In machines with lower efficiency demands, cores may be constructed from lower resistivity materials that are less expensive than the material used in the cores of the machines examined in this study (NO Steel D). The laminations may have a lower alloy content and they may also be thicker. In materials of this type, more of the losses are caused by eddy currents. In Chapter 2, we saw that classical eddy current losses in rotational fields can be predicted by superposition, but that rotational hysteresis losses cannot. We might expect that rotational losses would be least accurately predicted using the superposition of losses in the rd and td direction in those materials where the hysteresis component of the loss is proportionately greater than the eddy current losses. The data presented in Chapter 5, shows

that the rotational losses are least accurately predicted by the method of superposition of alternating losses for NO Steel D. As such, this material represents the worst case. Had the machines in this study been built of a different conventional silicon steel, the hypothesis would still be null. The same conclusion would have been arrived at if we had studied smaller machines made from MLQ steels as well. Materials with cubic or random cubic textures were not studied during this work. Conceptually, they would have lower rotational losses than conventional NO materials and therefore they may warrant further study.

7.1.6 The No-Load Core Loss Can Greatly Exceed The Fundamental Frequency Losses

Great debates concerning the applicability of Epstein test results to motor core losses have raged in the literature for many years; however it must be stressed that the fundamental frequency losses in the machine contribute only roughly between 35 and 60 percent of the total core loss. This was originally not understood. The manufacturer's method of predicting no-load losses suggested that the fundamental frequency component of the loss was much higher than was found by the FEA. Upon further investigation, it was found that empirical calibration factors in the manufacturer's formulation caused this discrepancy. Inaccuracies associated with non-rigorous estimates of fundamental frequency rotational losses are de-emphasized by the contributions through other mechanisms to the overall losses.

These other sources of no-load core loss are less well understood. A strong cooperation between industry and academia will be required to tackle these problems more thoroughly. Motor manufacturers have large databases of core loss test results and research in this field could be greatly benefited if this data could be shared with university researchers.

7.1.7 Importance of Multiple Machine Studies

Testing a core loss calculation scheme against multiple machines is important. It is

not sufficient to achieve good correlation between tested and calculated values for one or two machines and conclude that a new calculation scheme is generally valid. In the present study, good correlation was achieved for the six pole machine. If this had been the only machine in the study, we may have been tempted to conclude that all was well and no further work was necessary. While the proposed method does give good correlation for the six, eight and ten pole machines, the results for the two and four pole machines suggest that further work is still necessary.

7.1.8 Further Study Using Time-Stepping FEM With Rotor Motion is Warranted

Further study using a time-stepping FEM with rotor motion and induced rotor currents may help answer the question of how much the rotor permeance harmonics contribute to the no-load core loss of the machine. In induction machines with closed rotor slots, the assumption has been that these mechanisms will not have a major impact on the overall losses. If the rotor slot bridges are sufficiently saturated at no-load, this assumption may be incorrect, and as such, this topic warrants further investigation. To pursue this topic, a FE package that can model rotor motion and induced rotor currents must be purchased. This will allow the additional iron losses in the core and rotor bars to be modelled. MagNet 2D has no such capability.

7.1.9 Improved Texture May Lead to Lower Rotational Losses in Electrical Steels

Conceptually, a cubic or random cubic texture should yield the lowest loss steel under rotating flux conditions. If steels with these improved textures can be economically produced, they may find a market for use in machine cores. A machine designer might choose a cubic textured material over a conventional NO steel if it had similar W/kg alternating loss but a lower rotational loss and was no more expensive than the conventional material.

Research into improved textures may be the likeliest means by which rotational losses can be improved.

A review of the literature has shown that nearly all the research undertaken by steel producers is aimed at finding methods of reducing alternating losses as measured with the standard Epstein test frame or single sheet testers. Eddy current losses under alternating flux conditions are reduced by alloying the steel with silicon, aluminum, manganese, and phosphorous. The reduction in eddy current losses is achieved through an increase in the bulk resistivity of the material. Classical considerations of eddy current losses suggest that rotational eddy current losses can be reduced by the same method. Alternating losses are also reduced by reducing the amount of impurities in the steel; carbon, nitrogen, sulphur, and oxygen are particularly harmful to the magnetic properties of electrical steels. Unfortunately, the literature lacks any quantitative studies on the effects of impurity levels on rotational losses. The effects of grain size and texture on rotational losses are also not as well understood as they are with alternating losses.

7.1.10 Work Towards Standardization of a 2D Test Apparatus Should Continue

While the results of this thesis suggest that rotational loss data may be less important to machine designers than previously anticipated, a standardized 2D test apparatus may still prove useful. Such a tester would allow steel producers to make alternating, anisotropy, and rotational loss measurements with only one apparatus. Such a test apparatus could do all the functions of the Epstein frame or a single sheet tester while offering greater versatility. A review of the literature, and measurements made during this investigation, have shown that a 2D tester can provide useful information about the anisotropy of a material. A rotational core loss tester is useful for this purpose because the anisotropy measurements can be made on a single sample. The direction of magnetization is controlled by separately varying the excitation in the rd and td of the sample. The need to cut samples from various directions

to the rd of the material is eliminated because the direction of magnetization can be varied using the apparatus. Rotational loss data made available to the machine designer could easily be used in design work via the method presented in this thesis; thereby removing any uncertainty associated with rotational losses once and for all .

A review of the literature has revealed that hysteresis loss under alternating and rotating flux conditions is caused by fundamentally different mechanisms. Under alternating flux conditions, the hysteresis loss is predominantly attributable to domain wall motion and the annihilation and creation of domain walls. This is also the case for rotating flux conditions at low flux density levels. At higher flux density levels, rotational hysteresis is caused by domain rotation and vanishes as the material becomes saturated. Since the two mechanisms are fundamentally different, and the rotational hysteresis curve represents a characteristic of the material, a standardized test for making rotational loss measurements is also desirable from an academic viewpoint.

7.1.11 Edge Strains Make it Difficult to Use Horizontal Yoke Testers With Fully-Processed Steels

A standard test procedure for measuring rotational losses has not been established, although various teams of researchers have worked on rotational core loss testers for many years. Horizontal yoke testers have received much more attention in the literature than vertical yoke testers. Results of experiments undertaken during this research have revealed that measurements on fully processed materials can be difficult to make, using the horizontal yoke apparatus. It becomes necessary to stress relief anneal the samples before measurements can be made. This difficulty could be easily overcome with vertical yoke testers because the flux does not have to enter the sample through the edges.

7.2 Additional Considerations

7.2.1 Space Block Losses

The space blocks in a typical stator core of a large machine occupy on the order of 5% of the volume of the core. A novel method of estimating the space block losses using the standard Epstein test frame has been devised. This work is currently under way at the authors place of employment. Figures 7.1 and 7.2 help illustrate the basic concept of the proposed procedure. In figure 7.1, space blocks are oriented in similar fashion to that which would occur in the stator teeth. To estimate the losses that would occur in the stator teeth the following procedure is followed:

1. Take a number of standard sized Epstein strips and form the usual square in the frame of the tester. Fill in the spaces between the overlapping corner joints with shorter strips to eliminate the air apace between the laminations. This gives a solid stack of laminations that simulate the teeth of the machine. Measure the W/kg loss at various flux densities and create a curve of W/kg vs. flux density. At the same time note the voltage induced in a search coil wrapped around half the stack of the laminations.
2. Insert the space block material as shown in figure 7.1. Then stack the other half of the Epstein strips on top to form a square as shown in figure 7.1. Set the flux density values to the same values as before by using the same voltage on the search coil. Some flux will be carried by the space block and reduce the flux density in the laminations in the vicinity of the space block. This will occur because the space blocks and the laminations will form parallel paths for the flux. If the same voltage is induced in the search coil for both procedures, then the flux carried by the laminations should be the same in both cases. Take readings at each flux density value and create a second loss curve. Taking the difference between the two curves should give an estimate of the losses in the space blocks. Repeat the experiment but this time use the arrangement shown in figure 7.2. This more closely replicates the situation in the

stator yoke. Note that the losses in the yoke space blocks will be assessed under alternating flux conditions rather than the rotational flux patterns that would be encountered in the actual machine. Nevertheless, this method will give some estimate of the space block losses.

This data will help further refine the loss calculation in the stator so that the rotor surface losses and losses in other regions of the machine can be tackled more easily. A very accurate estimate of the stator losses based on FE work, leads to a more reasonable estimate for the remaining losses which can be calculated as the measured core loss minus the theoretical stator losses. Then the loss data for the remaining components of loss can be used to check theoretical equations. In large machines, stainless steel space blocks are sometimes used to minimize losses, even though the magnitude of these losses is not clearly defined. This work could help justify removal of the stainless steel space blocks, replacing them with mild steel, substantially reducing the material costs. Conversely, the results of the study may lead to increased use of stainless steel space blocks to reduce losses.

7.2.2 Normal Flux Losses

Flux enters normal to the laminations in the ducts due to fringing, at the end packets, and at the overlapping joints of the segmental punchings. When flux enters laminations in the normal direction, eddy currents are induced in the plane of the laminations. Consequently, the benefits of laminating are reduced because the eddy currents are not broken up. Under these conditions, the losses in the laminations could become very significant. It is very difficult to estimate losses due to normal flux because of the scarcity of data on the subject. A better understanding of losses due to normal flux would aid any effort to estimate losses in machines. The author believes that the current apparatus can be used in a novel arrangement to carry out experiments that will yield some insight to the problem. The idea is simple and is best illustrated with reference to figure 7.3a). A number of 8 cm by 2 cm

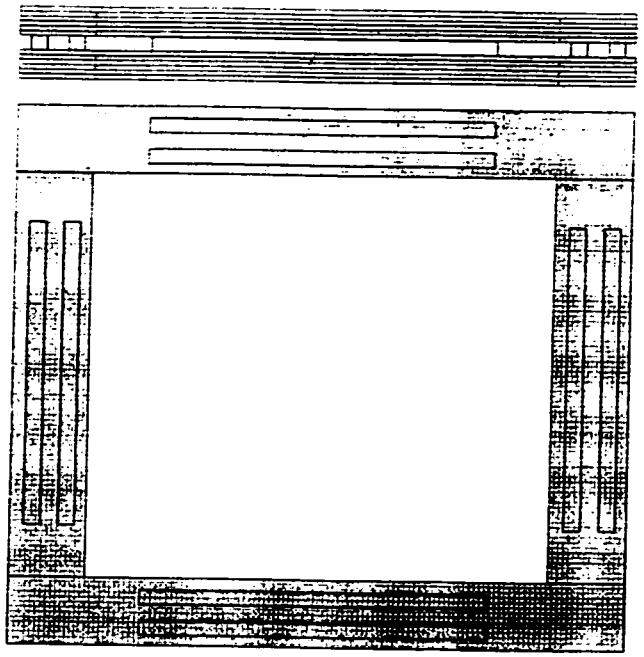

Figure 7.1 - Experiment to determine space block losses in stator teeth.

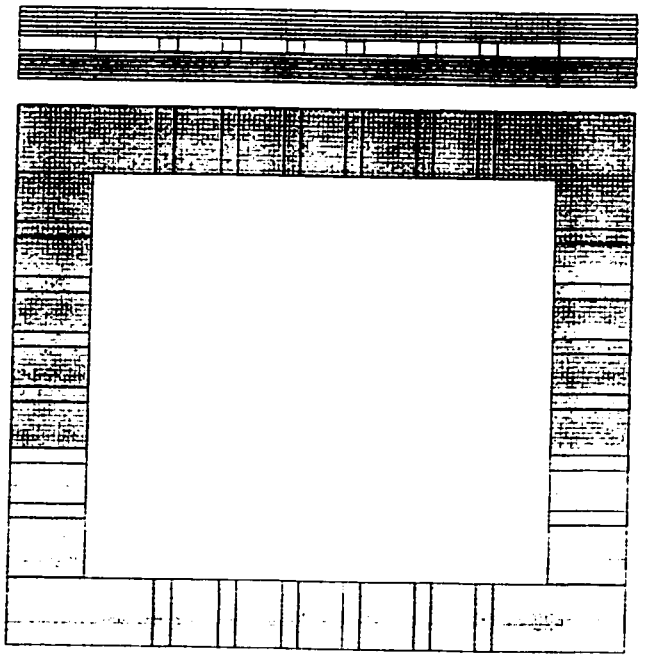

Figure 7.2 - Experiment to determine space block losses in stator yoke.

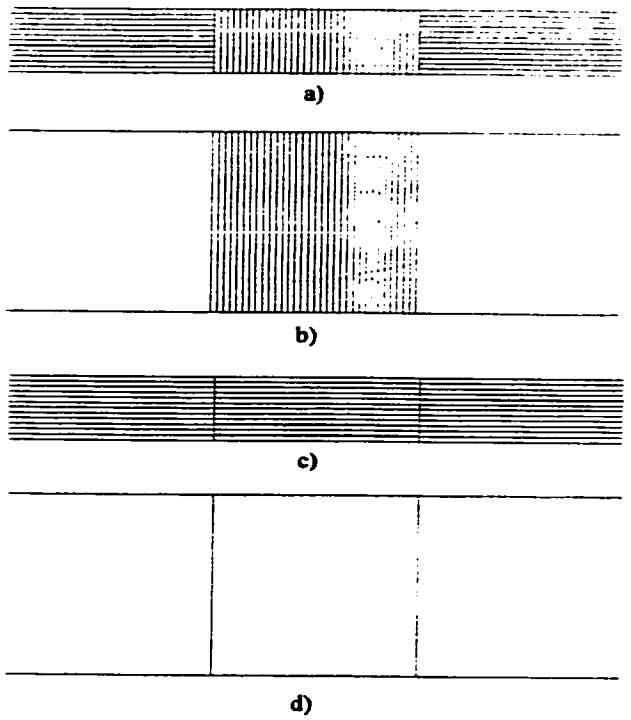

Figure 7.3 - Experimental procedure for determining losses when flux enters normal to the direction of the laminations. a) side view of test samples between poles of apparatus. b) same situation viewed from the top. c) side view with low loss grain oriented insert in place. d) same situation viewed from the top.

strips are cut and stacked one of top of the other. These are then inserted in a former to hold them together. The stack of laminations is then inserted between two of the pole pieces of the loss apparatus.

By energizing the coils on the two pole pieces, flux is forced in the normal direction through the stack of laminations. If a search coil is wrapped around the stack of laminations one can measure the flux density entering normal to the laminations. Using a separate set of search coils, the flux density in the yoke of the apparatus is measured. The total power into the system is measured and the copper losses are subtracted. This gives the losses in the yoke and samples. The samples are then removed and replaced with an insert made of low loss grain oriented material of the thinnest material possible, while eliminating air gaps between the insert and the pole pieces. The system is again energized and the flux density

level in the yoke of the tester is set to the same value as before. Now the losses in the insert should be much lower than the losses in the test samples because the eddy current losses are much larger for the normal flux situation. Total power into the system is measured and the copper winding losses are again subtracted. Subtracting the two input powers from each other should yield a reasonable estimate of the losses in the stack of test samples.

7.2.3 Third Harmonic Tooth Frequency Losses in Synchronous Machines Under Stray Load Loss Test Conditions

IEEE Std. 115 [215] describes the procedure for obtaining the measurement of stray load loss in a synchronous machine. The stray load loss is determined from additional readings taken when short circuit saturation curves are measured. Core loss under short circuit conditions is one component of the total stray load loss. Being able to predict the stray load loss in the machine during the design stage is important, since the stray load loss is included in the efficiency calculation. Traditional methods of predicting the core loss under short circuit conditions are based on formulations that were outlined by Rockwood [216] in the late 1920s. Results of these predictions show large variations in the test to calculated ratios of stray load loss.

Figure 7.4 shows a plot of the flux distribution in a 597 kW, 4kV, 28 pole, 60 Hz synchronous motor during short circuit conditions. A finite element analysis was done with the terminal voltage of the machine held at zero and the rated armature current flowing through the windings. Under these conditions a predominance of third harmonic flux exists in the machine. In the teeth of the machine, a large component of tangential flux is evident. This results in rotational flux throughout the body of the teeth. Third harmonic flux in the teeth is superimposed upon a small fundamental frequency flux. To predict the losses in the stator teeth accurately, it will be necessary to measure losses in samples under flux conditions

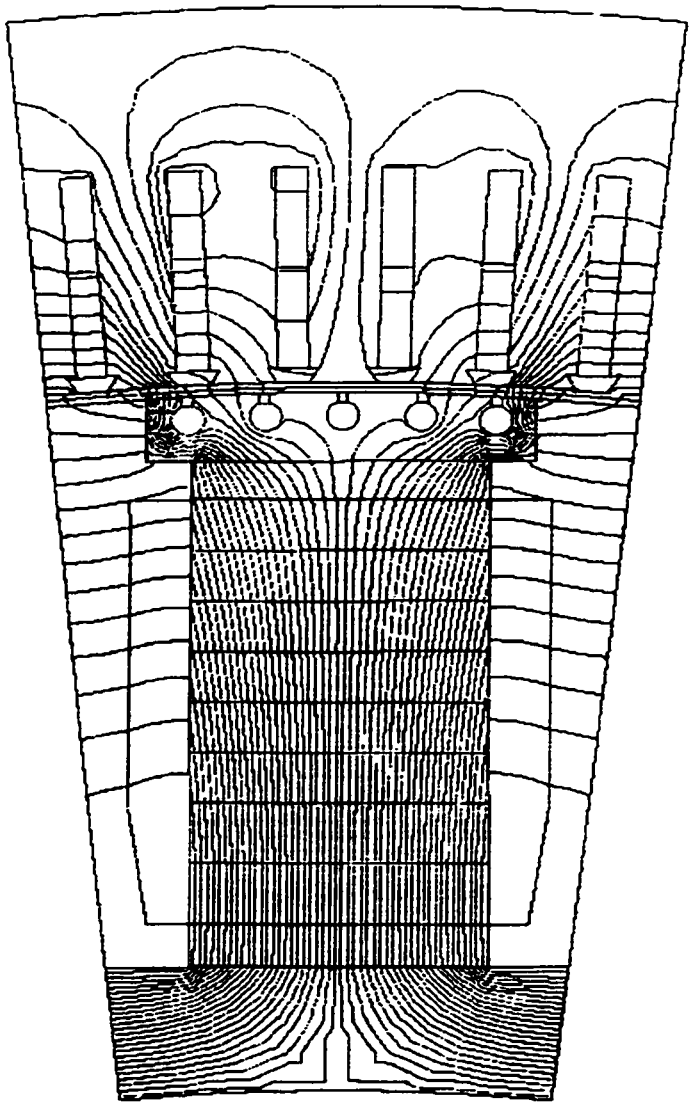

Figure 7.4 - Third harmonic flux distribution in a synchronous machine under short circuit conditions. Note the tangential components of flux in the teeth that lead to rotational component of flux.

that approximate those found in the machine when tested under short circuit conditions.

7.2.4 Lavers' Formulation for Harmonic Iron Losses

Lavers' formulation for harmonic losses was discussed in Chapter 2, Section 2.3.5. Some additional comments on the Lavers formulation may be of interest. In Section 2.3.5, we saw that Lavers' formulation is applicable to distorted flux density waveforms in

alternating fields; therefore, applying his formulation to find additional losses due to harmonics in the teeth of rotating machinery is reasonable. In Chapter 6, we saw that the flux density in the teeth of a machine is predominately alternating; except at the roots of the stator teeth where the flux density can be nearly circularly polarized. In the yoke of the machine, we saw that the fundamental frequency component of the flux density is elliptically polarized. The flux density is nearly circularly polarized at the tooth root and the polarization diminishes as we move towards the back of the core. At the very back of the core, the flux density can be considered as purely alternating. The question of how valid the correction for hysteresis losses via Lavers' formulation is in rotational fields immediately arises. The correction factor given by equation 2.9 is dependent on the notion of minor loops within the hysteresis loop of a material in an alternating magnetic field. In a rotational field, the notion of a minor loop becomes less clear; a hysteresis loop can be traced along two axes as for instance, along the rd and td of the material. As the material begins to saturate, we have seen that the hysteresis component of the loss will fall to zero in a purely rotating field. Given these two statements, it appears that further work in this area is warranted. Using a rotational loss tester, a series of experiments could be done along the lines followed by Lavers; however, the harmonics would be added to rotational flux patterns rather than alternating ones. In this way, the validity of equation 2.9 for use in rotational fields could be tested.

In section 2.2.3, we saw that the eddy current component of the rotational loss can be predicted by the method of superposition. Therefore, the eddy current correction factor given by Lavers in equation 2.7 is considered applicable to rotational fields if the flux density harmonics are decomposed into radial and tangential components and applied to each component separately.

The author wishes to raise one point of caution concerning the prediction of additional harmonic losses in machine cores. If a time-stepping FE with rotor motion and induced rotor bar currents is performed, predicting the theoretical flux density harmonics becomes possible

everywhere in the core. These harmonics are predicted, based on the assumption that the laminations in the core are nonconductive, i.e. the resistivity of the laminations is considered infinite (the usual assumption when doing 2D FEM simulations). This is very much not so in the motor core. Harmonic variations in flux will induce eddy currents in the laminations. The eddy currents cause additional losses, but they also serve a second purpose; they damp the variations in flux density. Based on this argument, we can envision that the flux density harmonics diminish in magnitude as we move further back along a tooth. In the yoke, they would be greatly diminished since the flux pulsation would be damped by the eddy currents in the machine teeth. Flux density pulsations predicted by the traditional FEM may in reality be much larger than actually occur in the core of the machine.

7.2.5 On The Use of Empirical Calibration Factors

In Chapter 6, we saw the manufacturer's use of what can be described as empirical calibration factors. They were introduced by the machine manufacturer to improve the correlation of tested to calculated values of no-load core loss. In the calculation of the iron loss in the stator yoke and teeth, we saw that the iron loss coefficient was multiplied by a factor of 1.53.

The inclusion of these empirical calibration factors makes the loss calculations misleading concerning the proportion that each component contributes to the overall losses. For instance, from an examination of Table 6.3, one would conclude that the fundamental frequency losses in the machine account for somewhere between 59% and 98% of the total measured no-load core losses. In fact, the results of Chapter 6 (using the TH formulation estimates) reveal that they range from about 36% for the two pole machine to 60% for the ten pole machine. The correlation to test values was greatly improved for the six, eight and ten pole machines once the calibration factor was removed; however, the results for the two and four pole machines were less satisfactory.

It is simply a matter of practicality that if a loss formulation does not yield adequate results, the practising engineer will calibrate it to test results via a correlation study; therefore, including as much rigour to the formulation as possible is important. In this way, most of the underlying phenomena that determine machine core loss will be captured. The importance of this is realized when the designer is working on a machine that falls outside the scope of the manufacturer's experience list. No reference designs are available, and if the calculations are not rigorous enough, they will fail the designer when they are most needed.

Correlation to tested values found by the methods described in this thesis are not wholly satisfactory. This is particularly the case for the two and four pole machines; nevertheless, the calculation scheme has clearly shown that the hypothesis is false. The small variations in the core loss predictions that arise because of rotational loss effects do not account for any large portion of the discrepancy between tested and calculated values of core loss. Finding a calculation scheme that correlated perfectly to test values for all five machines was beyond the scope of the present study. The TH formulation, when supplemented by the surface losses according to Grieg-Freeman formulae, and the correction for punching stresses given by Cole, does however, contain a great deal more rigour than the analytical methods in current use by the manufacturer.

As a recommendation for further work, the author suggests that the method of predicting space block losses described in Section 7.3.1 also be incorporated into the proposed method. A correlation study could then be run against a larger sample of the existing database of machine test data. It will be interesting to determine whether all two and four pole machines in the database test higher than the predicted values, or if this result is isolated to the two machines in the present study. The results obtained for the six, eight and ten pole machines are more satisfactory (within 15% of the tested values) and it will be interesting to see whether this result holds for all the slower speed machines.

7.3 Delineation of Contributions to the Science of Iron Losses

The specific original contributions claimed for this work are:

1. Insights into the topics of a) the origin of iron losses in rotating magnetic fields, b) the metallurgical factors that affect iron losses in alternating and rotating magnetic fields, c) loss measurements in electrical sheet steels, d) analytical predictions of magnetic flux distributions in induction motor cores, and e) analytical prediction of iron losses in motor cores. These insights result from a comprehensive review of the subject of iron losses in rotating magnetic fields. This review highlights the state of the art on the subject.

2. The establishment that rotational flux in induction motor cores does not account for the large differences observed between calculated and measured no-load core loss values. It is this result that is the major contribution to the body of knowledge in the art of machine design. For many years now (as indicated by the great body of work available in the literature), researchers in various countries have been keenly interested in establishing a standard test for measuring rotational iron losses in electrical sheets. This interest has been largely stimulated by the belief that data garnered from such a test would be of great value to the machine designer. The results of this dissertation clearly establish that such data can only be used as a minor refinement to the calculation of machine losses. Differences in the predicted values of core loss are too small to account for the discrepancies between tested and calculated values of no-load core loss. The findings of this study are of great importance to researchers who are pursuing the standardization of a rotational loss tester. They may wish to weigh the effort of achieving such a goal against the limited gain in calculation accuracy that can be achieved as shown in this thesis.

3. Presentation of a technique for using the time-harmonic finite element method for predicting the degree of flux density polarization in induction motor cores. This is a

novel method for predicting the fundamental frequency flux density polarization in the core of a machine core. The major advantage of the technique is the speed of solution. All the information necessary to determine the fundamental frequency flux density polarization in the machine stator is obtained from one solution of the time-harmonic FEM.

4. A method for using a family of loss curves, measured under various degrees of elliptical flux density polarization, to calculate the fundamental frequency iron losses in an induction motor core. This method includes the effects of rotational iron losses. It was originally believed that such an improvement to the calculation of no-load core loss might account for some discrepancy typically observed between calculated and tested values but this hypothesis has largely shown to be null. The method does provide a refinement to the iron loss calculation, particularly in the region of the stator tooth roots. This could very easily be incorporated into the design process if rotational iron loss data was made routinely available to the designer; however, the improvement over more traditional methods is not large.

5. We have compared rotational and alternating loss curves for a variety of materials. A comparative set of data using a single apparatus for all the materials was unavailable in the literature prior to this study.

6. An original idea for the measurement of space block losses as described in section 7.3.1. The author is currently undertaking this work at his place of employment and will report his findings in the near future.

7. An original idea for the measurement of normal flux losses as described in section 7.3.2. The method makes use of the horizontal yoke test apparatus and is still under development.

References

[1] A.J. Moses, "Importance of Rotational Losses in Rotating Machines and Transformers," Journal of Materials Engineering and Performance, Volume 1(2), April 1992, pp. 235-244.

[2] T. Sasaki, M. Imamura, S. Takada, Y. Suzuki, "Measurements of Rotational Power Losses in Silicon-Iron Sheets Using Wattmeter Method," IEEE Transactions on Magnetics, Vol. MAG-21, No. 5, September 1985, pp. 1918-1920.

[3] F. Fiorillo, A. M. Rietto, "Extended Induction Range Analysis of Rotational Losses in Soft Magnetic Materials," IEEE Transactions on Magnetics, Vol. 24, No. 2, March 1988, pp. 1960-1962.

[4] M. Enokizono, J.D. Sievert, "Magnetic Field and Loss Analysis in an Apparatus for the Determination of Rotational Loss," Physica Scripta, Vol. 39, 1989,pp. 356-359.

[5] J.G. Zhu, V.S. Ramsden, "Improved Formulations for Rotational Core Losses in Rotating Electrical Machines," IEEE Transactions of Magnetics, Vol. 34, No. 4, July 1998, pp.2234-2242.

[6] J.H. Walker, Large Synchronous Machines - Design, Manufacture, and Operation, Clarendon Press Oxford, 1981, ISBN 0-19-859364-3.

[7] Becker, R., "Elastische Spannungen und magnetische Eigenschaften," Physik. Z., 1932, 33, pp. 905-913.

[8] C. Kittel, "Ferromagnetic Domain Theory," Solid State Physics, Vol. 3, 1956, pp. 437-565.

[9] Becker, R., "Elastic Strains and Magnetic Properties," Physik. Z., 1932, 33, pp. 905-913.

[10] Becker, R., Magnetismus (Debye, Leipzig), 1933, pp. 82-90. The technical magnetization curve.

[11] R.M. Bozorth, Ferromagnetism, IEEE PRESS Classic Reissue, ISBN 0-7803-1032-2, Copyright 1978 - American Telephone and Telegraph Company.

[12] M.F. Littmann, "Iron and Silicon-Iron Alloys," IEEE Transactions on Magnetics, MAG-7, No. 1, March 1971, pp 48-60.

[13] Plonus, M.A., Applied Electromagnetics, McGraw-Hill, Inc., New York, Copyright 1978, ISBN 0-07-050345-1.

[14] Barkhausen, H., "Two Phenomena Uncovered With Help of the New Amplifiers," Physik. Z. 20, 1919, pp. 401-403.

[15] C.P. Steinmetz, Theory and Calculation of Alternating Current Phenomena, Vol. 4 McGraw- Hill Book Company, Inc., New York 1916.

[16] F. Brailsford, "Domain-Wall Energy and Hysteresis Loss in Ferromagnetic Material," Proceedings IEE, Vol.117, No. 5, May 1970, pp. 1052-1055.

[17] F. Brailsford, "Rotational Hysteresis Loss in Electrical Sheet Steels," Journal of IEE, Vol. 83, 1938, pp. 566-575.

[18] F. Brailsford, "Alternating Hysteresis Loss in Electrical Sheet Steels," Journal of IEE, Vol. 84, 1939, pp. 399-407.

[19] F. Brailsford, "A Survey of Electrical Sheet Steels for Power Plant and the Factors Affecting Their Magnetic Properties" Journal of IEE, Vol. 90 (II), 1943, pp. 307-326.

[20] G.C. Grimwood, A.M. Campbell, J.E. Evvetts, "Rotational Hysteresis in Polycrystalline Alloys, IEEE Transactions on Magnetics, Vol. MAG-14, No. 5, September 1978, pp. 359-361.

[21] F. Fiorillo, A.M. Rietto, "Rotational Versus Alternating Hysteresis Losses in Nonoriented Soft Magnetic Laminations," Journal of Applied Physics, Vol. 73, No. 10, 15 May 1993, pp. 6615-6617.

[22] C. R. Boon, J.E. Thompson, "Rotational Hysteresis Loss in Single-Crystal Silicon-Iron," Proc. IEE, Vol. 111 No. 3, March 1964, pp. 605-609.

[23] K. Narita, T. Yamaguchi, "Rotational Hysteresis Loss in Silicon-Iron Single Crystal with (001) Surfaces," IEEE Transactions on Magnetics, Vol. MAG-10, No. 2, June 1974, pp. 165-167.

[24] K. Narita, T. Yamaguchi, "Rotational and Alternating Hysteresis Losses in 4% Silicon-Iron Single Crystal with the {110} Surface," IEEE Transactions on Magnetics, Vol. MAG-11, No. 6, November 1975, pp. 1661-1666.

[25] J. Zbroszczyk, J. Drabecki, B. Wyslocki, "Angular Distribution of Rotational Losses in Fe-3.25%Si Single Crystals With Orientations (001) and (011)," IEEE Transactions on Magnetics, Vol. MAG-17, No. 3, May 1981, pp. 1275-1282.

[26] J.J. Thomson, "On the Heat Produced by Eddy Currents in an Iron Plate Exposed to an Alternating Magnetic Field," The Electrician, Volume 28, April 8, 1892, pp. 599-600.

[27] M. Latour, "Note on Losses in Sheet Iron at Radio Frequencies," Proceedings of the IRE, 1919, Vol. 7, pp. 61-71.

[28] P.D. Agarwal, "Eddy-Current Losses in Solid and Laminated Iron," Transactions of the AIEE, Vol. 78, Part II, May 1959, pp. 169-181.

[29] K.H. Stewart, "Losses in Electrical Sheet Steel," Journal of IEE, Vol. 97, 1950, pp. 121-125.

[30] R.M. Del Vecchio, "The Calculation of Eddy Current Losses Associated With Rotating Magnetic Fields in Thin Laminations," IEEE Transactions on Magnetics, Vol. MAG-18, No. 6, November 1982, pp. 1707-1709.

[31] I.D. Mayergoyz, "On Rotational Eddy Current Losses in Steel Laminations," IEEE Transactions on Magnetics, Vol. 34, No. 4, July 1998, pp. 1228-1230.

[32] F. Brailsford, "Investigation of the Eddy-Current Anomaly in Electrical Sheet Steels," Journal of IEE, Vol. 95, Part II, 1948, pp. 38-48.

[33] J.A. Robey, "Domain-Wall Motion and Eddy-Current Loss in Grain-Oriented Silicon -Iron," Journal of Science and Technology, Vol. 36, No. 1, 1969, pp. 3-10.

[34] R.H. Pry, C.P. Bean, "Calculation of the Energy Loss in Magnetic Sheet Materials Using a Domain Model," Journal of Applied Physics, 1958, Vol. 29, pp. 532-533.

[35] K.J. Overshott, I. Preece, J.E. Thompson,"Magnetic Properties of Grain-Oriented Silicon Iron," Proceedings of the IEE, Vol. 115, No. 12, December 1968, pp. 1840-1845.

[36] E.T. Stephenson, "Seperation of Losses in Low-Alloy Nonoriented Electrical Steels," Journal of Applied Physics, Vol. 57, No. 1, 15 April 1985, pp. 4226-4228.

[37] A.Cecchetti, G. Ferraro, F. Masoli, G.P. Saordo, "Rotational Power Losses in 3% SiFe as a Function of Frequency," IEEE Transactions on Magnetics, Vol. MAG-14, No. 5, September 1978, pp. 356-358.

[38] K.S. Tan, A. Datta, P.J. Flanders, C.D. Graham, Jr., "Rotational Loss in Thin Gage Soft Magnetic Materials," IEEE Transactions on Magnetics, Vol. MAG-21, No. 5, September 1985, pp. 1921-1923.

[39] P.J. Flanders, "Utilization of a Rotating Sample Magnetometer," The Review of Scientific Instruments, Vol. 41, No. 5, May 1970, pp. 697-710.

[40] P.J. Flanders, "A Hall Sensing Magnetometer for Measuring Magnetization, Anisotropy, Rotational Loss and Time Effects," IEEE Transactions on Magnetics, Vol. MAG-21, No. 5, September 1985, pp. 1584-1589.

[41] T. Yamaguchi, K. Narita, "Rotational Power Loss in Commercial Silicon-Iron Laminations," Electrical Engineering in Japan, Vol. 96, No. 4,1976, pp. 15-21.

[42] F. Fiorillo, A.M. Rietto, "Rotational and Alternating Energy Loss vs. Magnetizing Frequency in SiFe Laminations," Journal of Magnetism and Magnetic Materials, Vol. 83 (1990), pp. 402-404.

[43] S. Spornic, D. Moussaoui, A. Kedous-Lebouc, B. Cornut, "Frequency Magnetic behaviour of SiFe Sheets in a Rotational Field," Journal of Magnetism and Magnetic Materials, Vol. 160 (1996), pp. 147-148.

[44] T. Nakata, Y. Ishihara, M. Nokano, "Iron Losses of Silicon Steel Core Produced by Distorted Flux," Electrical Engineering in Japan, Vol. 90, No. 1. 1970, pp. 10-20.

[45] J.D. Lavers, P.P. Biringer, "Prediction of Core Losses for High Flux Densities and Distorted Flux Waveforms," IEEE Transactions on Magnetics, Vol. MAG-12, No. 6, November 1976, pp. 1053-1055.

[46] J.D. Lavers, P.P. Biringer, H. Hollitscher, "Estimate of Core Losses When the Flux Waveform Contains the Fundamental Plus a Single Odd Harmonic Component," IEEE Transactions on Magnetics, Vol. MAG-13, No. 5, September 1977, pp. 1128-1130.

[47] J.D. Lavers, P.P. Biringer, H. Hollitscher, "A Simple Method of Estimating the Minor Loop Hysteresis Loss in Thin Laminations," IEEE Transactions on Magnetics, Vol. MAG-14, No. 5, September 1978, pp. 386-388.

[48] T.D. Yensen, "Magnetic and Other Properties of Some Iron Alloys Melted in Vacuo," Transactions of the AIEE, 1915, Volume 34, pp. 2601-2641.

[49] T.D. Yensen, "Magnetic Properties Ternary Fe-Si-C Alloys," Transactions of the AIEE, 1924, Volume 43, pp. 145-175.

[50] P. Arató, I. Bóc, T. Gróf, "Effect of Composition on the Loss of Non-Oriented Medium Silicon Electric Sheets," Journal of Magnetism and Magnetic Materials, 41(1984) pp 53-55.

[51] C.K. Hou, "Effects of Silicon on the loss Separation and Permeability of Laminated Steels," Journal of Magnetism and Magnetic Materials 162 (1996) pp 280-290.

[52] C.K. Hou, P.C. Wang, "Effects of Composition and Process Variables on Core Loss and Hardness of Low Carbon Electrical Steels," Journal of Magnetism and Magnetic Materials 92 (1990) pp 109-115.

[53] K. Matsumura, B. Fukuda, "Recent Developments of Non-Oriented Electrical Steel Sheets," IEEE Transactions on Magnetics, vol. MAG-20, No. 5, September 1984, pp 1533-1538.

[54] Y. Takada, M. Abe, S. Masuda, J. Inagaki, "Commercial Scale Production of Fe-6.5 wt. % Si Sheet and its Magnetic Properties," Journal of Applied Physics, Vol. 64, No. 10, November 15, 1988 ,pp. 5367-5370.

[55] Metals Handbook - Ninth Edition, Volume 3 Properties and Selection: Stainless Steels, Tool Materials and Special Purpose Metals, American Society for Metals.

[56] W.T. Lankford, Jr., N.L. Samways, R.F. Craven, H.E. McGannon (Editors), The Making, Shaping and Treating of Steel-Tenth Edition, United States Steel, Copyrighted 1985 by Association of Iron and Steel Engineers, LCCCN 84-81539, ISBN 0-930767-00-4.

[57] Steels Products Manual - Electrical Steels, American Iron and Steel Institute, 1000 16th Street N.W., Washington, D.C. 20036, January 1983.

[58] T.F. Foley, D.A. Leak, R.A. Newbury, A.R. Pomeroy, A.R. Mathews, M.V. Tomkeieff, "A Study of Ferrous-Based Soft Magnetic Materials for Transformer and Similar Applications," Journal of the Iron and Steel Institute, February 1970, pp 147-156.

[59] I. Bóc, T. Gróf, "The Core-Loss Reducing Effect of Aluminum in Non-Oriented Fe-Si Steels," IEEE Transactions on Magnetics, Vol. MAG-22, No. 5, September 1986, pp 517-519.

[60] P. Brissonneau, "Session 2:Non-Oriented Electric Sheets, Non-Oriented Si-Fe Sheets," Journal of Magnetism and Magnetic Materials, 19 (1980), pp 52-59.

[61] Lyudkovsky, G., Rastogi, P.K., Bala, M., "Nonoriented Electrical Steels," Journal of Metals, January, 1986, pp. 19-26.

[62] F.E. Werner, R.I. Jaffee, "Energy Efficient Steels for Motor Laminations," Journal of Materials Engineering and Performance, Vol. 1, No. 2, 1992, pp. 227-233.

[63] R.P. Dunkle, R.H. Goodenow, "Closing the Gap With Lamination Steels - A Producer's Point of View," Soft and Hard Magnetic Materials With Applications, ASM Sym. Proc, October 1986, pp 41-54.

[64] P.K. Rastogi, "Effect of Manganese and Sulphur on the Texture and Magnetic Properties of Non-Oriented Steel," IEEE Transactions on Magnetics, Vol. Mag-13, No. 5, September 1977, pp 1448-1449.

[65] K.C. Liao, "The Effect of Manganese and Sulphur Contents on the Magnetic Properties of Cold Rolled Lamination Steels," Metallurgical Transactions A, Vol 17A, August 1986, pp 1259-1266.

[66] G. Lyudkovsky, "The Effect of Antimony on Internal Oxidation and Magnetic Properties of Si-Al Electrical Steels," IEEE Transactions on Magnetics, Vol. 22, No. 5, September 1986, pp 508-510.

[67] G. Lyudkovsky, A.G. Preban, J.M. Shappiro, "The Influence of Annealing Conditions on the Internal Oxidation and Magnetic Properties of Silicon-Aluminum Bearing Electrical Steels," Journal of Applied Physics, Vol. 53, No. 3, March 1982, pp 2419-2421.

[68] G. Lyudkovsky, P.K. Rastogi, "Effect of Antimony on Recrystallization Behaviour and Magnetic Properties of Nonoriented Silicon Steel," Metallurgical Transactions A, Volume 15A, Feb. 1984, pp 257-260.

[69] R.A. Higgins, Engineering Metallurgy - Part I: Applied Physical Metallurgy - 6th Edition, Published by Edward Arnold, a division of Hodder & Stoughton, London, 1993, ISBN 0-340-56830-5.

[70] F.E. Werner, "Steels for Laminations in Energy Efficient Motors," CMP Report No. 91-11, EPRI Project No. RP3070-24, June 1991.

[71] B. Deo, R. Boom, Fundamentals of Steelmaking Metallurgy, Copyrighted 1993 Prentice Hall International (UK), LCCN 92-38513, ISBN 0-13-345380-4.

[72] I. Bóc, J. Csébi, T. Gróf, A. Cziráki, B. Nádor, "Correlation of Aluminum Content, Inclusion Structure, and Core Loss of Non-Oriented Electrical Steels," Journal of Applied Physics, Vol. 64, No. 10, 15 November 1988, pp 5350-5351.

[73] K. Günther, F. Bölling, H. Huneus, "Detrimental Effect of Oxidation on Magnetic Properties of Nonoriented Electrical Steel Sheet," Journal of Applied Physics, Vol. 64, No. 10, November 15, 1988, pp. 5347-5349.

[74] Smith, W.F. . Principles of Materials Science and Engineering - Second Edition. McGraw Hill Book Publishing Co., Toronto, ISBN 0-07-059169-5, 1990.

[75] Hatherley, M., Hutchinson, W.B, An Introduction to Textures in Metals, The Institution of Metallurgists. Monograph No. 5, Chameleon Press Ltd., London, ISBN 0-901462-05-5, 1979.

[76] Y. Shimoyama, K. Miyoshi, M. Tanino, T. Wada, "Development of Non-Oriented Silicon Steel Sheet With Very Low Core Loss," IEEE Transactions on Magnetics, vol. MAG-19, No. 5, September 1983, pp 2013-2015.

[77] I. Bóc, A. Cziráki, J. Csébi, S. Németh, L. Szentmiklósi, "Limit of Al Content in Fe-Si Electrical Steels," IEEE Transactions on Magnetics, vol. 26, No. 5, September 1990, pp 2226-2228.

[78] H. Shimanaka, Y. Ito, K. Matsumura, B. Fukuda, "Recent Development of Non-Oriented Electrical Steel Sheets," Journal of Magnetism and Magnetic Materials, 1982, Vol 26 pp 57-64.

[79] P.K. Rastogi, G. Lyudkovsky, "Response of a Non-Oriented 2.0% Silicon Steel to Processing Variables," IEEE Transactions on Magnetics, Vol. MAG-20, No. 5, September 1984, pp. 1539-1541.

[80] K. Matsumura, B. Fukuda, K. Kinoshita, T. Imai, Y. Obata, S. Miyazaki, "Non-Oriented Silicon Steel Sheet "RM7" Newly Developed With Extremely Low Core Loss," Kawasaki Steel Technical Report No. 8, September 1983, pp 11-16.

[81] N.P. Goss, United States Patent 1 965 559 (Appl. 8/7/33), Electrical Sheet and Method and Apparatus for its Manufacture and Test

[82] N.P. Goss, "New Development in Electrical Strip Steels Characterized by Fine grain Structure Approaching Properties of a Single Crystal," Transactions of the American Society of Metals, Vol. 23, 1935, pp. 515-531.

[83] N.P. Goss, United States Patent 2 084 336-7 (Appl. 1/30/34 and 12/1/34), Magnetic Material and Method of Manufacture

[84] F. Assmus, R. Boll, K. Detert, D. Ganz, G. Ibe, F. Pfeifer, "Method for Producing Cube Texture in the Manufacture of Objects Made of Iron-Silicon Alloys," German Patent 1 029 845, May 14, 1958.

[85] F. Assmus, R. Boll, D. Ganz, P. Pfiefer, "Silicon-Iron with Cubic Texture - I Magnetic Studies," Translated from Zeitschrift für Metallkunde Band 48 Heft 6 June, 1957, pp. 341-349. Courtesy of Armco Inc. archives, Personal communication with Jerry W. Schoen, Principal Research Engineer, Armco Research and Technology.

[86] F. Assmus, K. Detert, G. Ibe. "Silicon-Iron with Cubic Texture - II Formation of the Texture," Reprint of material presented by F. Assmus at the session of the German Society for Metals in 1956 at Stuttgart, Courtesy of Armco Inc. archives, Personal communication with Jerry W. Schoen, Principal Research Engineer, Armco Research and Technology.

[87] D.M. Kohler, "Production of Silicon-Iron Sheets Having Cubic Texture," US Patent 3,130,093, April 21, 1964.

[88] D.M. Kohler, J.M. Jackson "Production of Oriented Silicon-Iron Sheets by Seondary Recrystallization," US Patent 3,130,095, April 21, 1964.

[89] E.B. Stanley, "Method of Producing Electrical Sheet Steel With Cube Texture," US Patent 3,640,780, Feb. 8, 1972.

[90] W. Salz, K.A. Hempel, "Magnetic Properties of Staboperm," Journal of Magnetism and Magnetic Materials, 112 (1992), pp. 242-244.

[91] R.G. Aspden, J.A. Berger, H.E. Trout, "New Texture in Iron and Iron Based Alloys," Journal of Applied Physics, Vol. 37, No. 3, March 1, 1966, pp. 1195-1196.

[92] Werner, F.E., "Electrical Steels: 1970-1990," Energy Efficient Electrical Steels, Proceedings of a symposium sponsored by the TMS-AIME Ferrous Metallurgy Committee at the Fall Meeting of The Metallurgical Society of AIME, Pittsburgh, PA, Ctober 5-9, 1980. Edited by A.R. Marder, E.T. Stephenson, LCCCN 81-80990, ISBN 0-89520-374-x, pp1-32.

[93] H. Shimanaka, T. Irie, K. Matsumura, N. Nakamura, "A New Non-Oriented Steel With Texture of {100}<ovw>, Journal of Magnetism and Magnetic Materials, 19 (1980), 63-64, pp. 63-64.

[94] B. Cornut, A. Kedous-Lebouc, Th. Waeckerlé, "From Metallurgy to modelling of Electrical Steels: a Multiple Approach to Their Behaviour and Use Based on Physics and Experimental Investigations," Journal of Magnetism and Magnetic Materials, 160 (1996), pp. 102-108.

[95] H. Shimanaka, Y. Ito, T. Irie, K. Matsumura, H. Nakamura, Y. Shono, "Non-Oriented Si - Steels Useful for Energy Efficient Electrical Apparatus," Energy Efficient Electrical Steels, Proceedings of a symposium sponsored by the TMS-AIME Ferrous Metallurgy Committee at the Fall Meeting of The Metallurgical Society of AIME, Pittsburgh, PA, Ctober 5-9, 1980. Edited by A.R. Marder, E.T. Stephenson, LCCCN 81-80990, ISBN 0-89520-374-x, pp193-204.

[96] "Selection of Electrical Steels for Magnetic Cores," Armco Electrical Steel Products, 1985, Armco Inc., Middleton, Ohio

[97] Cole, Guerney H. "Effect of Punching Strains on the Magnetic Properties of Electrical Steel," Electric Journal, February, 1924, pp 55-61.

[98] ASTM A343, "Standard Test for Alternating-Current Magnetic Properties of Materials at Power Frequencies Using Wattmeter-Ammeter-Voltmeter Method and 25-cm Epstein Test Frame," 1992 Annual Book of ASTM Standards, Vol. 03.04.

[99] ASTM A34, "Standard Practice for Procurement Testing, and Sampling of Magnetic Materials," 1992 Annual Book of ASTM Standards, Vol. 03.04.

[100] F.J. Wilkins, A.E. Drake, "Measurement of and Interpretation of Power Losses in Electrical Sheet Steel," Proc. IEE, Vol. 112, No. 4, April 1965.

[101] J.D. Sievert, "Determination of AC Magnetic Power Loss of Electrical Steel Sheet : Present Status and Trends," IEEE Transactions on Magnetics, Vol. MAG-20, No. 5, September 1984, pp. 1702-1707.

[102] J.D. Sievert, "Recent Advances in the One- and Two-Dimensional Magnetic Measurement Technique for Electrical Sheet Steel," IEEE Transactions on Magnetics, Vol. MAG-26, No. 5, September 1990, pp. 2553-2558.

[103] P. Beckley, C.H. Porter, D. Snell, "On-Line, Single Sheet and Epstein Power Loss Testing," Journal of Magnetism and Magnetic Materials, Vol. 26, 1982, pp. 168-175.

[104] T. Yamamoto, Y. Ohya, "Single Sheet Tester for Measuring Core Losses and Permeabilities in a Silicon Steel Sheet," IEEE Transactions on Magnetics, Vol. MAG-10, No. 2, June 1974, pp. 157-159.

[105] T. Nakata, Y. Kawase, M. Nakano, "Improvement of Measuring Accuracy of Magnetic Field Strength in Single Sheet Testers By Using Two H Coils," IEEE Transactions on Magnetics, Vol. MAG-23, No. 5, September 1987, pp. 2596-2598.

[106] J.D. Sievert, D. Son, "On The Effective Magnetic Path Length Used For Field Strength and Loss Determination," Journal of Magnetism and Magnetic Materials, Vol. 41, (1984), pp. 235-237.

[107] ASTM A804, "Standard Test for Alternating-Magnetic Properties of Materials at Power Frequencies Using Sheet-Type Test Specimens," 1992 Annual Book of ASTM Standards, Vol. 03.04.

[108] J.D. Sievert, H. Ahlers, "Is The Epstein Frame Replaceable?," Anales De Fisica, Serie B, Vol. 86, 1990, pp. 58-63.

[109] H. Pfützner, P. Schonhuber, "On the Problem of the Field Detection for Single Sheet Testers," IEEE Transactions on Magnetics, Vol. 27, No. 2, March 1991, pp. 778-785.

[110] F.G. Baily, "The Hysteresis of Iron and Steel in a Rotating Magnetic Field," Philosophical Transactions of The Royal Society, 1896, Vol. 107, pp. 715-746.

[111] P. Weiss, V. Planer, "Hystérèse Dans Les Champs Tournants," Journal De Physique Théorique et Apliquée, 1908, Vol. 6, pp.5.

[112] R. Aouli, Contributions a L'Etude des Pertes Fer en Champ Tournant Dans Les Toles Magnetiques Pour Machines Electriques Mobiles, PhD Thesis, Universite De Droit, D'Economie Et De Sciences Aix Marseilles III, December 8, 1995.

[113] M.A. Dami, M. Akroune, R. Aouli, A. Mouillet, "New Approach to Characterisation of Electric Alloys Under Rotating Flux Density", IEE Proceedings on Science, Measurement and Technology, Vol. 143, No. 6, November 1996, pp. 399-405.

[114] R. Aouli, A. Mouillet, M. Akroune, M.A. Dami, "New Characterisation Device for Electric Alloys", Journal de Physique IV, France 8, 1998, pp. Pr2-709 to Pr2-712.

[115] R. Aouli, M. Akroune, M.A. Dami, A. Mouillet, "Iron Loss Measurement Device Under Rotating Magnetic Field", IEE Proceedings on Science, Measurement and Technology, Vol. 146, No. 1, January 1999, pp. 399-405.

[116] J.M. Kelly, "New Technique for Measuring Rotational Hysteresis in Ferromagnetic Materials," The Review of Scientific Instruments, Vol. 28, No. 12, December 1957, pp. 1038-1040.

[117] J.M.Kelly, "Rotational Losses in 4-79 Molybdenum Permalloy at Low Frequencies," As a Letter to the Editor in Physical Review, Vol. 103, Number 2, pp. 499-500, July 15, 1956.

[118] W.F. Archenhold, H.F. Sandham, J.E. Thompson, "Rotational Hysteresis Loss in Grain-Oriented Silicon-Iron," British Journal of Applied Physics, Vol. 11, January 1960, pp. 46-49.

[119] W.F. Archenhold, A.C. Brown, J.E. Thompson, "Stabilized Torque Magnetometer," Journal of Scientific Instruments, Vol. 36, December 1959, pp. 505-506.

[120] F.J. Young, H.L. Schenk, "Method for Measuring Iron Losses in Elliptically Polarized Magnetic Fields," Journal of Applied Physics, Supplement to Vol. 31. No. 5, May 1960, pp 194S-195S.

[121] F.J. Young, H.L. Schenk, "Iron Losses in Elliptically Polarized Magnetic Fields," Journal of Applied Physics, Vol. 37, No. 3, March 1966, pp 1210-1211.

[122] C.R. Boon, J.E. Thompson, "Alternating and Rotational Power Loss at 50c/s in 3% Silicon-Iron Sheets," Proc. IEE, Vol. 112, No. 11, November 1965, pp. 2147-2151.

[123] D.A. Ball, H.O. Lorch, "An Improved Thermometric Method of Measuring Local Power Dissipation," Journal of Scientific Instruments, 1965, Vol. 42, pp. 90-93.

[124] A. Kaplan, "Magnetic Core Losses Resulting From a Rotating Flux," Journal of Applied Physics, Supplement to Vol. 32, No. 3, March 1961, pp. 370S-371S.

[125] R.E. Tompkins, L.H. Stauffer, A. Kaplan, "New Magnetic Core Loss Comparator," Journal of Applied Physics, Vol. 29, No. 2, March 1958, pp. 502-503.

[126] W. Brix, "Measurement of the Rotational Power Loss in 3% Silicon-Iron at Various Frequencies Using a Torque Magnetometer," Journal of Magnetism and Magnetic Materials, 26 (1982), pp. 193-195.

[127] W. Brix, K.A. Hempel, W. Schroeder, "Method for the Measurement of Rotational Power Loss and Related Properties in Electrical Steels," IEEE Transactions on Magnetics, Vol. MAG-18, No. 6, November 1982, pp. 1469-1471.

[128] M. Arabi, A.J. Moses, "An Improved Method for Measuring Rotational Power Loss in Electrical Steels," Journal of Magnetism and Magnetic Materials, 41 (1984) pp. 227-229.

[129] W. Brix, K. A. Hempel, F.J. Schulte, "Improved Method for the Investigation of the Rotational Magnetization Process in Electrical Steel Sheets," IEEE Transactions on Magnetics, Vol. MAG-20, No. 5, September 1984, pp. 1708-1710.

[130] M. Enokizono, T. Suzuki, J. Sievert, J. Xu, "Rotational Power Loss of Silicon Steel Sheet," IEEE Transactions on Magnetics, Vol. 26, No. 5, September 1990, pp. 2562-2564.

[131] M. Enokizono, J. Sievert, H. Ahlers, "Optimum Yoke Construction for Rotational Loss Measurements Apparatus," Proceedings of the Symposium on Soft Magnetic Materials 9 (Spain), Anales De Fisica, Serie B, Aplicaciones, Metodos e Instrumentos, Numero Especial 1, Volumen 86 (1-337), 1990, pp. 320-322.

[132] J. Sievert, J. Xu, L. Rahf, M. Enokizono, H. Ahlers, "Studies on the Rotational Power Loss Measurement Problem," Proceedings of the Symposium on Soft Magnetic Materials 9 (Spain), Anales De Fisica, Serie B, Aplicaciones, Metodos e Instrumentos, Numero Especial 1, Volumen 86 (1-337), 1990, pp. 35-37.

[133] M. Enokizono, T. Suzuki, J.D. Sievert, "Measurement of Dynamic Magnetostriction Under Rotating Magnetic Field," IEEE Transactions on Magnetics, Vol. 26, No. 5, September 1990, pp. 2067-2069.

[134] J. Sievert, H. Alhers, M. Birkfeld, B. Cornut, F. Fiorillo, K.A. Hempel, T. Kochmann, A. Kedous-Lebouc, T. Meydan, A. Moses, A.M. Rietto, "European Intercomparison of Measurements of Rotational Power Loss in Electrical Sheet Steels," Journal of Magnetism and Magnetic Materials, 160(1996) pp. 115-118

[135] J.G. Zhu, V.S. Ramsden, "Two Dimensional Measurement of Magnetic Field and Core Loss Using a Square Specimen Tester," IEEE Transactions on Magnetics, Vol. 29, No. 6, November 1993, pp. 2995-2997.

[136] A. Kedous-Lebouc, S. Zouzou, P. Brisonneau, "Anisotropy Influence on the Rotational and Alternating Field Behaviour of Soft Magnetic Materials," IEEE Transactions on Magnetics, Vol. 28, No. 5, September 1992, pp. 2796-2798.

[137] S. Zouzou, A. Kedous-Lebouc, P. Brisonneau, "Magnetic Properties Under Unidirectional and Rotational Field," Journal of Magnetism and Magnetic Materials, 112(1992), pp. 106-108.

[138] Y. Alinejad-Beromi, A.J. Moses, T. Meydan, "New Aspects of Rotational Field and Flux Measurement in Electrical Steel," Journal of Magnetism and Magnetic Materials, 112(1992), pp. 135-138.

[139] H. Morino, Y. Ishihara, T. Todaka, "Measuring Method of Magnetic Characteristics in any Direction for Silicon Steel," Journal of Magnetism and Magnetic Materials, Vol. 112(1992), pp. 115-119.

[140] Y. Tamura, Y. Ishihara, T. Todaka, "Measurement of Magnetic Characteristics of Silicon Steel in Any Direction by RSST and SST: Method and Relationship," Journal of Magnetism and Magnetic Materials, 133(1994) pp. 382-385.

[141] A. Hasenzagl, B. Weiser, H. Pfützner, "Novel 3-Phase Excited Single Sheet Tester for Rotational Magnetization," Journal of Magnetism and Magnetic Materials, Vol. 160 (1996), pp. 180-182.

[142] A. Iványi, J. Füzi, H. Pfützner, "2D/3D Models for a Three Phase Fed Single Sheet Tester," IEEE Transactions on Magnetics, Vol. 34, No. 5, September 1998, pp. 3004-3007.

[143] M. Enokizono, T. Todaka, T. Sashikata, J.D. Sievert, H. Ahlers, "Magnetic Field Analysis of Rotational Loss Tester With Vertical Yoke," Journal of Magnetism and Magnetic Materials, 112 (1992), pp. 81-84.

[144] J. Sievert, H. Ahlers, M. Enokizono, S. Kauke, L. Rhaf, J. Xu, "The Measurement of Rotational Power Loss in Electrical Sheet Steel Using a Vertical Yoke System," Journal of Magnetism and Magnetic Materials, 112 (1992), pp. 91-94.

[145] N. Nencib, A. Kedous-Lebouc, B. Cornut, "3D Analysis of a Rotational Loss Tester With Vertical Yokes," Journal of Magnetism and Magnetic Materials, 133 (1994), pp. 553-556.

[146] T. Nakata, N. Takahashi, K. Fujiwara, M. Nakano, "Measurement of Magnetic Characteristics Along Arbitrary Directions of Grain-Oriented Silicon Steel Up to High Flux Densities," IEEE Transactions on Magnetics, Vol. 29, No. 6, November, 1993, pp 3544-3546.

[147] W. Salz, "A Two-Dimensional Measuring Equipment for Electrical Steel," IEEE Transactions on Magnetics, Vol. 30, No. 3, May 1994, pp. 1253-1257.

[148] H. Pfutzner, "Rotational Magnetization and Rotational Losses of Grain Oriented Silicon Steel Sheets - Fundamental Aspects and Theory," IEEE Transactions on Magnetics, Vol. 30, No. 5, September 1994, pp. 2802-2807.

[149] M. Arabi, A.J. Moses, "An Improved Method for Measuring Rotational Power Loss in Electrical Steels," Journal of Magnetism and Magnetic Materials, 1984, vol. 41, pp 227-229.

[150] M. Enokizono, T. Suzuki, J. Sievert, J. Xu, "Rotational Power Loss of Silicon Steel Sheet," IEEE Transactions on Magnetics, vol. 26, No. 5., September 1990, pp. 2562-2564.

[151] J. Sievert, "On Measuring the Magnetic Properties of Electrical Sheet Steel Under Rotational Magnetization," Journal of Magnetism and Magnetic Materials, 112(1992), pp. 50-57.

[152] K. Atallah, D. Howe, "Calculation of the Rotational Power Loss in Electrical Steel Laminations From Measured H and B," IEEE Transactions on Magnetics, Vol. 29, No. 6, November 1993, pp. 3547-3549.

[153] H. Zijlstra, Experimental Methods in Magnetism - Vol 2. Measurement of Magnetic Quantities, North-Holland Publishing Company - Amsterdam, John Wiley and Sons, Inc - New York, 1967, LCCCN 67-29770.

[154] M. Mikulec, "Accuracy of Single Sheet Testers," Journal of Magnetism and Magnetic Materials, 112 (1992) pp. 112-114.

[155] W. Salz, K.A. Hempel, M. Mende. "Loss Separation Under Elliptically Rotating B-field With Bias Field in Electrical Steel, Journal of Magnetism and Magnetic Materials, 133 (1994), pp. 144-146.

[156] A.J. Moses, B. Thomas, J.E. Thompson, "Power Loss and Flux Density Distributions in the T-Joint of a Three Phase Transformer Core," IEEE Transactions on Magnetics, Vol. MAG-8, No. 4, December 1972, pp. 785-790.

[157] A.J. Moses, B. Thomas, "Measurement of Rotating Flux in Silicon Iron Laminations," IEEE Transactions on Magnetics, Vol. MAG-9, No. 4, December 1973, pp. 651-654.

[158] A.J. Moses, B. Thomas, "The Spatial Variation of Localized Power Loss in Two Practical Transformer T-Joints," IEEE Transactions on Magnetics, Vol. MAG-9, No. 4, December 1973, 655-659.

[159] K. Narita, T. Yamaguchi, I. Chida, "Distributions of Rotating Flux and Iron Loss in T-Joints of Three-Phase, Three-Limbed Model Transformer Cores," Electrical Engineering in Japan, Vol. 95, No. 5, 1975 pp. 42-48.

[160] G.S. Radley, A.J. Moses, "Apparatus for Experimental Simulation of Magnetic Flux and Power Loss Distribution in a Turbogenerator Stator Core," IEEE Transactions on Magnetics, Vol. MAG-17, No. 3, May 1981, pp. 1311-1316.

[161] A.J. Moses, G.S. Radley, "Experimental Simulation of Magnetic Flux and Power Loss Distribution in the Stator Core of a Large Rotating Machine," Journal of Magnetism and Magnetic Materials, 19 (1980), pp. 60-62.

[162] H.W. Lorenzen, R. Nuscheler, "The Calculation of Iron Loss and Field Distribution in Anisotropic Steel Laminations," IEEE Transactions on Magnetics, Vol. 24, No. 2, March 1988, pp. 1972-1974.

[163] M. Enokizono, "Measurement and Analysis of Magnetic Field of Inverter-Driven Three- Phase Squirrel-Cage Induction Motor," Electrical Engineering in Japan, Vol. 108, No. 5, 1988, pp. 103-111.

[164] M.K. Jamil, P. Baldassari, N.A. Demerdash, "No-Load Induction Motor Core Losses Using a Combined Finite Element State Space Model," IEEE Transactions on Magnetics, Vol. 28, No. 5, 1992, pp. 2820-2822.

[165] K. Atallah, D. Howe, "The Calculation of Iron Losses in Brushless Permanent Magnet DC Motors," Journal of Magnetism and Magnetic Materials, Vol. 133 (1994), pp. 578-582.

[166] G.H. Shirkoohi, A.M. Yahya, "Localised Flux and Iron Loss in the Tooth Tip Region of a Three-Phase Induction Machine Stator Core," Journal of Magnetism and Magnetic Materials, Vol. 133 (1994), pp. 644-646.

[167] G. Bertotti, A. Canova, M. Chiampi, D. Chiarabaglio, F. Fiorillo, A.M. Rietto, "Core Loss Prediction Combining Physical Models With Numerical Field Analysis," Journal of Magnetism and Magnetic Materials, Vol. 133 (1994), pp. 647-650.

[168] G. Bertotti, A. Boglietti, M. Chiampi, D. Chiarabaglio, F. Fiorillo, M. Lazzari, "An Improved Estimation of Iron Losses in Rotating Electrical Machines," IEEE Transactions on Magnetics, Vol. 27, No. 6, November 1991, pp. 5007-5009.

[169] F. Leonardi, T. Matsuo, T.A. Lipo, "Iron Loss Calculation For Synchronous Reluctance Machines," Proceedings of the 1996 International Conference on Power Electronics, Drives and Energy Systems for Industrial Growth, Paper 0-7803-2795-0, January 1996, pp. 307-312.

[170] M. Enokizono, Y. Sadanaga, "Improved Magnetic Field Analysis of Induction Motor Models," IEEE Transactions on Magnetics, Vol. 34, No. 5, September 1998, pp. 2621-2624.

[171] M. Enokizono, Y. Sadanaga, "Loss and Field Analysis of Induction Motor by Improved Finite Element Method," Proceedings of the International Conference on Electrical Machines, Vol. 2/3, September 2-4, 1998, Istanbul, Turkey, pp. 1312-1317.

[172] N. Stranges, Rotational Power Losses in Motor Lamination Quality Steels, A Thesis Submitted to the School of Graduate Studies in Partial Fulfilment of the Requirements for the Degree Master of Engineering, McMaster University, June, 1994

[173] ASTM A340, "Standard Terminology of Symbols and Definitions Relating to Magnetic Testing," 1992 Annual Book of ASTM Standards, Vol. 03.04.

[174] IEEE Standard Dictionary of Electrical and Electronics Terms, Fourth Edition, ISBN 1-55937-000-9, LCCCN 88-082198, 1988.

[175] ASTM 677, "Standard Specification for Nonoriented Electrical Steel Fully Processed Types," 1992 Annual Book of ASTM Standards, Vol. 03.04.

[176] E. Kreyszig, Advanced Engineering Mathematics - Seventh Edition , John Wiley & Sons, Inc., New York, 1993, ISBN 0-471-55380-8.

[177] A.J. Moses, "Rotational Magnetization - Problems in Experimental and Theoretical Studies of Electrical Steels and Amorphous Magnetic Materials," IEEE Transactions on Magnetics, Vol. 30, No. 2, March 1994, pp. 902-906.

[178] J.H.R. Page, "Some Observations on the Magnetic Anisotropy of Non-Oriented 3% Si Steels," IEEE Transactions on Magnetics, Vol. MAG-20, No. 5, September 1984, pp. 1542-1544.

[179] P.L. Alger, Induction Machines - Their Behaviour and Uses - Second Edition, Gordon and Breach Publishers, LCCCN 64-18799, Third printing with additions 1995.

[180] T. Spooner, "Tooth Pulsation in Rotating Machines," AIEE Transactions, Vol. 43, 1924, pp. 251-261.

[181] T. Spooner, I.F. Kinnard, "Surface Iron Losses With Reference to Laminated Materials," AIEE Transactions, Vol. 43, 1924, pp. 262-281.

[182] T. Spooner, "Squirrel-Cage Induction-Motor Core Losses," AIEE Transactions, Vol. 44, 1925, pp.155-163.

[183] T. Spooner, C.W. Kincaid, "No-Load Induction Motor Core Losses," AIEE Transactions, Vol. 48, April 1929, pp. 645-655.

[184] J.H. Walker, "A Theory of Induction-Motor Surface Losses," Journal of the IEE, Vol. 95 Pt. II, 1948, pp. 597-606.

[185] C.A. Adams, A.C. Lanier, C.C. Pope, C.O. Schooley, "Pole-Face Losses," AIEE Transactions, Vol. 28, 1909, pp. 1133-1156.

[186] F.W. Carter, "Pole-Face Losses," Journal of the IEE, Vol. 54, 1916, pp. 168-170.

[187] W.J. Gibbs, "Tooth-Ripple Losses in Unwound Pole-Shoes," Journal of the IEE, Vol. 94 Pt.II, No. 37, February 1947, pp. 2-12.

[188] H. Bondi, K.C. Mukherji, "An Analysis of Tooth-Ripple Phenomena in Smooth Laminated Pole-Shoes," Proc. IEE, Vol.104, Part C, 1957, pp. 349-356.

[189] J. Greig, E.M. Freeman, "Simplified Presentation of the Eddy-Current-Loss Equation for Laminated Pole-Shoes," Proc. IEE, Vol. 110, No.7, July 1963, pp. 1255-1259.

[190] R.D. Findlay, H.A. Briggs, "Open Circuit Tooth Ripple Eddy Current Loss in Smooth Laminated Poles," IEEE Transaction on Power Apparatus and Systems, Vol. 93, 1974, pp. 122-128.

[191] H.C. Karmaker, "Open Circuit Tooth Ripple Losses in Slotted Laminated Poles of Electrical Machines With Amortisseur Windings," IEEE Transactions on Power Apparatus and Systems, Vol. PAS-101, No. 5, May 1982, pp. 1122-1128.

[192] J.J.C. Gyselinck, L.R.L Dupré, L. Vandervelde, J.A.A. Melkebeek, "Calculation of No-Load Induction Motor Core Losses Using the Rate-Dependent Preisach Model," IEEE Transactions on Magnetics, Vol. 34, No. 6, November 1998, pp. 3876-3881.

[193] P.L. Alger, "Induced-High Frequency Currents in Squirrel-Cage Windings," IEEE Transactions on Power Apparatus and Systems, Vol. 76, Pt. III, October 1957, pp. 724-729.

[194] P.L. Alger, G. Angst, E. John Davies, "Stray-Load Losses in Polyphase Induction Machines," AIEE Trans., Vol. 78, Pt. III-A, pp. 349-357.

[195] J.H. Wray, "Induction Motor surface Losses, Load and No Load," General Electric Technical Information Series, Report #R52AE32, February 6, 1952.

[196] D. Birnstingl, "Iron Losses in Laminated Steel at Harmonic Frequencies," General Electric Technical Information Series, Report #R51AE29, November 15, 1951.

[197] IEEE Std 112 - 1996 (Revision of IEEE Std 112 -1991) - "IEEE Standard Test Procedure for Polyphase Induction Motors and Generators," ISBN 1-55937-891-3

[198] G.H. Shirkoohi, "Finite Element Solution of Single Phase Induction Machine Cores Constructed From Anisotropic Non-Oriented Steels," Journal of Magnetism and Magnetic Materials, 112 (1992), pp 451-453.

[199] S.J. Salon, D.W. Burow, R.E. Ashley III, L. Ovacik, M.J. DeBortoli, "Finite Element Analysis of Induction Machines in the Frequency Domain," IEEE Transactions on Magnetics, Vol. 29, No. 2, March 1993, pp. 1438-1441.

[200] S. Williamson, J.W. Ralph, "Finite-Element Analysis for Nonlinear Magnetic Field Problems With Complex Current Sources," Proceedings of the IEE, Vol. 129 Pt. A, No. 6, August 1982, pp. 391-395.

[201] S. Williamson, J.W. Ralph, "Finite-Element Analysis of an Induction Motor Fed From a Constant-Voltage Source," Proceedings of the IEE, Vol. 130 Pt. B, No. 1, January 1983, pp. 18-24.

[202] M. Ito, N. Fujimoto, H. Okuda, N. Takahashi, T. Miyata, "Analytical Model for Magnetic Field Analysis of Induction Motor Performance," IEEE Transactions on Power Apparatus and Systems, Vol. PAS-100, No. 11, November 1981, pp. 4582-4590

[203] R. Belmans, D. Verdyck, W. Geysen, R.D. Findlay, B. Szabados, S. Spencer, S. Lie "Magnetic Field Analysis in Squirrel Cage Induction Motors," IEEE Transactions on Magnetics, Vol. 28, No. 2, March 1992, pp. 1367-1370.

[204] P. Zhou, J. Gilmore, Z. Badics, Z.J. Cendes, "Finite Element Analysis of Induction Motors Based on Computing Detailed Equivalent Circuit Parameters," IEEE Transactions on Magnetics, Vol. 34, No. 5, September 1998, pp. 3499-3502.

[205] R. Belmans, R.D. Findlay, W. Geysen, "A Circuit Approach to Finite Element Analysis of a Double Squirrel Cage Induction Motor," IEEE Transactions on Energy Conversion, Vol. 5, No. 4, December 1990, 719-724.

[206] E. Vassent, G. Meunier, J.C. Sabonnadierre, "Simulation of Induction Machine Operation Using Complex Magnetodynamic Finite Elements," IEEE Transactions on Magnetics, Vol. 25, No. 4, July 1989, pp. 3064-3066.

[207] E. Vassent, G. Meunier, A. Foggia, "Simulation of Induction Machines Using Complex Magnetodynamic Finite Element Method Coupled With the Circuit Equations," IEEE Transactions on Magnetics, Vol. 27, No. 5, September 1991, 4246-4249.

[208] R.D. Findlay, N. Stranges, D.K. MacKay, "Losses Due to Rotational Flux in Three Phase Induction Motors," IEEE Transactions on Energy Conversion, Vol. 9, No. 3, September 1994, pp 543-549.

[209] R.D.Findlay, N.Stranges and D.K.MacKay, "Losses due to Rotational Flux in Three Phase Induction Motors," Second International Workshop on Electric and Magnetic Fields, Leuven, Belgium, 17-20 May, 1994, 6 pages.

[210] Nick Stranges, Raymond D. Findlay and James H. Dymond, "A Comparison of Two Finite Element Methods for Determining Flux Density Polarization in Induction Motor Cores", Proceedings of the Canadian Conference on Electrical and Computer Engineering, Calgary, 26-29 May 1996, pp 943-6.

[211] B.J. Chalmers, "AC Machine Windings With Reduced Harmonic Content," Proc. IEE, Vol. 111, No. 11, November 1964, pp. 1859-1863.

[212] D.A. Lowther, B. Forghani, E.M. Freeman, "On Equivalent Reluctivities for Time Harmonic Eddy Current Analysis," Advanced Computational and Design Techniques in Applied Electromagnetic Systems, edited by S.Y. Hahn, Proceedings of the International ISEM Symposium, Soeul, Korea, June 1994, Elsevier, pp. 647-650 (received as a personal communication from B. Forghani).

[213] R.D. Findlay, "Pole Face Losses: Development of Formulation for Prediction of Open Circuit Pole Face Losses and Correlation With Test Results," Canadian General Electric Industrial Apparatus Department, Engineering Laboratory, Report # DQF75-IAD-005, June 1975,

[214] E.M. Freeman, "The Calculation of Harmonics, Due to Slotting, In The Flux Density Waveform of a Dynamo-Electric Machine," Proceedings of the IEE, Vol. 109, Part C, No. 16, 1962, pp. 581-588.

[215] IEEE Std. 115 - 1983, IEEE Guide: Test Procedures for Synchronous Machines

[216] G.H. Rockwood, "Calculation of Stray Load Losses," AIEE Transactions, Vol. 46, 1927, pp. 1139-1147.

Appendix A

Ferromagnetism

A1.0 Introduction

Let us review the concept of ferromagnetic domain theory to aid in understanding the losses and magnetization processes in electrical steels. References [A1-A5] provide an excellent review of the theory. This material is included to give the reader a clear understanding of the differences in the mechanisms of magnetization encountered with alternating and rotating magnetic fields.

A2.0 Ferromagnetic Domain Theory

In ferromagnetic materials, magnetism arises mainly due to electron spins rather than from the orbital motions of the electrons around the nuclei [A1-A3]. At temperatures above the Curie temperature, the electron spins are agitated such that the magnetic moments are nearly randomly distributed. Each spin essentially behaves independently. As temperature is lowered below the Curie temperature, the spins are less violently agitated and a few neighbouring moments may randomly become parallel. When this happens, the internal field of these parallel moments is increased in proportion to the number of aligned spins. This increased internal field then acts on other neighbouring spins, causing them to be aligned also. This process spreads rapidly and soon all the spins in a region are aligned due to the internal field. This is known as "spontaneous magnetization".

Ferromagnetic specimens are composed of small regions called "domains". In each domain the local magnetization is saturated. Furthermore, the direction of

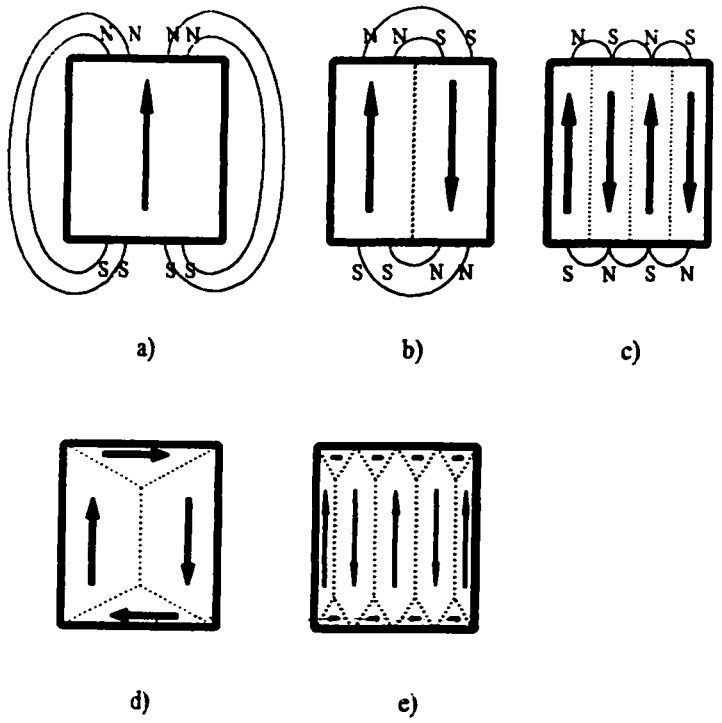

Figure A1 - The origin of domains. Domain structures (Taken after figure 9 in [A1]).

magnetization within each domain is not necessarily the same. In an unmagnetized sample, the magnetic moments in the domains of a ferromagnetic sample will align themselves in a random manner. This gives a zero net magnetization. Illustrations of "domains of closure" that give zero resultant magnetic moments are shown in figures A1d) and A1e).

A2.1 Domain Formation

As discussed by Plonus [A5], Kittel [A1], Kittel and Galt[A2], and Bozorth [A3], four energy mechanisms are involved in the magnetization of ferromagnetic materials. The energy mechanisms are [A5]:

$$W_{ferromagnetism} = W_{exchange} + W_{magnetostatic} + W_{anisotropic} + W_{magnetostrictive} \qquad \textbf{(A1)}$$

The sum of these energies tends towards a minimum in the absence of an externally applied

field. Therefore, the domains in the material arrange themselves in a minimum energy configuration. The four energy mechanisms are briefly described in the following sections.

A2.1.1 Exchange Energy

The exchange interaction that aligns adjacent spins is also known as the "spin-spin interaction" [A5]. The Pauli Exclusion principle states that two electrons of the same spin may not occupy the same region of space. Most substances are nonmagnetic because the outer electrons of adjacent atoms have a tendency to form antiparallel pairs. Ferromagnetic materials such as iron, cobalt, and nickel have unpaired electrons in an inner electron shell [A3,A5]. Here, they are not able to form antiparallel pairs with electrons from other atoms. These unpaired electron spins are the ones aligned by the molecular field of the exchange force.

The exchange energy is expressed as [A5]:

$$W_{spin-spin} = -C\cos\psi \qquad \textbf{(A2)}$$

where C is a positive constant and ψ is the angle between moments of adjacent atoms. This energy is minimized when the spins are aligned. The minimum energy of -C is obtained when the dipoles are aligned, whereas for antiparallel alignment $\psi = 180°$ gives W = +C. Exchange energy is minimized when all the spins in the material are aligned as in figure A1a).

A2.1.2 Magnetostatic Energy

The magnetostatic energy resides in the magnetic field of a magnet and is given by [A5]:

$$W_{magnetostatic} = \frac{1}{2}\iiint \mu H^2 dv \qquad \textbf{(A3)}$$

This energy is minimized when the external field of a magnet is reduced. Division of a region into two or more domains with opposite magnetic moments lowers the magnetostatic energy of the system by reducing the external magnetic field. This process is described in [A1,A2] is illustrated in figure A1b) and A1c).

A2.1.3 Anisotropy Energy

In the previous section we have seen that it possible for domains of closure to form which make the net magnetization of a sample zero. This situation is shown in figure A1d). The energy required to form a domain of closure comes primarily from the crystalline anisotropy energy. The anisotropy energy tends to make the magnetization of a domain lie along certain crystallographic axes. Favoured axes are called the axes of "easy" magnetization. Figure A2 shows a body centred cubic crystal of silicon-iron with the "easy", "medium" and hard directions of magnetization specified. A corresponding magnetization curve for a single crystal of silicon-iron is shown in figure A3. The anisotropy energy is defined as the excess energy required to saturate a crystal in the hard direction in comparison to the easy direction [A1,A2,A5]. For iron crystals, this energy can be expressed as [A1,A2]

$$W_{anisotropy} = K_1(\alpha_1^2\alpha_2^2 + \alpha_2^2\alpha_3^2 + \alpha_3^2\alpha_1^2) + K_2(\alpha_1^2\alpha_2^2\alpha_3^2) \qquad \textbf{(A4)}$$

where K_1, and K_2 are the anisotropy constants of the material and α_1, α_2 and α_3 are the direction cosines of the magnetization vector referred to the crystal axes. In an iron crystal, the magnetization vectors in the primary domains, and the domains of closure, can lie along easy directions of the crystal. Consequently, the domain configuration in figure A1d) is at a lower energy state than the one illustrated in figure A1c).

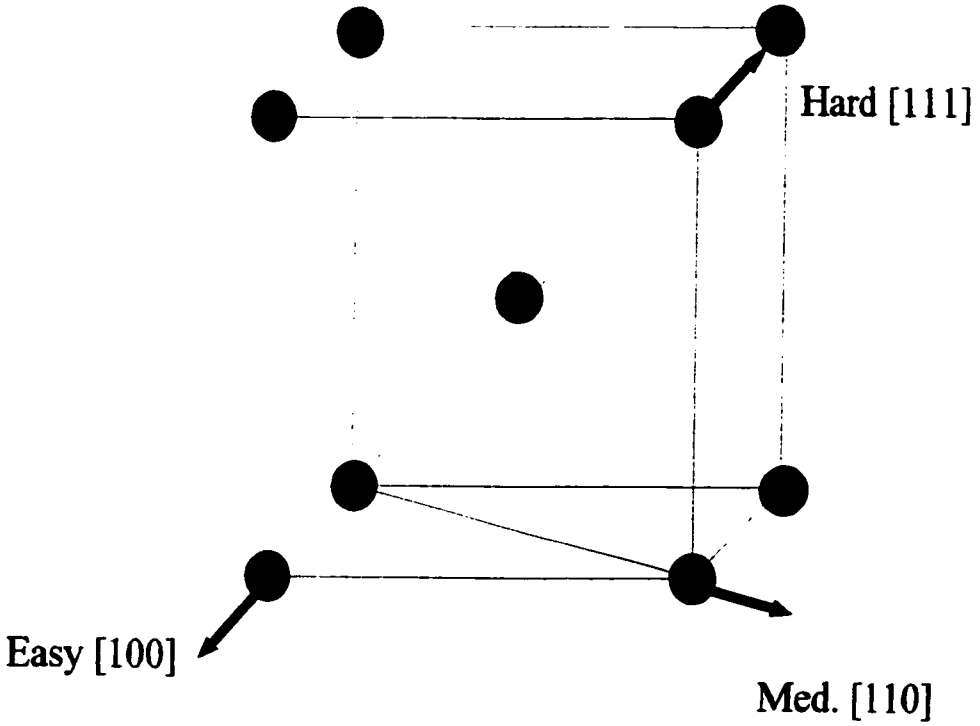

Figure A2 - "Easy", "Medium" and "Hard" directions for a body centred cubic crystal of silicon iron. Directions denoted by the indices [100], [110] and [111] respectively. Taken after figure 11-2 in Bozorth [A3].

A2.1.4 Magnetostrictive Energy

Some crystalline substances experience a stress when exposed to an applied magnetic field. The substance may change dimensions (strain) to relieve this stress. When a ferromagnetic material strains under stress, its magnetization and permeability are also affected. This phenomenon is known as magnetostriction. For an applied field parallel to a cube edge or easy direction, iron expands, whereas for a field applied along the body diagonal or hard direction, it contracts. When a field is applied parallel to the face diagonal, the iron crystal first expands and then contracts as the field is increased [A3,A5]. In iron, tension increases the magnetization in the direction of the applied tension and decreases the

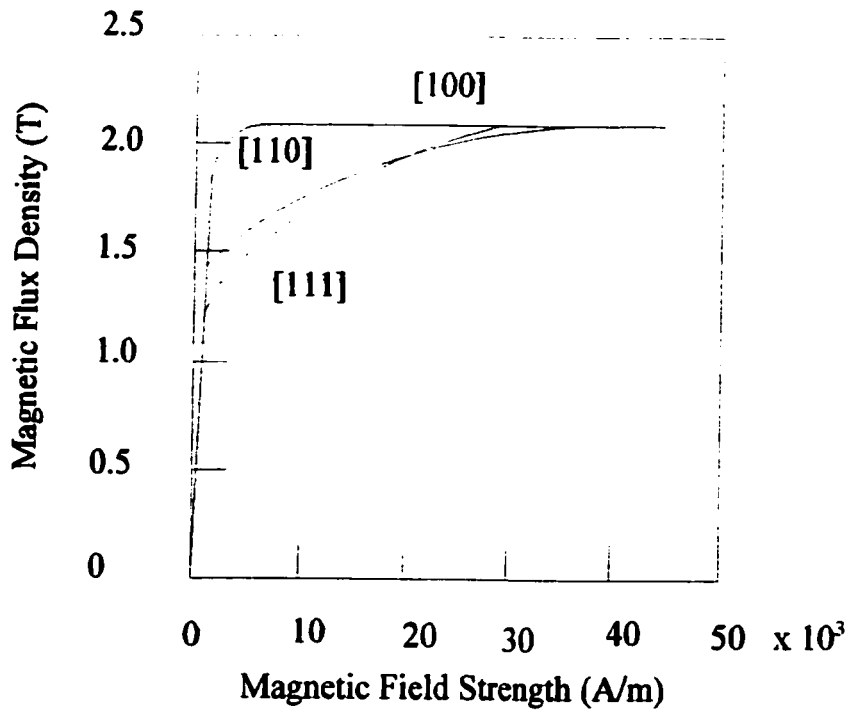

Figure A3 - Magnetization curves along three axes of a single crystal of 3% silicon-iron alloy. Based on results of Honda and Kaya [A4] as cited in figure 10 of Kittel [A1] and figure 10 of Kittel and Galt [A2]. Also shown in figure 11-2 of Bozorth [A3] magnetization in the direction perpendicular to the applied tension.

Magnetostrictive and anisotropy energies are closely related in that a crystal will deform if doing so will lower the anisotropy energy [A1,A2,A5]. The magnetostrictive energy is defined as zero for an unstrained lattice. The direction of the internal contraction or elongation in a ferromagnetic material prefers to orient itself along the direction of the internal magnetization. The magnetostrictive energy is given by Kittel [A1], Kittel and Galt [A2] and Bozorth [A3] as

$$W_{magnetostrictive} = \frac{3}{2}\lambda T \sin^2\theta \qquad \textbf{(A5)}$$

where λ is the isotropic magnetostriction constant and θ is the angle between the tension T and the magnetization.

Referring back to figure A1, we can summarize interactions between the four energies and show that the minimum energy configuration is obtained by the situation in figure A1e). In order to minimize the exchange energy term, all the spins in the material will be aligned and we will have the situation depicted in figure A1a). This is exactly the configuration that maximizes the contribution related to the magnetostatic energy. In order to decrease the magnetostatic energy, the domain splits into smaller domains with anti parallel alignments. As such there is a trade off between the exchange energy which is raised and the magnetostatic energy which is lowered and we arrive at the situation depicted in figure A1c). Now recall, in iron domains of closure can form in which the magnetic moments still lie along an "easy" direction of magnetization. As such the anisotropy term in equation (A1) is lowered as is the magnetostatic energy term. This situation is shown in figure A1d). Now recall that iron tends to expand when magnetized along an easy direction. This creates a stress at the boundary between the domains of closure and the primary domains. The energy term related to the magnetostrictive term is increased. To relieve the internal stresses more domains are created as in figure A1e). The process continues, until the increase in the exchange energy outweighs the benefits of creating more domains.

A2.2 Bloch Walls

Bloch ([A7] as cited by Kittel [A1,A2] and Bozorth [A3]) showed that the boundary between domains spreads over a region many atoms thick. The exchange force acts over only one or two atomic distances. This makes the exchange force highest at the boundary between two domains. The boundary wall separates regions of opposite spin. At the boundary wall, a region of spin transition exists as shown in figure A4. This smooth transition

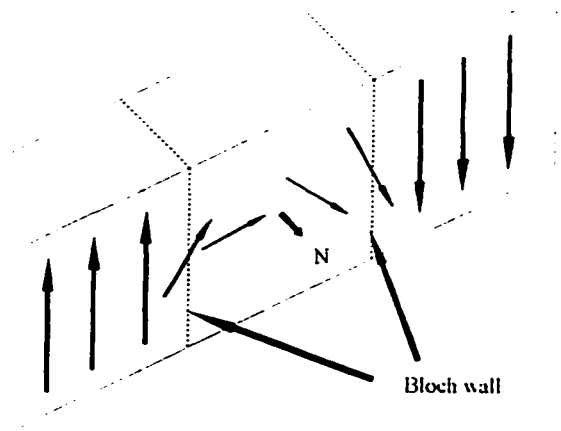

Figure A5 - A 180° Bloch wall. The region in which the dipole moments within adjacent domains gradually changes is known as a Bloch wall. Note the "visible" North dipole in the centre of the region. Taken after figure 9-38 in Plonus [A5] and figure 23 in Kittel [A1].

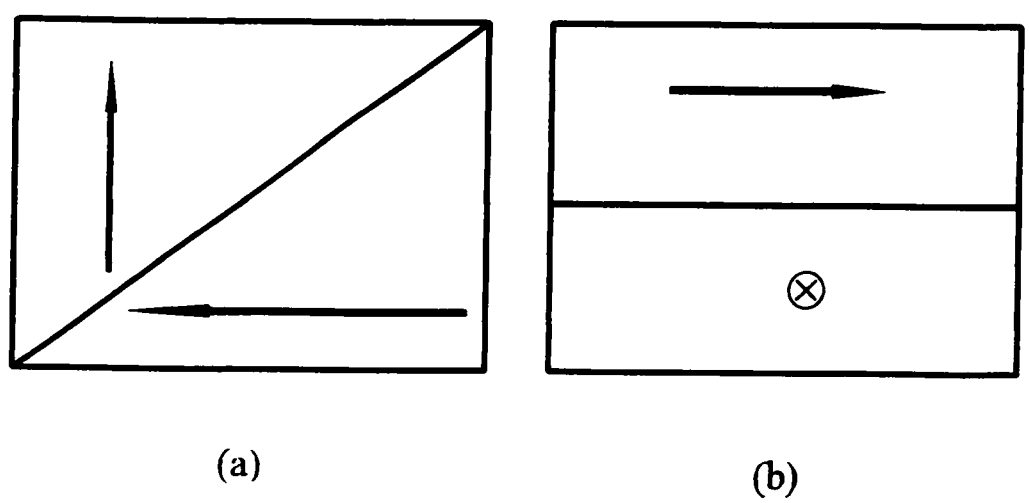

Figure A4 - Two types of 90° Bloch wall. a) All spins not parallel to wall. b) All spins parallel to the wall. Taken after figure 18-2 in Bozorth [A3].

of spin moments lowers the exchange energy. The angle between adjacent spins is very small so that by equation (A3) the spin energy between adjacent spins is near a minimum. This region of transition is called a "180° Bloch" wall, and according to Plonus [A5], is on the order of several hundred atomic diameters long. The energy of the walls is low enough to allow them to move when exposed to a small external field. As the wall moves, imagine the dipoles with the wall rotating through 180° as the wall moves to the left or the right. The configuration shown in figure A5 is called a 90° wall. Core materials used in large rotating machines are always polycrystalline; that is, each specimen is composed of many crystallites or grains. Each grain contains one or more domains.

References - Appendix A

[A1] C. Kittel, "Physical Theory of Ferromagnetic Domains", Review of Modern Physics. Volume 21, No. 4, October 1949, pp. 541-583.

[A2] C. Kittel, J.K Galt "Ferromagnetic Domain Theory", Solid State Physics. Vol. 3, 1956, pp. 437-565.

[A3] R.M. Bozorth, Ferromagnetism, IEEE PRESS Classic Reissue, ISBN 0-7803-1032-2, Copyright 1978 - American Telephone and Telegraph Company.

[A4] S. Chikazumi, Physics of Ferromagnetism, John Wiley & Sons, Inc., New York, London, Sydney, Copyright 1964, LCCN 64-14985.

[A5] Plonus, M.A., Applied Electromagnetics, McGraw-Hill, Inc., New York, Copyright 1978, ISBN 0-07-050345-1.

[A6] H. Honda, S. Kaya, "Magnetization of Single Crystals of Iron", Science Reports Tôhoku Imperial University, 1926, 15, pp. 721-753.

[A7] F. Bloch, "Theory of the Exchange Problem and of Residual Ferromagnetism", Z. Physik, Vol. 74, 1932, pp 295-335.

Appendix B

The Finite Element Method

B1.0 Introduction

This appendix provides a brief overview of the FEM and establishes some of the terminology used throughout the body of the thesis. Readers interested in probing the subject further are referred to some of the many excellent references available in the literature [B1-B6]. The description contained in this appendix is by no means complete. It does present a brief description of the finite element method, using first order elements, derived from a variational functional minimization.

Solutions to Laplace's and Poisson's equations for many practical electrical engineering problems are virtually impossible to obtain in closed form analytical expressions. This is especially true for problems relating to electric machines due to the complex geometries of the problems. The finite element method (FEM) is a numerical method based on discretization of the problem geometry into small regions called "finite elements". The elements form a mesh over the solution domain. A system of equations is created by systematically applying a formulation to this discretized problem. A variational formulation is commonly employed but other methods such as the Galerkin method are also common [B2-B5]. The solution to the problem is obtained by solving the system of equations resulting from the problem discretization. For magnetic problems, this solution yields a magnetic vector potential at the node of each element. To find the magnetic vector potential in any other region of the problem interpolation functions are employed.

B2.0 Field Formulation - Nonlinear Magnetostatic Case

For a two-dimensional (2D) magnetostatic field problem with field dependent permeability, the magnetic vector potential satisfies a partial differential equation described by the nonlinear Poisson equation:

$$\frac{\partial}{\partial x}\left(\nu \partial \frac{A}{\partial x}\right) + \frac{\partial}{\partial y}\left(\nu \partial \frac{A}{\partial y}\right) = -J \qquad \textbf{(B1)}$$

where ν is the reluctivity or reciprocal permeability, A is the magnetic vector potential and J is the source current density. As discussed by Silvester and Ferrari [B2] and Hoole [B4], this equation is derived from the differential form of Maxwell's equation (Maxwell's equations of electromagnetic theory are found in [B7,B8]) derived from Ampere's Law:

$$\nabla \times \bar{H} = \bar{J} \qquad \textbf{(B2)}$$

noting the magnetic flux density is derived from the magnetic vector potential such that

$$\nabla \times \bar{A} = \bar{B} \qquad \textbf{(B3)}$$

Also note that

$$\bar{H} = \nu \bar{B} = \nu \nabla \times \bar{A} \qquad \textbf{(B4)}$$

Substituting equation (B4) into equation (B2), we can write

$$\nabla \times (\nu \nabla \times \bar{A}) = \bar{J} \qquad \textbf{(B5)}$$

For 2D field problems, the vector quantities are assumed to be entirely z directed. Under these conditions, equation (B5) can be re-written in the form given by equation (B1).

B3.0 The Variational Method

Instead of directly solving the equations resulting from (B1), we may choose instead,

to minimize the corresponding energy functional. This forms the basis of the variational method. In mathematical terms, we replace the condition of satisfaction of a differential equation governing an unknown function by the equivalent requirement than an integral function of the unknown function will be at a minimum. The calculus of variations is described in rigorous formal detail in the classic text by Courant and Hilbert [B9] and as it applies to electromagnetic problems by Ida and Bastos [B3]. Suppose that a functional F exists, and that it is a function of a variable A and of its partial derivatives

$$A_x = \frac{\partial A}{\partial x} \tag{B6}$$

$$A_y = \frac{\partial A}{\partial y} \tag{B7}$$

Then the functional takes the form [B1]:

$$F = \iint_S f(A, A_x, A_y, x, y)dxdy \tag{B8}$$

where S is the region in which F is defined.

The functional is minimized when [B1,B3]:

$$\frac{\partial f}{\partial A} - \frac{\partial}{\partial x}\left(\frac{\partial f}{\partial A_x}\right) - \frac{\partial}{\partial y}\left(\frac{\partial f}{\partial A_y}\right) = 0 \tag{B9}$$

Any valid functional F, must satisfy this "Euler equation".

The energy functional corresponding to (B1) was given by Silvester and Chari [B1] as:

$$F = \iint_S \left[\int_0^B HdB - JA\right]dxdy \tag{B10}$$

To calculate the terms of the Euler equation, we note that $A_z = A$ and that the current density J is entirely z directed. Also note that

$$\frac{\partial f}{\partial A} = -J \tag{B11}$$

Since the magnetic flux density is given by the curl of the magnetic vector potential as in (B3), we may write expressions corresponding to the terms given by (B6) and (B7) as:

$$A_x = \frac{\partial A}{\partial x} = -B_y \qquad \text{and} \qquad A_y = \frac{\partial A}{\partial y} = B_x \tag{B12}$$

The terms of the Euler equation are found as follows [B3]:

$$\frac{\partial f}{\partial A_x} = -\frac{\partial}{\partial B}\left[\int_0^B HdB - JA\right]\frac{\partial B}{\partial B_y} = -H\frac{\partial}{\partial B_y}\sqrt{B_x^2 + B_y^2} \tag{B13}$$

which simplifies to

$$\frac{\partial f}{\partial A_x} = -H\frac{B_y}{B} = -\frac{1}{\mu}B_y = -H_y \tag{B14}$$

Using similar arguments, we may write

$$\frac{\partial f}{\partial A_y} = \frac{\partial}{\partial B}\left[\int_0^B HdB - JA\right]\frac{\partial B}{\partial B_x} = H\frac{\partial}{\partial B_x}\sqrt{B_x^2 + B_y^2} \tag{B15}$$

which simplifies to

$$\frac{\partial f}{\partial A'_y} = H\frac{B_x}{B} = \frac{1}{\mu}B_x = H_x \tag{B16}$$

Substituting equations (B15),(B16) and (B34) into the Euler equation (B9) we find

$$-J - \frac{\partial}{\partial x}(-H_y) - \frac{\partial}{\partial y}(H_x) = 0 \qquad \text{or} \qquad \nabla x\bar{H} = \bar{J} \tag{B17}$$

which is the equation we wish to solve. This shows that the functional given by (B9) is valid for solving problems of the type described by equation (B1) as derived from (B2).

B4.0 First Order Triangular Elements

B4.1 Interpolation Functions

As discussed in [B1-B3], for first order triangular elements, the magnetic vector potential must vary linearly inside the element as

$$A(x,y) = a_1 + a_2x + a_3y \tag{B18}$$

Equation (B18) must be satisfied at each node of an element such that

$$A_1 = a_1 + a_2x_1 + a_3y_1 \tag{B19}$$

$$A_2 = a_1 + a_2x_2 + a_3y_2 \tag{B20}$$

$$A_3 = a_1 + a_2x_3 + a_3y_3 \tag{B21}$$

The coefficients a1, a2, and a3 are readily found by solving the set of simultaneous equations given by equations (B19) to (B20).

Equation (B18) can be written as [B3,B4,B6]:

$$A(x,y) = \frac{1}{D}\sum_{i=1}^{3}(p_i + q_ix + r_iy)A_i \tag{B22}$$

where D is twice the triangle area triangle. The terms p_1, q_1, and r_1 are given as [B3,B4,B6]:

$$p_1 = x_2y_3 - y_2x_3 \tag{B23}$$

$$q_1 = y_2 - y_3 \tag{B24}$$

$$r_1 = x_3 - x_2 \tag{B25}$$

The remaining terms are obtained by cyclic permutation of the indexing variable ℓ, such that

$$\begin{aligned} p_2 &= x_3y_1 - y_3x_1 \qquad & q_2 &= y_3 - y_1 \qquad & r_2 &= x_1 - x_3 \\ p_3 &= x_1y_2 - y_1x_2 \qquad & q_3 &= y_1 - y_2 \qquad & r_3 &= x_2 - x_1 \end{aligned} \tag{B26}$$

According to Silvester and Chari [B1], the energy functional of equation (B10), is minimized when the first derivative with respect to every vertex value is equal to zero.

For a problem with m elements the following system of equations is required [B1,B3]:

$$\sum_{i=0}^{m} \frac{\partial F_i}{\partial A_k} = 0 \tag{B27}$$

The method is now applied to problems involving the solution of (B1). The functional for this case is given by (B10). For the first term of equation (B10) in element i ,we have

$$\frac{\partial F_i}{\partial A_k}_{\text{first term}} = \int_{S_i} \frac{\partial}{\partial A_k}\left[\int_0^B H dB\right] dS_i \tag{B28}$$

which can be shown [B3] to reduce to the following expression:

$$\frac{\partial F_i}{\partial A_k}_{\text{first term}} = \frac{\nu}{2D}\sum_{j=1}^{3}\left(r_jA_jr_k + q_jA_jq_k\right) \tag{B29}$$

The second term of equation (B10) for element i can now be evaluated as follows:

$$\left.\frac{\partial F_i}{\partial A_k}\right|_{\text{second term}} = \int_{S_i} \frac{\partial}{\partial A_k}[-JA]dS_i = -J\int_{S_i} \frac{\partial A}{\partial A_k} dS_i \qquad \textbf{(B30)}$$

which reduces to [B3,B6]

$$-J\int_{S_i} \frac{\partial A}{\partial A_k} dS_i = -J\frac{D}{6} \qquad \textbf{(B31)}$$

B4.2 Local and Global Matrix Equations

The results of equations (B29) and (B31) are summarized in matrix notation as follows [B3]:

$$\begin{bmatrix} \frac{\partial F_i}{\partial A_1} \\ \frac{\partial F_i}{\partial A_2} \\ \frac{\partial F_i}{\partial A_3} \end{bmatrix} = \begin{bmatrix} S_{11} & S_{12} & S_{13} \\ S_{21} & S_{22} & S_{23} \\ S_{31} & S_{32} & S_{33} \end{bmatrix} \begin{bmatrix} A_1 \\ A_2 \\ A_3 \end{bmatrix} - \frac{D}{6}\begin{bmatrix} J \\ J \\ J \end{bmatrix} \qquad \textbf{(B32)}$$

where

$$S(n,k) = \frac{\nu}{2D}(q_n q_k + r_n r_k) \qquad \textbf{(B33)}$$

This defines a system of local matrices which apply to each individual element when the nodes are numbered from 1 to 3. For a problem with more than one element, the contribution to the system of equations by each element must be accounted for. For a problem with m elements, it is necessary to calculate this sum of the individual element contributions in accordance to equation (B27). This results in a global matrix which takes account of all the nodes of the mesh. Each element contributes a system similar to equation

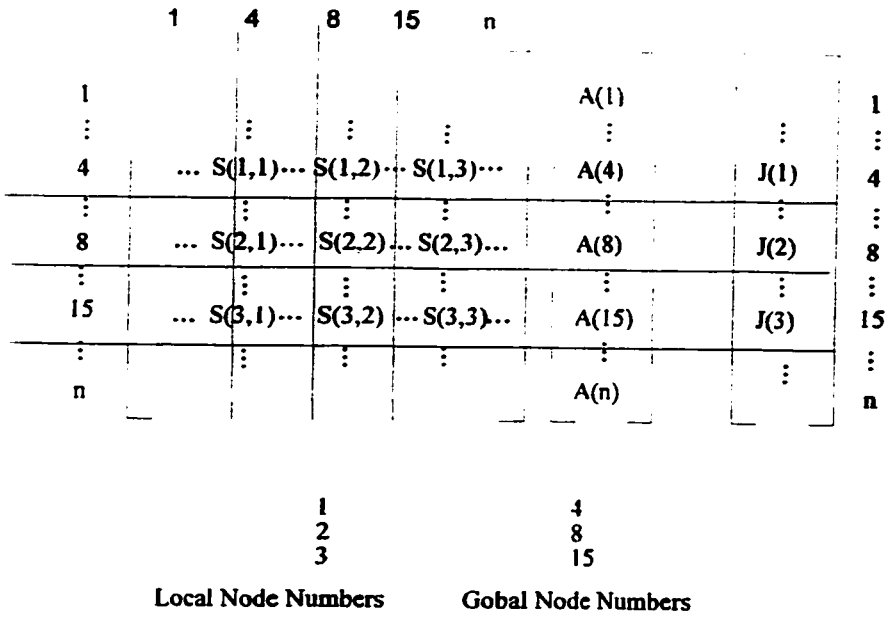

Figure B1 - Assembly of global matrix from local matrix contributions. Based on figure 8.19 in reference [B3]

(B32). The nodes numbered 1 through 3 for each element correspond to some global mesh numbers. The indices n and k in equation (B33) are replaced by these global mesh numbers and the resulting 3x3 S matrix of equation(B33) is placed into the global matrix SS which is n by n. Each element is evaluated and the 3x3 S matrix contributions are added to the SS matrix. A similar function is performed for the current density source terms. This procedure is illustrated in figure B1. The global system of equations is written [B3,B6]:

$$[SS][A] = [J] \qquad \textbf{(B34)}$$

The boundary conditions are imposed and the problem is then solved by an applying an appropriate algorithm for solving a system of equations.

B4.3 Boundary Conditions

A Dirichlet or unary boundary condition is encountered on a constant flux line boundary as is the case on the outer diameter of the machine yoke illustrated in figure B2. The imposition of the Dirichlet boundary condition is described by Silvester and Ferrari [B2] and Ida and Bastos [B3]. If a value of A is imposed at node i, the diagonal position of row i in matrix SS is set to one and all other coefficients in that row are set to zero. The known value of A is placed in row i of the J vector. Once the system of equations is solved, the value will be imposed. A Neumann boundary condition is imposed naturally [B2-B4]and if no other boundary condition is imposed, the magnetic flux lines will enter the boundary in a perpendicular direction. None of the problems modelled in this investigation make use of the Neumann boundary condition.

When analysing an electric machine, the problem is often modelled over one pole pitch of the machine and an anti-periodic or binary boundary condition is imposed. Briefly stated, the vector potentials along a radial line must be exactly the negatives of the corresponding vector potentials along another radial line one pole pitch away as illustrated in figure B2. Sivester and Ferrari [B2] describe the details of the algebraic implementation of this boundary condition as do Ida and Bastos [B3].

The procedure is explained by Ida and Bastos [B3]. The binary boundary condition is illustrated along the left and right edges of the one pole pitch model of the machine. Examine element 1 on the right. It's vertices are labelled i,j,k. Element 2 on the left has edge vertices labelled i' corresponding to vertex i and j' corresponding to vertex j in element 1. The binary boundary condition is implemented when the contributions to the global matrix made by nodes i and j (those that lie on the boundary) of element 1 are slightly modified. To do this, we treat these two vertices as if they belong to an element to the right of the pole edge in an identical image of the problem geometry in the next pole pitch. In this hypothetical adjacent pole pitch, the problem mesh and geometry would be identical to the

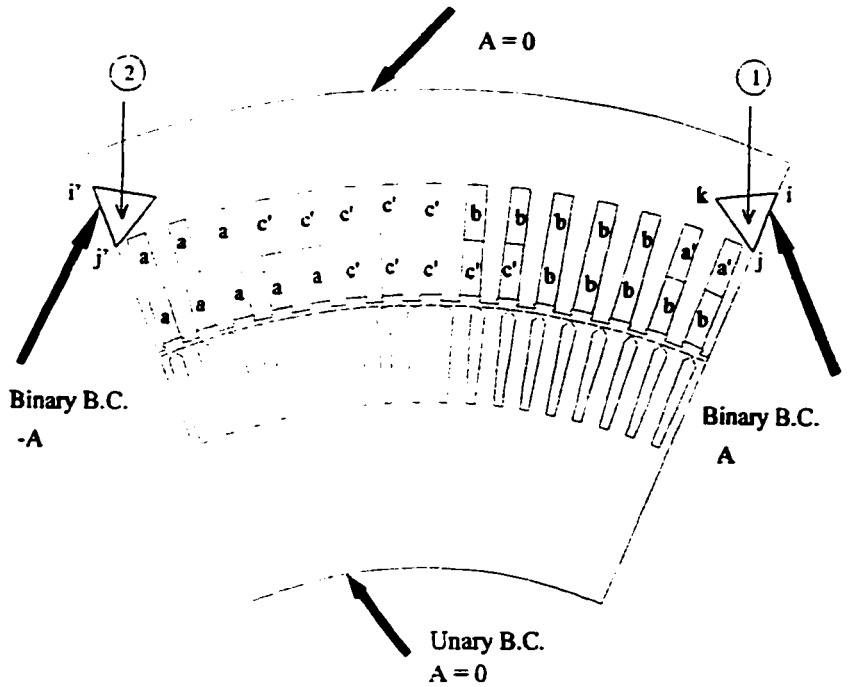

Figure 2 - Anti-periodic or binary boundary condition in an electric machine.

present one but the direction of the source current densities would be reversed. In other words, this hypothetical element would be identical to element 2, but the contributions of the edge vertices to the global matrix would be reversed. Earlier we saw that the contribution of an element to the global matrix is described by the local matrix defined in equation (B33). According to Ida and Bastos [B3], this equation is modified such that the off diagonal terms of the matrix are negated as shown in the equation

$$\begin{bmatrix} \dfrac{\partial F_i}{\partial A_i'} \\ \dfrac{\partial F_i}{\partial A_j'} \\ \dfrac{\partial F_i}{\partial A_k} \end{bmatrix} = \begin{bmatrix} S_{ii} & -S_{ij} & -S_{ik} \\ -S_{ji} & S_{jj} & -S_{jk} \\ -S_{ki} & -S_{kj} & S_{kk} \end{bmatrix} \begin{bmatrix} A_1 \\ A_2 \\ A_3 \end{bmatrix} - \frac{D}{6} \begin{bmatrix} -J \\ -J \\ J \end{bmatrix} \qquad \textbf{(B35)}$$

Note that if the element describes a source current density, the terms corresponding to the i and j vertices must be negated. The contribution made by node k is left unchanged. All elements on the right edge of the problem must be treated in similar fashion.

B4.4 Newton Raphson Method

The permeability (or reluctivity) within each element is dependent on the magnetic flux density. Ferromagnetic materials are characterized by an nonlinear BH curve. The assembly of the global matrix requires knowledge of permeability values for each element. In order to obtain these values before the solution is obtained, an iterative procedure must be employed. The Newton-Raphson procedure is often employed for this purpose.

According to Silvester and Ferrari [B2], the method is unconditionally stable and should yield an acceptable level of convergence in seven or eight steps. Silvester and Chari [B1] specify the Newton-Raphson method by forming the following iteration:

$$[A]^{m-1} = [A]^{m} - [JJ]^{-1}([SS]^{m}[A]^{m} - [J]) \qquad \textbf{(B36)}$$

where the Jacobian matrix [JJ] is given by

$$[JJ] = \frac{\partial}{\partial A_n}([SS][A])^{m} \qquad \textbf{(B37)}$$

Source terms are independent of A and therefore do not contribute to the Jacobian. F_i is non-zero only in element i. The derivatives are non-zero when taken with respect to one of the nodes of element i, such as A_n. Jacobian terms are given by Ida and Bastos [B3] as:

$$\frac{\partial}{\partial A_n}\frac{\partial F_i}{\partial A_k} = S(k,n) + \frac{4}{Dv^2}\frac{\partial v}{\partial B^2}\left[\sum_{\ell=1}^{3} S(k,\ell)A_\ell\right]\left[\sum_{\ell=1}^{3} S(n,\ell)A_\ell\right] \qquad \textbf{(B38)}$$

The reluctivity and its derivative with respect to the square of the flux density are easily found from the BH curves. Assembly of the above terms gives the global Jacobian and as pointed out by Ida and Bastos [B3] and Silvester and Ferrari [B2], equation (B36) can be re-arranged in the following form:

$$[JJ][\Delta A] = [R] \qquad \textbf{(B39)}$$

The residual vector [R] and it and the solution vector tend to zero as the iteration proceeds. The procedure for imposing the boundary conditions also applies for the Jacobian and the residual vector and Newton-Raphson algorithm proceeds as follows [B2,B3]:

1. An approximation to the A vector is made and the flux density in each element is found using equation (B3).
2. The reluctivities are found from the BH curve and their derivatives with respect to the square of the flux density are obtained from a plot of the reluctivity of the material vs. B squared.
3. The Jacobian of equation (B38) is formed and using the current A vector the residual vector [SS][A] - [J] is calculated.
4. The system in equation (B39) is solved.
5. Using the solution for [ΔA], the values of the A vector are updated.

Steps 1 through 5 are repeated until convergence is achieved.

B4.5 Solution of Equations

The final requirement for the FEM is to solve the system of equations given by

$$[SS][A] = [J] \qquad \text{or} \qquad [J][\Delta A] = [R] \qquad \textbf{(B40)}$$

MagNet 2D uses the Conjugate Gradient Method with matrix preconditioning via incomplete Cholesky Factorization to solve the equations. Both methods are described in [B2-B4].

B4.6 Time-Harmonic Formulation

The time-harmonic FEM formulation is described by Chari [B10]. The equation describing a nonlinear time-dependant problem in terms of the vector potential is [B2]:

$$\nabla x(\nu \nabla x\bar{A}) + \sigma\frac{\partial\bar{A}}{\partial t} = \bar{J}_s \qquad \textbf{(B41)}$$

where σ is the conductivity of the material and the term on the right hand side of the equation represents a source current density. Note that

$$\nabla x\bar{E} = = -\frac{\partial\bar{B}}{\partial t} = -\frac{\partial}{\partial t}(\nabla x\bar{A}) = \nabla x\left(-\frac{\partial\bar{A}}{\partial t}\right) \qquad \textbf{(B42)}$$

This is possible only if:

$$\bar{E} = -\frac{\partial\bar{A}}{\partial t} - \nabla\phi \qquad \textbf{(B43)}$$

Taking the curl on both sides forces the second term to disappear.

The imposed electric field is given by:

$$-\nabla\phi \qquad \textbf{(B44)}$$

and the induced electric field is given by:

$$-\frac{\partial\bar{A}}{\partial t} \qquad \textbf{(B45)}$$

The imposed source and the induced eddy current densities are expressed as:

$$J_s = -\sigma\nabla\phi \qquad \textbf{(B46)}$$

and

$$J_{eddy} = -\sigma \frac{\partial \bar{A}}{\partial t} \tag{B47}$$

Equation (B42) can be re-written in a slightly different form for the two dimensional case with a sinusoidal variation [B2]. Consider a geometry where the source current density exists only in the axial direction. Using the identity in equation (B4), we can write

$$\nabla^2 \hat{A}_z - j\mu\omega\sigma\hat{A}_z = -\mu\hat{J}_z \tag{B48}$$

where $\hat{A}_z$ and $\hat{J}_z$ are now complex phasor quantities. The current source density varies at frequency ω and the permeability is considered a constant quantity over each element.

The matrix equation representing the functional minimization given by Chari [B8] as:

$$\begin{bmatrix} \frac{\partial F_i}{\partial A_1} \\ \frac{\partial F_i}{\partial A_2} \\ \frac{\partial F_i}{\partial A_3} \end{bmatrix} = \begin{bmatrix} S_{11} & S_{12} & S_{13} \\ S_{21} & S_{22} & S_{23} \\ S_{31} & S_{32} & S_{33} \end{bmatrix} \begin{bmatrix} A_1 \\ A_2 \\ A_3 \end{bmatrix} + \begin{bmatrix} Q_{11} & Q_{12} & Q_{13} \\ Q_{21} & Q_{22} & Q_{23} \\ Q_{31} & Q_{32} & Q_{33} \end{bmatrix} \begin{bmatrix} A_1 \\ A_2 \\ A_3 \end{bmatrix} - \frac{D}{6} \begin{bmatrix} J \\ J \\ J \end{bmatrix} \tag{B49}$$

where

$$S(n,k) = \frac{\nu}{2D}(q_n q_k + r_n r_k) \tag{B50}$$

as before and,

$$Q(n,k) = \frac{j\omega D}{24\rho} \tag{B51}$$

$$Q(n,n) = \frac{j\omega D}{12\rho} \tag{B52}$$

A global matrix is formed from the local matrices defined above and the resulting system of complex linear equations is solved. Note that in this case the magnetic vector potentials and the source current densities are both complex numbers since they are expressed as phasor quantities.

B5.0 Higher Order Elements

Higher order elements are described by Silvester [B11]. When using second order triangular elements, the interpolation polynomial (prescribed for instance by Hoole [B4]) is

$$A(x,y) = a_1 + a_2x + a_3y + a_4x^2 + a_5xy + a_6y^2 \tag{B53}$$

An additional node is placed on the midpoint of each edge of the triangular element for a total of six nodes. Second order elements increase the accuracy of the FE solution at the cost of additional computation time. Higher order elements are not often employed in low frequency electromagnetic problems. Commonly, the number of first order elements used in the problem domain is increased in order to increase accuracy. Second order elements provide a first order approximation to the flux density in each element. This contrasted to the constant value for flux density obtained with first order elements.

References - Appendix B

[B1] P. Silvester, M.V.K. Chari, "Finite Element Solution of Saturable Magnetic Field Problems", IEEE Transactions on Power Apparatus and Systems, Vol. PAS-89, No. 7, September/October 1970, pp. 1642-1651.

[B2] P.P Silvester, R.L. Ferrari, Finite Elements for Electrical Engineers, Second Edition, Cambridge University Press, Cambridge 1983, 1990, ISBN 0 521 37219 4 hardcover, ISBN 0-521-37829-X paperback.

[B3] N. Ida, J.P.A. Bastos, Electromagnetics and Calculation of Fields, Springer-Verlag, New York, 1992, ISBN 0-387-97852-6.

[B4] S.R.H. Hoole, Computer-Aided Analysis and Design of Electromagnetic Devices, Elsevier Science Publishing Co., Inc., New York 1989, ISBN 0-444-01327-X.

[B5] M.V.K. Chari, P.P. Silvester (editors), Finite Elements in Electrical and Magnetic Field Problems, John Wiley and Sons, New York, 1980, ISBN 0-471-27578-6.

[B6] M.V.K. Chari, P. Silvester, "Analysis of Turboalternator Magnetic Fields by Finite Elements", IEEE Transactions on Power Apparatus and Systems, Vol. PAS-90, No. 2, March/April 1971, pp. 454-464.

[B7] J.C. Maxwell, "A Dynamical Theory of the Electromagnetic Field", printed in The Scientific Papers of James Clerk Maxwell-Volume I, pp. 526-597, Edited by W.D. Niven, Dover Publications Inc., New York, 1965, LCCN A53-9813.

[B8] J.C. Maxwell, A Treatise on Electricity & Magnetism - Volume 2, Dover Publications Inc., Third Edition, 1954, ISBN 0-486-60637-6

[B9] R. Courant, D. Hilbert, Methods of Mathematical Physics, Volume 1, Interscience Publishers, Inc., New York, 1953 LCCN 53-7164.

[B10] M.V.K. Chari, "Finite-Element Solution of the Eddy Current Problem in Magnetic Structures", IEEE Transactions on Power Apparatus and Systems, Vol. PAS-93, pp 62-72, 1974.

[B11] P. Silvester, "High-Order Polynomial Triangular Finite Elements for Potential Problems", International Journal of Engineering Science, Vol. 7. pp 849-861, 1969.

Publications to Date on the Topic of Rotational Iron Losses

1. R.D. Findlay, N. Stranges and D.K. MacKay, "Losses due to Rotational Flux in Three Phase Induction Motors," IEEE Trans. on Energy Conversion, Vol. 9, No. 3, Sept., 1994, pp 543-9.

2. R.D. Findlay and N. Stranges, "Importance of Rotational Iron Loss Data for Accurate Prediction of Rotating Machine Core Loss," Proceedings Industry Applications Society Annual Meeting, Denver, Oct.. 2-6, 1994, pp 123-7.

3. R.D. Findlay, N. Stranges and D.K. MacKay, "Losses due to Rotational Flux in Three Phase Induction Motors," Second International Workshop on Electric and Magnetic Fields, Leuven, Belgium, 17-20 May, 1994, 6 pages.

4. N. Stranges, R.D. Findlay, J.H.. Dymond, "A Comparison of Two Finite Element methods for Determining Flux Density Polarization in Induction Motor Cores", Proc. Canadian Conference on Electrical and Computer Engineering, Calgary, 26-29 May 1996, pp 943-6.

5. R.D. Findlay, N. Stranges, "Measurement of Iron Losses Under 2D Flux Conditions for Accurate Determination of Stator Losses," The Global Market and Technical Outlook for Soft Magnetic Materials '98, Barcelona, Spain, 20-22 April, 1998.

6. N. Stranges, R.D. Findlay, "Methods for Predicting Rotational Iron Losses in Three Phase Induction Motor Stators," presented at IEEE INTERMAG 2000, April 9-13, Royal York Hotel, Toronto, peer reviewed and accepted for publication in IEEE Transactions on Magnetics.

7. N. Stranges, R.D. Findlay, "Measurement of Rotational Iron Losses in Electrical Sheet Steel," presented at IEEE INTERMAG 2000, April 9-13, Royal York Hotel, Toronto, peer reviewed and accepted for publication in IEEE Transactions on Magnetics.

8. R.D. Findlay, N. Stranges, "Predicting Rotational Flux Distributions in Three Phase Induction Motor Stators," Presented at the Canadian Conference on Electrical and Computer Engineering, World Trade and Convention Centre, Halifax, May 7-10, 2000

Publications on Other Topics

9. R.D.Findlay, N.Stranges, R. Belmans, "Tank Wall Shielding: Effects of Positioning and Variegation of the Shields," International Workshop on Electric and Magnetic Fields, Liege, Belgium, 28-30, Sept., 1992, Paper #102, 6 pages.

10. J. Dymond, N. Stranges, K. Younsi, "Stator Winding Failures: Contamination, Surface Discharge, and Tracking," Presented at the 1999 IEEE Petroleum and Chemical Industry Committee (PCIC 1999) Technical Conference, US Grant Hotel, San Diego, CA, USA, September 13-15, 1999.

11. M. Clark, J. Dymond, J. Hayward, B. Moore, D. Snopek, K. Younsi, "Changing Insulation Systems - Benefits and Problems," Presented at the International Symposium on Electrical Insulation (ISEI 2000), Anaheim Convention Center and Disneyland Hotel, Anaheim, CA, USA, April 2-5, 2000

12. M. Clark, J. Dymond, R.H. Rehder, N. Stranges, "Impulse Testing is Not Surge Testing", Third Annual IRIS Rotating Machine Conference, Le Meridien, New Orleans, LA, USA, June 19-22, 2000